

The Pennsylvania State University
The Graduate School
Department of Materials Science and Engineering

COMPUTATIONAL MODELING OF HEAT TRANSFER AND
VISCO-PLASTIC FLOW IN FRICTION STIR WELDING

A Dissertation in
Materials Science and Engineering
by
Rituraj Nandan

© 2008 Rituraj Nandan

Submitted in Partial Fulfillment
of the Requirements
for the Degree of

Doctor of Philosophy

December 2008

The dissertation of Rituraj Nandan was reviewed and approved* by the following:

Tarasankar DebRoy
Professor of Materials Science and Engineering
Dissertation Advisor, Chair of Committee

Long-Qing Chen
Professor of Materials Science and Engineering

Christopher L. Muhlstein
Associate Professor of Materials Science and Engineering

Panagiotis Michaleris
Associate Professor of Mechanical Engineering

Joan M. Redwing
Professor of Materials Science and Engineering
Chair, Intercollege Materials Science and Engineering Graduate Degree
Program

*Signatures are on file in the Graduate School.

Abstract

Friction stir welding (FSW) is a relatively new welding technique and a review of pertinent literature reveals that a quantitative understanding of the process is just beginning. FSW is characterized by complex physical processes like non-Newtonian viscoplastic flow, frictional and deformational heat generation and stick-slip flow boundary condition at the tool workpiece interface. To add to the complexity, large convective heat transport aided by viscoplastic material flow makes the process three dimensional in nature. A review of literature reveals the following gaps in numerical modeling of FSW: (a) no three dimensional model exists which considers spatially variable heat generation, variable slip condition at the tool workpiece interface and viscoplastic flow, (b) robustness of existing models has not been tested by modeling FSW of different alloys, (c) the transport of alloying elements across weld interface in dissimilar welds has not been studied numerically and (d) the existing models do not have mechanism for improving reliability and they cannot work backwards, i.e. provide a set of welding process variables that will result in the desired weld characteristics. The goal of this thesis is to address these important issues.

With a focus to develop a quantitative understanding of the FSW process, a comprehensive three dimensional heat transfer and plastic flow model is developed. The model can predict variables such as temperature and velocity fields and torque based on the given welding parameters like weld velocity, tool rotational speed and axial pressure. It considers tool design dependent spatially variable heat generation rates, deformational work, non-Newtonian viscosity as a function of local strain rate, temperature and the nature of the material and temperature dependent thermal conductivity, specific heat capacity and yield stress. It is shown that the temperature fields, cooling rates, the plastic flow fields and the geometry of the thermo-mechanically affected zone (TMAZ) can be adequately described by solving the equations of conservation of mass, momentum and energy in three

dimensions with appropriate boundary conditions and constitutive equations for viscosity. The model is tested for four different alloys: 1) AA 6061-T6, 2) 1018 Mn steel, 3) 304L stainless steel and 4) Ti-6Al-4V which have widely different thermophysical and rheological properties. Numerically computed temperature fields, variations of peak temperatures with FSW variables and TMAZ geometry were compared with the experimental results.

Currently, due to unknown parameters in existing transport phenomena based models, the computed temperature and velocity fields and torque may not always agree with the corresponding experimentally determined values and may not show the same trend as experimental results for a range of welding variables. Here, it is shown that this problem can be solved by combining the rigorous phenomenological process sub-model with a multivariable optimization scheme called Differential Evolution. The values of the uncertain model input parameters from a limited volume of independent experimental data which includes temperature measurements obtained using thermocouples and torque measured using dynamometers. This approach resulted in agreement between the phenomenological model and the experimental results with a greater degree of certainty. It is tested for FSW of: 1) dissimilar AA 6061-T6 to AA 1200, 2) 1018 Mn steel and 3) Ti-6Al-4V. Independent thermocouple and dynamometer measurements are also used for validation and verification of results. Improvement in the reliability of the numerical model is an important first step towards increasing its practical usefulness.

Also, one of the reasons why current models do not find extensive applications is because they cannot be used to tailor weld attributes. The aim of the present research is to develop a reliable bi-directional model which can find wide use in manufacturing and process control. It is shown that by coupling a reliable model with an evolutionary search algorithm, we can find multiple sets of welding parameters to achieve a target peak temperature and cooling rate in welds. The model is tested for dissimilar welds of AA 6351 and AA 1200.

FSW is being increasingly used for dissimilar metal joining. Models are needed to calculate the redistribution of alloying elements when two alloys with dissimilar alloying element contents are joined. The transport and mixing of magnesium from Mg-rich AA 6061 alloy into a commercially pure aluminum AA 1200 was examined experimentally and numerically at various locations in the welded workpiece. The concentration of the solute is measured in transverse cross-sections across the weld-center line at various depths from the top surface of the workpiece. The measurement was done using electron probe micro-analysis (EPMA) of polished transverse-cut friction-stir welded samples. The comparison of the experimental and computed concentration profiles of magnesium shows imperfect mixing of the plasticized alloys during FSW. The plasticized material seem to move in layers without significant diffusive interlayer mixing.

A comprehensive model for FSW is developed with capability of calculating temperature fields, material flow patterns and concentration fields in both similar and dissimilar welds in three dimensions. The model is tested for the FSW of alloys with widely different thermophysical properties. A mechanism for improving reliability and ability to provide guidance to tailor weld attributes is incorporated into the model to increase its practical usefulness. This is done by combining the transport phenomena based model with Differential Evolution algorithm to minimize the objective function based on limited volume of experimental thermal cycles and torque measurements.

Table of Contents

List of Figures	ix
List of Tables	xvii
Acknowledgments	xix
Chapter 1	
Introduction	1
1.1 General Background	1
1.2 Important Issues	2
1.3 Thesis Layout	7
Chapter 2	
Background	9
2.1 Principles of heat transfer and material flow in FSW	10
2.2 Asymmetry in heat transfer and plastic flow	21
2.3 Nature of plasticized material and its flow	25
2.4 Heat generation rate and torque	33
2.4.1 Welding variables	35
2.5 Peak temperature	37
2.6 Tool Design	38
2.7 Defects	42
2.8 Residual Stresses	44
2.9 Current status and needs	48
Chapter 3	
Heat transfer and viscoplastic flow	51
3.1 Mathematical Formulation	53

3.1.1	Assumptions	53
3.1.2	Governing equations	54
3.1.3	Boundary conditions	56
3.2	Numerical scheme	60
3.3	Results and discussion	63
3.3.1	Materials and thermophysical properties	63
3.3.2	Heat generation rate and torque	64
3.3.2.1	AA 6061	64
3.3.2.2	1018 steel	65
3.3.2.3	304L stainless steel	68
3.3.3	Computed temperature fields	70
3.3.3.1	AA 6061	70
3.3.3.2	1018 Mn steel	74
3.3.3.3	304L stainless steel	75
3.3.3.4	Ti-6Al-4V	77
3.3.4	Dimensional Analysis	78
3.3.5	Computed viscosity and plastic flow fields	81
3.3.6	Shape of TMAZ	87
3.3.7	Pressure Distribution in the flow regime	89
3.3.8	Material condition in flow region	92
3.3.9	Effect of Material Properties on Heat Transfer	93
3.4	Summary and conclusions	95

Chapter 4

	Enhancement of model reliability and tailoring weld attributes	97
4.1	Improving reliability	97
4.1.1	Uncertain parameters	98
4.1.2	Sensitivity to uncertain parameters	100
4.1.2.1	Ti-6Al-4V alloy	101
4.1.2.2	1018 Mn Steel	102
4.1.2.3	AA 6061-T6 to AA 1200	106
4.1.3	Differential Evolution	107
4.1.3.1	Initialization	108
4.1.3.2	Mutation	109
4.1.3.3	Crossover	111
4.1.3.4	Selection	113
4.1.4	Results	113
4.1.4.1	FSW of Ti-6Al-4V	113
4.1.4.2	FSW of 1018 Mn steel	116
4.1.4.3	FSW of AA 6061-T6 to AA 1200	118

4.2	Tailoring weld attributes	121
4.3	Results	123
4.4	Summary and conclusions	129
Chapter 5		
	Species transport in dissimilar metal joining	131
5.1	Experiments	132
5.2	Mathematical model	133
5.3	Results and Discussion	135
5.4	Summary and conclusions	145
Chapter 6		
	Concluding Remarks	146
6.1	Summary and conclusions	146
6.2	Future Work	150
Appendix A		
	Numerical solution of governing equations for heat transfer and plastic flow	153
Appendix B		
	Calculation of heat generated at the pin's vertical surface	157
	Bibliography	160

List of Figures

1.1	Schematic illustration of the friction stir welding process.	2
1.2	Inter-relation between sub-models of FSW.	4
1.3	Steps in the development of a reliable and bi-directional heat transfer and viscoplastic flow model in FSW.	6
2.1	Schematic of Kolsky pressure bar with infrared temperature measurement.	12
2.2	Fraction β of plastic work rate converted into heating as a function of plastic strain for rate-sensitive α -titanium.	14
2.3	Fraction β of plastic work rate converted into heating as a function of plastic strain for rate-insensitive AA 2024-T351.	14
2.4	Temperature distribution along the intersection of horizontal mid-plane and transverse plane through the tool axis, for FSW of stainless steel	22
2.5	Stream traces on different horizontal planes (a) 0.35 mm, (b) 1.59 mm and (c) 2.28 mm below the top surface for a 304 stainless steel plate of thickness 3.18 mm. Welding speed 4 mm s ⁻¹ with tool rotation at 300 rpm.	24
2.6	Streamlines for isothermal model that used a limiting shear stress of 40 MPa: a) <i>Triflute</i> tool, b) single streamline for <i>Triflute</i> tool showing vertical movement and c) Trivex tool. Tool rotation 457 rpm and translation at 457 mm min ⁻¹	26
2.7	Schematic cross-section of a typical FSW weld showing four distinct zones: (A) base metal, (B) heat-affected, (C) thermomechanically affected and (D) stirred (nugget) zone.	27
2.8	“Stop action” technique to capture material flow patterns during FSW. An enlargement of the AA 6061 specimen in the region behind the pin after the pin has been extracted. A: area with no material filling behind the pin, B: fully filled threads and C: material filling behind the pin from below.	27

2.9	Optical image showing the macroscopic features in a transverse section of a friction stir welded material. Note the onion ring and the adjacent large upward movement of material.	28
2.10	Analogy between chip morphology in machining and material flow in FSW	29
2.11	Concentration profiles of Fe and Ni at a location in stir region for FSW of pure Fe and Ni. Points represent data obtained by atomic emission spectroscopy and the solid lines indicate computed results.	31
2.12	Computed contours of \log_{10} (viscosity in Pa s) as a function of temperature and strain rate for AA 6061-T6.	31
2.13	Spatial variation of viscosity and velocity in AA 6061-T6 at planes corresponding to $z = 1.27, 4.67, 8.07$ and 11.47 mm for a plate thickness of 12.7 mm. Distances in x and y direction were equivalent, but that in the z -direction was increased eight fold to enhance clarity. The welding velocity was 1.59 mm s^{-1} and the rotational speed was 637 rpm.	32
2.14	Heat input at various welding speeds used to weld 6.35 mm thick AA 7075-T7351 plates using MX-Triflute, MX-Trivex and Trivex tools.	34
2.15	Variation of torque on the tool with weld pitch.	35
2.16	Relationship between rotational speed and peak temperature in FS-welds of AA 6063.	36
2.17	Relationship between (a) peak temperature and grain size in AA 6063 and (b) grain size and volume fraction of PFZs.	38
2.18	Material condition maps for a) Triflat, b) Trivex and c) Cylindrical tool pin at 80 and 200 rpm.	43
2.19	Void formation at the lower advancing side due to incomplete filling modeled using ALE formulation of FEM. Temperature contours are shown in $^{\circ}C$	45
2.20	Measured (a) longitudinal x -direction and (b) the lateral y -direction stresses in AA5083 welds at different welding speeds.	46
2.21	Normal stresses in Pa in (a) the longitudinal x -direction, (b) the lateral y -direction and (c) the vertical z -direction when the tool is mid-way between the two ends of AA 6061 weld plates.	47
3.1	Computed contours of \log_{10} (viscosity in Pa s) as a function of temperature and strain rate for (a) AA 6061-T6, (b) 1018 C-Mn steel. (c) 304L stainless steel and (d) Ti-6Al-4V.	56

3.2	Variations of (a) yield strength (b) thermal conductivity and (c) specific heat capacity of AA 6061-T6 with temperature. Symbols denote data points from literature while the curves are obtained by spline interpolation of the data points.	57
3.3	Interfaces for heat generation in FSW: (1) Tool shoulder, (2) Tool pin's vertical surface and (3) Tool pin's bottom surface-workpiece. .	58
3.4	Influence of forming velocity and forming angle on the accumulative global slip for cross-wedge rolling when tool translation velocity is 1.0 m/s in AA 1100.	59
3.5	Top view of the rotating tool moving in the negative x-direction. $\theta = 0$ corresponds to plane $y = 0, x < 0$	60
3.6	A typical grid mesh used for calculations, with length in z-direction increased 20 fold to enhance clarity.	62
3.7	Spatially variable heat generation rate in 1018 Mn steel at (a) tool shoulder, (b) bottom of tool pin (contour values are in kW/m^2), and (c) curved surface of tool pin. The welding velocity was 0.42 mm/s and the rotational speed was 450 rpm.	66
3.8	Heat generation rate for the welding of 304L stainless steel increases with increase in welding velocity. Peak temperature in the work-piece still decreases.	68
3.9	Computed temperature profiles (K) in (a) y-plane, (b) x-plane and (c) z-plane <i>i.e</i> top surface of 12.7 mm thick workpiece of AA 6061-T6 welded with tool translational speed of 1.59 mm/s and rotational speed of 344 rpm.	71
3.10	Obtaining thermal cycle from steady state temperature profile. . . .	72
3.11	Comparison between experimental and calculated time-temperature profile in AA 6061-T6 at points (a) 2 mm below the top surface and 8 mm from the centerline, (b) 2 mm below the top surface and 16 mm from the centerline, (c) 8 mm below the top surface and 8 mm from the centerline and (d) 8 mm below the top surface and 16 mm from the centerline. The points are located in advancing side and the distances are perpendicular to the weld center line. The welding velocity was 1.59 mm/s and the rotational speed was 637 rpm.	73
3.12	Comparison between experimental and calculated time-temperature profile at two points on the top surface a) at a distance of $y = 16.7$ mm on the advancing side b) at a distance of $y = 16.7$ mm on the retreating side. The welding velocity was 0.4 mm/s and the rotational speed was 450 rpm. Other process and model parameters are given in Table 3.8.	74

3.13	Plot of temperature and velocity fields at $z = 2.78, 1.72,$ and 0.66 mm planes. The welding velocity was 1.693 mm/s and the rotational speed was 300 rpm. Other process and model parameters are given in Table 3.8.	75
3.14	Comparison between experimental and computed thermal cycles in 304L stainless steel at three monitoring locations on the top surface of the retreating side at distances of 18 mm, 21 mm and 26.5 mm from the weld centerline. The welding velocity was 1.693 mm/s and the rotational speed was 300 rpm. Other process and model parameters are given in Table 3.8.	76
3.15	Computed temperature profiles (K) in (a) y-plane, (b) xz-plane and (c) z-plane <i>i.e</i> top surface of 7.2 mm thick workpiece of Ti-6Al-4V alloy welded with translational speed of 1.6 mm/s and rotational speed of 275 rpm.	77
3.16	Variation of dimensionless peak temperature with dimensionless heat input.	79
3.17	Plot of variation of (a) u-velocity and (b) v-velocity as a function of distance from tool surface for corresponding to $z = 11.47, 8.07, 4.67$ and 1.27 mm for a 12.7 mm thick plate of AA 6061, where z is the vertical distance from the bottom of the workpiece. The welding velocity was 1.59 mm/s and the rotational speed was 344 rpm. The thickness of the workpiece was 12.7 mm.	82
3.18	Plot of variation of (a) x-direction velocity and (b) y-direction velocity as a function of distance from tool surface for corresponding to $z = 0.64, 2.33, 4.02$ and 5.72 mm planes in 1018 Mn steel, where z is the vertical distance from the bottom of the workpiece. The thickness of the workpiece was 6.22 mm.	83
3.19	Computed strain rate in (a) AA 6061, (b) 1018 Mn steel and (c) 304L stainless steel, decreases along the weld centerline, away from the tool pin surface opposite to the welding direction at different horizontal planes. The plot labels indicate the vertical distance from the bottom of the workpiece in mm. The thickness of the three workpieces are given in Table 3.8.	84
3.20	Variation of viscosity in (a) AA 6061 (b) 1018 Mn steel and (c) 304L stainless steel, as a function of distance from the tool pin surface opposite to the welding direction. The plot labels indicate the vertical distance from the bottom of the workpiece in mm. The thickness of the three workpieces are given in Table 3.8.	86

3.21	Viscosity contours in (a) AA 6061 at 344 RPM and 1.59 mm/s, (b) 1018 Mn Steel at 528 RPM and 0.42 mm/s, (c) 304 L stainless steel at 300 RPM and 1.69 mm/s and (d) Ti-6Al-4V at 275 RPM and 1.6 mm/s.	87
3.22	Streamline in 1018 Mn steel on horizontal planes (a) $z=5.72$ mm, (b) 4.02 mm and (c) 0.64 mm. The welding velocity was 0.42 mm/s and the rotational speed was 450 rpm.	88
3.23	Side view of workpiece showing computed movement of four different tracer particles around the tool pin in Ti-6Al-4V welds performed at rotational speed of 275 rpm and welding velocity of 1.6 mm/s.	89
3.24	(a) Computed iso-viscosity surface (5×10^6 Pa-s) that defines viscoplastic flow region and TMAZ geometry and (b) Comparison of the numerically computed thermo-mechanically affected zone (TMAZ) geometry with corresponding experimentally determined macrostructure. The welding velocity was 1.59 mm/s and the rotational speed was 637 rpm.	90
3.25	Distribution of pressure around the tool at different elevations in the workpiece: (a) $z = 1$ mm, (b) $z = 3$ mm, (c) $z = 5$ mm and (d) $z = 7$ mm for 7.2 mm thick workpiece of Ti-6Al-4V welded at rotational speed of 275 rpm and welding velocity of 1.6 mm/s. . . .	91
3.26	Computed pressure distribution at mid-plane in plasticine.	91
3.27	In Ti-6Al-4V, welded at rotational speed of 275 rpm and welding velocity of 1.6 mm/s, computed pressures are high in front of the tool, resisting tool motion. Contour labels indicate pressure in MPa.	92
3.28	Flow stress, temperature and strain-rate condition in the stir zone of Ti-6Al-4V at: (a) 100 RPM and (b) 550 RPM indicated using density plot. The contour labels indicate strain-rate in s^{-1} . The shaded region indicates the material condition in the stir zone. . . .	92
3.29	Temperature contours in yz-plane showing asymmetry across the weld centerline, with higher temperatures in the advancing side for (a) AA 6061-T6, (b) 1018 C-Mn steel. (c) 304L stainless steel and (d) Ti-6Al-4V. The computation was performed for the with the same welding process parameters for all four alloys. The shoulder radius of 10 mm, pin radius of 3 mm, axial pressure of 25 MPa, welding velocity of 2mm/s and tool rotational speed of 600 RPM. . . .	94

3.30	Plot of asymmetry in temperature across the weld centerline as a function of Peclet number for three different sets of welding velocity and rotational speeds indicated. The computation was performed for the same tool dimension (shoulder radius = 10 mm and pin radius = 3mm) and same axial pressure of 25 MPa for all four alloys.	95
4.1	Definition of width of thermal cycle.	101
4.2	Computed dimensionless values of peak temperature, width of the temperature cycle and the torque with change in (a) slip, (b) friction coefficient, (c) heat transfer coefficient at the bottom surface, (d) mechanical efficiency and (e) scaling factor for plastic deformational heat generation rate for the FSW of Ti-6Al-4V alloy. In each case, when one of the parameters is varied, other parameters were kept constant. The welding velocity was 1.6 mm/s and the rotational speed was 275 rpm.	103
4.3	Computed dimensionless values of peak temperature, width of the thermal cycle and the torque with change in (a) friction coefficient, (b) slip, (c) heat transfer coefficient at the bottom surface, (d) mechanical efficiency and (e) scaling factor for plastic deformational heat generation rate for the FSW of 1018 Mn steel. In each case, when one of the parameters is varied, other parameters were kept constant. The welding velocity was 0.42 mm/s and the rotational speed was 450 rpm.	104
4.4	Computed dimensionless values of peak temperature, width of the thermal cycle and the torque with change in (c) friction coefficient, (b) slip, (c) heat transfer coefficient at the bottom and (d) scaling factor for plastic deformational heat generation rate for the FSW of dissimilar aluminum alloys. In each case, when one of the parameters is varied, other parameters were kept constant. The welding velocity was 0.42 mm/s and the rotational speed was 450 rpm.	106
4.5	Differential Evolution algorithm. MF denotes the mutation factor.	109
4.6	Schematic of mutation in 2D space showing how mutant vector \vec{V}_m is produced by adding a weighted differential vector, $MF \cdot (\vec{V}_1 - \vec{V}_2)$ to the base vector \vec{V}_0 .	110
4.7	Schematic of bounce-back in 2D space showing how new mutant vector \vec{V}_m is obtained if the original mutant vector falls outside the upper boundary constraint of variable x_1 . The first sub-script denotes direction while second sub-script denotes vector. For <i>e.g.</i> $x_{1,2}$ denotes component of vector 2 in direction 1.	111
4.8	Uniform crossover in DE.	111

4.9	Effect of crossover probability on population evolution. The problem and its objective function are defined in section 4.2	112
4.10	Comparison between experimental and calculated temperature profile (indicated as dashed lines) obtained using optimized parameters: $\mu_0 = 0.7$, $\delta_0 = 2.8$, $h_{b0} = 418W/m^2 - K^{5/4}$, $\eta = 0.7$, $\beta = 0.1$. Locations 1, 2 and 3 are indicated in Table 4.2. The distance is measured from the interface between the two plates.	115
4.11	Comparison between experimental and calculated time-temperature profile at the top surface, 12.7 mm away from the centerline on the advancing side. The welding velocity was 0.42 mm/s and the rotational speed was 450 rpm.	117
4.12	Performance of DE with iterations.	120
4.13	Thermal cycle in (a) advancing and (b) retreating sides of dissimilar welds of AA 6061 (advancing) and AA 1200 (retreating) at rotational speed of 710 RPM, translational speed of 0.67 mm/s and axial pressure of 18.47 MPa.	121
4.14	Thermal cycle in advancing and retreating sides of AA 6351-AA 1200 dissimilar weld performed at 355 RPM and 0.67 mm/s with axial force of 4.7kN. Solid lines indicate advancing side while broken lines indicate retreating side. Experimentally measured values are indicated in color (gray in BW) while computed thermal cycles are indicated in black. (For interpretation of the references to color in this figure legend, the reader is referred to the electronic version of the thesis.)	126
4.15	Performance of DE with iterations.	127
4.16	Comparison of target thermal cycle with that obtained using differential evolution. Solid lines indicate advancing side while broken lines indicate retreating side. Experimentally measured values are indicated in color (gray in BW) while computed thermal cycles are indicated in black. The calculated thermal cycles correspond to the set of welding parameters in Table 4.9. (For interpretation of the references to color in this figure legend, the reader is referred to the electronic version of the thesis.)	129
5.1	Comparison between experimental and calculated time-temperature profile at a point 13 mm away from the centerline on the advancing side. The welding velocity was 1.05 mm/s and the rotational speed was 710 rpm.	136

5.2	Stream-lines in a horizontal plane (a) 3.66mm and (b) 7mm below the top surface, showing plastic flow during FSW. Material flows along the retreating side around the pin, and a stagnant zone forms in the advancing side. The welding velocity was 1.05 mm/s and the rotational speed was 710 rpm.	137
5.3	(a) Measured and (b) computed concentration profile of Mg at depths of 1, 3 and 5 mm from the top surface, across the weld center-line for AA 6061 (advancing) and AA 1200 (retreating side) weld at 710 RPM and a weld velocity of 1.05 mm/s.	138
5.4	(a) Measured and (b) computed concentration profile of Mg at depths of 1, 3 and 5 mm from the top surface, across the weld center-line for AA 1200 (advancing) and AA 6061 (retreating side) weld at 710 RPM and a weld velocity of 1.05 mm/s.	139
5.5	Comparison between computed and measured concentration profiles in a transverse weld cross-section of AA 6061 (advancing side) and AA 1200 (retreating) along line 1 mm below the top surface. The rotational speed was 710 RPM and a welding velocity of 1.05 mm/s.	140
5.6	Computed concentration profile for magnesium (wt%) near the tool for AA 1200 (retreating) and AA 6061 (advancing side) weld in horizontal planes corresponding to depths of (a) 1, (b) 3 and (c) 5 mm from the top surface. The rotational speed was 710 RPM and a welding velocity of 1.05 mm/s.	141
5.7	(Computed concentration profile for magnesium (wt%) near the tool for AA 1200 (advancing) and AA 6061 (retreating side) weld in horizontal planes corresponding to depths of (a)1, (b) 3 and (c) 5 mm from the top surface. The rotational speed was 710 RPM and the weld velocity was 1.05 mm/s.	142
5.8	Top surface of plasticine welds showing material flow.	143
5.9	Tomographic volume data depicting Ti-marker flow in AA 2024 T351 alloy, with two different tool pins: 1) conical and threaded and 2) conical, threaded with flats. The markers were placed in both A) advancing and R) retreating sides.	144
6.1	A schematic diagram showing dissolution and re-precipitation in age-hardenable aluminum alloys. HV denotes the Vickers hardness number.	151
B.1	Calculation of intercepted arc length for rectangular grids.	158

List of Tables

2.1	Material parameters for the simplified Harts model for annealed 304 stainless steel.	19
2.2	Temperature dependent thermophysical properties of various work-piece and tool materials.	20
2.3	A selection of tools designed at TWI.	39
3.1	Reported values of friction coefficient, μ_f	61
3.2	Reported values of slip, δ	61
3.3	Reported values of bottom heat transfer coefficient, h_b	61
3.4	Reported values of mechanical efficiency, η	61
3.5	Effect of mesh refinement on predicted process variables. Coarse mesh had 300288 grid points ($96 \times 92 \times 34$) while fine mesh had 522648 grid points ($126 \times 122 \times 34$).	63
3.6	Tool and workpiece materials for systems modeled in this research .	64
3.7	Temperature dependent thermophysical properties of various work-piece and tool materials.	65
3.8	Data used in calculations	67
3.9	Heat generation rate at different tool–workpiece interfaces, peak temperature and total torque on the tool for different welding parameters in AA 6061. Process and model parameters are given in Table 3.8.	68
3.10	Heat generation rate at different tool–workpiece interfaces, peak temperature and total torque on the tool for different welding parameters in 1018 Mn steel. Process and model parameters are given in Table 3.8.	69
3.11	Comparison between peak temperatures obtained using 3D calculation and using non-dimensional relation 3.17.	80
3.12	Peclet number for different alloys.	93
4.1	Optimized sets of uncertain parameters after 200 iterations and the corresponding objective functions, with best set indicated in bold. .	114

4.2	Position of thermocouple, measured peak value and widths of thermal cycles.	115
4.3	Optimized sets of uncertain parameters after 50 iterations and the corresponding objective functions, with best set indicated in bold. .	116
4.4	Input data used for calculations. Thermophysical properties are obtained by curve-fitting of temperature dependent data available in <i>ASM Handbook</i> and <i>Smithells Metals Reference book</i>	119
4.5	Optimized sets of uncertain parameters after 25 iterations and the corresponding objective functions, with best set indicated in bold. .	121
4.6	Data used in calculations.	123
4.7	Measured thermal cycle attributes used for determining the uncertain parameters.	124
4.8	Optimized sets of uncertain parameters after 50 iterations and the corresponding objective functions, with best set indicated in bold. .	125
4.9	Various combinations of welding variables, <i>i.e.</i> , welding velocity and tool rotational speed, obtained using Differential Evolution to achieve the following target thermal cycle: advancing side (12.7 mm from weld centerline) peak temperature = 610 K, retreating side (12.7 mm from weld centerline) peak temperature = 605 K, width of thermal cycle in advancing side at 250°C = 29 mm and width of thermal cycle in advancing side at 300°C = 16 mm.	127
5.1	Input data used for calculations. Thermophysical properties are obtained by curve-fitting of temperature dependent data available in <i>ASM Handbook</i> and <i>Smithells Metals Reference book</i>	134
5.2	Constants used in constitutive equation for viscosity.	135
B.1	Arc angles calculated for Fig. B.1 ($R = 2.0$, $\Delta x = 0.97$, $\Delta y = 0.726666$).	159

Acknowledgments

This thesis is the result of four years of work at Penn State whereby I have been accompanied and supported by many people. I would first like to express my deep appreciation and sincere gratitude to my adviser, Dr. Tarasankar DebRoy. He gave me many opportunities to advance my research as well as my professional development. His enthusiasm and integral view on research has made a deep impression on me. I owe him lots of gratitude for his guidance.

I would like to acknowledge Dr. Long-Qing Chen, Dr. Christopher Muhlstein and Dr. Panagiotis Michaleris for their valuable advice and suggestions on my work while serving on my thesis committee. I am very appreciative to them for giving their time to review and comment on this thesis. I would also like to express my thanks to Dr. Thomas J. Lienert at Los Alamos National Laboratory, Dr. Gour Gopal Roy at Indian Institute of Technology, Kharagpur and Dr. Amitava De at Indian Institute of Technology, Bombay for their helpful discussions on various topics during the progress of my research work and also for their help in code-writing.

Many thanks to the senior members of my research group, Dr. Amit Kumar, Dr. Xiuli He and Dr. Saurabh Mishra, who helped me get started with my research and also helped me adjust in a new environment. I am also indebted to my current colleagues Mr. Rohit Rai, Mr. Brandon Ribic and Mr. Amit Arora not only for their help in my research but also for keeping the workplace lively. I am also grateful to my friend, Dr. Ravindra Akarapu, for his keen interest in my work and patient help with code debugging.

I am grateful to my family and friends for their love, support and constant encouragement. My parents made many sacrifices and had to forgo many pleasures

in life to support their children and give them a good education and I am greatly indebted to them. I am also grateful to my Kanjhle Papa. His passion for science and mathematics was a constant source of motivation.

Finally, I am also grateful to the American Welding Society Foundation, which provided me with a graduate fellowship and to the Office of Naval Research for supporting my research at Penn State.

Dedication

To my parents, Ram Nandan Prasad and Rupa Prasad

Introduction

1.1 General Background

Friction stir welding (FSW) is a solid-state, hot-shear joining process [1, 2] in which a rotating tool with a larger-diameter shoulder and terminating in a smaller-diameter threaded pin, moves along the butting surfaces of two rigidly clamped plates placed on a backing plate as shown in Fig. 1.1. The shoulder makes firm contact with the top surface of the work-piece. Heat generated by friction at the shoulder and to a lesser extent at the pin surface, softens the material being welded. Severe plastic deformation and flow of this plasticised metal occurs as the tool moves along the length of the plate. Material is transported from the front of the tool to the trailing edge where it is forged into a joint.

Since its discovery in 1991 [2], FSW has evolved as a widely used technique in the joining of aluminum components; its applications for joining difficult metals and metals other than aluminum are growing, albeit at a slower pace. There have been widespread benefits resulting from the application of FSW in aerospace, shipbuilding, automotive and railway industries [3].

In Fig. 1.1, the *advancing* side corresponds to the plate over which the direction of tool rotation is same as the tool translation direction and the other side is called the *retreating* side. In the advancing side the relative velocity between the tool and the work-piece goes through a maximum while it goes through a minimum in the retreating side. This difference can lead to asymmetry in heat transfer [4], material flow and the properties of the two sides of the weld. For example, the hardness

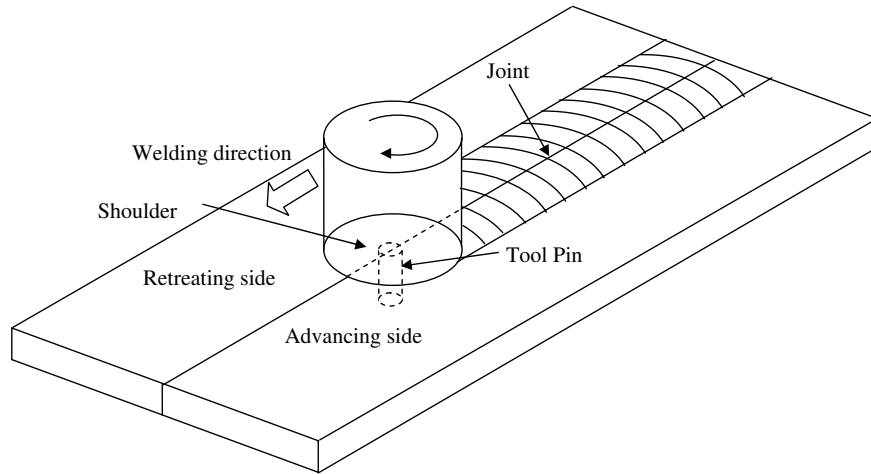


Figure 1.1. Schematic illustration of the friction stir welding process.

of particular age-hardened aluminum alloys tends to be lower in the heat-affected zone on the retreating side, which then becomes the location of tensile fracture in cross-weld tests [5]; this is also the case for pure titanium [6]. Any quantitative model for FSW must be able to predict the asymmetry due to asymmetrical heat transfer away from the weld-centerline.

Even though there is no molten metal involved in FSW, visco-plastic flow of the workpiece material takes place close to the rotating tool. The heat and mass transfer depend on material properties as well as welding variables including the rotational and welding speeds of the tool and its geometry. In FSW, the joining takes place by extrusion and forging of the metal at high strain rates. Jata and Semiatin [7] estimated a typical deformation strain rate of 10 s^{-1} by measuring grain-size and using a correlation between grain-size and Zener-Holloman parameter which is temperature compensated strain-rate [7]. Kokawa *et al.* estimated an effective strain rates in the range 2 to 3 s^{-1} [8]. The plastic flow must clearly feature in any theory for the process, and the behavior of the metal at high strain rates and the effects of heating and cooling rates must also be considered.

1.2 Important Issues

Understanding heat transfer during FSW is essential for understanding the weld attributes. Initial 2D conduction-based models are inadequate to accurately pre-

dict the temperature profile in welds. Most of the previous efforts to model heat transfer did not consider three dimensional nature of the problem and the convective heat transfer due to visco-plastic flow. Previously, only two 3D modeling efforts have been reported. Ulysse [9] used a solid mechanics approach assuming a rigid visco-plastic material where the flow stress depended on strain rate and temperature. Colegrove and Shercliff [10] computed material flow in 3D using the computational fluid dynamics software *FLUENT*, for the friction stir welding of 7075 Al alloy. However, in both cases, much higher temperatures were predicted than that measured using thermocouples. Therefore, there is a need for reliable 3D model for plastic flow in FSW to accurately calculate the convective heat transfer which will lead to accurate thermal cycles in weld. Also, there remain several unanswered questions. For example, can the visco-plastic flow of metals be reliably predicted based on the previous work in extrusion and thermo-mechanical processing of metals? Can our current understanding of thermo-mechanical processing adequately represent the spatial variation of viscosity and strain rate in the workpiece during FSW? Can the cooling rates and the shape of the thermo-mechanically affected zone be reliably predicted for alloys with widely different thermophysical properties? Can the asymmetry in thermal profile across weld centerline be predicted? To answer these questions, the complex physical phenomena associated with FSW must be adequately modeled. The complexity arises because of several reasons. In FSW, the workpiece material does not melt and the plasticized material flows with temperature and strain-rate dependent viscosity. Also, the heat generation in FSW is both due to friction and plastic deformation and takes place at the tool-workpiece interface and inside the workpiece as well. Spatial variation in heat generation rate must also be considered to accurately predict the temperature profile. Then the stick-slip boundary condition between the workpiece material in contact with the tool must also be represented accurately in the model. The amount of slip and friction coefficient between the tool and workpiece cannot be same at all points on the interface. A model for spatially variable slip and friction coefficient is essential to correctly represent the physical boundary condition for material flow.

With FSW being used more widely used to join dissimilar alloys, there is a need to characterize the intermixing of dissimilar alloys due to material transport near

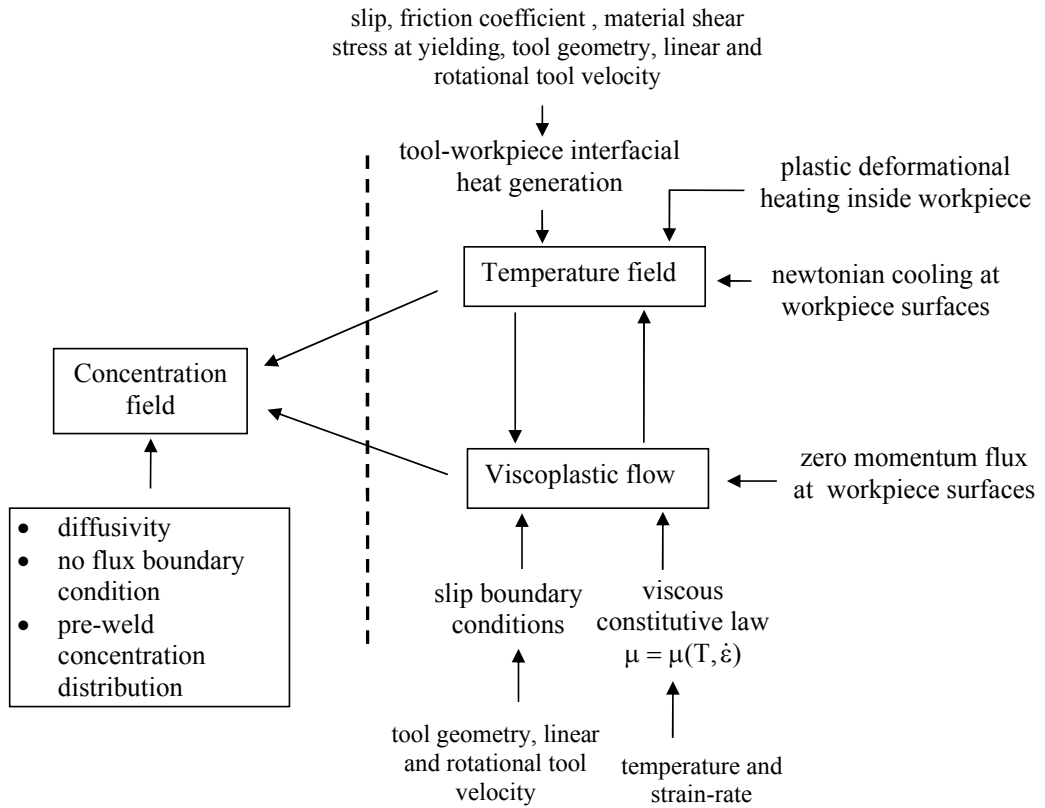


Figure 1.2. Inter-relationship between sub-models of FSW.

the tool. For example, if a pure metal is welded to a binary alloy containing an alloying element present at a low concentration, can a continuum mechanics based model be developed to characterize the concentration distribution across the weld interface? Currently there is no model for material transport in dissimilar FSW. Any such model must consider species transport due to diffusive and convective material flow, latter being much more significant in determining the concentration redistribution during welding. To capture the various physical processes associated with FSW, the sub-models needed and their inter-links are indicated in Fig. 1.2. It shows how temperature, viscoplastic flow and concentration fields are related to each other.

Current FSW process models suffer from lack of reliability of the predicted results because the underlying physics is highly complex and the current phenomenological models do not contain any model component designed to ensure compliance with experimental results. Recent work in the fusion welding suggests

that the lack of reliability of the phenomenological models may be contributed, at least to a large extent, by the uncertainty in several input parameters. So the question arises is that what are the uncertain parameters in FSW and how can they be determined ? The uncertain parameters include the friction coefficient, the extent of slip between the tool and the work-piece, the heat transfer coefficient at bottoml work-piece surface, the mechanical efficiency and the scaling factor for viscous dissipation. The uncertainty occurs because these parameters cannot be determined either from scientific principles or from straight-forward experiments. Sensitivity studies show that the uncertain parameters greatly affect the result. Current phenomenological models of FSW do not have any built in mechanism to determine the value of these uncertain parameters. An important question which arises is whether a mechanism for reliability can be introduced in the complex heat and material transport model for FSW by determining the uncertain parameters? Here, the transport phenomena model is coupled with evolutionary search algorithm to search the parameter space for the optimum value of those parameters. The optimum values are those for which results from transport phenomena model, like, thermal cycle and torque on tool, are similar to experimentally measured values. Another question which arises is whether a large volume of experimental data is required for this purpose or is it feasible with few sets of welding experiments?

An important difficulty in tailoring weld attributes based on fundamental scientific principles is that the existing process models are unidirectional in the sense that require as input welding parameters, thermophysical properties, tool and work-piece geometry and provide, as output, the temperature and velocity fields and the cooling rates at various locations. In contrast, engineers should be able to specify cooling rates, the geometry of the stir zone and/or other attributes of the FSW as input and obtain as output several alternative sets of welding parameters involving combinations of the welding speed, rotational speed, tool dimensions and other variables as output. Previous work in fusion welding show that such restructuring of the process, structure and property sub-models is both necessary and achievable [11–13]. This leads to the question of possibility of restructuring FSW models for bi-directional modeling as it has not been attempted before for FSW and provides the benefit of increasing the utility of models in industrial setting. Can an evolutionary algorithm also search the input space to determine multiple

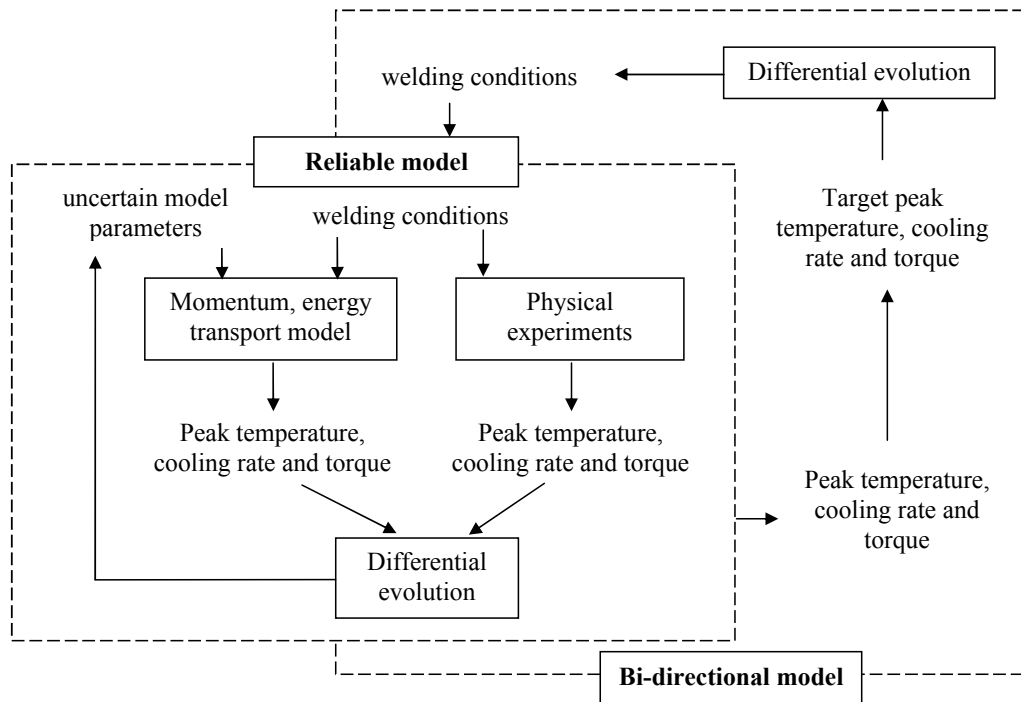


Figure 1.3. Steps in the development of a reliable and bi-directional heat transfer and viscoplastic flow model in FSW.

sets of welding variables to achieve a target weld attribute? How do the results obtained using these sets of welding variables compare with the desired weld attribute?

Figure 1.3 shows the overall organization in which a transport phenomena based model is linked to an evolutionary search and optimization technique to obtain reliable, bi-directional model for heat transfer and viscoplastic flow in FSW.

In summary, through synthesis of concepts from diverse disciplines, physics of friction stir welding, real number-based evolutionary algorithm and transport phenomena, the current research makes these specific contributions:

- Development of a numerical model for heat transfer and plastic flow in Friction Stir Welding adequately representing the complexities in flow boundary conditions, heat generation and spatial variation in material flowability that can be used to understand FSW of various alloys with significantly different properties.

- Integrating three-dimensional species transport equations with the numerical heat and plastic flow model to calculate redistribution of alloying element during FSW of pure metal with a dilute binary alloy.
- Improving the reliability of the transport phenomena based model by determining the values of uncertain model input parameters from a limited volume of experimental data so that the model predictions comply with experimental results using Differential Evolution search and optimization algorithm.
- The model outputs like peak temperature, torque and cooling rates were compared with experimental results for a wide range of welding speed and tool rotational speed.
- Development of bi-directional model by combining reliable transport phenomena model with DE to predict multiple sets of welding parameters required to obtain a specific weld attribute.

1.3 Thesis Layout

The thesis consists of six chapters. Chapter 1 describes the friction stir welding process, lists important issues related to modeling of friction stir welding process, outlines the research objectives and methodology, and the thesis content. The available knowledge for friction stir welding process is reviewed in chapter 2. At first, the principles of heat transfer and viscoplastic flow are examined, with discussion of fluid-dynamics and solid-mechanics based models for flow and deformation, respectively. Then we see how asymmetry in flow leads to asymmetrical properties about the weld-centerline. The calculation heat generation in FSW and torque on tool is a critical component of FSW modeling and its mathematical formulation is reviewed. Tool design is an important consideration in FSW and its effect on weld properties is reviewed. Then there is a discussion of defects in FSW and how material condition maps can be useful indicators for defect prediction. Finally, after reviewing pertinent literature, the gaps in the quantitative knowledge-base for FSW are identified and the research needs are outlined.

In chapter 3, the mathematical model for heat transfer and visco-plastic material flow in FSW is discussed. The model output includes the temperature, velocity

and viscosity fields. Four different alloys were studied using the model. The effect of material property on the heat transfer and material transport is discussed.

The thermal cycles and torques obtained using the transport phenomena model may not always match with experimental results because of uncertain parameters in the model. The uncertain parameters include the friction coefficient, the extent of slip between the tool and the work-piece, the heat transfer coefficient at bottoml work-piece surface, the mechanical efficiency and the scaling factor for viscous dissipation. In chapter 4, the sensitivity study performed showed that these parameters greatly affect the results. Hence, a computational procedure is developed and tested where the transport phenomena based model is combined with a differential evolution (DE) and physical experiments. Using this approach, the value of uncertain parameters are obtained. With these values in the transport phenomena based model, the calculated and experimental thermal cycles and torques are compared to examine the reliability of results. The reliable model is then combined with DE to develop a bi-directional model which can be used to predict multiple sets of welding parameters to achieve target weld attribute.

In chapter 5, species transport in dissimilar FSW of AA 6061 (Mg-rich) and AA 1200 (negligible Mg) is examined using modeling and experiments. Electron micro-probe analysis (EPMA) was used to measure the distribution of magnesium after weld was performed. The experimentally measured profile was compared with that computed using a 3D model for solute transport. The important findings of the research are summarized in chapter 6. Some areas are also identified that require further investigation.

Background

Heat generation rates, heat transfer and plastic flow are important physical phenomena associated with FSW process. The initial studies focused on aluminum alloys and heat transfer models which neglected the consequences of rapid plastic flow. These studies were followed by better calculations that included plastic flow, but fully three dimensional calculations are more recent and have revealed detailed insight into the FSW process, some of which cannot be understood using experimental techniques alone.

Material flow in FSW affects the convective heat transfer around the tool. The asymmetry in flow in the advancing and retreating sides of the workpiece leads to asymmetry in temperature fields in the two sides. Even though plastic flow in FSW is quite complex due to variation in strain-rates and flow stress leading to variation in viscosity which affects the flow, the flow should not be ignored. Ignoring convective heat transport may result in over-prediction of temperature in the workpiece around the tool. A good understanding of material flow is also necessary to improve the tool design so that drag on the tool and void formation due to insufficient material flow could be reduced.

2.1 Principles of heat transfer and material flow in FSW

During FSW, heat is generated by friction between the tool and the work piece and via plastic deformation. Frictional heating does not increase the stored energy of the weld, and may reduce it by promoting recovery or recrystallization phenomena [14]. In contrast, a fraction of the plastic deformation energy is stored within the thermomechanically processed region in the form of increased defect densities. Deformation not only increases the dislocation density but also the amount of grain surface and grain edge per unit volume [15] and by cutting precipitates that may force them to dissolve [16–21].

Except for transients during tool–pin insertion, dwell and extraction, the generation of heat should occur at a constant rate if the tool rotates and moves forward at a constant speed; this steady–state is justified by the fact that the weld profile and properties remain roughly constant during the welding phase. The temperature and velocity fields in pseudo-steady state are obtained by solving the generally available continuity, momentum and energy equations for incompressible single–phase flow. The steady state thermal energy conservation equation in index notation, for $i = 1, 2$ and 3 , representing x, y and z directions, respectively, is given by:

$$\rho C_p \frac{\partial(u_i T)}{\partial x_i} = -\rho C_p U \frac{\partial T}{\partial x_1} + \frac{\partial}{\partial x_i} \left(k \frac{\partial T}{\partial x_i} \right) + S_{in} + S_b \quad (2.1)$$

where ρ is the density, C_p is the specific heat capacity at constant pressure, u_i is the material velocity in i –direction, T is the temperature, x_i is i –coordinate, U is the welding velocity, k is the thermal conductivity of the work piece, S_{in} is the interfacial heat generation term and $S_b = d\dot{e}_p/dV = \beta\mu\phi$ is the heat generation rate per unit volume, due to plastic deformation in the work–piece away from the interface.

In FSW, the tool moves along the weld joint at a constant speed U , as it rotates about its axis with speed ω . At any point on the tool workpiece interface, the tangential speed of the tool with respect to the workpiece is given by $v_r = \omega r - U \sin \theta$ where r is the radial distance from the tool-axis and θ is the angle between radial vector, \mathbf{r} , and the welding direction. The term $U \sin \theta$ may be

neglected when ωr is much larger. Heat is generated due to friction and plastic deformation at the tool-workpiece interface and due to plastic deformation in the TMAZ. The local interfacial heat generation due to friction is the product of frictional force and the sliding velocity. The interfacial deformation heat is the product of shear stress and the velocity of the workpiece material which sticks to the tool as it moves.

The local heat generation rate due to friction, $d\dot{e}_f$, when the tool slides against the work-piece material, is approximately given by [22–34]:

$$d\dot{e}_f = \delta (\omega r - U \sin \theta) \mu_f p dA \quad (2.2)$$

where δ is the extent of slip, μ_f is the friction coefficient and p is the local pressure applied by the tool on the elemental area dA . When δ is 1, no material sticks to the tool and all the heat is generated by friction. In contrast, when $\delta = 0$, all the heat is generated by plastic deformation. Schmidt *et al.* [31] provide an excellent discussion on the calculation of interfacial heat generation rates during FSW. A problem in the calculations of heat generation is that the friction coefficient cannot be determined from fundamental principles or it seems, by straightforward representative experiments of relevance to the conditions of FSW.

When the work-piece material sticks to the tool, heat is generated at the tool-workpiece contact due to shear deformation. The resulting heat generation, assuming 100% efficiency of conversion of deformational work into heat, may be approximated as:

$$d\dot{e}_s = (1 - \delta) (\omega r - U \sin \theta) \tau_Y dA \quad (2.3)$$

where τ_Y is the shear yield stress related to that in tension (σ_Y) by the von Mises criterion $\tau_Y = \sigma_Y/\sqrt{3}$. It is possible to use an effective τ_Y , back calculated from the experimentally determined average power input to the system, [35,36], or estimated from the local shear stress using a temperature and strain-rate dependent yield stress [37–39].

Therefore, the total heat generated at the interface between vertical and horizontal surfaces of the tool pin and the workpiece may be defined as:

$$S_{in} = [(1 - \delta)\eta\tau_Y + \delta\mu_f p] (\omega r - U \sin\theta) dA \quad (2.4)$$

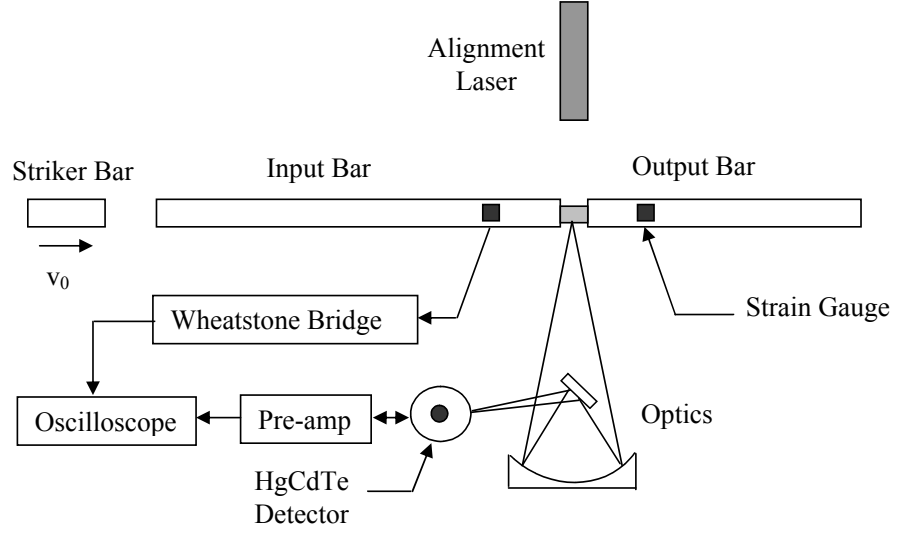


Figure 2.1. Schematic of Kolsky pressure bar with infrared temperature measurement. [42].

In equation 2.4 the first term within the square bracket when multiplied by the other terms represents the rate of deformational work per unit volume that is transferred to heat with a mechanical efficiency of η [40]. The fraction of plastic deformation work which is converted to heat, has been reported in [40] for α -titanium as ranging between 0.6 for low strain rate (1 s^{-1}) and 0.8 for high strain rate (3000 s^{-1}), practically independent of plastic strain (Fig. 2.2). For AA 2024, experimental values of β are not sensitive to strain-rate but dependent on strain. It initially decreases with an increase in strain, reaching a minimum, and then increasing with strain as shown in Fig. 2.3. These results indicate that aluminum stores a higher fraction of plastic work as cold work than α -titanium [40]. The second term represents the rate of frictional work per unit volume that is converted to heat with 100% efficiency [41].

The fraction of plastic work rate ($\sigma\dot{\epsilon}^p$) converted into thermoplastic heating ($\rho C_p \dot{T}$) was determined assuming adiabatic conditions and negligible thermoelastic heating [40]. Therefore, $\eta = \frac{\sigma\dot{\epsilon}^p}{\rho C_p \dot{T}}$. The measurement was done using a Kolsky pressure bar shown in Fig. 2.1. The apparatus consists of a striker bar, an input bar and an output bar, all of which are assumed to remain elastic during a test.

A test sample of length L is placed between the input and output bars. The time-resolved strain is measured using the strain gauges while temperature is measured using infra-red detectors.

Plastic deformation also occurs away from the tool/work-piece interface and its effect on the local heat generation rate may be estimated as $d\dot{e}_p = \beta\mu\phi dV$, where β is the fraction of plastic deformation work which is dissipated as heat and ϕ is given by [43]:

$$\phi = 2 \sum_{i=1}^3 \left(\frac{\partial u_i}{\partial x_i} \right)^2 + \left(\frac{\partial u_1}{\partial x_2} + \frac{\partial u_2}{\partial x_1} \right)^2 + \left(\frac{\partial u_1}{\partial x_3} + \frac{\partial u_3}{\partial x_1} \right)^2 + \left(\frac{\partial u_3}{\partial x_2} + \frac{\partial u_2}{\partial x_3} \right)^2 \quad (2.5)$$

The deformational heat away from the tool workpiece interface has been calculated by Bastier *et al.* [44] and has been found to be a small fraction of the total heat generation (4.4% for the welding condition considered). The term $\mu\phi$ represents the heat generation in fluids which have several orders lower magnitude of viscosity. The symbol β is used to scale down this heat generation term to fit into the context of high viscosity plasticized materials and to confirm to the low value of deformational heat generation rate, away from tool-workpiece interface, experimentally observed in FSW. This approach has also been used by Simar *et al.* [43] and Schmidt *et al.* [33].

Of the heat generated at the shoulder/work-piece interface, some of it is transported to the tool material while the rest enters the work-piece. The total heat generated at the shoulder/work-piece interface can be partitioned between the work piece (J_W) and the tool (J_T), based on their thermophysical properties [45]:

$$f = \frac{J_W}{J_T} = \frac{(k\rho C_P)_W^{1/2}}{(k\rho C_P)_T^{1/2}} \quad (2.6)$$

Equation 2.6 assumes steady-state, one-dimensional heat flow from the workpiece shoulder interface [45]. At 1000 K, the estimated heat flux into the work piece is calculated to be 43% of total heat generated in 1018 Mn steel Welded using Tungsten tool. This relation has been examined experimentally by Lienert *et al.* [45] and found to be reliable.

The extent of slip is estimated by curve fitting the measured values at various

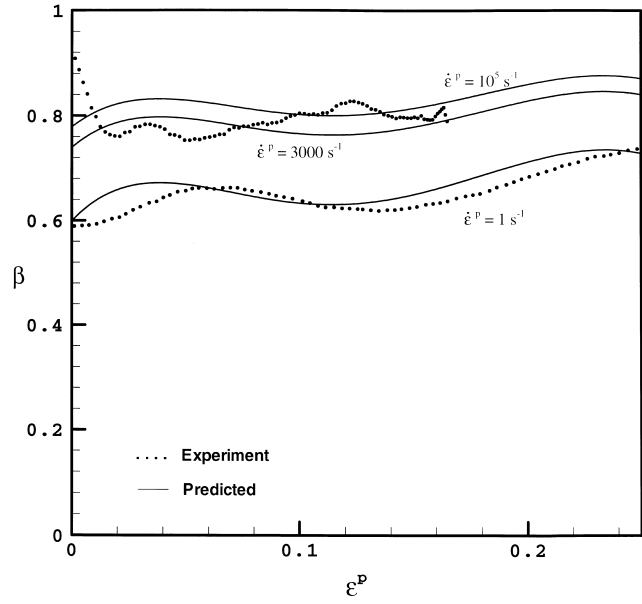


Figure 2.2. Fraction β of plastic work rate converted into heating as a function of plastic strain for rate-sensitive α -titanium [40].

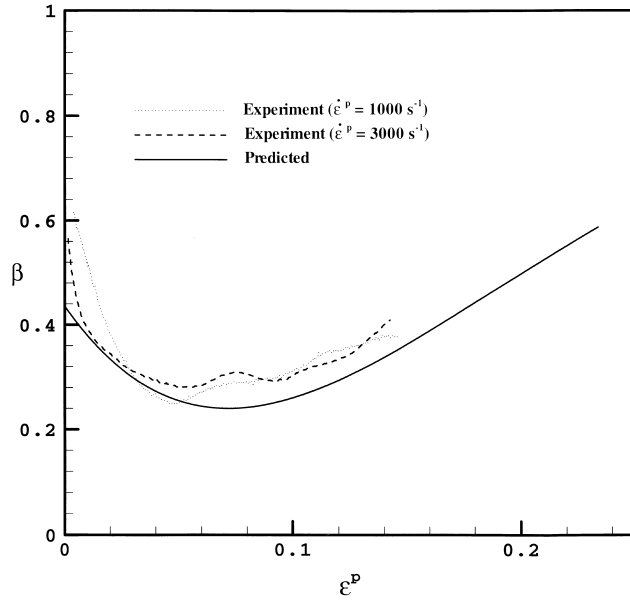


Figure 2.3. Fraction β of plastic work rate converted into heating as a function of plastic strain for rate-insensitive AA 2024-T351 [40].

relative velocities [46]:

$$\delta = 0.2 + 0.6 \left(1 - \exp\left(-\delta_0 \frac{\omega r}{\omega_0 R_S}\right) \right) \quad (2.7)$$

where δ_0 is an adjustable parameter, R_S is the radius of the tool shoulder, ω_0 is the normalizing rotational velocity which can be taken as the mid-point of the range of rotational speeds.

Values of friction coefficient can be estimated considering the relative velocity between the tool and the work-piece according to previous work in the context of friction [41]. The relative velocity increases from zero at the axis of rotation to ωR_S at the periphery of the tool shoulder. Evidence suggests [41] that μ_f has the form $\mu_f = \mu_0 \exp(-\delta \frac{\omega r}{\omega_0 R_S})$, where μ_0 is a fitting constant.

The boundary condition for heat exchange between the top surface of the work piece and the surroundings beyond the shoulder involves consideration of both convective and radiative heat transfer as

$$-k \frac{\partial T}{\partial z} \Big|_{\text{top}} = \sigma \epsilon (T^4 - T_a^4) + h(T - T_a) \quad (2.8)$$

where σ is the Stefan-Boltzmann constant ($5.67 \times 10^{-12} \text{ J K}^{-4} \text{ cm}^{-2} \text{ s}^{-1}$), ϵ is the emissivity, T_a is the ambient temperature and h is the heat transfer coefficient at the top surface.

At the bottom surface, the heat transfer into the backing plate is modeled by an enhanced heat transfer coefficient [36]:

$$k \frac{\partial T}{\partial z} \Big|_{\text{bottom}} = h_b (T - T_a) \quad (2.9)$$

where h_b is the heat transfer coefficient at the bottom surface.

Several investigators [35, 36, 47, 48] have examined the effects of uncertain parameters related to the specification of the boundary conditions at the bottom surface. These investigations included an estimation of the thermal contact resistance at the interface between the work-piece and backing plate and the determination of the convective heat transfer coefficient at the bottom surface. Khandkar *et al.* [36] reported that for FSW of AA6061-T651 plates, an overall convective heat

transfer coefficient of $1000 \text{ W m}^{-2}\text{K}^{-1}$ might be appropriate for the bottom surface of the work-piece if the backing plate is not considered. However, they observed that when a stainless steel backing plate is taken into account, a variable gap conductance would be appropriate for the work-piece/backing-plate interface, and recommended an average gap conductance somewhat less than $5000 \text{ W m}^{-2}\text{K}^{-1}$. They suggested that significant variations in the heat transfer rates can occur depending on the specific experimental conditions and recommended determining the rate experimentally.

The development of models which include the consequences of material flow is relatively recent. There are two essential approaches in the modeling of flow. In one scenario, the plasticised material is treated as a high viscosity fluid and the flow field is obtained using computational fluid dynamics. The other approach treats plastic deformation using solid mechanics with the finite volume method used to solve for displacements.

In computational fluid dynamics, the continuity equation is given by (assuming incompressible flow):

$$\frac{\partial u_i}{\partial x_i} = 0 \quad (2.10)$$

The momentum conservation equations with reference to a co-ordinate system with origin at the tool-axis and moving with the tool at a constant speed U along the x-axis are:

$$\rho \frac{\partial u_i u_j}{\partial x_i} = -\frac{\partial P}{\partial x_i} + \frac{\partial}{\partial x_i} \left(\mu \frac{\partial u_j}{\partial x_i} + \mu \frac{\partial u_i}{\partial x_j} \right) - \rho U \frac{\partial u_j}{\partial x_1} \quad (2.11)$$

where P is the pressure. Notice that in contrast to equation 2.2 where p is the pressure applied by the tool on the work-piece, P is a relative pressure which drives flow.

The speeds with which material moves at the tool-pin periphery, u , v and w , along the welding direction, the normal to the welding direction in the plane of the plate being welded, and normal to the horizontal plane respectively, are given by:

$$u = (1 - \delta)(\omega r \sin \theta - U) \quad v = (1 - \delta)\omega r \cos \theta \quad w = \Psi \omega \quad (2.12)$$

where Ψ is the pitch of the threads on the cylindrical tool. At the shoulder $w = 0$

The non-Newtonian viscosity μ must be estimated as a function of strain rate

and temperature using experimentally determined constitutive equations for the material of interest. According to Perzyna, μ can be expressed in terms of effective flow stress σ_e (*i.e.* deviatoric stress) and effective strain rate $\dot{\epsilon}$ (*i.e.* deviatoric strain rate) [49],

$$\mu = \frac{\sigma_e}{3\dot{\epsilon}} \quad \text{where} \quad \dot{\epsilon} = \left(\frac{2}{3} \dot{\epsilon}_{ij} \dot{\epsilon}_{ij} \right)^{\frac{1}{2}} \quad \text{and} \quad \dot{\epsilon}_{ij} = \frac{1}{2} \left(\frac{\partial u_i}{\partial x_j} + \frac{\partial u_j}{\partial x_i} \right) \quad (2.13)$$

The strain rate is found to correlate with the flow stress and temperature as follows [50]:

$$\dot{\epsilon} = A(\sinh \alpha\sigma)^n \exp\left(-\frac{Q}{RT}\right) \quad (2.14)$$

where A , n , α and the apparent activation energy Q are derived by fitting the equation to experimental data, and are all supposed to be independent of temperature. On rearranging this equation [51, 52],

$$\sigma_e = \frac{1}{\alpha} \sinh^{-1} \left[\left(\frac{Z}{A} \right)^{\frac{1}{n}} \right] \quad (2.15)$$

where $Z = \dot{\epsilon} \exp(Q/RT)$ is known as the Zener–Holloman temperature compensated strain rate [53]. Sheppard and Jackson determined the fitting constants for a number of aluminum alloys [54]. Bruschi *et al.* [55] studied hot workability of Ti-6Al-4V alloys and estimated values of the constants in the constitutive equation for this alloy. Material constants could be determined for other alloys from their hot working literature. The form of the equations could also be different, but flow stress and viscosity, as functions of temperature and strain rate are hyperbolic in nature for several alloys.

Flow stress for 304L stainless steel

A somewhat different approach is used for modeling the flow stress of stainless steel, because appropriate parameters of the kind employed for aluminum, are not available. In the analysis presented below, the equations for stainless steel take into account work hardening, but this introduces many additional empirical terms which may be specific to the experiments used to derive them.

Cho *et al.* [4] calculated the viscosity of 304L stainless steel based on simplified Harts model [56], where the flow stress is expressed as the summation of a

plastic contribution (σ_P), and a viscous contribution (σ_V). The latter represents the frictional force resisting dislocation glide, which obeys an Arrhenius type temperature dependence. The plastic contribution represents the resistance from the dislocation entanglement:

$$\begin{aligned}\sigma_P &= \kappa \exp\left[-\left(\frac{b}{\dot{\epsilon}}\right)^\lambda\right] & \text{where} & \quad b = b_0 \left(\frac{\kappa}{G}\right)^N \exp\left[-\frac{Q}{RT}\right] \\ \sigma_V &= G \left(\frac{\dot{\epsilon}}{a}\right)^{1/M} & \text{where} & \quad a = a_0 \exp\left[-\frac{Q'}{RT}\right]\end{aligned}\quad (2.16)$$

Here κ is scalar state variable for strength and it represents the upper limit for σ_P , κ_0 is the initial strength for the undeformed material and is determined experimentally, R is the universal gas constant (8.314 J/mol-K), $\dot{\epsilon}$ is the effective strain rate. The material parameters G , Q , Q' , a_0 , b_0 , λ , N , and M have to be determined experimentally. For 304L stainless steel, the values have been reported by Cho et al. [4]. Given the high deformation rate in FSW, saturation value of strength is defined as a function of the strain rate as follow: [4, 57]:

$$\kappa_S = \left(\frac{C}{T \ln \frac{\dot{\epsilon}_0}{\dot{\epsilon}}}\right)^{m_0} \quad (2.17)$$

where the material parameters $\dot{\epsilon}_0$, C and m_0 have to be determined experimentally, as in [4]. Value of these material parameters is given in Table 2.1.

It should be emphasised that in equation 2.14 the derived parameters A , n , α are strictly a function of strain in a work-hardening solid. However, they should become independent of strain once a steady-state is reached during deformation in which the work-hardening is balanced by recovery-softening. It is generally the case that this situation is reached before strain, $\epsilon = 1$, and since the strains involved in FSW are much larger, it may be assumed that a single set of material constants corresponding to steady-state deformation can be utilised with the assumption that they are independent of strain.

Temperature dependent thermal conductivity, specific heat and yield stress for the work-piece [9, 37–39, 58, 59] have been considered. The tool material commonly used for the FSW of aluminum alloys, steels and Ti-6Al-4V are tool steel and tungsten, respectively. Table 2.2 presents the thermophysical properties for these

Table 2.1. Material parameters for the simplified Harts model for annealed 304 stainless steel [4].

$a_0(s^{-1})$	1.36×10^{35}
$b_0(s^{-1})$	8.03×10^{26}
$G(MPa)$	73.1
$\kappa_0(MPa)$	150
$Q(kJ/mol)$	410
$Q'(kJ/mol)$	91
λ	0.25
M	7.8
N	5.0
$\dot{\epsilon}_0(s^{-1})$	10^8
m_0	2.148

alloys.

Ulysse [9] used a solid mechanics approach assuming a rigid visco-plastic material where the flow stress depended on strain rate and temperature. The heat generation rate was expressed as the product of the effective stress and the effective strain rate. Temperature profiles were determined for the work-piece and the tool, using a three-dimensional finite analysis code.

Schmidt *et al.* [34] used adaptive boundary conditions to determine conditions for void-free welds using finite element analysis and flow stress determined according to the Johnson-Cook law. Zhang *et al.* [29] also applied finite element analysis to develop a two-dimensional transient heat and plastic flow model for FSW. To overcome the computational expense for transient analysis, they increased the rotational and translational speeds of the tool by 1000 times, keeping the ratio $U/\omega R_P$ same. Though this reduces the total time of simulation by 1000, it assumes that keeping the ratio $U/\omega R_P$ same leads to same welding conditions, which is incorrect. A better alternative for reducing computational time could be solving with a pseudo-steady state assumption. Buffa *et al.* [66] developed a thermomechanically coupled, rigid-visco-plastic, three-dimensional finite-element model to study the effect of tool geometry and welding velocity on material flow pattern and the grain size distribution in the welded joints.

Table 2.2. Temperature dependent thermophysical properties of various work-piece (AA 6061-T6 [60], 304L Stainless Steel [61], 1018 Mild Steel [62], Ti-6Al-4V [63]) and tool materials(M2 Tool Steel [64], Tungsten [65]).

Property		AA 6061-T6	304L Stainless Steel	1018 Mild Steel	Ti-6Al-4V	M2 Tool Steel	Tungsten
Temperature range, K		300 - 750	293 - 1073	298 - 1273	273 - 1150	293 - 948	293 - 2500
Density, kg/ m ³		2700	7800	7860	4420	8100	19400
Specific heat capacity, J/kg-K C ₀ + C ₁ T + C ₂ T ² + C ₃ T ³	C ₀	9.29 x 10 ²	2.76 x 10 ²	4.68 x 10 ²	6.22 x 10 ²	3.89 x 10 ²	1.58 x 10 ²
	C ₁	-6.27 x 10 ⁻¹	8.51 x 10 ⁻¹	-8.49 x 10 ⁻²	-3.67 x 10 ⁻¹	2.08 x 10 ⁻¹	1.06 x 10 ⁻¹
	C ₂	1.48 x 10 ⁻³	-8.51 x 10 ⁻⁴	3.03 x 10 ⁻⁴	5.45 x 10 ⁻⁴	0	-1.63 x 10 ⁻⁵
	C ₃	-4.33 x 10 ⁻⁸	3.00 x 10 ⁻⁷	1.82 x 10 ⁻⁷	2.39 x 10 ⁻⁸	0	0
Thermal conductivity, W/m-K C ₀ + C ₁ T + C ₂ T ² + C ₃ T ³	C ₀	2.52 x 10 ¹	1.43 x 10 ¹	3.77 x 10 ²	1.92 x 10 ¹	1.57 x 10 ¹	3.67 x 10 ⁻¹
	C ₁	3.98 x 10 ⁻¹	-9.02 x 10 ⁻³	9.24 x 10 ⁻²	1.89 x 10 ⁻²	1.74 x 10 ⁻²	-2.29 x 10 ⁻⁴
	C ₂	7.36 x 10 ⁻⁶	4.52 x 10 ⁻⁵	-1.79 x 10 ⁻⁴	-1.53 x 10 ⁻⁵	-3.83 x 10 ⁻⁶	1.25 x 10 ⁻⁷
	C ₃	-2.52 x 10 ⁻⁷	-2.49 x 10 ⁻⁸	7.81 x 10 ⁻⁸	-1.41 x 10 ⁻⁸	0	0
Yield strength, MPa C ₀ + C ₁ T + C ₂ T ² + C ₃ T ³	C ₀	1.16 x 10 ³	7.96 x 10 ²	1.11 x 10 ²	9.09 x 10 ²	-	-
	C ₁	-8.88 x 10 ⁰	-1.60 x 10 ⁰	1.11 x 10 ⁰	1.11 x 10 ⁰	-	-
	C ₂	2.97 x 10 ⁻²	2.25 x 10 ⁻³	-1.90 x 10 ⁻³	-3.05 x 10 ⁻³	-	-
	C ₃	-3.32 x 10 ⁻⁵	-1.30 x 10 ⁻⁶	7.51 x 10 ⁻⁷	1.26 x 10 ⁻⁶	-	-
Solidus temperature, K		855	1697	1600	1933	-	3683

The mechanical response on an element is obtained using force balance:

$$\rho \ddot{u} + c \dot{u} + k u = p \quad (2.18)$$

where ρ is the density, c the damping coefficient, k the stiffness coefficient, p the body force and u is the displacement vector. In a finite-element framework, the equation can be written as:

$$\mathbf{M} \ddot{\mathbf{u}} + \mathbf{C} \dot{\mathbf{u}} + \mathbf{K} \mathbf{u} = \mathbf{P} \quad (2.19)$$

where \mathbf{M} is the discrete mass matrix, \mathbf{C} the viscous damping matrix, \mathbf{K} the stiffness matrix, \mathbf{P} the vector of external discrete forces, which include body forces, surface forces and concentrated loads acting on the system, and u , \dot{u} and \ddot{u} are the nodal displacement, velocity and acceleration vectors, respectively. The thermal response

is governed by an energy balance:

$$\rho C_p \dot{T} = \frac{d}{dx_i} \left(k \frac{dT}{dx_i} \right) + \eta s_{ij} \dot{\epsilon}_{ij}^{pl} \quad (2.20)$$

where C_p is the specific heat capacity at constant pressure, k the thermal conductivity, η the fraction of plastic energy dissipation, s_{ij} the deviatoric stress tensor and $\dot{\epsilon}_{ij}^{pl}$ is the plastic strain rate tensor. In FE framework, we obtain

$$\mathbf{C}\dot{\mathbf{T}} + \mathbf{B}\mathbf{T} = \mathbf{S} \quad (2.21)$$

where \mathbf{C} is the discrete capacity matrix, \mathbf{B} the conductivity matrix, \mathbf{S} the source vector accounting for all thermal sources and \mathbf{T} and $\dot{\mathbf{T}}$ are the nodal temperature and temperature rate vectors, respectively.

FSW involves large plastic deformation. Eulerian shock-wave physics code, a finite-difference 3D code that solves time-dependent equations for continuum mechanics has also been used to model friction stir welding in aluminum [67, 68]. This is well suited for modeling very large deformations at high strain rate, such as during ballistic impact.

In polycrystalline materials, large plastic deformation alters microstructure and hence changes the macroscopic response. Hence to adequately model the deformation of a polycrystalline material it is necessary to understand the interaction of the material on two length scales. Multi-scale modeling of deformation in FSW has been performed by Boyce *et al.* [69] with one length scale of the order of the dimension of the work-piece (in cm), and the other of the order of the grain-diameter (in μ m).

2.2 Asymmetry in heat transfer and plastic flow

Some of the early work on heat transfer during FSW was based on simple analytical or numerical heat conduction models that neglected convective heat transfer due to motion of the plasticised material. Models which neglect convective heat transfer are limited to materials with high thermal conductivity (aluminum alloys) or low

Péclet number, Pe , the latter defined as:

$$Pe = \frac{\rho C_P u_c L}{k} \quad (2.22)$$

where u_c is the characteristic velocity, and L is the characteristic length. The Péclet number indicates the relative importance of heat transfer by convection to that by conduction. When Pe is much lower than one, heat is transported mainly by conduction. Under these conditions, the errors in the calculation of temperature fields would not be significant if convection were ignored. Let us consider a typical FSW of an aluminum alloy. Considering approximate values of ρ , C_P and k as 2700 kg m^{-3} , $3.77 \text{ J kg}^{-1} \text{ K}^{-1}$ and $7.02 \text{ J m}^{-1} \text{ s}^{-1} \text{ K}^{-1}$, respectively, and assuming L to be the average length of stir-zone (6 mm) and $u \simeq 150 \text{ mm s}^{-1}$, the Péclet number is 12. Therefore, even for a high thermal conductivity material such as aluminum, convective heat transfer is an important mechanism for heat transfer near the tool during FSW. The Péclet number for steel is much higher at about 100, where heat conduction alone cannot satisfactorily explain the temperature profiles. This may be the reason why some authors [9, 70] overestimated the peak temperature, size of the deformation zone and tool forces. It may also lead to an underestimation of the flow stress (and hence tool force) in the stir region.

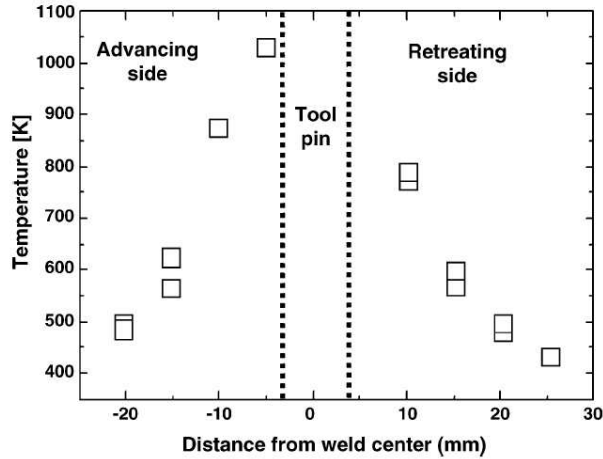


Figure 2.4. Temperature distribution along the intersection of horizontal midplane and transverse plane through the tool axis, for FSW of stainless steel [4].

Cho *et al.* [4] developed a two dimensional steady-state heat transfer and mate-

rial flow model for the FSW of 304L stainless steel. They used the simplified Harts model to calculate the flow stress [56]. Isotropic strain hardening was included in the finite element solution procedure. The work piece temperatures were computed assuming various tool temperatures and heat transfer coefficients. Interestingly, the experimental and the computed results indicated that the temperatures were about 100 K higher on the advancing side than the retreating side, as shown in Fig. 2.4.

Two dimensional models [71,72] naturally do not consider vertical mixing during FSW, a feature which has been observed experimentally. Nandan *et al.* [37–39] therefore conducted a comprehensive three–dimensional material flow study for the FSW of aluminum and steels. They solved the equations of conservation of mass, momentum and energy using spatially variable thermophysical properties and non–Newtonian viscosity using a computational method adapted from previous work on fusion welding. It was found that the typical peak strain rate during FSW reaches about 100 s^{-1} , at locations where the velocity gradient is highest, such as near the shoulder edge at the work–piece surface and at the pin surface at lower elevations. The strain rate drops sharply to about 30 s^{-1} a few mm below the top surface. The strain rate decreases rapidly with depth due to a significant decrease in velocities through viscous dissipation. The computed strain rates are comparable but somewhat higher than the 20 s^{-1} value estimated based on measured grain size and calculated peak temperature from a thermal model reported by Frigaard *et al.* [73]; this discrepancy may result from the expected variation of strain rate with distance [37,38].

The stream traces on horizontal planes around the tool pin at three different elevations are shown in Fig. 2.5. The stream lines indicate the presence of rotational zone, which implies the recirculating flow of a plug of material around the tool pin. The thickness of the recirculating material flow region is affected by material properties, welding parameters and rate of heat transfer into the tool. This zone occupies larger areas at higher elevations due to greater momentum transport from the rotating shoulder. The streamlines indicate that beyond the region of recirculating plastic flow, i.e. in the transition zone, material transfer occurs mainly on the retreating side. Figure 2.5 also shows a flow reversal in the advancing side close to the pin, leading to a relatively stagnant zone, which forms

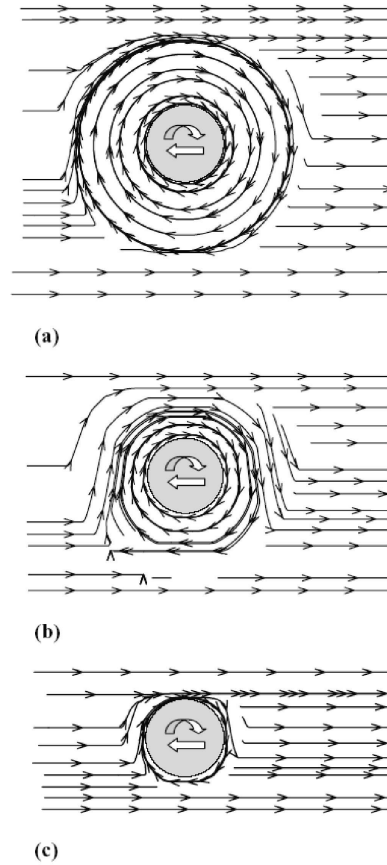


Figure 2.5. Stream traces on different horizontal planes (a) 0.35 mm, (b) 1.59 mm and (c) 2.28 mm below the top surface for a 304 stainless steel plate of thickness 3.18 mm. Welding speed 4 mm s^{-1} with tool rotation at 300 rpm [38].

closer to the pin at lower elevations. An important consequence of the lack of adequate material flow on the advancing side has been related to the formation of “wormhole” defects [71]. The streamlines show that beyond the rotational zone the material transport occurs mainly along the retreating side. Flow visualisation using tracers also indicates the presence of a zone where the material rotates and advances with the tool and transitional zone where the materials move on the retreating side [74–76].

Understanding the asymmetry in material flow is important for optimal tool design. Colegrove and Shercliff [10, 77] calculated material flow using the computational fluid dynamics, for the FSW of AA 7075. They compared the mechanical

efficiency of a triangular tool with convex surfaces (*Trivex*) with that of a conventional tool (*Triflute*) by examining the streamlines around these tools. It was suggested that the *Triflute* tool produced a strong auguring action, thus increasing the tools downward force (Fig. 2.6).

2.3 Nature of plasticized material and its flow

Experimentally, optical microscopy, movement of tracer particles and spatial variations of texture have been used to understand materials flow. Although, post weld characterisation of the welds does not provide any direct information, the observations provide some indication of materials flow in FSW.

A typical cross-section of the FSW joint consists of a number of zones (Fig. 2.7) [73, 78–80]. The heat-affected zone (HAZ) is similar to that in conventional welds although the maximum peak temperature is significantly less than the solidus temperature, and the heat-source is rather diffuse. This can lead to somewhat different microstructures when compared with fusion welding processes. In age-hardened aluminium alloys, mechanical failure is most likely in the HAZ. The central nugget region containing the “onion ring” appearance is the one which experiences the most severe deformation, and is a consequence of the way in which a threaded tool deposits material from the front to the back of the weld. It has dynamically recrystallized equiaxed grains which are much smaller than the base metal grains. The thermomechanically affected zone (TMAZ) lies between the HAZ and nugget; the grains of the original microstructure are retained in this region, but often in a deformed state. The figure also shows a flow arm on the upper surface of the weld. It is made when plasticized metal is moved to the advancing side from the retreating side of the weld, around the rear of the tool, due to drag exerted by the shoulder.

Steel balls have been used to trace flow in butt welds of 6061 and 7075 aluminium alloys [81], their positions after welding being determined using radiography. Several initial configurations of balls were investigated and the “stop action technique” was used by suddenly interrupting the forward motion of the pin which is then quickly unscrewed from the work-piece, leaving the threading in the keyhole intact. When the trailing edge of the keyhole was examined using metallography,

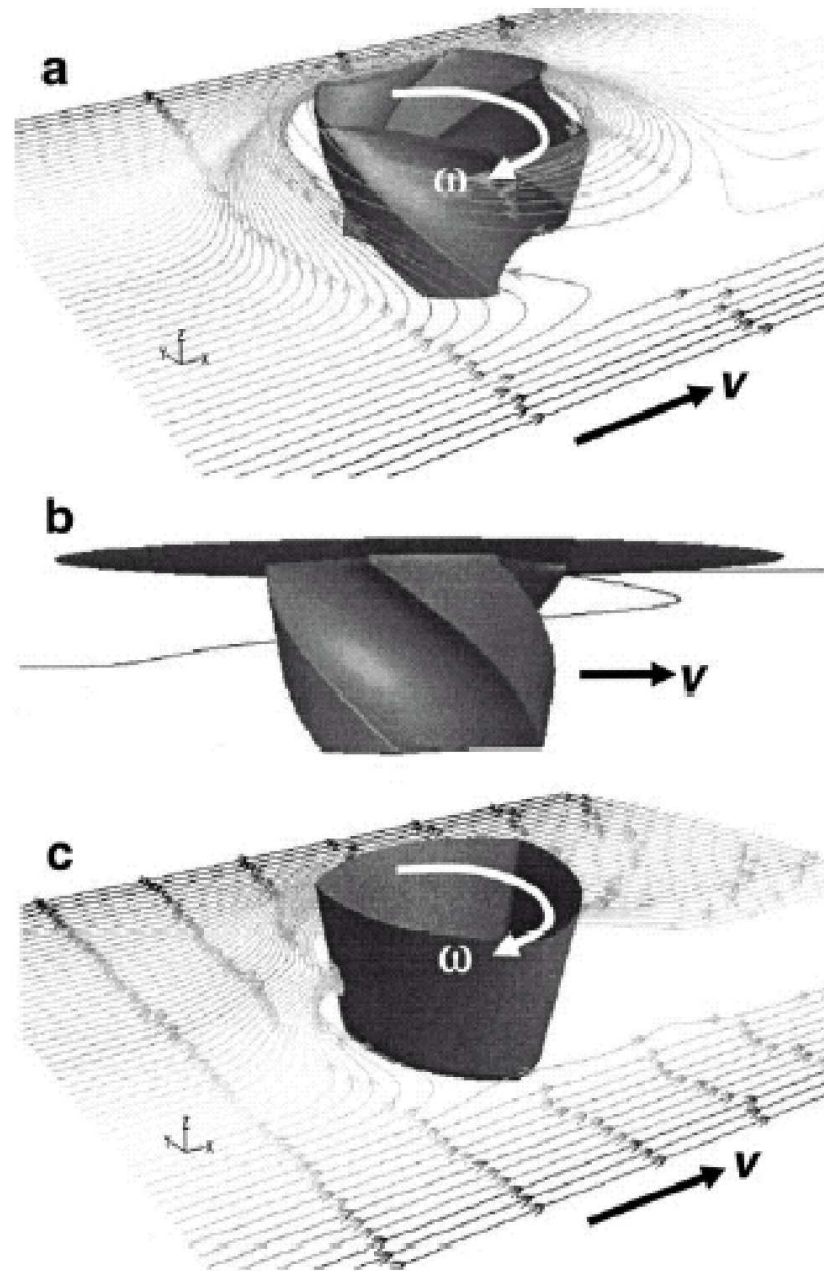


Figure 2.6. Streamlines for isothermal model [10] that used a limiting shear stress of 40 MPa: a) *Triflute* tool, b) single streamline for *Triflute* tool showing vertical movement and c) *Trivex* tool. Tool rotation 457 rpm and translation at 457 mm min⁻¹.

it showed microstructural banding of extruded material (Fig. 2.8). The vertical striations in the bottom portion indicate plastic material which has been distorted

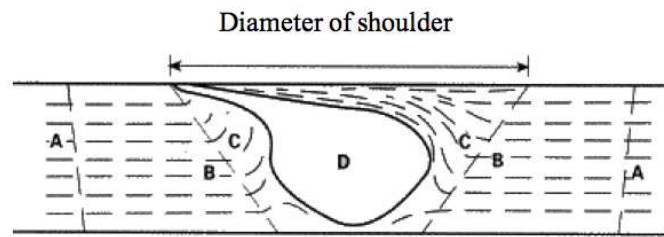


Figure 2.7. Schematic cross-section of a typical FSW weld showing four distinct zones: (A) base metal, (B) heat-affected, (C) thermomechanically affected and (D) stirred (nugget) zone [73].

in the upward direction due to the pin-threads, while close to the shoulder, the striations are horizontal, indicating rotational flow along the shoulder.

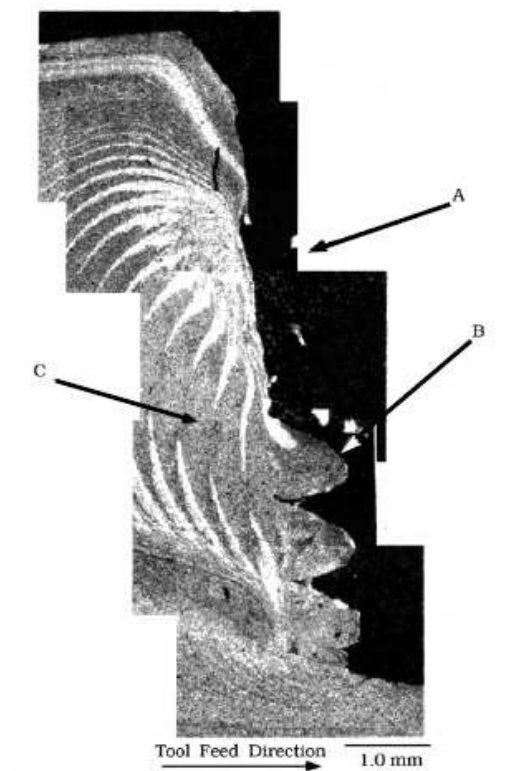


Figure 2.8. “Stop action” technique [81] to capture material flow patterns during FSW. An enlargement of the AA 6061 specimen in the region behind the pin after the pin has been extracted. A: area with no material filling behind the pin, B: fully filled threads and C: material filling behind the pin from below.

Another way to understand flow experimentally is to use inert markers before starting the weld [76], and then characterising their final positions using serial sectioning parallel to the top surface. The material near the top of the work-piece was obviously stirred under the action of the shoulder with vertical transport occur-

ring due to threading on the tool-pin. The stirred material from the top is carried down by the threads and deposited in the weld nugget. The vertical mixing becomes prominent at low *weld pitch*, which is the ratio of welding speed to rotational speed. Schmidt *et al.* [74] estimated the average velocity of material flow through shear layers during FSW of aluminum alloy based on experimental investigation of tracer flow. The estimated average velocity was found to be approximately 0.1 to 0.3 times the shoulder rotational speed. The tracer technique does not provide information about the actual flow path of the material. It only shows the final position of the tracer.

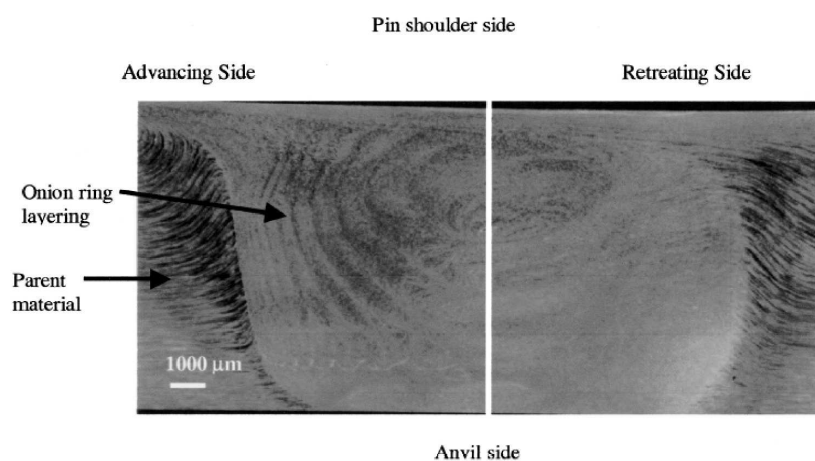


Figure 2.9. Optical image showing the macroscopic features [82] in a transverse section of a friction stir welded material. Note the onion ring and the adjacent large upward movement of material.

Macrostructural observations of transverse cross-sections of FS-welded aluminum alloy specimens reveals “onion-ring” shaped structures of the type illustrated in Fig. 2.9. These have been linked to the nature of material flow during FSW [82–84], but the detailed mechanism of pattern formation is not completely understood. They have been attributed to the geometry of the extrusion of cylindrical sheets of material during each rotation of the tool [84]. Measurement of the spacing of the markings has been found to be equal to the weld pitch, *i.e.*, the length the tool moves forward in one rotation. Electron back scattered diffraction studies indicate that the bands have different densities of second-phase particles, rather than any significant difference in the local grain structure or texture [85].

This is confirmed by studies of crack propagation in FS-welds [86], where it is observed that cracks deflect around the onion ring structure, consistent with local variations in hardness.

In FSW of dissimilar aluminum alloys of cast A356 and wrought 6061, onion ring patterns consist of lamellar mixture of the two alloys in equal width [87]. Apart from welding parameters, the base metal microstructure also affects the rings. Base materials with banding of intermetallic particles show a definite onion-ring structure with banded grain and particle features, whereas the rings are diffuse when the starting material is homogeneous [88]. Intermetallic particle distribution had a greater effect on ring formation than welding parameters [88].

Microscopy on its own does not reveal details of material flow behavior, but some clarity is obtained when this is combined with a knowledge of the crystallographic texture and microtexture [89]. There appears to be a continuous evolution of the undeformed grains far from the tool, to the refined grains in the close proximity of the tool, beginning with elongation, followed by subdivision into equiaxed subgrains and then the development on increasing misorientation between these subgrains as the intensity of deformation increases [90].

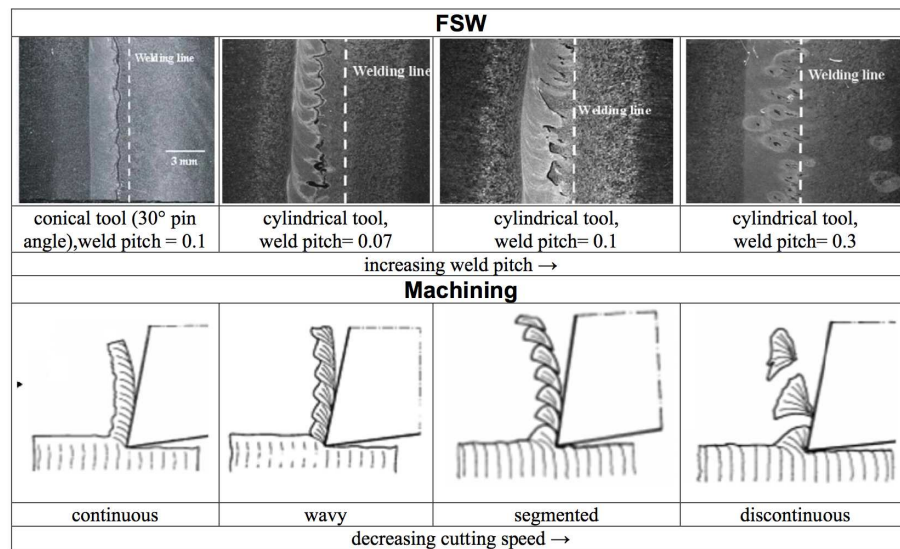


Figure 2.10. Analogy between chip morphology in machining and material flow in FSW [91].

One of the problems with plastic flow models is that their rigorous validation

is difficult. An interesting experiment involved the introduction of copper markers parallel and perpendicular to the weld–centerline, in both real experiments and computational models [91]. The positions of the markers after welding were then compared for the two cases, enabling them to draw some qualitative conclusions about material flow as a function of position, and on the nature of the material bonding that takes place in the advancing side. It was concluded that weld pitch (welding velocity/rotational speed) and tool pin shape determined whether flow was simple or complex in nature. When pitch was small, markers were continuous rather than dispersed, indicating better welds. A conical tool pin led to more effective material flow with fewer defects. This is analogous to chip formation in machining processes – just as chip formation morphology changes from discontinuous to segmented to wavy to continuous with increase in cutting speed, the flow pattern in FSW also changes with weld pitch [91] as shown in Fig. 2.10.

The plastic flow models for FSW have been successful in predicting the magnitude of velocities around the tool pin. These values have been confirmed by strain rate measurements which are obtained by using grain-size and strain-rate correlation [7]. Also, an indication of reliability of plastic flow models is the reliability of easily measured thermal cycles at different locations in the workpiece because plastic flow affects convective heat transfer which in turn affects the thermal cycle. Comparison of the shape of the TMAZ predicted by flow models with macrostructural observation has shown a satisfactory match [37]. The computed variation of viscosity as a function of strain rate and temperature has been reported for three materials: 6061 aluminum alloys [37], 304 stainless steel [38] and 1018 C–Mn steel [39]. Fig. 2.12 shows that the viscosity decreases significantly with both strain rate and temperature with the former being the dominant factor for the conditions typical of FSW.

The maximum velocity attained near the shoulder edge at the top surface of the work–piece was of the order of 200 mm s^{-1} , followed by a rapid decrease away from this region to below 10 mm s^{-1} [37–39]. At planes near the bottom of the work piece, the peaks in velocity were attained near the tool surface. The computed contours at different horizontal planes (Fig. 2.13) show that the viscosity lies in the range of 10^5 to $5 \times 10^6 \text{ Pa s}$ for FSW of aluminum alloys. It is also seen that no significant flow occurs when the viscosity is high and that the region of plastic flow

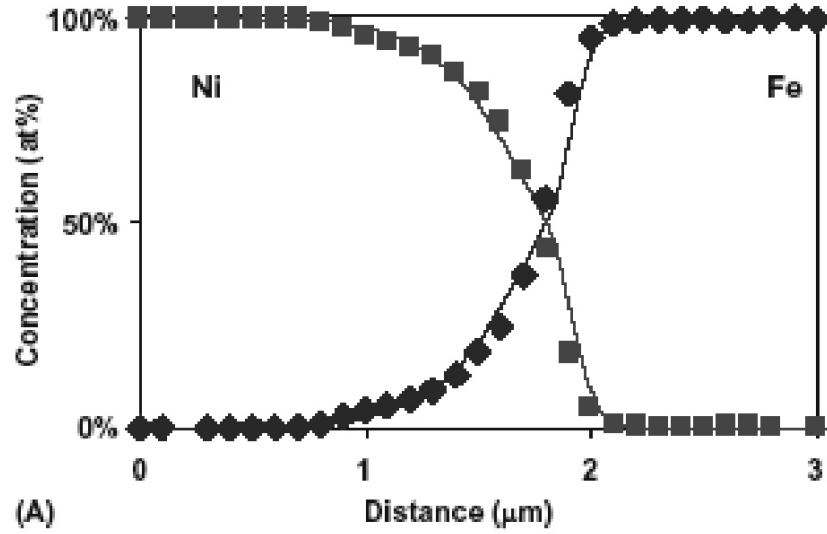


Figure 2.11. Concentration profiles of Fe and Ni at a location in stir region for FSW of pure Fe and Ni. Points represent data obtained by atomic emission spectroscopy and the solid lines indicate computed results [92].

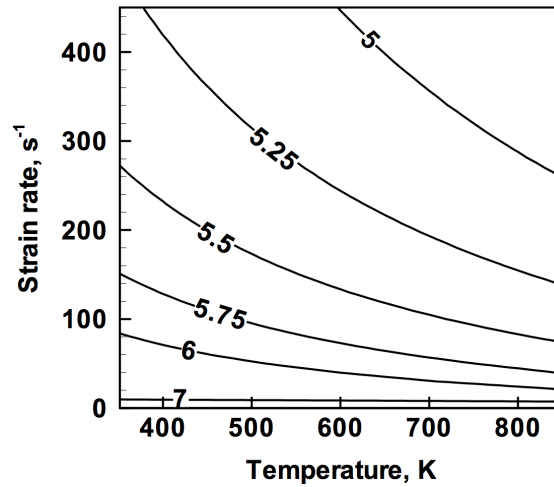


Figure 2.12. Computed contours of $\log_{10}(\text{viscosity in Pa s})$ [39] as a function of temperature and strain rate for AA 6061-T6.

decreases with depth. It was observed that plastic flow ceases beyond a certain critical value of viscosity. This cut-off viscosity surface defines the geometry of the thermomechanically affected zone.

The viscosities near the tool/work-piece interface affect the torque required for welding. The temperatures near the interface during FSW are about 400 K

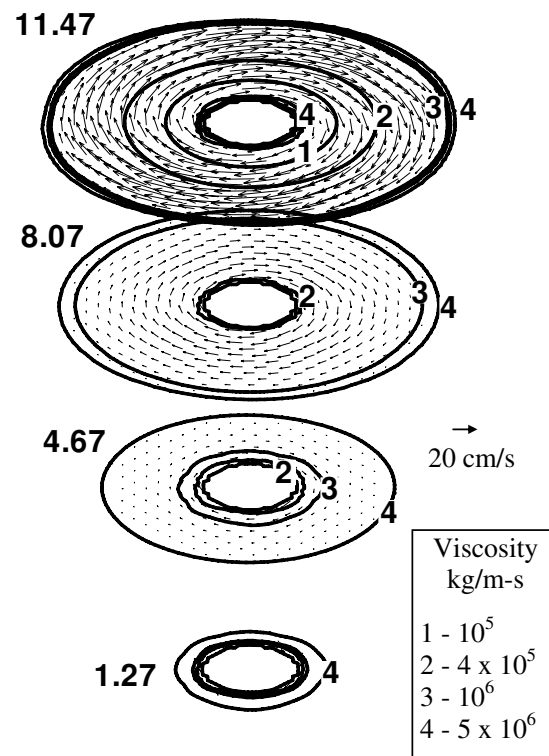


Figure 2.13. Spatial variation of viscosity and velocity in AA 6061-T6 [37] at planes corresponding to $z = 1.27, 4.67, 8.07$ and 11.47 mm for a plate thickness of 12.7 mm. Distances in x and y direction were equivalent, but that in the z -direction was increased eight fold to enhance clarity. The welding velocity was 1.59 mm s^{-1} and the rotational speed was 637 rpm .

higher for the 1018 C-Mn steel when compared with the aluminum alloys, and slightly lower than for stainless steel for typical welding conditions. Considering this difference in temperature, and given same order of magnitude of viscosities, it is expected that the torques should be similar for different materials for the same welding parameters and tool design.

In spite of the successes of the flow models, certain observations cannot be explained using these models because flow during FSW differs in character from material flow in the liquid state during conventional fusion welding. This is evident from studies of the welding of dissimilar metals. If melting takes place, there is a more or less homogeneous fusion zone after solidification. However, in the absence

of melting, plastic deformation takes place, as in FSW, and it is possible to find larger concentration differences and the deformed region is far from homogeneous. For example Fig. 2.11 shows a diffusion couple formation between Fe and Ni at a certain location in stir region, when pure Fe and Ni plates are joined together using FSW. The diffusion couple has a length scale of only 2–3 μm . Such diffusion couples would not exist had melting and homogenisation of weld metal occurred.

2.4 Heat generation rate and torque

High temperature and significant plastic deformation during FSW leads to the development of characteristic microstructure consisting of three distinct zones, which are, the stirred zone, the thermomechanically affected zone and the heat affected zone. These zones often have different mechanical properties than the base material. For example, in age hardenable aluminum alloys, precipitate dissolution can lead to significant reduction of strength in the HAZ. The temperature fields are important for the understanding and interpreting microstructure and mechanical properties of FSW weldments. Reliable temperature fields can be obtained if heat generation rates can be calculated accurately.

The principles for the calculations of heat generation rates have been discussed in the previous section. In practice, the errors in the calculation of heat generation rates can arise from a number of sources, for example, in the value of the friction coefficient. As the work-piece is heated, localised softening reduces friction and the heat generation rate. Some investigators have considered this effect by adjusting the coefficient of friction. However, as pointed out previously, there is no straightforward method to estimate the coefficient of friction or how it changes with temperature or relative velocity. In the context of plastic deformation heating, the decrease in yield strength with increasing temperature leads to a reduction in the heat generation rate by this mechanism. Since strain rates depend on velocity gradients, which diminish rapidly away from the tool, most of the heat generation due to plasticity occurs close to the tool/work-piece interface. Verification of the heat generation rate calculations has been done indirectly either by measuring thermal cycles or by measuring mechanical energy expended during FSW [36].

It is found that the heat generation rate is influenced by the rotational speed but

is not sensitive to the welding speed [38]. Surprisingly, tool design does not seem to have a significant effect on the total heat generation rate during FSW (Fig. 2.14) [10, 77] although the heat generation pattern becomes non-uniform because of the differences in the relative velocity as a function of location on the uneven tool surface as opposed to a cylindrical tool which has constant radial distance from axis. These differences lead to corresponding variations of temperature on the tool surface. It is necessary therefore to model temperature and plastic flow fields in a three-dimensional framework.

Though heat generation cannot be measured, total torque on the tool can be measured using a dynamometer. It can be used to calculate the average power on the tool which can be used to verify the numerically predicted value.

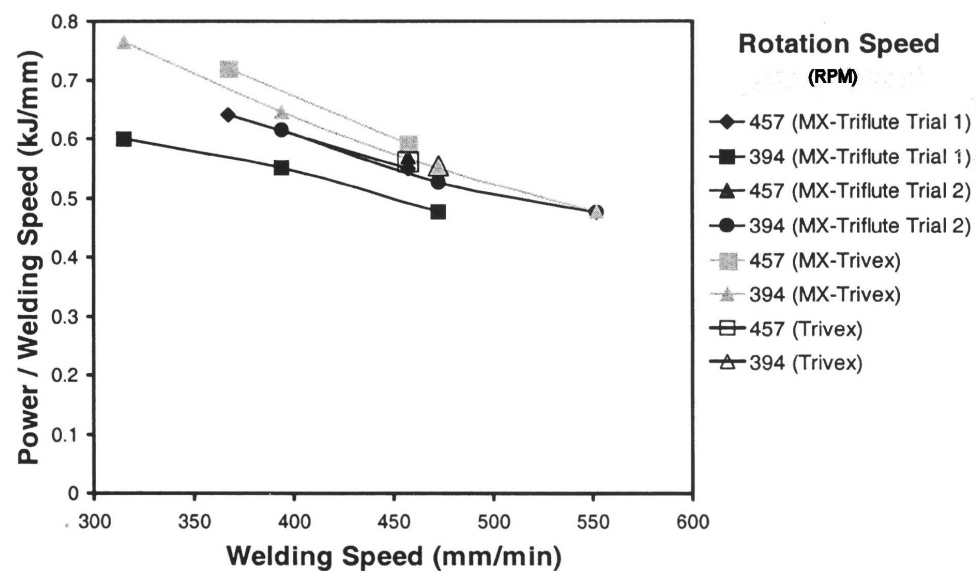


Figure 2.14. Heat input at various welding speeds used to weld 6.35 mm thick AA 7075-T7351 plates using MX-Triflute, MX-Trivex and Trivex tools [77].

The torque values depend on the welding variables, tool design and work-piece material. Tool rotational speed has a greater influence on torque than traverse speed as shown in Fig. 2.15.

Avila [94] derived a formula using variational calculus to estimate the average shear stress based on the shape of the TMAZ. The model applies calculus of

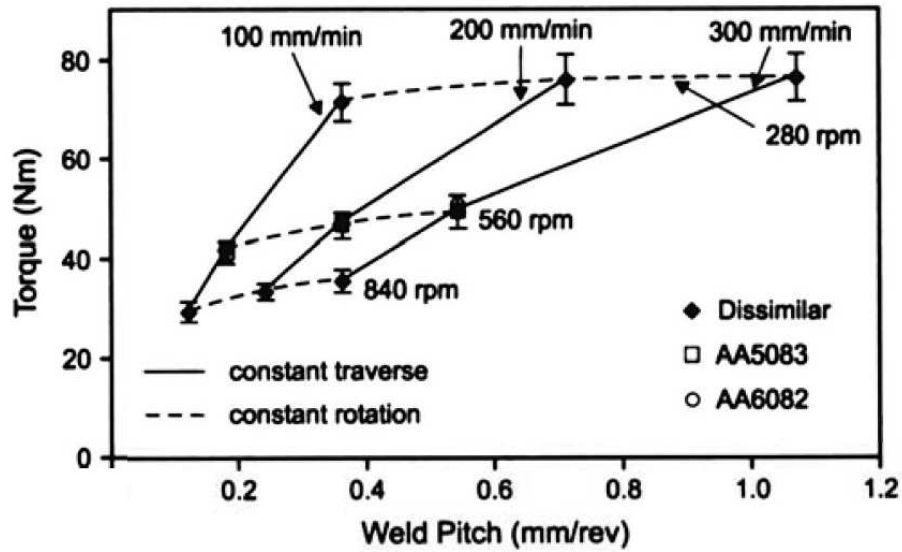


Figure 2.15. Variation of torque on the tool with weld pitch [93].

variations to minimise a functional corresponding to the work done to shear the material rotating around the tool, thus allowing calculation of an average value for the shear stress at the interface of tool and work-piece. This procedure can be used for rough estimate of torque on the tool and to validate numerical models.

2.4.1 Welding variables

The welding speed, the tool rotational speed, the vertical pressure on the tool, the tilt angle of the tool and the tool design are the main independent variables that are used to control the FSW process. The heat generation rate, temperature field, cooling rate, x-direction force, torque, and the power depend on these variables. The effects of several of the independent variables on the peak temperature have been discussed in the previous section. In short, peak temperature increases with increasing rotational speed and decreases slightly with welding speed. Peak temperature also increases with increase in the axial pressure. Fig. 2.16 shows significant increase in peak temperature with increase in rotational speed.

During FSW, the torque depends on several variables such as the applied vertical pressure, tool design, the tilt angle, local shear stress at the tool material

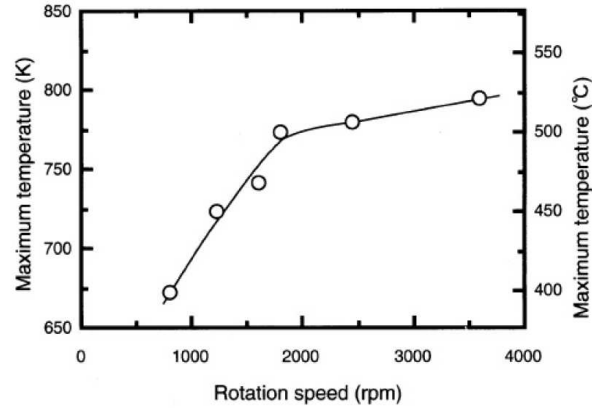


Figure 2.16. Relationship between rotational speed and peak temperature in FS-welds of AA 6063 [95].

interface, the friction coefficient and the extent of slip between the tool and the material. Measured torque values can provide some idea about the average flow stress near the tool and the extent of slip between the tool and the workpiece for certain conditions of welding, when other variables are kept constant.

The torque decreases with an increase in the tool rotation speed due to increases in the heat generation rate and temperature when other variables are kept constant. It becomes easier for the material to flow at high temperatures and strain rates. However, torque is not significantly affected by the change in welding speed as shown in Fig. 2.15. The relative velocity between the tool and the material is influenced mainly by the rotational speed. Therefore, the heat generation rate is not significantly affected by the welding speed. High traverse speeds tend to reduce heat input and temperatures. The torque increases only slightly with the increase in traverse speed because material flow becomes somewhat more difficult at slightly lower temperatures. The torque on the tool can be used to calculate the power required from $P = \omega M$, where M is the total torque on the tool.

Excessive x-direction force can be an important indicator of potential for tool erosion and, in extreme cases, tool breakage. Axial pressure also affects the quality of the weld. Very high pressures lead to overheating and thinning of the joint while very low pressures lead to insufficient heating and voids. Power requirement also increases with the increase in axial pressure.

2.5 Peak temperature

Thermal cycles affect the structure and properties of welded materials. Peak temperatures in the work piece are attained close to the edge of the tool shoulder and significant spatial gradients of temperature exist in the vicinity of the tool surfaces. Measurements of temperatures close to a rotating tool are difficult for two reasons. The material transport caused by the motion of the tool makes it difficult to focus on a single location; any embedded thermocouple will be displaced due to plastic flow. The strong temperature gradient near the tool means that a small error in thermocouple location can lead to a large error in temperature. Therefore, it is useful to compute temperature fields using models, which can range from simple two dimensional conduction calculations to complex three dimensional convection methods.

Fig. 2.17(a) shows that for FS-welded AA 6063, the grain size in TMAZ increases with increase in peak temperature caused by increase in rotational speed. Here grain size is related to peak temperature by assuming static grain-growth of dynamically recrystallised grains, during the cooling of the thermal cycle [95]:

$$D^2 = D_0^2 + Ate^{(-Q/RT_p)} \quad (2.23)$$

where D_0 and D are the initial and recrystallized grain size, A is a constant, t is the time to cool to 448 K, Q is the activation energy for grain-growth, T_p is the peak temperature. Assumption of isothermal condition leads to over-prediction of grain-sizes [95]. Precipitate free zones form near the grain boundaries because grain boundaries act as sinks for nearby dislocations, reducing nucleation sites for precipitates and also as precipitation sites, effectively reducing the solute content around them. As grain size increase, assuming constant width of PFZs, their volume fraction decreases with increase peak temperature as shown in Fig. 2.17(b) [95].

Not all alloys of aluminium are precipitation hardened. In the 2000 series alloys, the strength depends more on grain size (d), which has been expressed in terms of the Zener-Holloman parameter [96]:

$$\log d = a + b \log Z \quad (2.24)$$

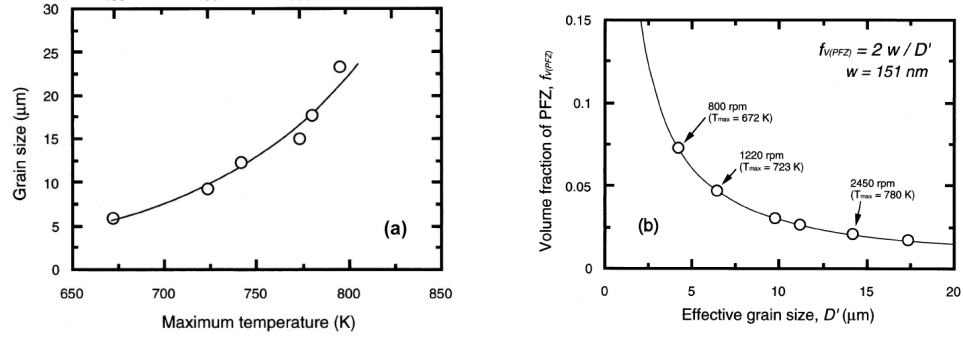


Figure 2.17. Relationship between (a) peak temperature and grain size in AA 6063 [95] and (b) grain size and volume fraction of PFZs.

where a and b are empirical constants based on data from extrusion experiments [97] and the hardness is then related to d using a form typical of the Hall–Petch type equation:

$$HV = HV_0 + c/\sqrt{d} \quad (2.25)$$

where c is a constant.

2.6 Tool Design

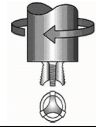
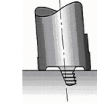
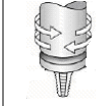
Tool design is one of the most exciting areas in FSW research. Colegrove and Shercliff [98] numerically examined the effect of tool design in welding 20 mm thick plates of 7449 aluminum alloys. They first developed a 3D heat transfer model and then tested tool designs using a two-dimensional plastic flow model. They could predict traversing force values close to those experimentally observed for a variety of tools. However, a 2D model is a simplification of the essentially 3D FSW process. This is particularly true when thick plates are being welded. Hence a complete 3D model for calculation of transverse force on the tool during FSW would be useful. Though, numerical modeling of plastic flow can aid tool design and the optimization of weld quality, there does not appear to have been an application of models towards the prediction of practical processing maps [99].

Tool design influences heat generation, plastic flow, the torque required for welding, and the uniformity of the welded joint. The shoulder generates most of the heat and prevents the plasticized material from escaping from the work-piece, while the tool-pin controls the material flow. Although, the shoulder design has

not changed much over the years, various features have been introduced on the conventional cylindrical threaded pin based on a better understanding of FSW. Some tools designed at TWI are summarised in Table 2.3. The *Whorl* and *MX-Triflute* have smaller volumes than the cylindrical tool [100, 101]. The tapered threads induce a vertical velocity that facilitates plastic flow. The flute in the *MX-Triflute* also increases the interfacial area between tool and the work-piece, leading to increased heat generation rates, softening and flow of material. Consequently, more intense stirring reduces both the traversing force for the forward tool motion and the welding torque [100, 101].

Although these tools are suitable for butt welding, they are not necessarily so for lap welding, where excessive thinning of the upper plate can occur together with the trapping of adherent oxide between the overlapping surfaces. *Flared-Triflute* and *A-skew* tools were developed to ensure fragmentation of the interfacial oxide layer and a wider weld than is usual for butt welding [102]. The *Flared-Triflute* tool is similar to *MX-Triflute* with an expanded flute, while *A-skew*™ tool is a threaded tapered tool with its axis inclined to that of the machine spindle. Both of these tools increase the swept volume relative to that of the pin, thus expanding the stir region and resulting in a wider weld and successful lap joints.

Table 2.3. A selection of tools designed at TWI [100, 103].

Tool	Cylindrical	Whorl™	MX triflute™	Flared triflute™	A-skew™	Re-stir™
Schematics						
Tool pin shape	Cylindrical with threads	Tapered with threads	Threaded, tapered with three flutes	Tri-flute with flute ends flared out	Inclined cylindrical with threads	Tapered with threads
Ratio of pin volume to cylindrical pin volume	1	0.4	0.3	0.3	1	0.4
Swept volume to pin volume ratio	1.1	1.8	2.6	2.6	depends on pin angle	1.8
Rotary reversal	No	No	No	No	No	Yes
Application	Butt welding; fails in lap welding	Butt welding with lower welding torque	Butt welding with further lower welding torque	Lap welding with lower thinning of upper plate	Lap welding with lower thinning of upper plate	When minimum asymmetry in weld property is desired

Motion due to rotation and translation of the tool induces asymmetry in struc-

ture and properties of the weld across the tool pin, due to asymmetric heating and material flow across the tool pin. It has been demonstrated that during FSW, material flows primarily on the retreating side, *i.e.*, the side of the pin where the linear velocity of the tool points opposite to welding direction [38, 39, 48, 71, 76]. To overcome this problem, TWI devised a new tool, *Re-stir*, which applies cyclic reversal of tool rotation within one revolution or after one or more revolutions. This cyclic reversal of rotation eliminates most problems associated with inherent asymmetry of conventional FSW.

Zhao *et al.* [104] studied the effect of pin geometry on the weldability and mechanical properties of welded 2014 Al plates using the FSW process. The effect of four tool pins shown in Table 2.3 inclined at 2° relative to the work-piece, was considered. Under the operating conditions mentioned above, the tool-3 broke suggesting maximum resistance for the column pin. No defects were found for 1 and 2 while 3 and 4 produced defective joints. It was suggested that these defects were formed due to insufficient material flow when the unthreaded pin was used. Screw threads generate more heat and hence improved flow of the more plastic material. Besides, the threads exert a downward force that further facilitates flow. It has been found that material flows mainly on the retreating side making a “wormhole” on the advancing side [34, 75]. This effect becomes more prominent at low temperatures with sluggish flow. Tool-2 was found to be the best among the four and produced welds of superior mechanical properties [104]. The results demonstrate how testing provides important information in the selection of tool geometry. The choice of pin angle, which is the angle between the vertical and the conical surface of the pin, is another important parameter which influences the FSW process; increasing the angle leads to a more uniform temperature distribution along the z -direction, which helps in reducing distortion [66]. An angle of $\simeq 40^\circ$ is predicted to be optimum for 7xxx aluminum alloys [66], although this result has yet to be verified experimentally.

Design of tools based on a quantitative understanding is in its infancy. Colegrove and Shercliff [10, 77] used a thermal model based on *FLUENT* to design a tool to minimise the traversing force during FSW of aluminum alloy. They examined alternative geometries and considered *Trivex*, which is triangular in shape with convex surfaces, and *MX-Trivex* which has the similar shape but with threads

in it. They observed that the traversing force and down forces were considerably lower for the *Trivex* tools relative to those for *Triflute*, especially at lower applied shear stress where considerable slip occurs between the tool and the work-piece. They suggested that *Trivex* with its convex surfaces avoids sticking to the material that reduces the shear force at the tool-metal interface and consequently reduces the traversing force. *Triflute*, on the other hand, has features that impede flow and the tool sticks to the material even at low applied shear stress. The entrapped material in the tool leads to a large shearing effect causing correspondingly greater tool forces. Interestingly, they [10, 77] observed no change in terms of heat input or power requirement by different tool design.

The quantitative prediction of the forces that the tool experiences is particularly useful in designing tools for hard materials such as steel. Such predictions should ideally include a consideration of plastic flow in the thermal model [37–39]. The errors resulting from a neglect of plastic flow for high thermal conductivity alloys are smaller than for low thermal conductivity materials such as steel. The errors are greatest near the tool where an accurate knowledge of temperature is important for the smooth operation of the FSW process.

Tools have also been designed for the FSW of high melting temperature and high thermal conductivity materials. Pure titanium sheets have been successfully friction stir welded using sintered TiC welding tools. A water cooling arrangement was required to extract heat from the tool. Copper which has much higher thermal diffusivity than steel cannot easily be welded by conventional fusion welding techniques. Heat input required for copper is much higher than conventional FSW because of the greater dissipation of heat through the work-piece. FSW with high rpm (1250) and low welding speed (0.01 mm/s) has produced successful welds [105, 106].

Tool wear is an important concern for FSW process. Mandal *et al.* [107] proposed a technique to reduce tool wear. Heat sources were introduced in front of the tool to preheat the work-piece, creating a hot channel for the tool to move in, and thus reducing wear on the tool. The model was tested using a modified Rosenthal equation for a combination of three heat sources, one corresponding to the tool and two for the pre-heat ahead of the tool. Though the concept is novel, the computational modeling is simplistic. However, the wear on the tool was not

quantified and the conclusion about reduction in wear was intuitive. There is a need for the development of a reliable wear-model for the FSW tool.

2.7 Defects

Common defects in friction stir welds include porosity and surface defects. At a constant rotational speed, an increase in the travel speed leads to wormhole initiation near the bottom of the weld. Furthermore, the size of the wormholes increases with the travel speed [108] because of inadequate material flow towards the bottom of the weld. There are indications that the travel speed to rotational speed ratio is an important variable in the formation of the wormhole defect [109]. For the same material and tool geometry, a low ratio tends to favor the formation of wormhole defects [61]. Since most of the heat generation occurs at the interface between the tool shoulder and the work-piece, significant heterogeneity in heat generation can lead to defect formation in the form of excess flash due to surface overheating [108, 110].

The propensity for cracks or voids increases with the welding speed although there is an alloy-dependence [111]. For example, defects dominated in AA 5083-O and AA 2024-T3 but not in AA 6063-T6 in which there is a significant drop in hardness within the TMAZ. The defects tend to occur on the advancing side where an abrupt microstructural transition occurs from the highly refined nugget zone to the TMAZ while the transition was gradual on the relatively defect-free retreating side.

Cast Al-12Si wt% alloys contain coarse particles of silicon which can be used to reveal the flow and defect evolution during FSW [112]. Insufficient heating causes the brittle Si particles to crumble so that the observation of fine Si particles after FSW is indicative of defect formation due to limited material flow. It is not surprising therefore that finer particles were detected on the advancing side near the bottom of the tool pin where inadequate flow is associated with void formation.

It has been suggested that the force on the tool in the x -direction, which can be measured using a dynamometer, could be used to predict defect formation in FSW on the assumption that large forces indicate sluggish flow [113]. Maps showing the fraction of stirred material which is at a given flow stress and temperature, with

superimposed strain rate contours, (Figure 2.18) can also indicate the tendency for defect generation [98]. Referring to Figure 2.18, at 80 rpm a greater amount of material is being deformed at a higher strain rate with both the Triflat and Trivex tools than with the Cylindrical tool. At 200 rpm, greater amount of material was deformed at moderate temperatures ($725\text{--}735\text{ K}$) and strain rates ($1\text{--}50\text{ s}^{-1}$) with the Trivex tool which shows largest deformation domain. It was concluded [98] that optimum welds correspond to maps with large regions of moderate to high strain rates and temperatures 30–50 K below the solidus temperature. Higher temperatures will lead to softening of the material and reduce the size of the deformation region.

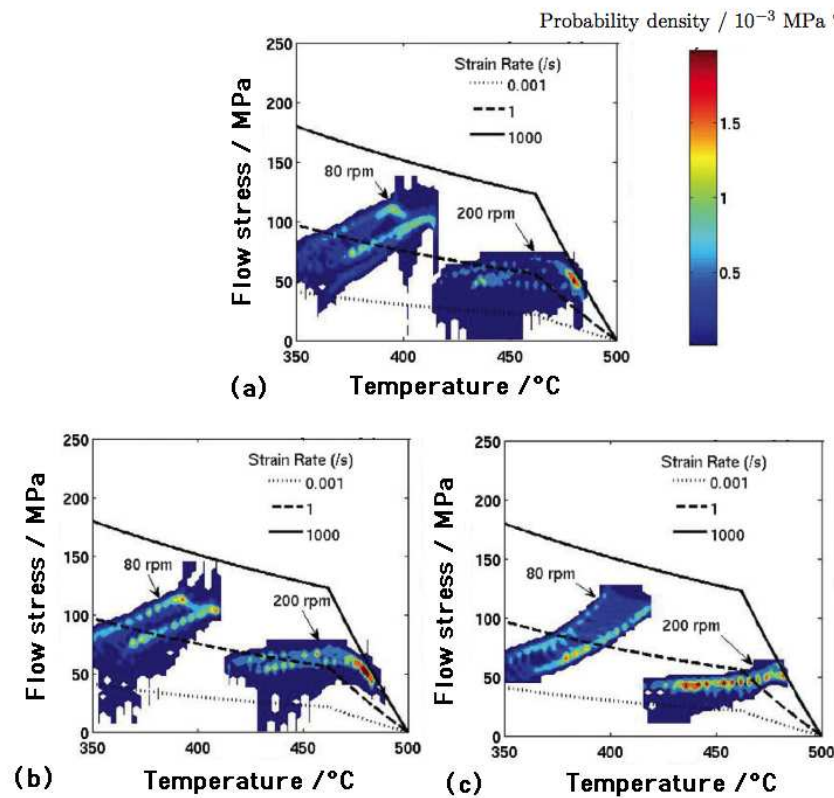


Figure 2.18. Material condition maps for a) Triflat, b) Trivex and c) Cylindrical tool pin at 80 and 200 rpm [98].

Tool design and welding variables affect materials flow patterns. However, no specific character of the material flow has been related with the porosity formation

and no unified mechanism of porosity formation exists.

Elangovan *et al.* [114] examined the effects of rotational speed and tool pin design on defect formation in friction stir processing of AA 2219. Five pin profiles (straight cylindrical, tapered cylindrical, threaded cylindrical, triangular and square) were used to fabricate joints at various tool rotational speeds. The square tool pin profile produced the least defect content in the weld as the flat faces produced a pulsating action which led to more effective stirring. Also, a square tool has higher eccentricity; the ratio of the dynamic volume swept by the tool to the static volume of the tool. For example, a square tool has eccentricity of $\pi d^2/4 : d^2/2 = \pi/2 \approx 1.57$ where d is the diagonal of the square.

In FSW lap joints of AA5083 and SS400, the size of the voids increases with increase in diameter of the tool pin and tool tilt angle [115]. Large diameter pin produces ($> 5\text{mm}$) more heat and forms intermetallic compound $FeAl_3$ instead of $FeAl$ formed at lower temperature. Since $FeAl_3$ is harder and more brittle than $FeAl$, voids form at higher temperature. Increasing the tool tilt angle ($> 1^\circ$) also increases the heat generation rate, forming aluminum rich Fe_2Al_5 , leading to decrease in joint strength.

Void formation during FSW can be predicted using FEM. The advantage of the FEM model [34] lies in the fact that the the arbitrary–Langrangian–Eulerian formulation allows for large material deformation and for the grid to track the material so that separation can occur between the work–piece and tool. For example, Figure 2.19 shows void formation at the lower advancing side, near the trailing edge of the pin/work–piece interface, due to incomplete deposition of plastic material.

2.8 Residual Stresses

The presence of residual stress in a weld plate affects its distortion behavior and ability to sustain applied loads while maintaining structural integrity [116–118]. While compressive stresses can in some circumstances be beneficial [119], tensile stresses can cause crack initiation and aid its propagation leading to catastrophic failure.

Residual stresses in the weld can be measured by using: 1) diffraction studies using X-ray or neutron sources without destroying the weld and 2) destructive

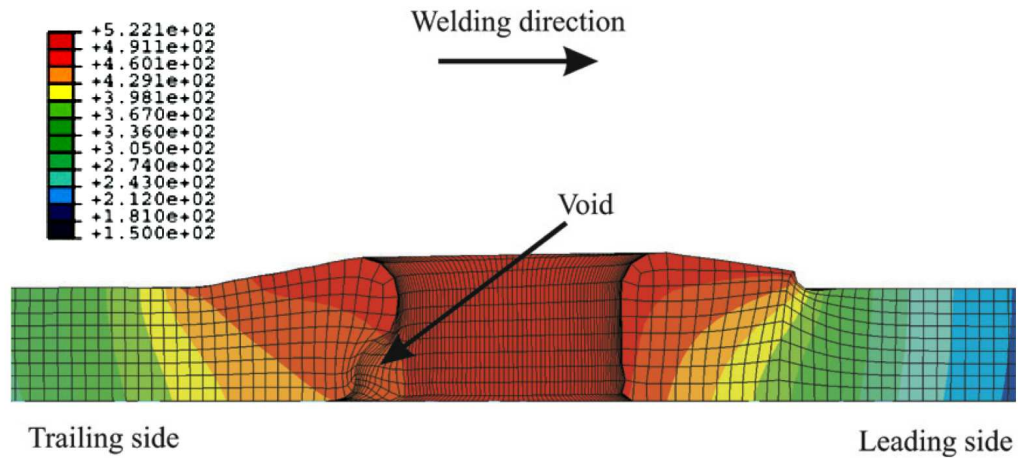


Figure 2.19. Void formation at the lower advancing side due to incomplete filling [34] modeled using ALE formulation of FEM. Temperature contours are shown in °C.

hole-drilling methods [116,117,120]. Since diffraction is expensive and conventional hole-drilling is only suited to uniform plane stress around the hole, Ya *et al.* [121] used Moiré interferometry incremental-hole drilling method to assess residual stress in a friction stir weld. Synchrotron diffraction has also been used to measure residual stress in such welds in the context of fatigue behavior [122].

Using neutron diffraction, Peel *et al.* [123] showed that longitudinal stress increases as traverse speed increases due to steeper thermal gradients and reduced time for stress-relaxation. Figure 2.20 shows that transverse stresses do not display a direct dependence on the rotational speed. It also shows that the weld zone is under tension and the workpiece material is under compression.

As in ordinary welds, residual stresses develop in constrained assemblies during FSW due to heterogeneous expansion during heating and contraction during cooling; a feature unique to FSW is the additional stress caused by the rotational and translational components of the tool so that the welding parameters of FSW must have a consequence on the final state of stress [124]. The stirring action of the tool is believed to relieve some of the stresses within the thermomechanically affected zone [125]. A finite element analysis of clamped FS-welded AA 6061 samples has shown that lateral and longitudinal residual stresses decrease with an increase in the rotational speed [124]. A higher welding speed enhances the longitudinal resid-

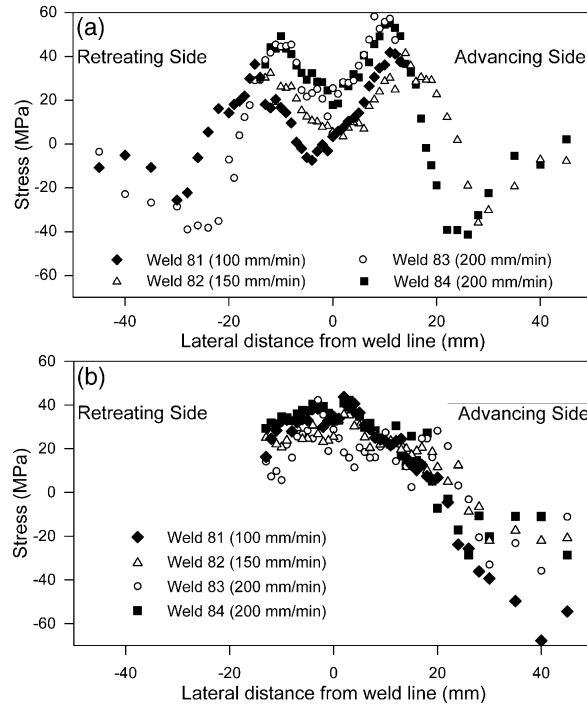


Figure 2.20. Measured (a) longitudinal x -direction and (b) the lateral y -direction stresses in AA5083 welds at different welding speeds [123].

ual stress but reduces it along the lateral direction. The analysis also showed that the maximum temperature gradients in the sample are located just beyond the edge of the tool-shoulder. As might be expected, the residual stress distribution is dramatically altered on unclamping the samples after friction stir welding and this must be taken into account in any modeling effort.

The role of plasticity during the friction stir welding process is known to be important in the calculation of residual stress; a large overestimation of the magnitudes of the residual stress may result if this effect is neglected [125]. Nevertheless, the outcome that the longitudinal stress along the weld centerline is tensile and larger than all the other component stresses is believed to be correct. Figure 2.21 shows some detail at a point where the FSW tool is half way along the length [126]; the longitudinal stress is lower in front of the tool (marked by A) as it has not been affected by thermal stress or by structural loading. Behind the tool, marked by D, compressive stresses exist. Transverse stress shows similar trend though it

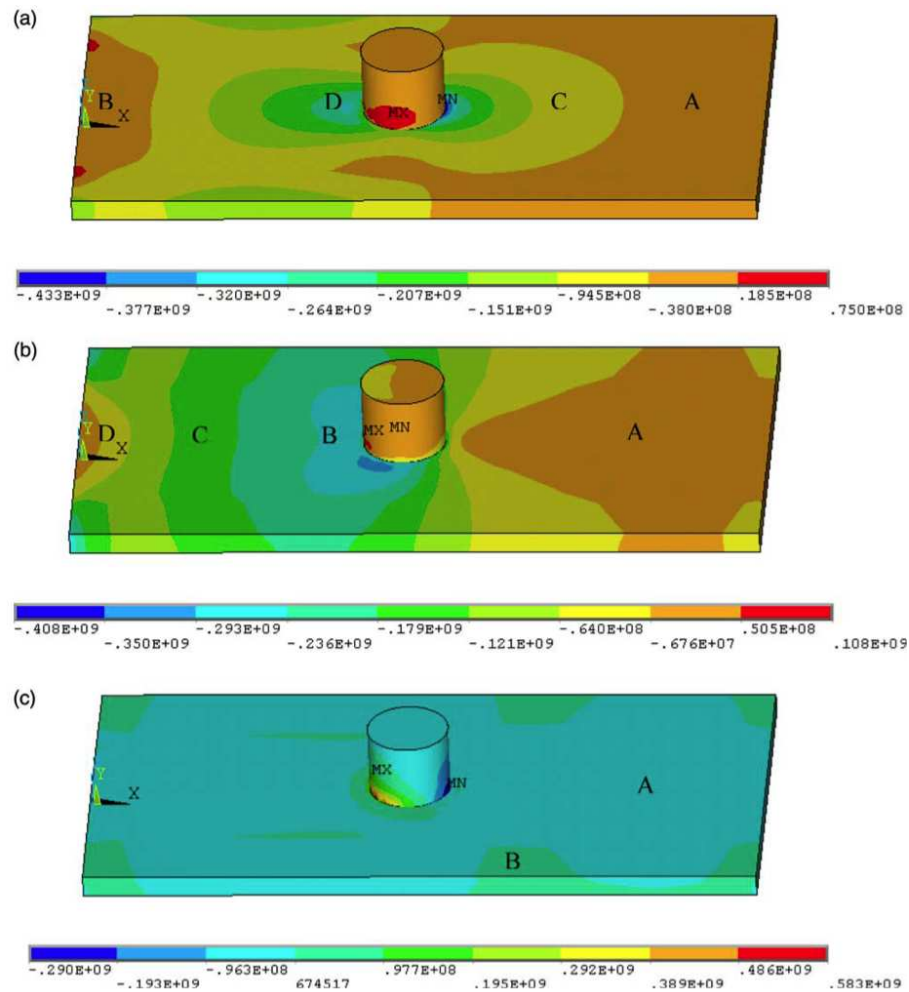


Figure 2.21. Normal stresses in Pa in (a) the longitudinal x -direction, (b) the lateral y -direction and (c) the vertical z -direction when the tool is mid-way between the two ends of AA 6061 weld plates [126].

is spread over a very larger area behind the tool compared to that in longitudinal stress as the end of work-piece right behind the tool is not constrained leading to free thermal expansion. The stress in the vertical direction is negligible along the edges of the work-piece (region B) while it is compressive in the remaining regions.

Tensile stresses present in FS-welded samples lead to poor mechanical properties. Applying external tensioning during welding [127] induces compressive stresses which have the benefit of inhibiting crack-propagation. Models predict that increasing tensioning levels to values higher than 50% of the room temper-

ature yield stress in AA2024 aluminum alloys, leads to tension in the weld being replaced by desirable compressive stresses [128]. This is an important finding and can be used by welders as a guiding principle to produce high-quality welds. Not surprisingly, crack propagation rates are known to correlate strongly with the state of stress [129].

There has been systematic work on the resistance to fatigue of friction stir welds in aluminum and titanium alloys [130], which demonstrates the key role of residual stresses in controlling crack growth within the HAZ along the welding direction. Although the levels of residual stress can be smaller than in conventional welding scenarios, they have a large effect on near-threshold crack propagation rates. These observations have been related also to microstructure and specimen geometry. In precipitation-hardened aluminum alloys the particles in the HAZ are much coarser and less coherent than the base material. This should in general reduce the fatigue crack growth rate in the HAZ relative to the base material, but only if residual stress does not exacerbate effects within the HAZ [130].

2.9 Current status and needs

Friction stir welding technology has been a major boon to industry advanced since its inception. In spite of its short history, it has found widespread applications in diverse industries. Hard materials such as steel and other important engineering alloys can now be welded efficiently using this process. Significant progress has also been made in the fundamental understanding of both the welding process and the structure and properties of the welded joints. The understanding has been useful in reducing defects and improving uniformity of weld properties and, at the same time, expanding the applicability of FSW to new engineering alloys. With better quantitative understanding of the underlying principles of heat transfer, material flow, tool-work-piece contact conditions and effects of various process parameters, efficient tools have been devised. At the current pace of development, FSW is likely to be more widely applied in the future.

Several important key problems and issues remain to be addressed. First, the fundamental knowledge of the FSW process and the knowledge of the evolution of the structure and properties needs to be combined to build intelligent process con-

trol models with a goal to achieve, defect free, structurally sound and reliable welds. Tailoring weld structure and properties based on fundamental knowledge still remains an important milestone in FSW. Attainment of this important goal would require new, more reliable and efficient process sub-models and reliable sub-models to describe the evolution of structure and properties of the welded joints. Current FSW process sub-models are complex, time consuming, and cannot be used in real time. Furthermore they all suffer from lack of reliability of the predicted results because the underlying physics is highly complex and the current phenomenological models do not contain any model component designed to ensure compliance with experimental results. Recent work in the fusion welding suggests that the lack of reliability of the phenomenological models may be contributed, at least to a large extent, by the uncertainty in several input parameters. In FSW, these uncertain parameters include the friction coefficient, the extent of slip between the tool and the work-piece, the heat transfer coefficient at several work-piece surfaces, partitioning of the heat between the work-piece and the tool at the tool-work piece interface, and the computed values of non-Newtonian viscosity based on the available constitutive models. Current phenomenological models of FSW do not have any built in mechanism to address these uncertainties. This problem can be solved by combining a rigorous phenomenological process sub-model with an appropriate multivariable optimisation scheme to determine optimised values of the uncertain variables from a limited volume of experimental data. Such an approach would result in agreement between the phenomenological models and the experimental results with greater degree of certainty [13, 131–133].

However, the lack of reliability is not the only obstacle for tailoring weld attributes based on fundamental scientific principles. An important difficulty is that the existing process models are unidirectional. In other words, the process sub-models require as input welding parameters, thermophysical properties, tool and work-piece geometry and provide, as output, the temperature and velocity fields and the cooling rates at various locations. In contrast, engineers should be able to specify cooling rates, the geometry of the stir zone and/or other attributes of the FSW as input and obtain as output several alternative sets of welding parameters involving combinations of the welding speed, rotational speed, tool dimensions and other variables as output. Unless the models have a reliability component built

into them and are bi-directional in nature, their use is likely to be restricted to researchers with only limited use in manufacturing and process control. Since the quantitative knowledge base in FSW is embodied in process, structure and property sub-models, these sub-models must be made more useful to manufacturing. Previous work in fusion welding show that such restructuring of the process, structure and property sub-models is both necessary and achievable [11–13]. Success of such an undertaking will ensure availability of practically the entire quantitative knowledge base of FSW to the whole FSW community for the purpose of tailoring FSW weld attributes and fabricating defect free, structurally sound, and reliable welds. Attainment of this milestone is well within the reach of the welding community within the next ten years.

Heat transfer and viscoplastic flow

Heat transfer and fluid flow models have provided significant insight into fusion welding process. Since friction stir welding process is relatively new, models are still evolving. Even though several investigators have used numerical heat transfer to understand the FSW process, many ignored the plastic flow. For example, Frigaard *et al.* [73] developed a numerical three-dimensional (3-D) heat flow model for friction stir welding (FSW) based on finite difference method. They assumed that heat was generated at the tool shoulder due to frictional heating and adjusted the coefficient of friction so that the calculated peak temperature did not exceed the melting temperature. Chao *et al.* [64] formulated heat transfer in FSW process based on overall heat balance and inverse modeling into two boundary value problems (BVP), a steady BVP for the tool and a transient BVP for the workpiece and solved them using finite element method (FEM). They found that only 5% of the heat generated was transported into the tool and about 80% of the mechanical work was dissipated as heat. They calculated input power by measuring the pressure drop across the hydraulic spindle motor, efficiencies of the motor and the gearbox, and the torque from the free running spindle at the particular RPM. The heat generation rate was calculated by inverse modeling, that is, assuming a value for heat generation and then calculating the temperature field to see if it matches with experimental results, repeating the process until a good match is obtained. Song and Kovacevic [26] presented a detailed three dimensional numerical model of FSW where heat input from the tool was modeled as a moving heat source. Heat transfer during tool penetration and pulling was modeled. Later,

Song and Kovacevic [27] developed a transient three dimensional thermal model both for the tool and the workpiece. They achieved good agreement between the experimentally determined and computed temperatures. Khandkar *et al.* [36] developed a three dimensional thermal model where the heat generation was modeled based on experimentally measured torque distribution. They adjusted the bottom heat transfer coefficient to achieve good agreement between the computed and the measured temperatures. However, none of these models considered plastic flow of material.

Some investigators have considered three dimensional plastic flow in their models of heat transfer in FSW. Ulysse [9] used a three dimensional viscoplastic model to obtain temperature profile in AA 7050-T7451 joints produced by FSW. However, the predicted temperatures were consistently higher than the corresponding experimental values. The discrepancy was attributed to inadequate representation of the constitutive behavior of the metal for a wide range of strain rates and temperatures typical of FSW. Colegrove and Shercliff [70] developed a three dimensional model of heat and mass transfer using a commercial computer code, FLUENT, to understand the temperature distribution and material flow around a complex threaded tool. No slip condition was assumed at the tool workpiece interface. The model over predicted the size of the deformation zone and the effect of the rotational speed on peak temperature could not be adequately represented by the model. They suggested that these problems could be addressed in the future by either using a material slip at the tool interface or dramatically reducing the viscosity near the solidus temperature in the FLUENT code.

The previous computational work represents significant progress in the quantitative understanding of the FSW process. However, several important questions remain unanswered. For example, can the visco-plastic flow of metals be reliably predicted based on the previous work in extrusion and thermo-mechanical processing of metals? Can our current understanding of thermo-mechanical processing adequately represent the spatial variation of viscosity and strain rate in the workpiece during FSW? Can the cooling rates and the shape of the thermo-mechanically affected zone be reliably predicted? Do the velocity stream-lines used to visualize the flow pattern indicate asymmetry of flow ?

Here it is shown that the temperature fields, cooling rates, the plastic flow

fields and the geometry of the thermo–mechanically affected zone (TMAZ) can be adequately described by solving the equations of conservation of mass, momentum and energy in three dimensions with appropriate boundary conditions. The model considers tool design dependent spatially variable heat generation rates that accounts for the deformation work, non-Newtonian viscosity as a function of local strain rate, temperature and the nature of the material, and temperature dependent thermal conductivity, specific heat and yield stress. The model was tested for four different alloys: 1) AA 6061-T6, 2) 1018 Mn steel, 3) 304L stainless steel and 4) Ti–6Al–4V. Testing with materials having a widely different thermophysical properties is not only necessary to test the flexibility of the model but also allows for comparison of trends in output as a function of these properties. Numerically computed temperature fields, variations of peak temperatures with FSW variables and TMAZ geometry were compared with the corresponding independently measured values reported in the literature and from experiments done at Los Alamos National Laboratory and Indian Institute of Technology, Bombay.

3.1 Mathematical Formulation

3.1.1 Assumptions

Except at the beginning and end of welding, heat is generated at a constant rate during most of the intermediate period and the cross sections of the welds demonstrate similar geometry, structure and properties indicating a quasi-steady behavior. Shortly after the start of welding, the cylindrical tool shoulder and the tool pin rotate at a constant rotational speed with the tool pin completely inserted within the workpiece. The mass flow is treated as a flow of a non-Newtonian, incompressible, visco-plastic material. The maximum shear stress for yielding was assumed to be $\tau = \sigma_Y/\sqrt{3}$, where σ_Y is the yield stress, based on distortion energy theory for plane stress. The density variation was ignored following Boussinesq's approximation.

3.1.2 Governing equations

The temperature and velocity fields in pseudo-steady state are obtained by solving the generally available continuity, momentum and energy equations for incompressible single-phase flow. The steady state thermal energy conservation equation in index notation, for $i = 1, 2$ and 3 , representing x, y and z directions, respectively, is given by:

$$\rho C_p \frac{\partial(u_i T)}{\partial x_i} = -\rho C_p U \frac{\partial T}{\partial x_1} + \frac{\partial}{\partial x_i} \left(k \frac{\partial T}{\partial x_i} \right) + S_b + S_{in} \quad (3.1)$$

where ρ is the density, u_i is the material velocity in i -direction, T is the temperature, x_i is i -coordinate, C_p is the specific heat capacity at constant pressure, U is the welding velocity, k is the thermal conductivity of the work piece and $S_b = d\dot{e}_p/dV = \beta\mu\phi$ is the heat generation rate per unit volume, due to plastic deformation in the work-piece away from the interface. Symbol β denotes the fraction of plastic deformation work which is dissipated as heat, μ is the non-Newtonian viscosity of the plasticized material and ϕ is given by [43]:

$$\phi = 2 \sum_{i=1}^3 \left(\frac{\partial u_i}{\partial x_i} \right)^2 + \left(\frac{\partial u_1}{\partial x_2} + \frac{\partial u_2}{\partial x_1} \right)^2 + \left(\frac{\partial u_1}{\partial x_3} + \frac{\partial u_3}{\partial x_1} \right)^2 + \left(\frac{\partial u_3}{\partial x_2} + \frac{\partial u_2}{\partial x_3} \right)^2 \quad (3.2)$$

The symbol S_{in} is the source term due to interfacial heat generation rate per unit volume at the tool pin-work piece interface:

$$S_{in} = [(1 - \delta)\eta\tau + \delta\mu_f P_N](\omega R_P - U \sin \theta) \frac{A_r}{V} \quad (3.3)$$

where A_r is any small area on the interface, V is the control volume enclosing the area A_r , η is the mechanical efficiency, *i.e.* the fraction of mechanical energy converted into heat, δ denotes the spatially variable fractional slip between the tool and work-piece interface, τ is the maximum shear stress for yielding, μ_f is the spatially variable coefficient of friction, R_P is the tool pin radius and P_N is the pressure on the interface.

A mechanical efficiency or the fraction of plastic work which is converted to heat is a material dependent parameter which is a complex function of strain, strain rate and temperature and can range from 0.3 to 0.95 [40, 134]. In equation 3.5 it

was assumed that the radial pressure is much smaller than the axial pressure so that it can be approximated as zero.

The continuity equation is given by (assuming incompressible flow):

$$\frac{\partial u_i}{\partial x_i} = 0 \quad (3.4)$$

The momentum conservation equations with reference to a co-ordinate system with origin at the tool-axis and moving with the tool at a constant speed U along the x-axis are:

$$\rho \frac{\partial u_i u_j}{\partial x_i} = -\frac{\partial P}{\partial x_i} + \frac{\partial}{\partial x_i} \left(\mu \frac{\partial u_j}{\partial x_i} + \mu \frac{\partial u_i}{\partial x_j} \right) - \rho U \frac{\partial u_j}{\partial x_1} \quad (3.5)$$

where P is the pressure. Notice that in contrast to equation 2.2 where p is the pressure applied by the tool on the work-piece, P is a relative pressure which drives flow. The material viscosity is a strong function of local strain rate and temperature. Figure 3.1 shows the computed variation of viscosity, expressed as logarithm to the base of ten, with strain rate and temperature for (a) AA 6061-T6, (b) 1018 C-Mn steel, (c) 304L stainless steel and (d) Ti-6Al-4V alloys. The different temperature range for different alloys corresponds to the usual range of temperature expected in the flow-regime of FSW for the respective alloys. The order of non-Newtonian viscosity is consistent with the values usually observed in typical viscoplastic processing of metals like extrusion. For example, Bhattacharya *et. al.* [135] calculated a maximum strain-rate of 0.24 s^{-1} and a viscosity of 3.6 MPa-s in lead. The trends in viscosity with variation in temperature and strain rate, is as expected. Viscosity decreases significantly with both strain rate and temperature. In all four alloys, the strain rate is the more dominant factor for the conditions typical of FSW. The sensitivity to strain rate increases with increase in temperature. If the viscosity of the four alloys is compared at $T = 0.5 T_{solidus}$ for each alloy ($T_{solidus}$ is given in Table 3.7), Ti-6Al-4V has the highest viscosity for a given strain-rate and 1018 C-Mn steel has the lowest viscosity.

Temperature-dependent thermophysical material properties have been used for the modeling and simulation. Figure 3.2 shows the variation for AA 6061-T6, which is one of alloys for which heat transfer and plastic flow during FSW was modeled. Data for other materials is given in Table 3.7. These alloys have widely different thermophysical properties.

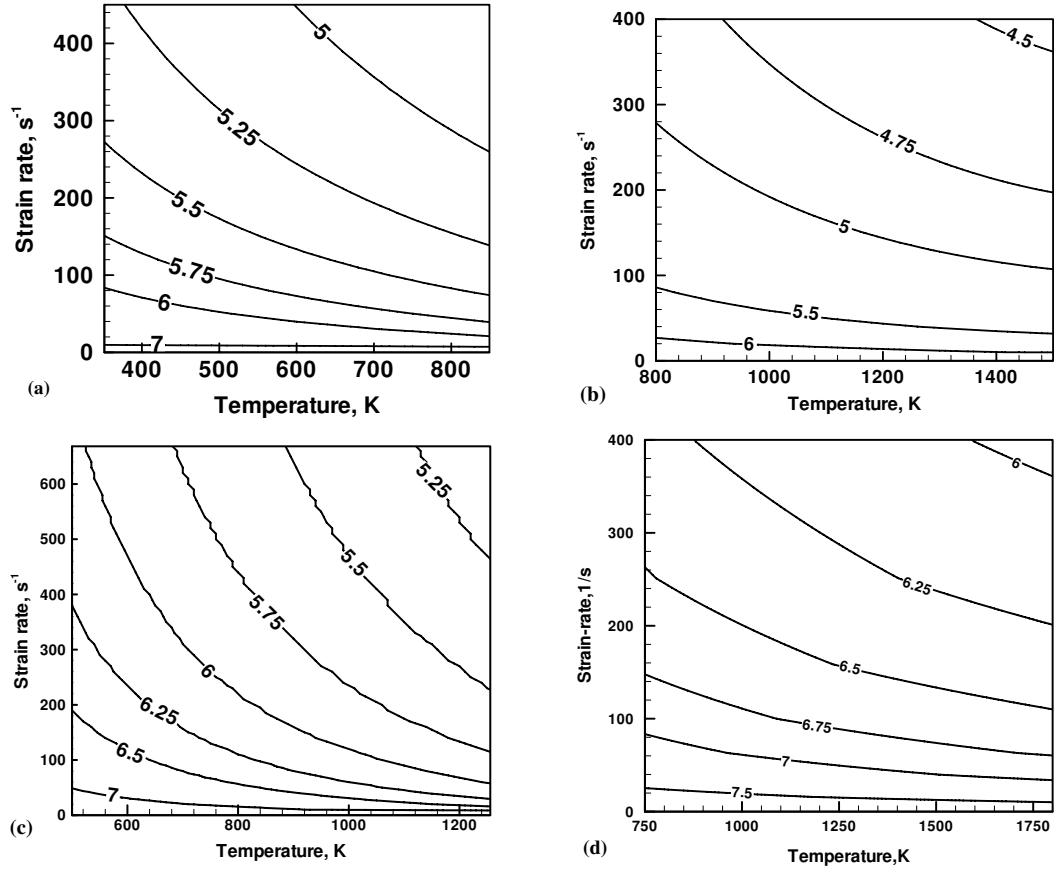


Figure 3.1. Computed contours of $\log_{10}(\text{viscosity in Pa s})$ as a function of temperature and strain rate for (a) AA 6061-T6, (b) 1018 C-Mn steel. (c) 304L stainless steel and (d) Ti-6Al-4V.

3.1.3 Boundary conditions

The interface between the tool and the workpiece can be separated into three regimes: 1) shoulder, 2) pin's vertical surface and 3) pin's horizontal surface, as indicated in Fig. 3.3. Of the heat generated at the shoulder-workpiece interface, some of it is transported to the tool material while the rest enters the workpiece. The total heat generated at the shoulder/work-piece interface can be partitioned between the work piece (J_W) and the tool (J_T), based on their thermophysical properties [45]:

$$f = \frac{J_W}{J_T} = \frac{(k\rho C_P)_W^{1/2}}{(k\rho C_P)_T^{1/2}} \quad (3.6)$$

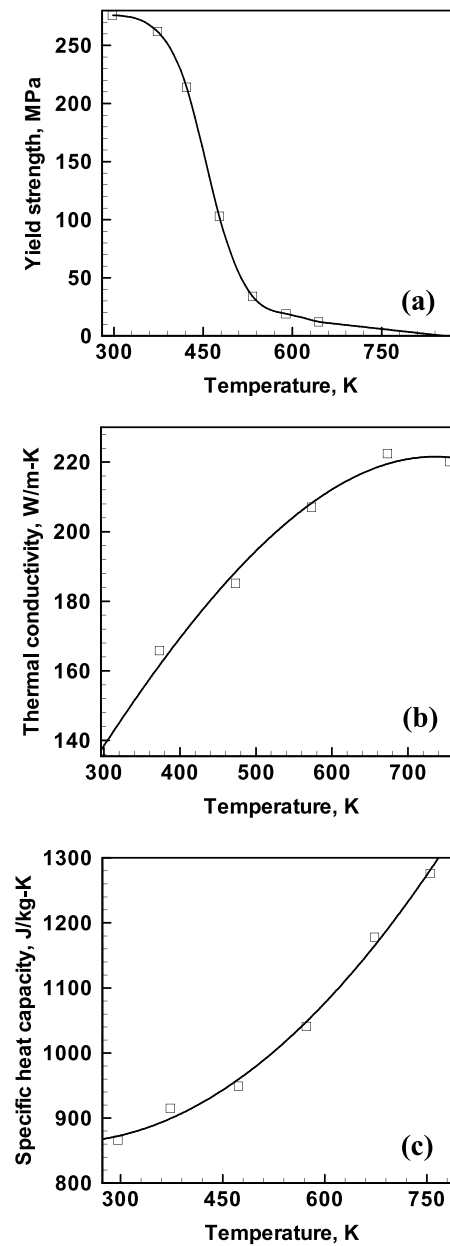


Figure 3.2. Variations of (a) yield strength [60] (b) thermal conductivity [9] and (c) specific heat capacity [9] of AA 6061-T6 with temperature. Symbols denote data points from literature while the curves are obtained by spline interpolation of the data points.

Equation 3.6 assumes steady-state, one-dimensional heat flow from the interface of dissimilar metal joints [48]. At 1000 K, the estimated heat flux into the work piece is calculated to be 43% of total heat generated in 1018 Mn steel Welded

using Tungsten tool. This relation has been examined experimentally by Lienert *et al.* [45] and found to be reliable.

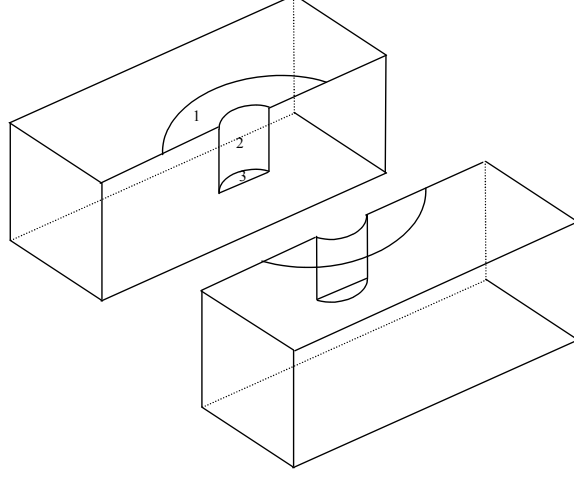


Figure 3.3. Interfaces for heat generation in FSW: (1) Tool shoulder, (2) Tool pin's vertical surface and (3) Tool pin's bottom surface–workpiece.

Heat flux continuity at the shoulder matrix interface yields:

$$k \frac{\partial T}{\partial z} \Big|_{\text{top}} = \frac{J_W}{J_W + J_T} \dot{q} \quad \text{in the range} \quad R_P \leq r \leq R_S \quad (3.7)$$

where \dot{q} is the rate of heat generation due to friction and plastic deformation at the shoulder–work piece interface, given by:

$$\dot{q} = [\eta(1 - \delta)\tau + \delta\mu_f P_T] (\omega r - U \sin \theta) \quad (3.8)$$

The boundary condition for heat exchange between the top surface of the work piece and the surroundings beyond the shoulder involves consideration of both convective and radiative heat transfer as

$$-k \frac{\partial T}{\partial z} \Big|_{\text{top}} = \sigma\epsilon(T^4 - T_a^4) + h(T - T_a) \quad (3.9)$$

where σ is the Stefan-Boltzmann constant ($5.67 \times 10^{-16} \text{ W K}^{-4} \text{ m}^{-2}$), ϵ is the emissivity, T_a is the ambient temperature and h is the heat transfer coefficient at the

top surface.

In literature, constant values of bottom heat transfer coefficient have been used (Table 3.3). Here at the bottom surface of the workpiece, the heat transfer into the backing plate is modeled by a temperature dependent enhanced heat transfer coefficient [136]:

$$k \frac{\partial T}{\partial z} \Big|_{\text{bottom}} = h_b(T - T_a) \quad \text{where} \quad h_b = h_{b0}(T - T_a)^{0.25} \quad (3.10)$$

where h_b is the enhanced heat transfer coefficient at the bottom surface.

In all FSW models available in the literature, constant values of friction coefficient (Table 3.1) and slip at the tool workpiece interface (Table 3.2) have been used. Here, spatial variation of these variables has been introduced in a functional form based on data available from other material processes like friction welding [41] and rolling [41].

The extent of slip, δ , is estimated by curve fitting the measured values (Fig. 3.4) at various relative velocities [46]:

$$\delta = 0.2 + 0.6 \left(1 - \exp\left(-\delta_0 \frac{\omega r}{\omega_0 R_S}\right) \right) \quad (3.11)$$

where δ_0 is an adjustable parameter, R_S is the radius of the tool shoulder, ω_0 is the normalizing rotational velocity which can be taken as the mid-point of the range of rotational speeds.

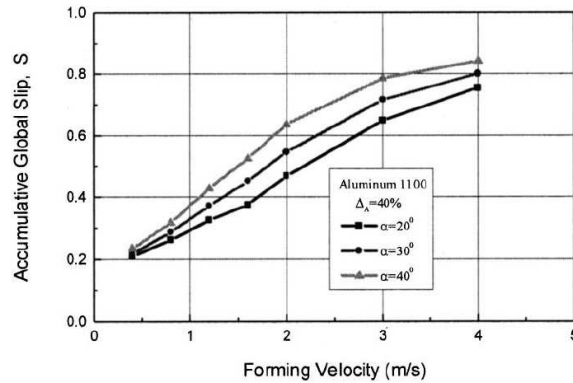


Figure 3.4. Influence of forming velocity and forming angle on the accumulative global slip for cross-wedge rolling when tool translation velocity is 1.0 m/s in AA 1100 [46].

Values of friction coefficient, μ_f , can be estimated considering the relative velocity between the tool and the work-piece according to previous work in the context of friction [41, 46]. The relative velocity increases from zero at the axis of rotation to ωR_S at the periphery of the tool shoulder. Evidence suggests [41, 46] that μ_f has the form $\mu_f = \mu_0 \exp(-\delta \frac{\omega r}{\omega_0 R_S})$, where μ_0 is a fitting constant.

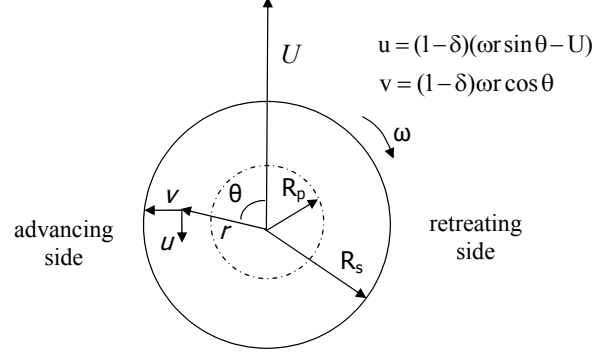


Figure 3.5. Top view of the rotating tool moving in the negative x-direction. $\theta = 0$ corresponds to plane $y = 0, x < 0$.

The speeds with which material moves at the tool-pin periphery, u , v and w , along the welding direction, the normal to the welding direction in the plane of the plate being welded, and normal to the plane of the plate respectively, are given by (as shown in Fig. 3.5):

$$u = (1 - \delta)(\omega r \sin \theta - U) \quad v = (1 - \delta)\omega r \cos \theta \quad w = \Psi\omega \quad (3.12)$$

where Ψ is the pitch of the threads on the cylindrical tool. At the shoulder, workpiece interface, the z-direction velocity, $w = 0$.

3.2 Numerical scheme

In FSW, plasticized material near the tool undergoes severe deformation. When large visco-plastic deformation occurs, elastic deformations are negligible and material flows in a viscous manner. The viscoplastic flow is modeled using a rheological model in which fluid never yields but always flows, albeit the flow is very sluggish (high viscosity values) at low strain rates. The viscosity of the non-Newtonian fluid

Values of coefficient of friction (μ_f), slip (δ), bottom heat transfer coefficient (h_b) and mechanical efficiency (η) available in literature

Table 3.1. Reported values of friction coefficient, μ_f

Value	Workpiece	Reference	Comment
0.4	AA 6061-T6	Song <i>et. al.</i> [25]	Best-fit
0.35-0.55	AA 5182	Colligan <i>et. al.</i> [137]	Expt., $\frac{3M}{2F_z R_s}$ ^a
0.6-1.3	F-357	Colligan <i>et. al.</i> [137]	Expt., $\frac{3M}{2F_z R_s}$
0.4-0.5	AA 6061	Soundarajan <i>et. al.</i> [126]	Best-fit
0.4	AA 6082, AA 7108	Frigaard <i>et. al.</i> [73]	Best-fit
0.3	AA 2024-T3	Schmidt <i>et. al.</i> [34]	Best-fit
0.27-0.35	AA 2024-T3	Schmidt <i>et. al.</i> [31]	Best-fit
0.57	Plasticine	Liechty <i>et. al.</i> [138]	$\frac{\tau_Y}{\sigma_Y} = \frac{1}{\sqrt{3}}$ ^b

^a M :measured torque, F_z : measured axial force, R_s : shoulder radius

^b τ_Y :shear yield stress, σ_Y : tensile yield stress

Table 3.2. Reported values of slip, δ

Value	Workpiece	Reference	Comment
0.0	AA 2024-T3	Schmidt <i>et. al.</i> [31]	Best-fit
0.0-0.99	AA 2024-T351	Rosakis <i>et. al.</i> [138]	Best-fit
0.6-0.9	α -titanium	Rosakis <i>et. al.</i> [40]	Kolsky-bar experiment

Table 3.3. Reported values of bottom heat transfer coefficient, h_b

Value	Workpiece	Reference	Comment
350 W/m^2K	AA 2195	Chao <i>et. al.</i> [64]	Inverse modeling
30-4000 W/m^2K	AA 6061	Soundarajan <i>et. al.</i> [126]	$f(\sigma_z)$ ^a
1000 W/m^2K	AA 6061	Khandkar <i>et. al.</i> [36]	Best-fit
1000 W/m^2K	AA 2024-T3	Schmidt <i>et. al.</i> [34]	Best-fit

^a σ_z :normal stress; non-uniform with highest directly below tool pin

Table 3.4. Reported values of mechanical efficiency, η

Value	Workpiece	Reference	Comment
0.77-0.82	AA 2195	Chao <i>et. al.</i> [64]	$\frac{\text{heat generated (best-fit)}}{\text{power input (experiment)}}$
0.25-0.6	AA 2024-T351	Rosakis <i>et. al.</i> [40]	Kolsky-bar experiment
0.6-0.9	α -titanium	Rosakis <i>et. al.</i> [40]	Kolsky-bar experiment

can be expressed as a function of the temperature and strain rates. The equations of conservation of mass, momentum and energy in three dimensional rectangular Cartesian co-ordinates are discretized using control volume method where the work piece is divided into small rectangular control volumes. Each control volume surrounds a grid point where the scalar variables are stored. Vectors such as the velocities are stored at grid points which are staggered with respect to those of scalar variables like pressure and temperature to ensure the stability of numerical calculation. The discretized equations are formulated by integrating the corresponding governing equation over the control volumes using fully implicit hybrid power law scheme and are solved iteratively using Tri-Diagonal Matrix Algorithm (TDMA) [139]. The solution methodology is called Semi-Implicit Pressure Linked Equations (SIMPLE) and was proposed by Patankar [139].

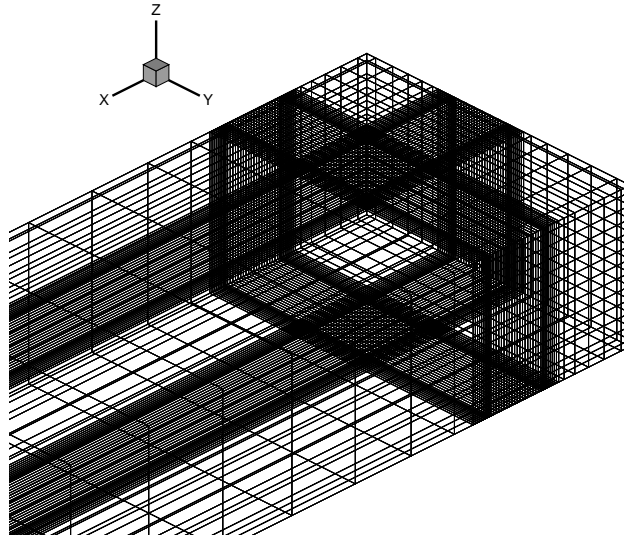


Figure 3.6. A typical grid mesh used for calculations, with length in z-direction increased 20 fold to enhance clarity.

The model takes in temperature dependent material properties of the tool and work piece, weld parameters and tool and work piece geometry as input and returns temperature and velocity fields as output. Typically $96 \times 92 \times 34$ non-uniform fixed rectangular grid points were used for maximum resolution of variables. The grids were fine near the tool and progressively coarser away from the tool shoulder

periphery as shown in Fig. 3.6. The minimum element size was $0.33 \text{ mm} \times 0.33 \text{ mm} \times 0.20 \text{ mm}$. The total number of grid points used in most runs were 300288 ($96 \times 92 \times 34$). To test the grid dependence, runs were made for 6061 aluminum alloy. Increasing the total number of grid points to 522648 ($126 \times 122 \times 34$) resulted in a maximum of 4.5 K difference in peak temperature and less than 0.1 cm/s difference in the x, y and z direction maximum velocities for 10 different welding conditions, which are given in Table 3.5. Convergence is usually achieved within 3000 iterations which requires about 15 minutes in a PC with 3.2 GHz Intel P4 CPU and 1024 MB PC2700 DDR-SDRAM memory.

Table 3.5. Effect of mesh refinement on predicted process variables. Coarse mesh had 300288 grid points ($96 \times 92 \times 34$) while fine mesh had 522648 grid points ($126 \times 122 \times 34$).

Welding speed (mm/s)	Rotation speed (RPM)	Torque (N-m)			Power (W)		
		Fine mesh	Coarse mesh	Percent difference	Fine mesh	Coarse mesh	Percent difference
1.27	300	64.8	63.7	1.7	1906.9	1872.7	1.8
2.11	300	65.5	64.4	1.7	1925.7	1891.5	1.8
3.38	300	67.4	65.8	2.4	1979.6	1930.2	2.5
4.23	300	68.4	66.7	2.5	2006.6	1956.7	2.5
2.11	150	111.0	109.2	1.7	1572.7	1543.5	1.9
2.11	200	88.8	87.4	1.6	1704.9	1674.4	1.8
2.11	300	65.5	64.4	1.7	1925.7	1891.5	1.8
2.11	480	51.5	51.0	1.1	2411.5	2384.7	1.1
2.11	600	47.4	46.8	1.3	2765.0	2724.9	1.5

3.3 Results and discussion

3.3.1 Materials and thermophysical properties

Four different tool-workpiece material combinations were modeled to test the robustness of the model for materials with widely different thermophysical and rheological properties and also to study the effect of these properties on temperature

and plastic flow fields. They are listed in Table 3.6. The thermophysical properties of workpiece and tool materials used in calculations are indicated in Table 3.7. The process parameters, tool and workpiece dimensions are given in Table 3.8. The values of mechanical efficiency, η , are different for different materials and are determined by the stored energy of cold work, the strain hardening, strain-rate hardening and thermal softening characteristics of the different materials [40]. The values reported in literature (Table 3.4) also show a wide range.

Table 3.6. Tool and workpiece materials for systems modeled in this research

	Workpiece	Tool	Experimental work
1	AA 6061-T6	Tool steel	Song <i>et. al.</i> [27]
2	1018 Mn steel	Tungsten	Lienert <i>et. al.</i> [45]
3	304L stainless steel	Tungsten	Zhu <i>et. al.</i> [140]
4	Ti-6Al-4V	Tungsten	Lienert <i>et. al.</i> [141]

3.3.2 Heat generation rate and torque

3.3.2.1 AA 6061

The variation in computed heat generation rates at the tool shoulder and the pin surfaces with welding velocity and rotational speed is given in Table 3.9. Even though heat generation rate and torque increases with welding speed, peak temperature decreases. The torque, M , is computed using the following relation:

$$M = \int r_A \times \tau_t dA \quad (3.13)$$

where τ_t is total shear stress at the tool-workpiece interface given by:

$$|\tau_t| = (1 - \delta) \tau + \delta \mu_f p \quad (3.14)$$

Because heat generation rate is a stronger function of rotational speed, when rotational speed is kept constant and welding velocity is increased, peak temperature decreases as nearly same amount of heat energy is diffused through a greater volume. This decrease in peak temperature leads to increase in yield strength which

Table 3.7. Temperature dependent thermophysical properties of various work-piece (AA 6061-T6 [60], 304L Stainless Steel [61], 1018 Mild Steel [62], Ti-6Al-4V [63]) and tool materials(M2 Tool Steel [64], Tungsten [65]).

Property		AA 6061-T6	304L Stainless Steel	1018 Mild Steel	Ti-6Al-4V	M2 Tool Steel	Tungsten
Temperature range, K		300 - 750	293 - 1073	298 - 1273	273 - 1150	293 - 948	293 - 2500
Density, kg/ m ³		2700	7800	7860	4420	8100	19400
Specific heat capacity, J/kg-K $C_0 + C_1T + C_2T^2 + C_3T^3$	C ₀	9.29 x 10 ²	2.76 x 10 ²	4.68 x 10 ²	6.22 x 10 ²	3.89 x 10 ²	1.58 x 10 ²
	C ₁	-6.27 x 10 ⁻¹	8.51 x 10 ⁻¹	-8.49 x 10 ⁻²	-3.67 x 10 ⁻¹	2.08 x 10 ⁻¹	1.06 x 10 ⁻¹
	C ₂	1.48 x 10 ⁻³	-8.51 x 10 ⁻⁴	3.03 x 10 ⁻⁴	5.45 x 10 ⁻⁴	0	-1.63 x 10 ⁻⁵
	C ₃	-4.33 x 10 ⁻⁸	3.00 x 10 ⁻⁷	1.82 x 10 ⁻⁷	2.39 x 10 ⁻⁸	0	0
Thermal conductivity, W/m-K $C_0 + C_1T + C_2T^2 + C_3T^3$	C ₀	2.52 x 10 ¹	1.43 x 10 ¹	3.77 x 10 ²	1.92 x 10 ¹	1.57 x 10 ¹	3.67 x 10 ⁻¹
	C ₁	3.98 x 10 ⁻¹	-9.02 x 10 ⁻³	9.24 x 10 ⁻²	1.89 x 10 ⁻²	1.74 x 10 ⁻²	-2.29 x 10 ⁻⁴
	C ₂	7.36 x 10 ⁻⁶	4.52 x 10 ⁻⁵	-1.79 x 10 ⁻⁴	-1.53 x 10 ⁻⁵	-3.83 x 10 ⁻⁶	1.25 x 10 ⁻⁷
	C ₃	-2.52 x 10 ⁻⁷	-2.49 x 10 ⁻⁸	7.81 x 10 ⁻⁸	-1.41 x 10 ⁻⁸	0	0
Yield strength, MPa $C_0 + C_1T + C_2T^2 + C_3T^3$	C ₀	1.16 x 10 ³	7.96 x 10 ²	1.11 x 10 ²	9.09 x 10 ²	-	-
	C ₁	-8.88 x 10 ⁰	-1.60 x 10 ⁰	1.11 x 10 ⁰	1.11 x 10 ⁰	-	-
	C ₂	2.97 x 10 ⁻²	2.25 x 10 ⁻³	-1.90 x 10 ⁻³	-3.05 x 10 ⁻³	-	-
	C ₃	-3.32 x 10 ⁻⁵	-1.30 x 10 ⁻⁶	7.51 x 10 ⁻⁷	1.26 x 10 ⁻⁶	-	-
Solidus temperature, K		855	1697	1600	1933	-	3683

leads to increase in both torque and heat generation rate. With increase in rotational speed, heat generation rates increase, which increases the peak temperature. In this case, the accompanying decrease in yield strength is not strong enough to offset the increase in the value of ω . But decrease in yield strength results in decrease in torque as the torque term only contains the yield strength and does not contain ω . Another way of looking at this is that higher temperature leads to better flowability which reduces the torque on the tool.

3.3.2.2 1018 steel

The proportion of the heat generated at the tool shoulder and the pin surfaces is determined by the tool geometry and the welding variables. Figs. 3.7(a) to (c) show the spatial variation of heat generation pattern at the tool-work piece interfaces in 1018 Mn steel. Heat generation pattern at the tool shoulder is nearly symmetric

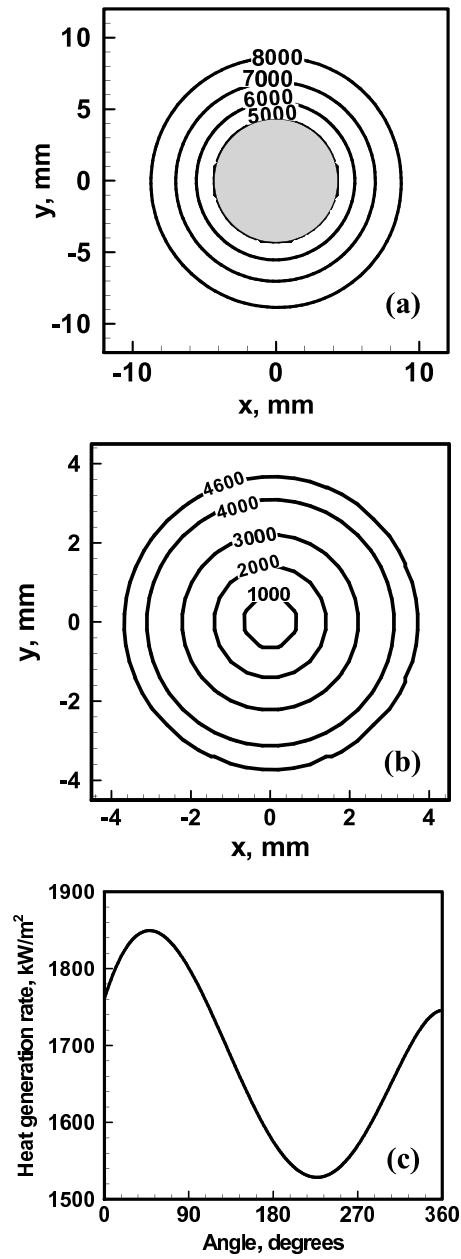


Figure 3.7. Spatially variable heat generation rate in 1018 Mn steel at (a) tool shoulder, (b) bottom of tool pin (contour values are in kW/m^2), and (c) curved surface of tool pin. The welding velocity was 0.42 mm/s and the rotational speed was 450 rpm.

Table 3.8. Data used in calculations

	AA 6061	1018 steel	304L SS	Ti-6Al-4V
Process parameters				
Workpiece length (mm)	254	410	300	330
Workpiece half-width (mm)	102	78	150	100
Workpiece thickness (mm)	12.7	6.35	3.18	7.2
Shoulder radius (mm)	25	9.5	9.53	9.5
Pin radius (mm)	6	3.95	3.17	3.95
Pin length (mm)	12.7	6.22	3.18	6.4
Weld speed (mm/s)	0.4-1.8	0.42	0.85-2.55	1.6
Rotational speed (RPM)	100-800	450	300-500	275
Model parameters				
δ, δ_0	$\delta = 0.65$	$\delta_0 = 1.77$	$\delta = 0.7$	$\delta_0 = 2.84$
μ, μ_0	$\mu = 0.4$	$\mu_0 = 0.25$	$\mu = 0.4$	$\mu_0 = 0.7$
$h_b(W/m^2K), h_{b0}(W/m^2K^{5/4})$	$h_b = 50$	$h_b = 209$	$h_b = 125$	$h_{b0} = 418$
η	1	0.5	1	0.7
β	0	0.05	0	0.1

about the tool axis as can be seen in Fig. 3.7(a). More heat is generated further away from the axis owing to higher relative velocity between the workpiece and the shoulder. The heat generation rate at the bottom of the pin shown in Fig. 3.7(b) indicates a similar behavior. The x and y scales are expanded with respect to Fig. 3.7(a) as the pin has a smaller dimension. Here, the total amount of heat generated is considerably lower than that at the shoulder because of the smaller radius of the pin and the lower relative velocity between the pin and the work piece. The y-scale is expanded to illustrate the angular variation of heat generation rate on the tool surface in Fig. 3.7(c). The non-uniformity in the heat generation pattern results from the difference in the relative velocity at different angular locations on the pin surface, which arises due to the variation in term $U \sin\theta$. The local differences in the heat generation rates lead to angular variations of temperature on the tool surface. As a result, meaningful modeling of temperature and plastic flow fields must consider three dimensional heat transfer.

Table 3.9. Heat generation rate at different tool–workpiece interfaces, peak temperature and total torque on the tool for different welding parameters in AA 6061. Process and model parameters are given in Table 3.8.

Welding speed (mm/s)	Rotational speed (RPM)	Shoulder (W)	Pin's vertical surface (W)	Pin's bottom (W)	Peak temperature (K)
0.5	200	2.97	250.1	45.6	700.2
1.0	200	3.05	252.8	46.1	694.4
1.5	200	3.17	258.5	47.7	688.2
0.5	400	3.72	213.9	61.9	762.7
1.0	400	3.72	215.5	62.1	756.0
1.5	400	3.88	216.2	63.4	749.6
0.5	600	4.23	164.3	76.2	807.4
1.0	600	4.31	168.1	77.0	801.5
1.5	600	4.47	172.3	77.4	797.3

3.3.2.3 304L stainless steel

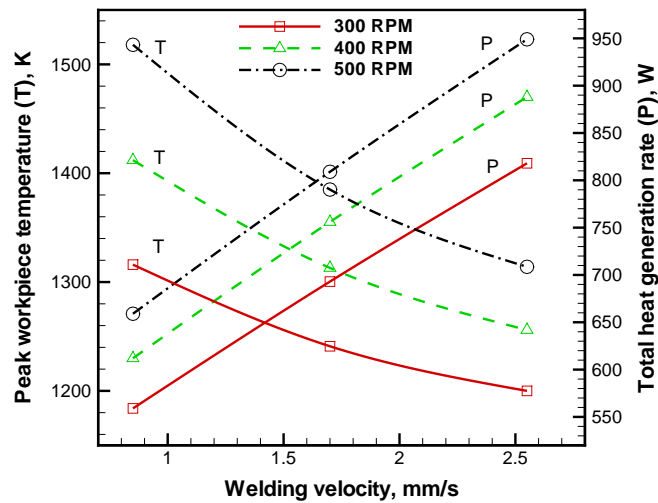


Figure 3.8. Heat generation rate for the welding of 304L stainless steel increases with increase in welding velocity. Peak temperature in the workpiece still decreases.

Table 3.10. Heat generation rate at different tool–workpiece interfaces, peak temperature and total torque on the tool for different welding parameters in 1018 Mn steel. Process and model parameters are given in Table 3.8.

Welding speed (mm/s)	Rotational speed (RPM)	Shoulder (W)	Pin's vertical surface (W)	Pin's bottom (W)	Viscous dissipation (W)	Peak temperature (K)	Torque (N-m)
0.02	350	608.7	272.7	135.4	54.1	1170.0	68.8
0.06	350	616.0	288.3	141.5	143.9	1137.6	70.9
0.10	350	620.3	304.1	147.6	166.5	1106.9	72.6
0.14	350	630.4	325.6	154.8	187.4	1061.0	75.5
0.02	450	694.8	247.7	162.2	25.5	1229.2	55.2
0.06	450	706.2	276.0	172.5	91.6	1168.0	58.0
0.10	450	709.8	290.2	178.6	129.3	1140.1	59.2
0.14	450	716.6	310.3	186.0	154.7	1097.2	61.1
0.02	550	763.0	211.7	185.8	16.8	1292.7	45.6
0.06	550	775.5	248.7	199.5	41.4	1210.5	48.4
0.10	550	780.9	267.6	207.4	99.5	1170.0	49.8
0.14	550	785.6	285.4	214.6	123.3	1128.3	51.0
0.02	650	819.8	176.5	207.9	13.3	1350.6	38.9
0.06	650	831.2	216.2	223.6	21.4	1253.9	41.3
0.10	650	837.8	241.4	234.0	81.5	1193.2	42.8
0.14	650	841.0	256.2	240.6	99.6	1152.3	43.7

For the tool geometry given in Table 3.8, the computed heat generation rates at different welding speeds and rotational speeds are plotted in Fig. 3.8. Heat generation rate increases with welding speed and tool rotational speed. The reason for increase with rotational speed is clear from Eqn. 3.3. However, with increase in welding speed, the increase in heat generation is not so straight forward and is related to decrease in temperature. At higher welding velocities, the weld temperature decreases as heat energy is distributed over a larger area. This reduction in temperature, increases the yield strength of the workpiece material in contact with the tool pin which, in turn, increases the heat generation rate as can be seen from Eqn. 3.3.

3.3.3 Computed temperature fields

3.3.3.1 AA 6061

The computed temperature profiles along the longitudinal and transverse sections through tool axis and at the top surface of AA 6061 work piece are shown in Fig. 3.9(a), (b) and (c), respectively. The temperature profiles on the longitudinal mid-section (Fig. 3.9(a)) and on the top surface of the work piece (Fig. 3.9(c)) are compressed in front of the tool and expanded opposite to the direction of tool movement.

Thermal cycles at various locations are calculated from the steady-state temperature profile. Thermal cycle for any point depends on its (y,z) co-ordinate. For a point on the weld-centerline, Fig. 3.10 shows how the thermal cycle can be extracted from the steady state temperature profile.

The computed thermal cycles in AA 6061-T6 at four monitoring locations are compared with independent experimental data from literature [27] in Fig. 3.11. Good agreements between the experimentally determined and the computed results at different monitoring locations indicate that the model can be used to examine the temperature profiles and cooling rates. The results show a rapid increase in temperature during heating followed by a comparatively slower cooling as the heat source moves away from the monitoring locations. Cooling rate of 4-5 K/s in the temperature range of 700 to 500 K is fairly low compared to that in fusion welding. This behavior may be further explained from the temperature contours

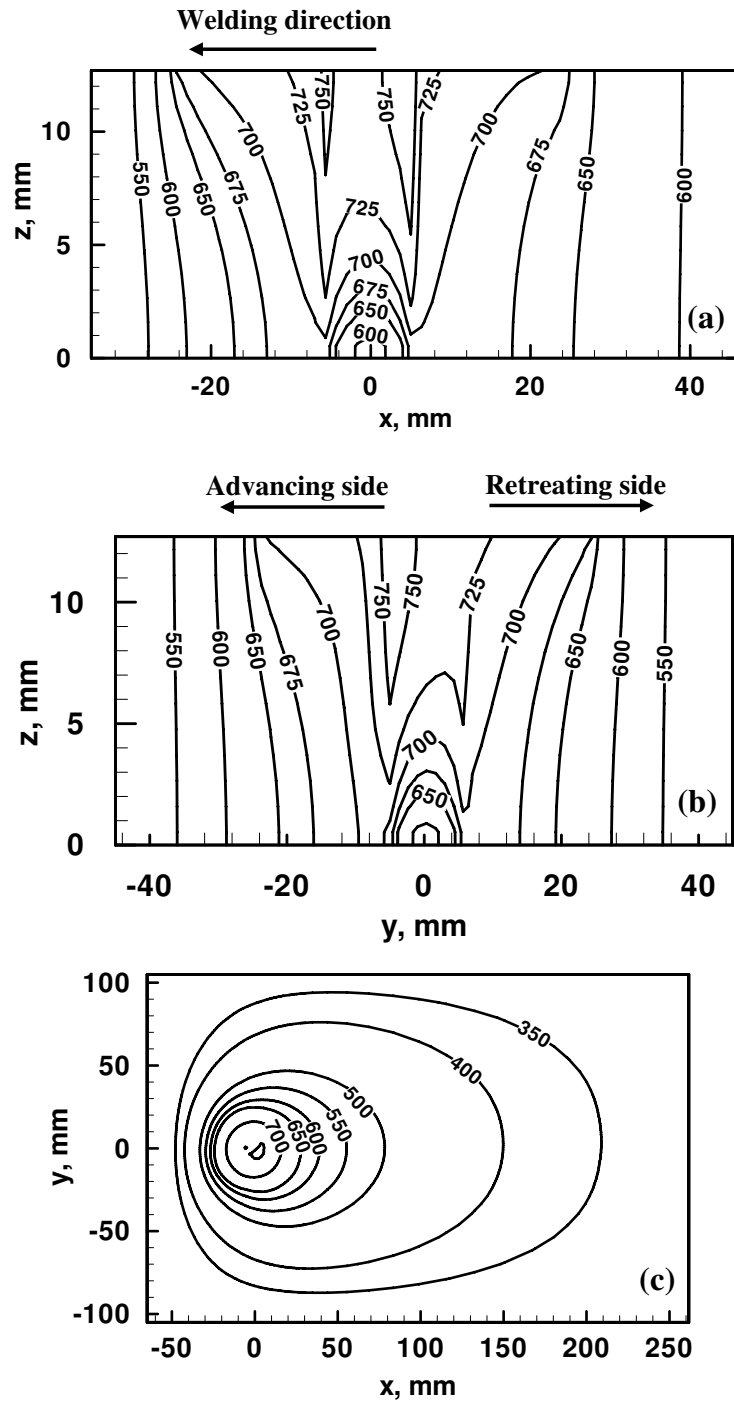


Figure 3.9. Computed temperature profiles (K) in (a) y-plane, (b) y-plane and (c) z-plane *i.e.* top surface of 12.7 mm thick workpiece of AA 6061-T6 welded with tool translational speed of 1.59 mm/s and rotational speed of 344 rpm [37].

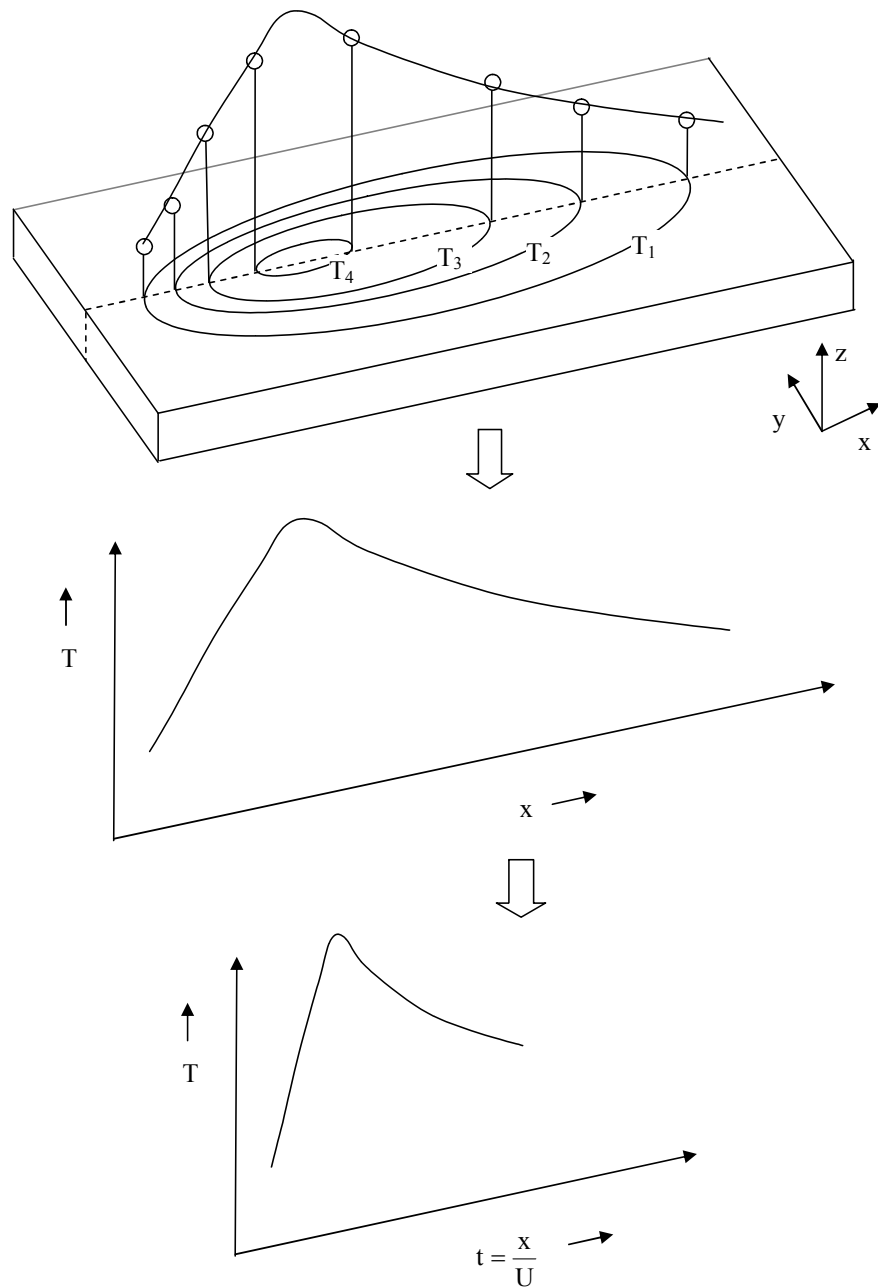


Figure 3.10. Obtaining thermal cycle from steady state temperature profile.

similar to those in figure Fig. 3.9(c). The initial steep heating is observed as the monitoring locations encounter compressed thermal contours ahead of the tool. As the tool moves ahead of the monitoring locations, the expanded temperature

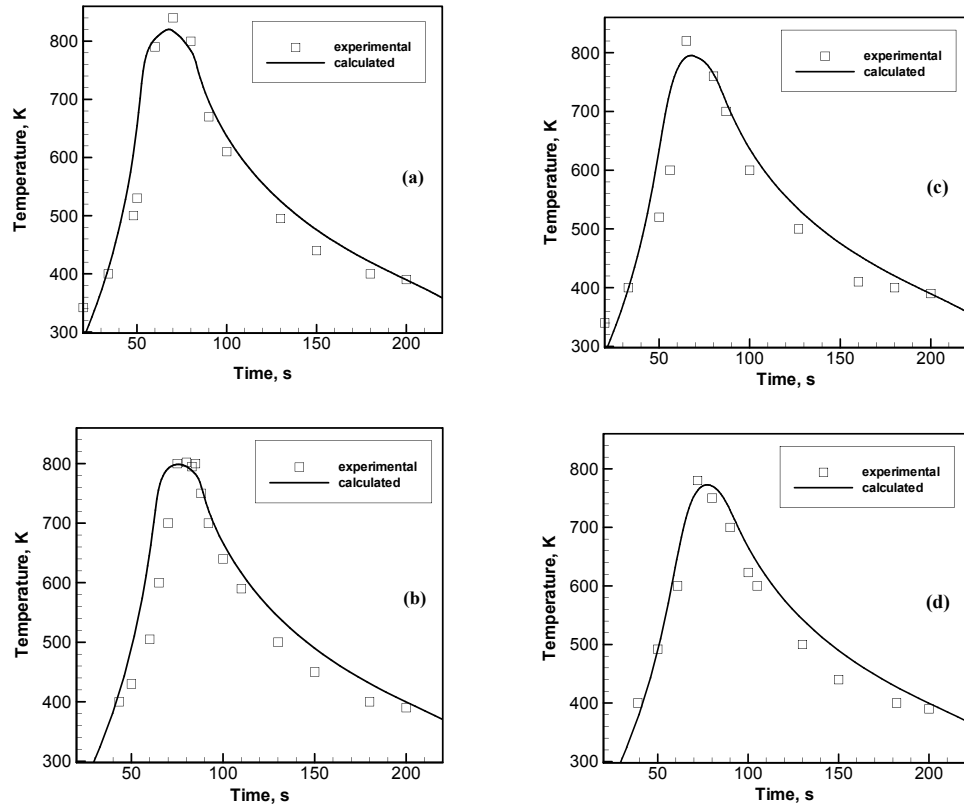


Figure 3.11. Comparison between experimental [27] and calculated time-temperature profile in AA 6061-T6 at points (a) 2 mm below the top surface and 8 mm from the centerline, (b) 2 mm below the top surface and 16 mm from the centerline, (c) 8 mm below the top surface and 8 mm from the centerline and (d) 8 mm below the top surface and 16 mm from the centerline. The points are located in advancing side and the distances are perpendicular to the weld center line. The welding velocity was 1.59 mm/s and the rotational speed was 637 rpm.

contours lead to slow cooling. The higher the welding velocity, the faster the temperature changes during both heating and cooling. It may also be noted here that the peak temperatures in four locations are in the range of about 780 to 800K. The relatively small differences in the peak temperatures in these locations result from two factors. First, all the locations lie within the thermo-mechanically affected zone where rapid heat transfer occurs due to convective flow. Second, the high thermal conductivity of the aluminum alloy also contributes to thermal homogeneity.

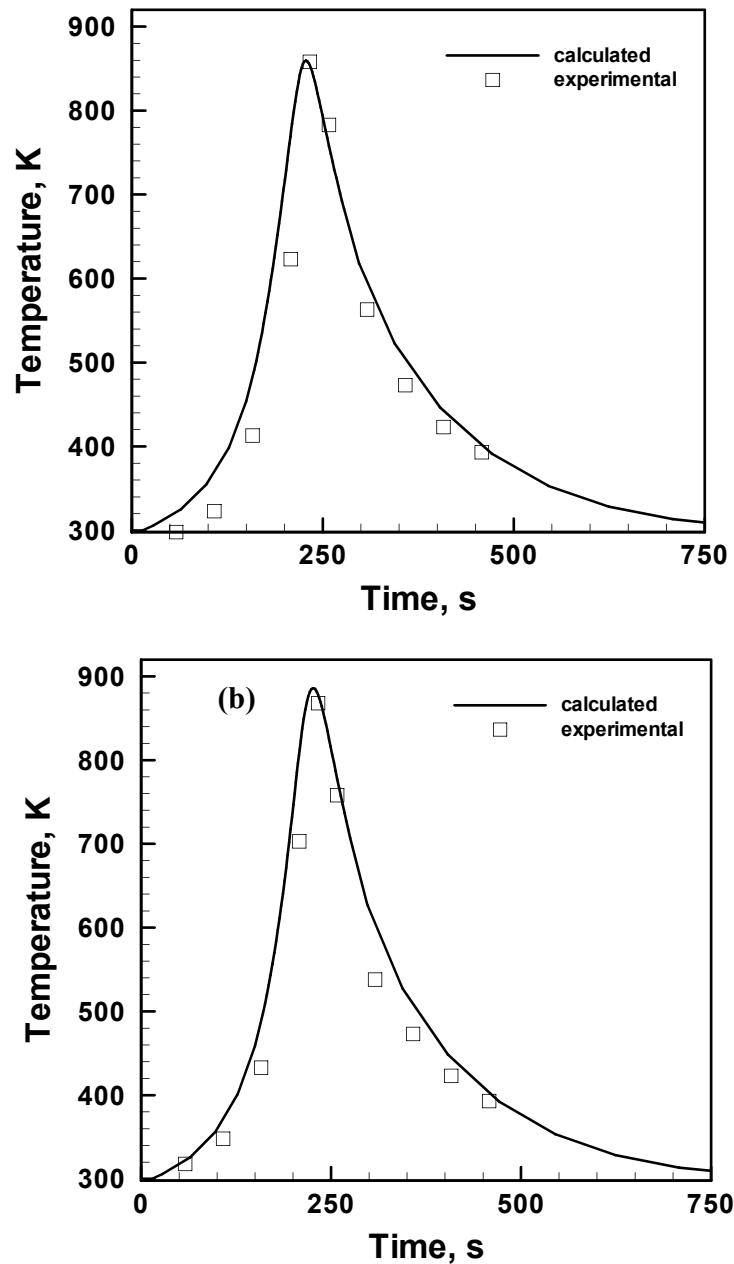


Figure 3.12. Comparison between experimental [45] and calculated time-temperature profile at two points on the top surface a) at a distance of $y = 16.7$ mm on the advancing side b) at a distance of $y = 16.7$ mm on the retreating side. The welding velocity was 0.4 mm/s and the rotational speed was 450 rpm. Other process and model parameters are given in Table 3.8.

3.3.3.2 1018 Mn steel

The computed temperature profiles at two monitoring locations are compared with the experimental data in Fig. 3.12. Figure Fig. 3.12(a) compares the temperatures

at a distance of $y = 14.0$ mm from axis of the tool on the advancing side and Fig. 3.12(b) compares the temperatures at a similar distance on the retreating side. Good agreements between the experimentally determined and the computed results at different monitoring locations indicate that the model can be used to examine temperature profiles and cooling rates. The peak temperatures in the workpiece varied in the range of 1150 to 1450 K depending on welding variables. These values are higher than those observed in the FSW of aluminum where the peak temperatures were in the range of 700 to 800 K.

3.3.3.3 304L stainless steel

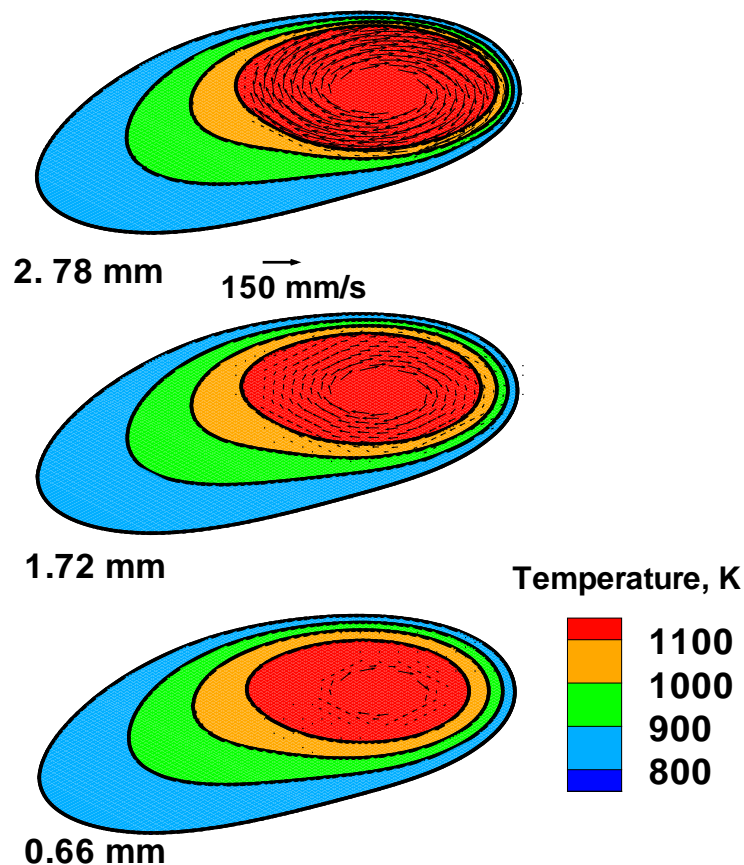


Figure 3.13. Plot of temperature and velocity fields at $z = 2.78$, 1.72 , and 0.66 mm planes. The welding velocity was 1.693 mm/s and the rotational speed was 300 rpm. Other process and model parameters are given in Table 3.8.

Figure 3.13 depicts the temperature contours and velocity vectors on different

horizontal planes. An interesting feature to note here is that the area that contains the high plastic flow decreases with distance from the work piece top surface. The effect of the tool shoulder as a source of momentum is most pronounced in the upper half of the work piece. But, as only about 20% of the heat is generated at the tool pin surface, and the thickness of the work piece is much smaller than its width or length, heat is transported mainly in the vertical direction from shoulder. As a result, the high temperature region does not shrink significantly with distance from top surface. The reduction in the area where the flow occurs with distance from the shoulder produces the characteristic shape of the nugget or stir zone.

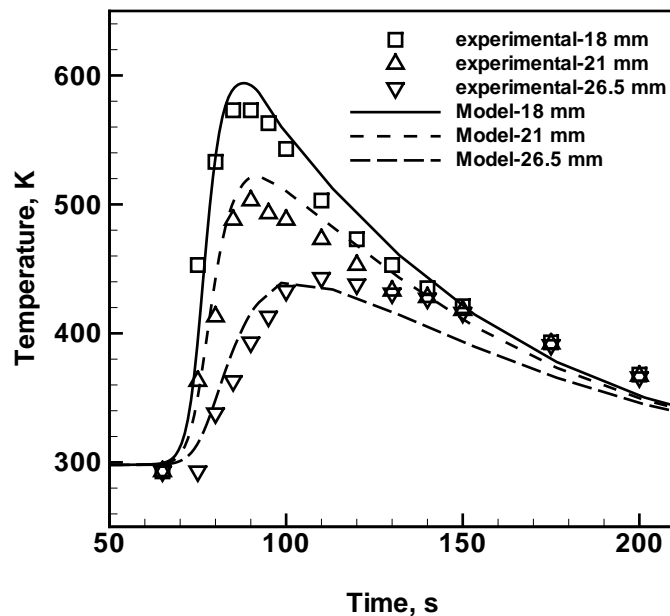


Figure 3.14. Comparison between experimental [140] and computed thermal cycles in 304L stainless steel at three monitoring locations on the top surface of the retreating side at distances of 18 mm, 21 mm and 26.5 mm from the weld centerline. The welding velocity was 1.693 mm/s and the rotational speed was 300 rpm. Other process and model parameters are given in Table 3.8.

The computed temperature profiles in 304L stainless steel are similar in nature to that in AA 6061. In Fig. 3.14, the predicted thermal cycles at three monitoring locations (distances of 18 mm, 21 mm, and 26.5 mm from the weld centerline on the top surface of the retreating side) are compared with the experimentally measured values published by Zhu *et. al.* [140].

3.3.3.4 Ti-6Al-4V

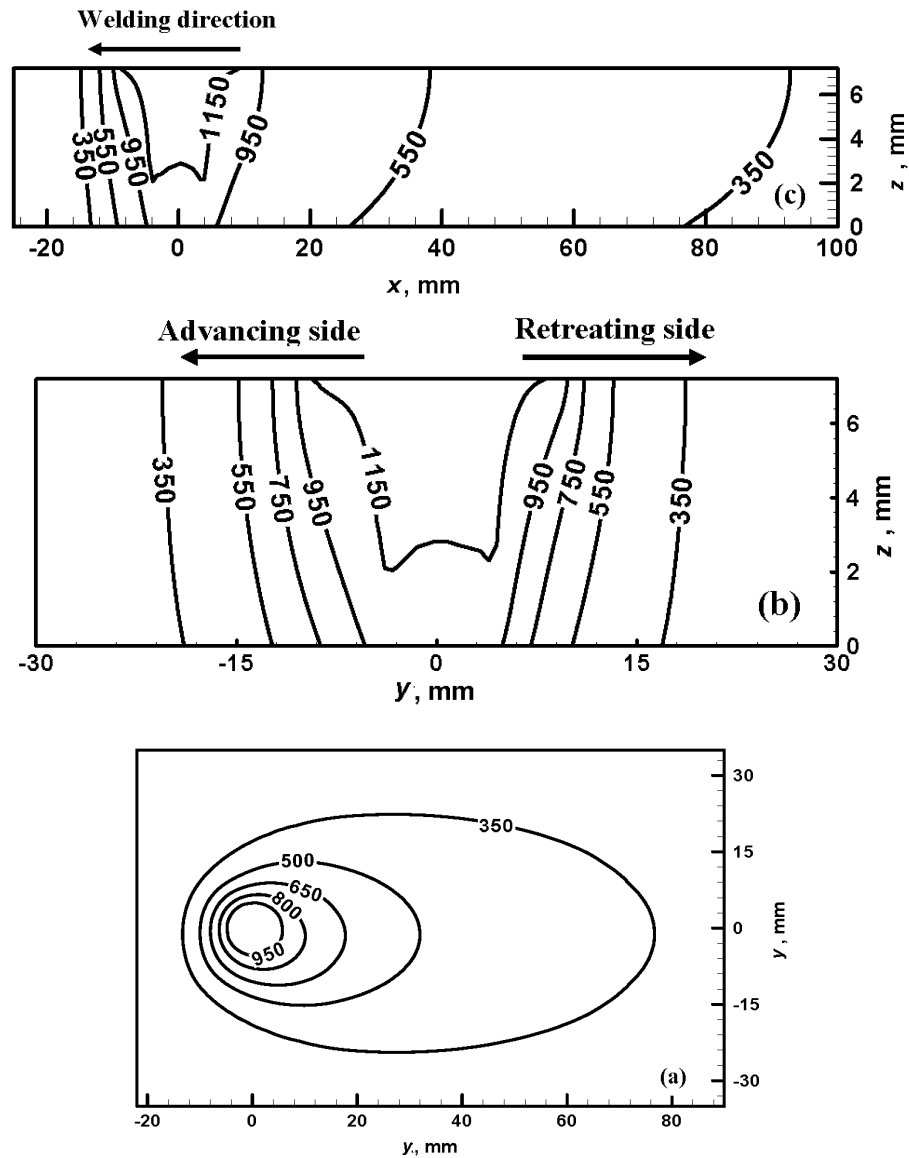


Figure 3.15. Computed temperature profiles (K) in (a) xz-plane, (b) yz-plane and (c) z-plane *i.e.* top surface of 7.2 mm thick workpiece of Ti-6Al-4V alloy welded with translational speed of 1.6 mm/s and rotational speed of 275 rpm [141].

The computed temperature profiles along the longitudinal and transverse sections through tool axis and at the top surface of Ti-6Al-4V work piece are shown in Fig. 3.15(a), (b) and (c), respectively. The temperature profiles on the longitudinal mid-section (Fig. 3.15(a)) and on the top surface of the work piece (Fig. 3.15(c))

are compressed in front of the tool and expanded behind it. The computed results are consistent with the fact that heat is supplied rapidly to the cold region of the work piece ahead of the tool while heat is transported at a slower rate to material already preheated behind the tool. It can be observed that the region near the tool pin is hotter towards the advancing side compared to the retreating side. This asymmetry originates from the local differences in the heat generation rates due to local variations in the relative velocities between the tool surface and the workpiece.

The three dimensional nature of heat transport is evident from these results for all four alloys. However, a rough estimate of peak temperature can be made based on the specific heat capacity, thermal conductivity, solidus temperature, tool geometry and and rotational and translation tool velocity without doing the coupled heat and momentum transport calculations in 3D. This provides a readily usable guideline to practicing engineers interested in knowing the maximum attainable temperature based on tool geometry and and welding variables.

3.3.4 Dimensional Analysis

Dimensional analysis, a useful tool for understanding a complex situation, can be used to estimate peak temperature in the workpiece using available numerically computed and experimentally measured thermal cycles for different alloys [142]. The non-dimensional peak temperature, T^* , and heat input, Q^* , are given by:

$$T^* = \frac{T_P - T_{in}}{T_S - T_{in}} \quad \text{and} \quad Q^* = \frac{f\sigma_8 A\omega C_P}{kU^2} \quad (3.15)$$

where T_{in} , and T_S are the peak, initial and solidus temperatures of the work-piece, respectively, f represents the fraction of heat that is transported into the work-piece, σ_8 is the yield strength value at a temperature which is 0.8 times the solidus temperature, A is the surface area of the shoulder. Note that Q^* is similar to recovery factor, or the ratio of actual to theoretical temperature recovery [143].

$$Q^* = \underbrace{\frac{f\sigma_8 A\omega}{k}}_{\text{actual}} \bigg/ \underbrace{\frac{U^2}{C_p}}_{\text{theoretical}} \quad (3.16)$$

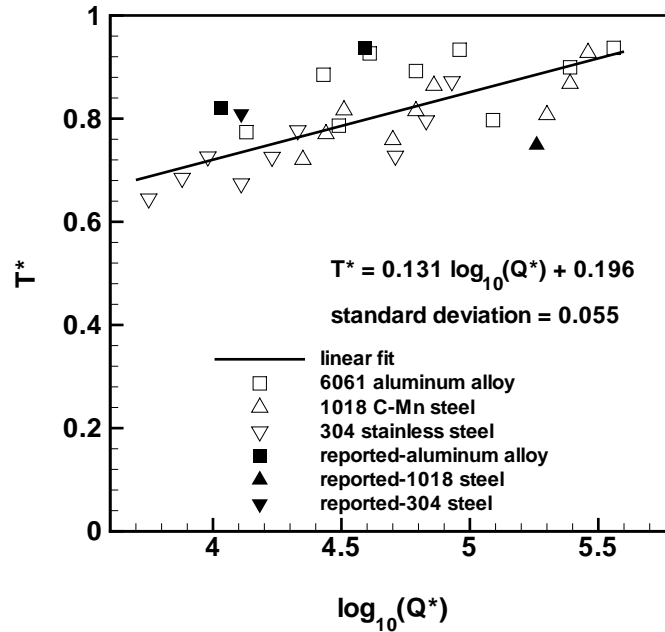


Figure 3.16. Variation of dimensionless peak temperature [142] with dimensionless heat input.

The thermal properties were taken at the mean temperature, defined as $(T_S + 298)/2$. The following correlation was proposed based on a plot of dimensionless peak temperature versus dimensionless heat input shown in Fig. 3.16:

$$T^* = 0.131 \log(Q^*) + 0.196 \quad (3.17)$$

Some independent experimental data, depicted as filled symbols, superimposed in Fig. 3.16, show fair agreement with the correlation. A comparison between peak temperatures obtained using 3D calculation and using non-dimensional relation 3.17 is also given in Table 3.11. Exact values require a more detailed calculation. However, non-dimensional values provide a good quantitative understanding of trends. For example, Eqn. 3.17 and 3.15 indicate that the peak temperature is higher for a tool with larger shoulder dimensions and it increases with increasing rotational speed and decreasing welding velocity.

Even though FSW is generally regarded as a solid-state joining process, it is possible that localized melting can and does occur under certain conditions.

Table 3.11. Comparison between peak temperatures obtained using 3D calculation and using non-dimensional relation 3.17.

Alloy	f	σ_8 (MPa)	k (W/m - K)	C_p (J/kg - K)	A (m ²)	ω (s ⁻¹)	U (m/s)	Q^*	T^* eqn. 3.17	T^* 3D soln.
AA 6061	0.9	7.8	208.6	1049.2	0.00191	10.62	0.0016	2.80×10^5	0.91	0.93
1018 steel	0.4	13.0	34.1	515.1	0.00023	7.50	0.0016	5.39×10^4	0.82	0.77
304 L steel	0.4	12.6	25.6	572.7	0.00025	5.00	0.0016	5.55×10^4	0.82	0.75
Ti-6Al-4V	0.45	16.2	23.6	677.2	0.00023	4.58	0.0016	8.79×10^4	0.84	0.74

Incipient melting has been reported in the nugget zone at high travel speeds in an aluminum alloy (AA 7100) [144], and locally melted films in a cast alloy AZ91 [145].

Recent work has suggested a self-stabilizing effect which depends on the fact that the yield stress of the material drops dramatically as the solidus temperature is approached. If the yield stress decreases, so does the rate of heat generation, reaching zero in the limiting case of melting. The decrease in temperature in turn allows the material to recover its strength, thus permitting a steady temperature to be established below the solidus [146].

3.3.5 Computed viscosity and plastic flow fields

Figure 3.17 shows the variation of u-component of velocity at different elevations, *i.e.*, z values. It is observed that at $z = 11.47$ mm, u-velocity increases and attains a maximum at around $x = 20$ mm, followed by a rapid decrease, while at planes near the bottom of the work piece, the velocity peaks are attained at the tool surface. Here the value of slip was assumed constant. Therefore, highest value of ωr is close to the shoulder periphery where ωr is greatest. Near the top surface, the effect of shoulder and the viscous momentum transfer is fairly pronounced resulting in high peak velocity. But since momentum decays rapidly in the z -direction away from the shoulder, the effect of rapid rotation of the shoulder does not reach the lower elevations.

The plot of x and y -components of velocity in 1018 Mn steel at different elevations indicates that the peak value of velocity is attained close to the tool surface (Fig. 3.18). Though the value of ωr is highest at the shoulder periphery, slip also increases as we move away from the tool axis. Therefore, the velocity transmitted to the plasticized work piece material is not the highest at the periphery unlike the case for AA 6061 where a constant value of slip was assumed.

Figure 3.19 shows the computed strain rate behind the tool opposite to the direction of welding at different elevations in the workpiece. The figure shows that maximum strain rate occurs near the surface of the pin where the maximum velocity gradient is present. For lower planes, strain-rate rapidly decreases with distance away from the tool axis. For higher planes, close to the shoulder, the velocity gradient decreases gradually away from the tool axis till below the shoulder

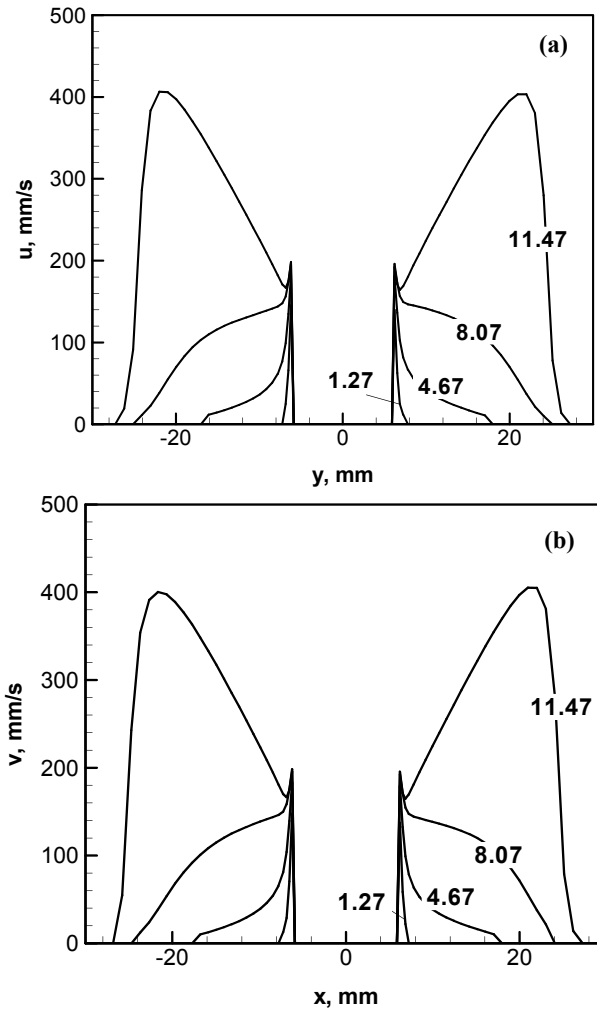


Figure 3.17. Plot of variation of (a) u-velocity and (b) v-velocity as a function of distance from tool surface for corresponding to $z = 11.47, 8.07, 4.67$ and 1.27 mm for a 12.7 mm thick plate of AA 6061, where z is the vertical distance from the bottom of the workpiece. The welding velocity was 1.59 mm/s and the rotational speed was 344 rpm. The thickness of the workpiece was 12.7 mm.

periphery. Beyond the periphery, the velocity gradient decreases sharply because of the rapid decay of velocity. It is also observed that strain rates decrease rapidly with depth, which may be attributed to large decrease in velocities away from the shoulder through viscous dissipation. Strain rates are much higher in aluminum alloy because the tool pin was much larger compared to the other cases and also a fixed value of slip was used, instead of a slip decreasing radially outwards (refer Table 3.8).

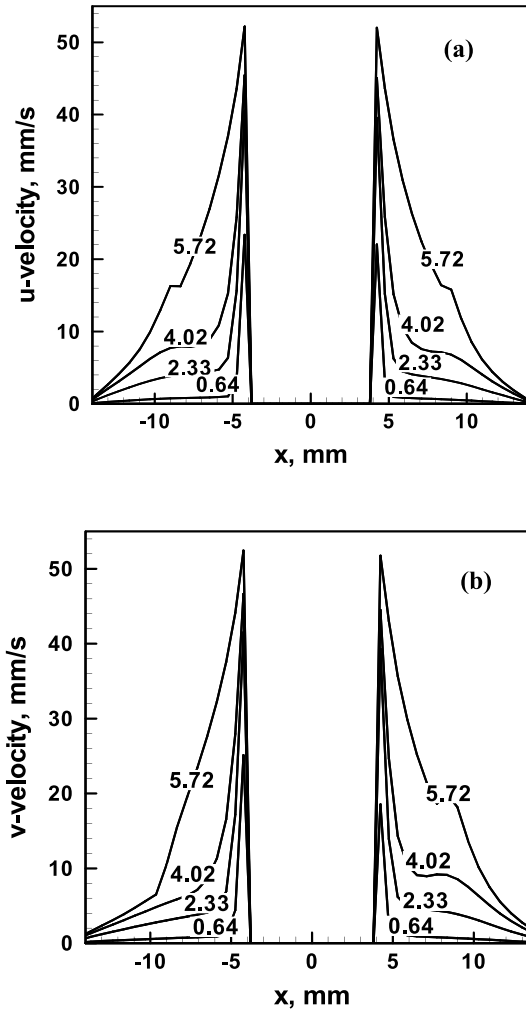


Figure 3.18. Plot of variation of (a) x-direction velocity and (b) y-direction velocity as a function of distance from tool surface for corresponding to $z = 0.64, 2.33, 4.02$ and 5.72 mm planes in 1018 Mn steel, where z is the vertical distance from the bottom of the workpiece. The thickness of the workpiece was 6.22 mm.

Figure 3.20 shows the variation of viscosity along the x-direction at different elevations, *i.e.*, values of z . It is seen that at $z = 5.72$ mm, viscosity decreases with increase in x followed by a sharp increase at high values of x . Since the viscosity is inversely proportional to local strain rate, this observation may be explained considering the values of strain rates presented in Fig. 3.19, where the strain rate trends are just opposite to those of the viscosity values presented in Fig. 3.20. At lower values of z , the viscosity progressively increases with x -distance, which is

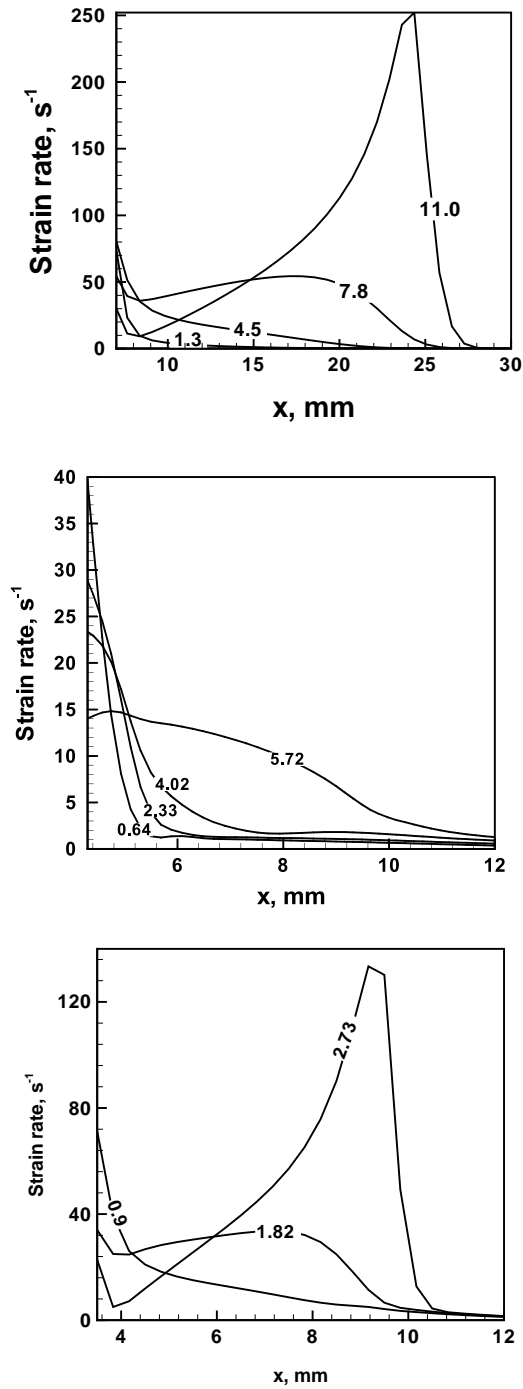


Figure 3.19. Computed strain rate in (a) AA 6061, (b) 1018 Mn steel and (c) 304L stainless steel, decreases along the weld centerline, away from the tool pin surface opposite to the welding direction at different horizontal planes. The plot labels indicate the vertical distance from the bottom of the workpiece in mm. The thickness of the three workpieces are given in Table 3.8.

also consistent with the strain rate variations. An important consequence of the computed viscosity profiles is that high viscosity values beyond a certain critical high value results in lack of plastic flow and define the geometry of the thermo-mechanically affected zone (TMAZ).

Figure 3.21 depicts the viscosity contours and velocity vectors on different horizontal planes in four different alloys modeled. An interesting feature to note here is that the area of plastic flow decreases with distance from the work piece top surface. The effect of the tool shoulder as a source of heat and momentum is most pronounced in the upper half of the work piece. The reduction in the area where the flow occurs with distance from the shoulder produces the characteristic shape of the thermo-mechanically affected zone(TMAZ). [27, 73] The cut-off viscosity above which no significant material flow occurs can also be determined. The iso-viscosity contour enclosing the flow field is used to determine the TMAZ which is comparable to macrostructures obtained experimentally. The limiting viscosity is in the range of 5×10^6 to 10^7 Pa-s for the four different alloys even though their mechanical properties are widely different.

Streamlines of the velocity field in 1018 Mn steel are given in Fig. 3.22. The lines show the paths that material particles follow from the inlet (opposite to the welding direction) to the outlet of the Eulerian region. The interesting features of the flow field occur close to the tool. Streamlines near the top and bottom boundaries exhibit almost straight paths. Near the tool, however, reversals in the direction of flow occurs on the advancing side. A stagnation point, where velocity is zero, exists in the vicinity of reversal point. Circular stream-lines close to the tool pin indicate material region swept out by the pin.

From 3D flow computations, it is possible to determine the pathline of a material particle traced in the welding region. In Fig. 3.23, it can be seen that particles close to the pin undergo more than one rotation around the pin before being deposited. Also, particles move from the retreating side to the advancing side. Marker insert technique has been used for flow visualization as discussed in Chapter 2. Correlation of experimentally determined marker position with numerical predictions can be useful in validation of flow model in FSW.

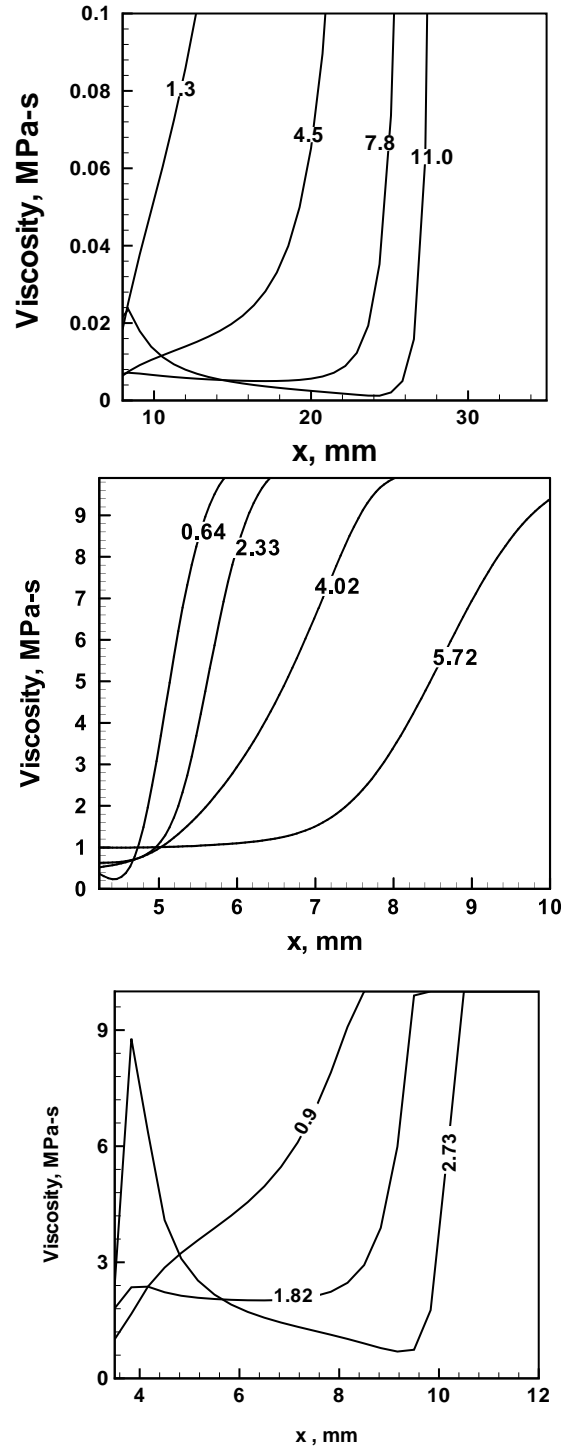


Figure 3.20. Variation of viscosity in (a) AA 6061 (b) 1018 Mn steel and (c) 304L stainless steel, as a function of distance from the tool pin surface opposite to the welding direction. The plot labels indicate the vertical distance from the bottom of the workpiece in mm. The thickness of the three workpieces are given in Table 3.8.

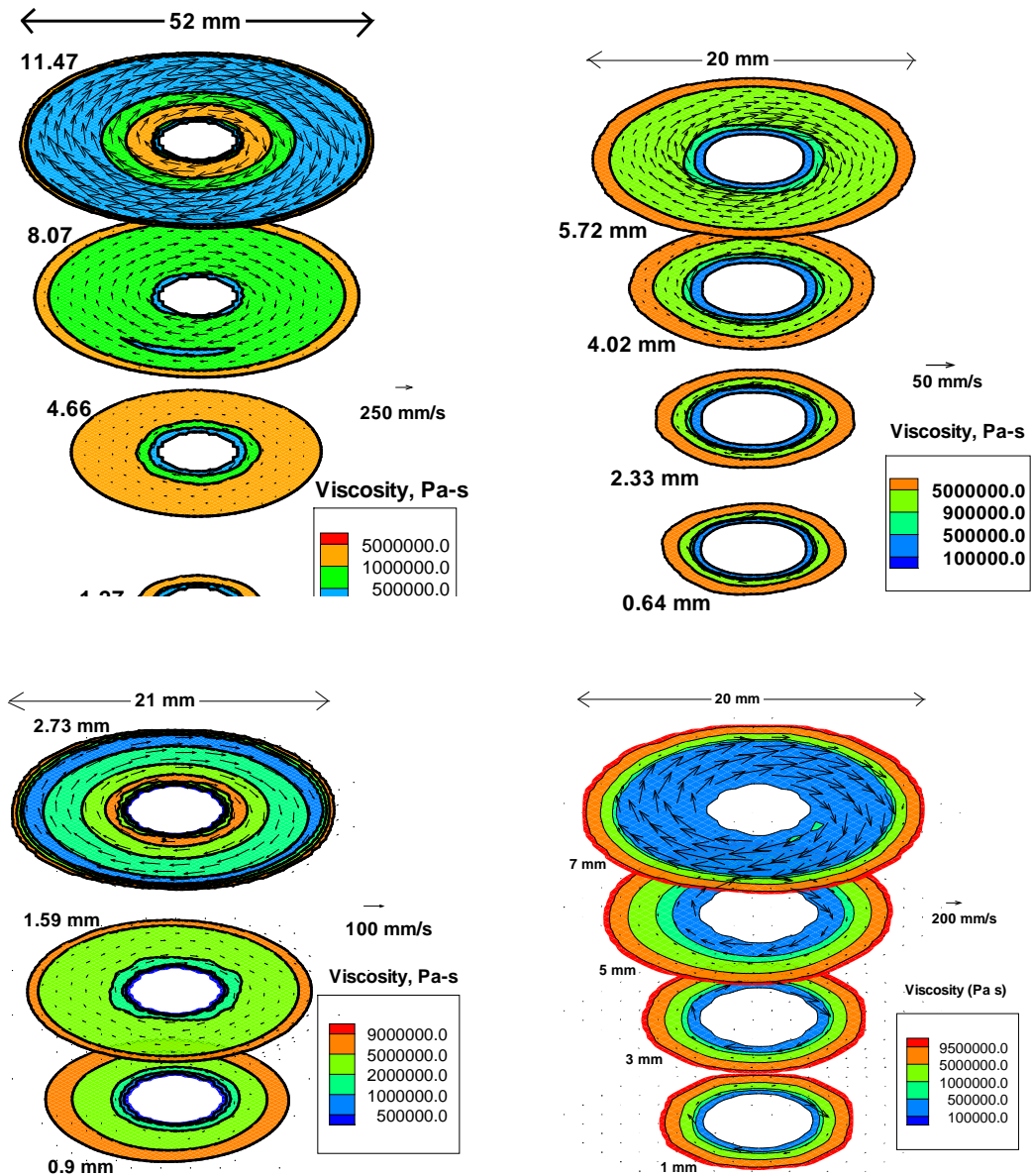


Figure 3.21. Viscosity contours in (a) AA 6061 at 344 RPM and 1.59 mm/s, (b) 1018 Mn Steel at 528 RPM and 0.42 mm/s, (c) 304 L stainless steel at 300 RPM and 1.69 mm/s and (d) Ti-6Al-4V at 275 RPM and 1.6 mm/s.

3.3.6 Shape of TMAZ

Figure 3.24(a) depicts the shape of the TMAZ as obtained by drawing the iso-viscosity surface for the critical viscosity, 5×10^6 Pa-s, above which no significant plastic flow occurs. Figure 3.24(b) compares the predicted TMAZ profile with that

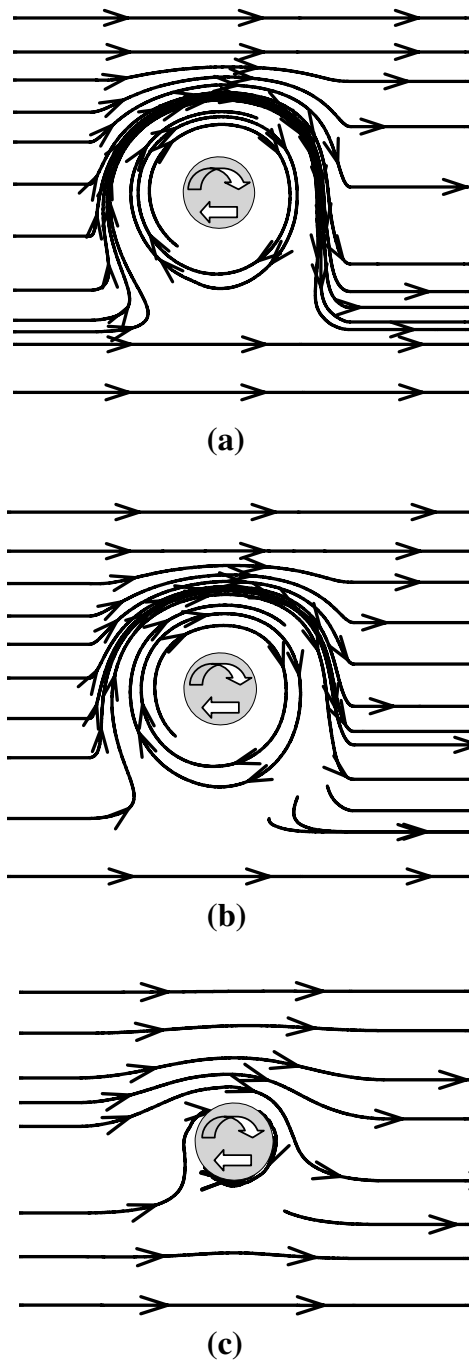


Figure 3.22. Streamline in 1018 Mn steel on horizontal planes (a) $z=5.72$ mm, (b) 4.02 mm and (c) 0.64 mm. The welding velocity was 0.42 mm/s and the rotational speed was 450 rpm.

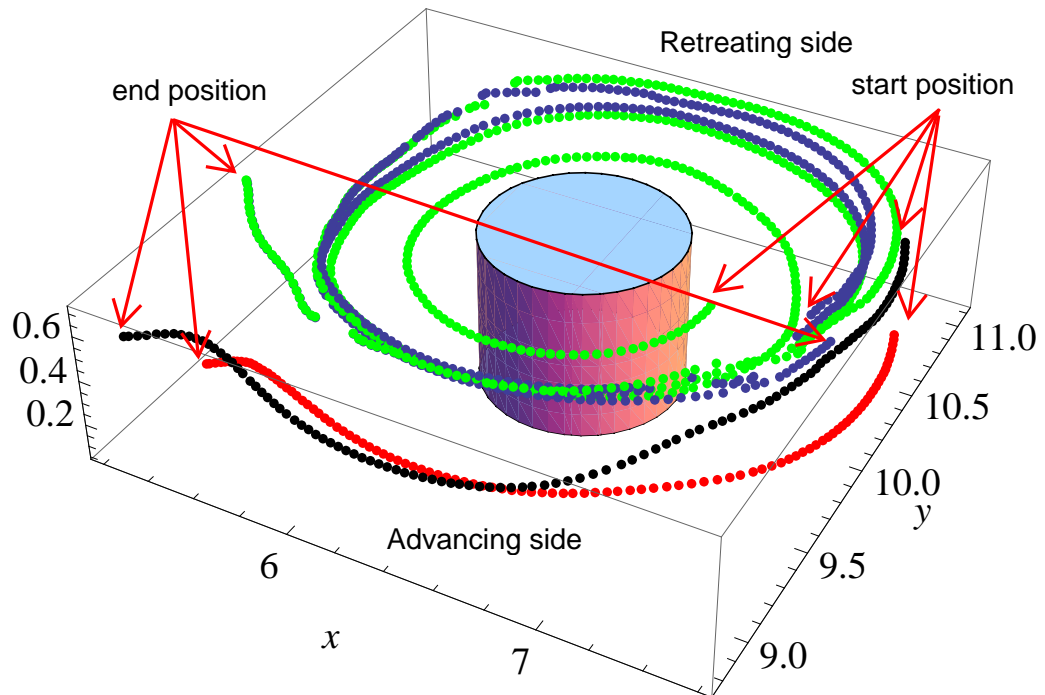


Figure 3.23. Side view of workpiece showing computed movement of four different tracer particles around the tool pin in Ti-6Al-4V welds performed at rotational speed of 275 rpm and welding velocity of 1.6 mm/s.

reported in an independent investigation [27]. It may be seen that the predicted TMAZ geometry agrees well with the observed macrostructure.

3.3.7 Pressure Distribution in the flow regime

In CFD approach, pressure is relative and only pressure gradients arise in the computational procedure. Therefore, pressure difference has physical significance and not the actual value of pressure at any location. A careful analysis of the pressure distribution could provide clues about the forging of the plasticized alloy behind the tool and the formation of defects in FSW. Fig 3.25 shows the distribution of pressure in different horizontal planes for 7.2 mm thick workpiece of Ti-6Al-4V welded at rotational speed of 275 rpm and welding velocity of 1.6 mm/s.. Pressure is higher in front of the tool as expected compared to the trailing edge. The pressure distribution is asymmetric about the weld centerline due to asymmetry in the velocity profile. Pressure is somewhat higher on the retreating side than the

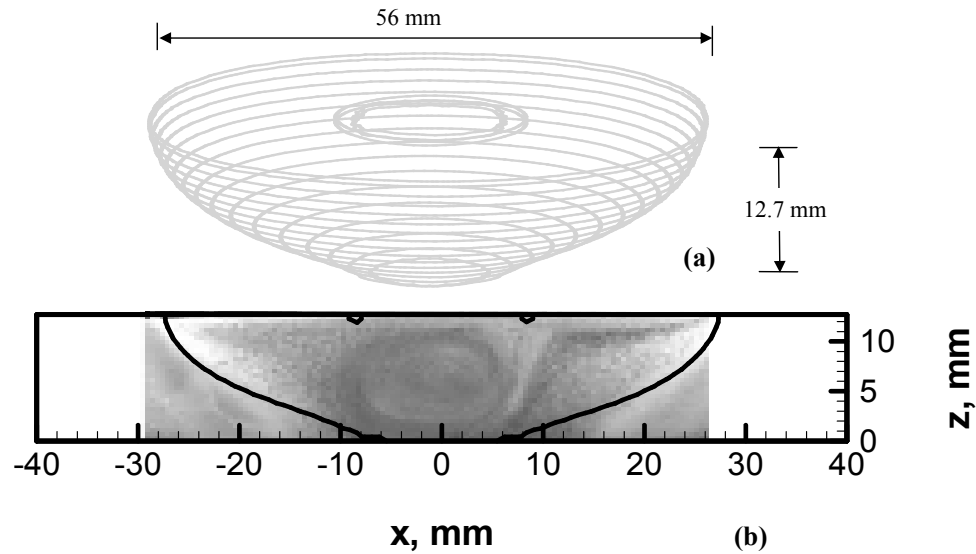


Figure 3.24. (a) Computed iso-viscosity surface (5×10^6 Pa-s) that defines visco-plastic flow region and TMAZ geometry and (b) Comparison of the numerically computed thermo-mechanically affected zone (TMAZ) geometry with corresponding experimentally determined macrostructure [27]. The welding velocity was 1.59 mm/s and the rotational speed was 637 rpm.

advancing side.

Liechty *et. al.* [138] performed friction stir welding on plasticine and modeled computed pressure field at the mid-pin depth and pressure-dependent tool shear stress (Fig. 3.26). They noted that material is not pressed against the tool at the back advancing side of the pin and this may be the region of void formation. Figures 3.25 and 3.26 show similar trend.

Fig 3.27 shows pressure distribution in longitudinal direction in the plane of weld centerline. Pressure difference between the leading and the trailing edge is higher at lower portions of the tool pin than at points close to the shoulder. This is so because the lower portion of the workpiece experiences lower temperatures and strain-rates and hence has higher flow stress which indicating that the material is more reluctant to flow and therefore higher pressure difference is required for flow to occur.

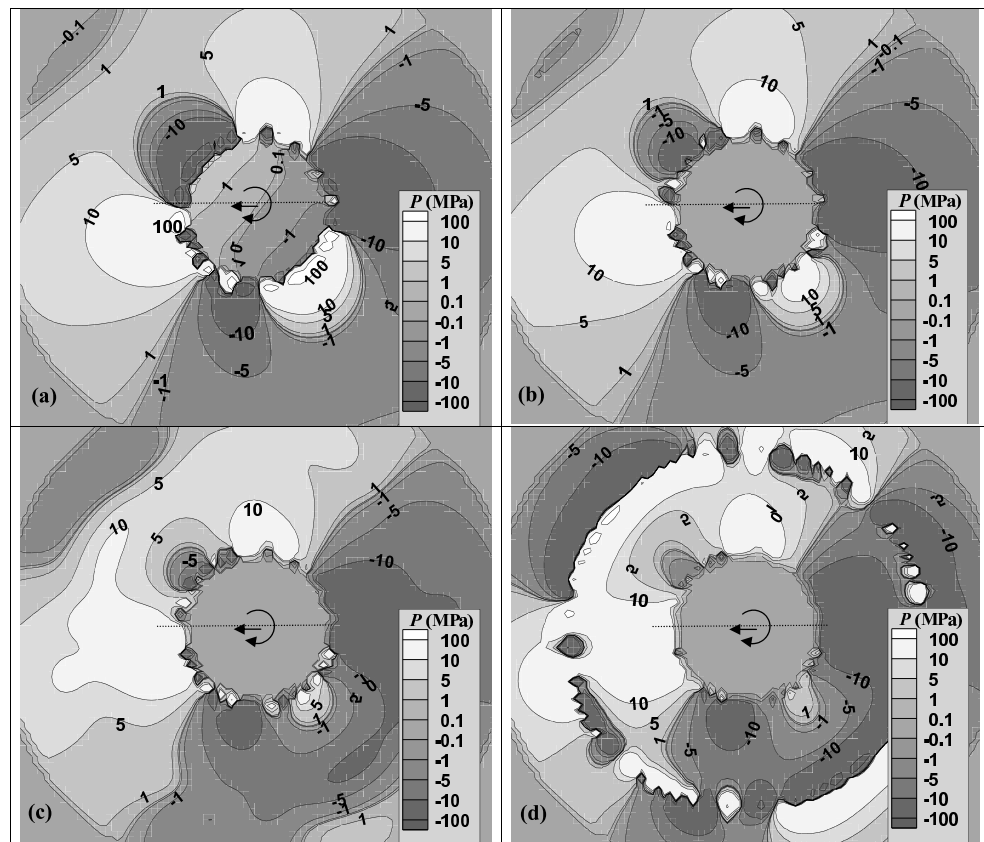


Figure 3.25. Distribution of pressure around the tool at different elevations in the workpiece: (a) $z = 1$ mm, (b) $z = 3$ mm, (c) $z = 5$ mm and (d) $z = 7$ mm for 7.2 mm thick workpiece of Ti-6Al-4V welded at rotational speed of 275 rpm and welding velocity of 1.6 mm/s.

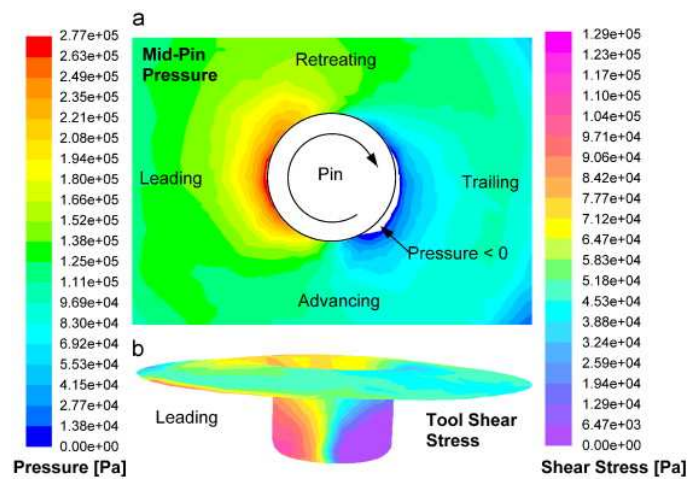


Figure 3.26. Pressure distribution at mid-plane in plasticine [138].

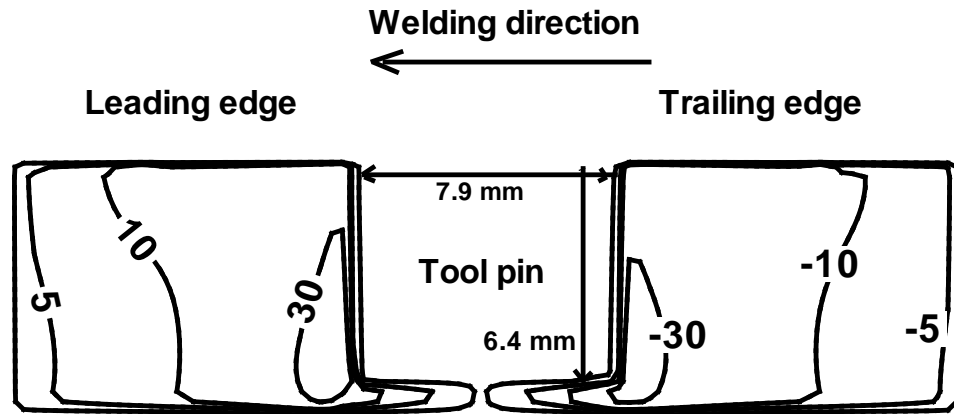


Figure 3.27. In Ti-6Al-4V, welded at rotational speed of 275 rpm and welding velocity of 1.6 mm/s, computed pressures are high in front of the tool, resisting tool motion. Contour labels indicate pressure in MPa.

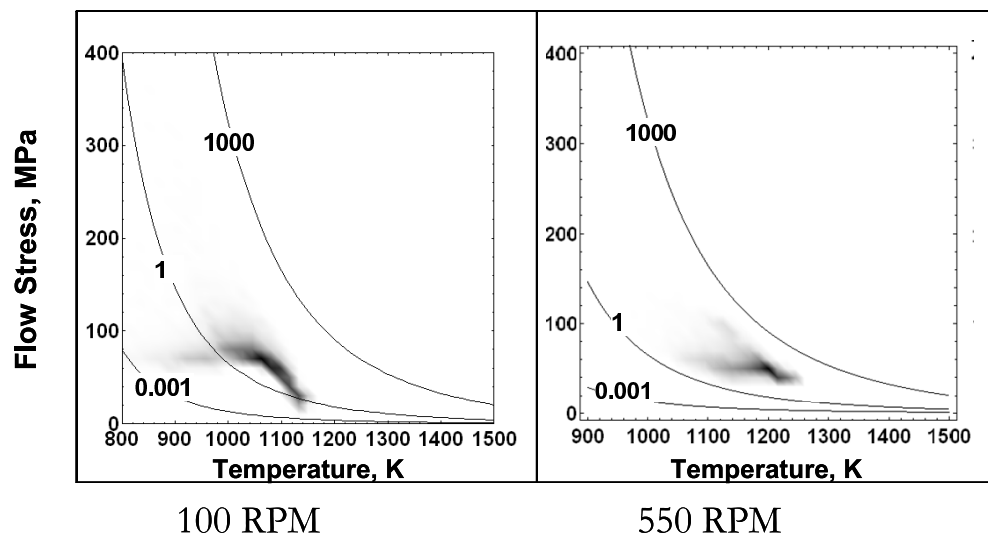


Figure 3.28. Flow stress, temperature and strain-rate condition in the stir zone of Ti-6Al-4V at: (a) 100 RPM and (b) 550 RPM indicated using density plot. The contour labels indicate strain-rate in s^{-1} . The shaded region indicates the material condition in the stir zone.

3.3.8 Material condition in flow region

Figure 3.28 shows the temperature and strain-rate distribution of locations in the TMAZ of the weld. On average, temperatures and strain-rates are higher at higher rotational speed, as expected. The density map, where higher concentration of points indicate higher fraction of stirred material at a given flow stress and tem-

perature, with superimposed strain rate contours, (Figure 3.28) can also indicate the tendency for defect generation [98]. Very low strain-rate is indicative of poor flowability due to reduced plasticization. Insufficient flowing material may result in surface lack of fill, wormhole, or lack of consolidation defects on the advancing side [147]. On the other hand, if rotational speed is very high defects like flash formation, surface galling and nugget collapse may occur [147]. The optimum material condition for making successful welds is to have most material points within a minimum strain-rate contour without increasing the tool rotational speed drastically. The minimum value of strain-rate may be decided based on correlation between modeling results and defects observed experimentally.

3.3.9 Effect of Material Properties on Heat Transfer

Table 3.12. Peclet number for different alloys.

	AA 6061 [37]	304L SS [38]	1018 Mn Steel [39]	Ti-6Al-4V [141]
Density (kg/m^3)	2700	7800	7860	4420
Solidus temperature (K)	855	1697	1745	1933
Specific heat capacity at $0.7T_{solidus}$ ($J/kg K$)	1200	575	586	675
Thermal conductivity at $0.7T_{solidus}$ ($W/m K$)	210	30	28	16
Peclet number ($U = 0.02ms^{-1}, L = 0.005m$)	1.5	15	16.4	18.5

High value of Peclet number in Table 3.12 indicates that convective heat transfer mechanism is dominant and any conduction based model would over-predict the temperature because the main mechanism of heat transfer is convection. Peclet number is lowest for aluminum alloy and hence it shows minimum asymmetry in temperature field about the weld centerline. On the other hand, asymmetry is more pronounced for other lower conducting engineering alloys. For example, Cho *et al.* [4] reported 100 K difference between peak temperature at the same distance from the weld centerline on either side (Fig. 2.4). The Fig. 3.30 shows

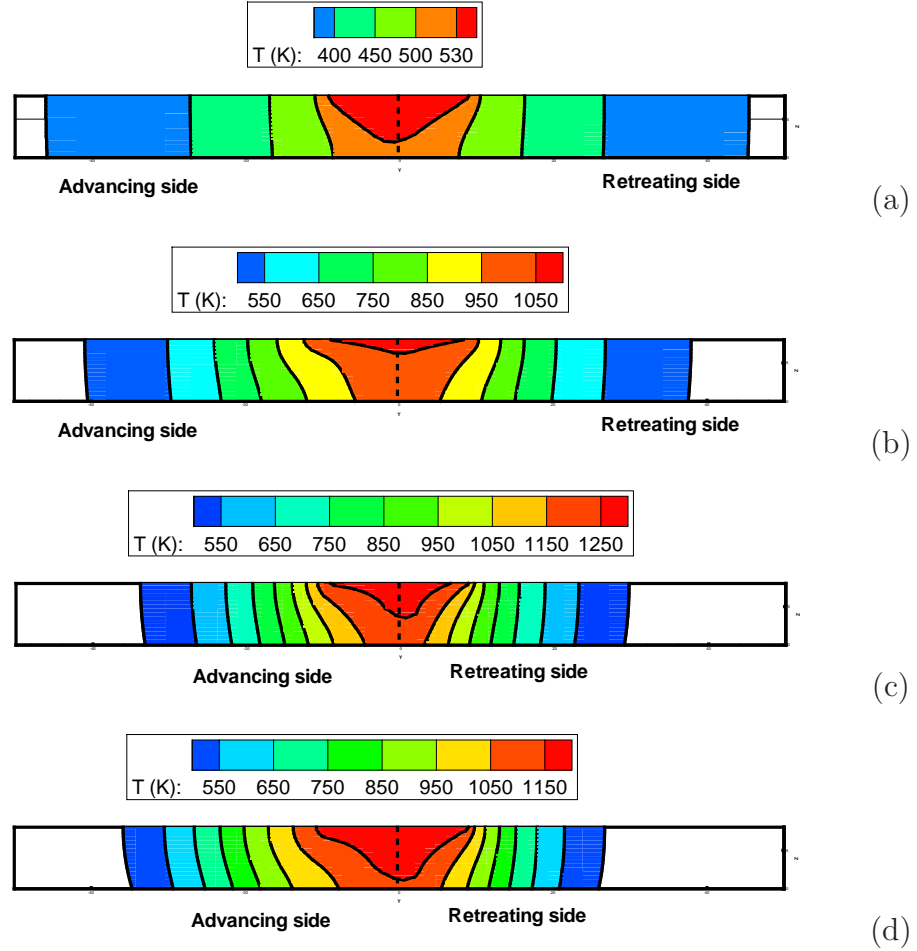


Figure 3.29. Temperature contours in yz -plane showing asymmetry across the weld centerline, with higher temperatures in the advancing side for (a) AA 6061-T6, (b) 1018 C-Mn steel. (c) 304L stainless steel and (d) Ti-6Al-4V. The computation was performed for the with the same welding process parameters for all four alloys. The shoulder radius of 10 mm, pin radius of 3 mm, axial pressure of 25 MPa, welding velocity of 2mm/s and tool rotational speed of 600 RPM.

the asymmetry in temperature between equidistant locations from weld centerline in the advancing and retreating sides for three different welding conditions. The asymmetry is characterized by the following equation:

$$Ay = \frac{1}{2} \frac{T_{A,1} - T_{R,1}}{T_{A,1}} + \frac{1}{2} \frac{T_{A,2} - T_{R,2}}{T_{A,2}} \quad (3.18)$$

where subscript A is for advancing and R is for retreating side and 1 and 2 denote 2 sets of equidistant points from the weld centerline. Location 1 is 20 mm away

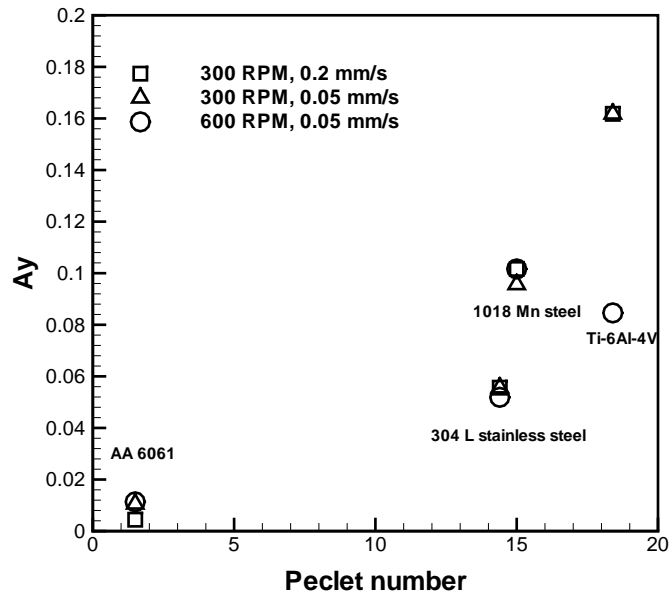


Figure 3.30. Plot of asymmetry in temperature across the weld centerline as a function of Peclet number for three different sets of welding velocity and rotational speeds indicated. The computation was performed for the same tool dimension (shoulder radius = 10 mm and pin radius = 3mm) and same axial pressure of 25 MPa for all four alloys.

from the centerline at the top surface and location 2 is 5 mm from the centerline at the bottom surface. Figure 3.30 clearly shows that asymmetry is insignificant only for aluminum alloys. Figure 3.29 shows the transverse cross-section of the workpiece. In aluminum alloy, the temperature contours are symmetrical about the weld centerline while marked asymmetry is observed for other three alloys. The greatest asymmetry is seen in Ti-6Al-4V alloys as its thermal diffusivity is lowest as is clear from Table 3.12.

3.4 Summary and conclusions

The equations of conservation of mass, momentum and energy were numerically solved with appropriate boundary conditions to obtain three-dimensional temperature and plastic flow fields during friction stir welding. Temperature dependent thermophysical properties were considered. The heat generation rate was calculated from the tool geometry, rotational speed and the shear stress for yielding.

The spatial variation of non-Newtonian viscosity was determined from the computed values of strain rate, temperature and material properties. The model was tested for four different alloys: 1) AA 6061-T6, 2) 1018 Mn steel, 3) 304L stainless steel and 4) Ti-6Al-4V. The following are the main findings. The computed temperature fields show asymmetry about the weld centerline because of the rotational and linear motion of the tool and asymmetry of heat generation around the tool pin surface. The asymmetry is least in aluminum alloy and is more pronounced for other alloys. Cooling rates were lower for FSW in comparison to fusion welding. For example, for aluminum alloy cooling rate of 5 K/s was obtained in the temperature range of 700 to 500 K. The relatively low cooling rate is consistent with fairly high energy input per unit length. The computed velocity fields show that significant plastic flow occurs in close proximity of the tool. The plastic flow significantly affects heat transport within the work piece even for 6061 aluminum alloy that has a high thermal conductivity. Strain rates depend on the tool geometry, rotational speed and boundary condition for stick-slip at the tool-workpiece interface. Maximum strain rate upto 250 s^{-1} were observed in aluminum alloy. Strain-rates were lower in other alloys as the shoulder radius was almost 2.5 times smaller in all other cases. High strain rate values are consistent with reported values of 350 s^{-1} in literature [148] for aluminum alloy welded at different rotational speeds (400-600 rpm) and translational speeds (0.847-2.540 mm/s). The cut-off viscosity above which no significant material flow occurs can also be determined. The iso-viscosity contour enclosing the flow field is used to determine the TMAZ which is comparable to macrostructures obtained experimentally. The limiting viscosity is in the range of 5×10^6 to 10^7 Pa-s for the four different alloys even though their mechanical properties are widely different. The computed stream trace in the horizontal planes around the tool pin showed the presence of nearly circular closed streamlines indicating the presence of a plug of material. The region of this recirculating flow expands with elevation because of proximity to the relatively larger rotating shoulder. The stream traces also showed that most of the material flow occurred mainly on the retreating side. Torque on the tool was also calculated based on shear stresses on the tool and compared with experimental values. Reasonably accurate prediction of torque is possible by using this model.

Enhancement of model reliability and tailoring weld attributes

4.1 Improving reliability

Numerical modeling of heat transfer and materials flow during FSW has provided significant insight into the welding processes and the welded materials. However, a major difficulty in FSW models is that the computed values of important variables such as temperature and torque do not always agree with the experimental results due to unknown model parameters. For example, the friction coefficient between the tool and the workpiece cannot be determined experimentally or through physical principles. The reliability of the model predictions for FSW can be significantly enhanced if the values of several uncertain input variables can be determined from a limited volume of experimental data like torque on the tool and thermal cycles at several monitoring locations. The methodology involves identification of the important uncertain input variables by conducting a sensitivity analysis where the effects of each of these variables on important output variables are examined. After the important uncertain input variables are identified, their values are optimized by combining the transport phenomena based model with a genetic algorithm (GA).

Search and optimization technique of genetic algorithm was chosen for optimization because of its ability to search for global minima for non-differentiable complex functions. GA employs natural selection, from a group of possible solu-

tions, inspired from evolution in living beings [149]. The group of possible solutions is called a population. Each individual of the population is characterized by an ordered set of values representing a possible solution. These values may be the unknown variables to be determined. A genetic algorithm uses three main genetic operators for population evolution toward possible solutions: 1) crossover, 2) mutation and 3) selection. Different flavors of GA have been developed over number of years and these techniques basically differ in their definition of genetic operators. Here Differential Evolution (DE) was used to optimize the uncertain parameters for FSW.

4.1.1 Uncertain parameters

Among the necessary input variables in the FSW model, there are five uncertain input parameters that affect the reliability of the model output. These parameters are the heat transfer coefficient from the bottom of the workpiece (h_b), the spatially variable slip between the tool and the workpiece interface (δ), the spatially variable coefficient of friction (μ_f), the mechanical efficiency (η) and the scaling term for viscous dissipation (β). Of these, h_b , δ and μ_f are spatially variable and their variation is encoded in functional form based on trends available in literature.

Schuhmann [136] suggested that heat transfer coefficient is proportional to fourth root of the difference between surface temperature and ambient temperature:

$$h_b = h_{b0} (T - T_a)^{1/4} \quad (4.1)$$

where h_{b0} is a proportionality constant with units of $W/m^2 - K^{5/4}$, T is the temperature of the surface point and T_a is the ambient temperature.

The extent of slip is estimated by curve fitting the measured values at various relative velocities [46]:

$$\delta = 0.2 + 0.6 \left(1 - \exp \left(-\delta_0 \frac{\omega r}{\omega_0 R_S} \right) \right) \quad (4.2)$$

where δ_0 is an adjustable parameter, r is the distance of the point from tool axis, ω is the angular velocity of the tool, R_S is the radius of the tool shoulder, ω_0 is the normalizing rotational velocity which can be taken as the mid-point of the range

of rotational speeds considered in a specific case.

Values of friction coefficient can be estimated considering the relative velocity between the tool and the work-piece according to previous work in the context of friction [41]. The relative velocity increases from zero at the axis of rotation to ωR_S at the periphery of the tool shoulder. Evidence suggests [41] that μ_f has the form $\mu_f = \mu_0 \exp(-\delta \frac{\omega r}{\omega_0 R_S})$, where μ_0 is the maximum value of friction coefficient.

To optimize the spatially varying values of h_b , δ and μ_f , we optimize the values of h_{b0} , δ_0 and μ_0 , respectively.

Mechanical efficiency [40], η , is the factor which is multiplied to the deformational work-rate to obtain the heat generation rate (\dot{e}_s) given by [31]:

$$d\dot{e}_s = (1 - \delta) (\omega r - U \sin \theta) \eta \tau_Y dA \quad (4.3)$$

where U is the welding velocity and θ is the angle between the radial vector of any location and the welding direction.

The variable β is used to scale down the plastic deformational heat generation (\dot{e}_p) away from the tool/work-piece interface so that it fits into the context of high viscosity plasticized materials and confirms to the low value of deformational heat generation rate, away from tool-workpiece interface, experimentally observed in FSW [33, 43]:

$$d\dot{e}_p = \beta \mu \phi dV \quad (4.4)$$

where μ is the viscosity, ϕ is given by equation 2.5.

To summarize, the following parameters have to be optimized to improve model reliability:

Unknown model parameters and their functional occurrence	
h_{b0}	$h_b = h_{b0} (T - T_a)^{1/4}$
δ_0	$\delta = 0.2 + 0.8 \left(1 - \exp \left(-\delta_0 \frac{\omega r}{\omega_0 R_S} \right) \right)$
μ_0	$\mu_f = \mu_0 \exp \left(-\delta \frac{\omega r}{\omega_0 R_S} \right)$
η	$d\dot{e}_s = (1 - \delta) (\omega r - U \sin \theta) \eta \tau_Y dA$
β	$d\dot{e}_p = \beta \mu \phi dV$

In order to optimize the values of these parameters from a limited volume of experimentally measured torque and thermal cycle data, the following objective function is minimized:

$$O = \sqrt{\sum_i \left\{ \sum_j \left[(1 - T_{ij}^*)^2 + (1 - W_{ij}^*)^2 \right] + (1 - M_i^*)^2 \right\}} \quad (4.5)$$

Subscript i denotes different welding conditions and j represents different locations. The peak temperature, width of thermal cycle at a specified temperature and torque on the tool were non-dimensionalized using the simple formula given below:

$$T^* = \frac{T_{cal}}{T_{exp}}, \quad W^* = \frac{W_{cal}}{W_{exp}}, \quad M^* = \frac{M_{cal}}{M_{exp}} \quad (4.6)$$

where T is the peak temperature in the workpiece at a monitoring location, W is the width of thermal cycle at a specified temperature and M is the torque. The width of thermal cycle at a particular temperature is calculated by first measuring the time taken to heat from that temperature and then cool back to the same temperature. The measured time is then converted to length as shown in Fig. 3.10. Figure 4.1 shows the width of thermal cycle at 450 K. The width of thermal cycle characterizes the cooling rate and higher width means slower cooling rate. The normalization of the calculated value is done by the experimental value at the same monitoring location for the same welding condition. The subscripts cal and exp refer to calculated and experimental values respectively. The objective function value depends on the choice of the five uncertain parameters.

4.1.2 Sensitivity to uncertain parameters

Three different tool-workpiece material combinations were examined. This was done because apart from aluminum, the use of FSW for steels and titanium alloys is also increasing. Also, these alloys have widely different thermophysical properties. So, this enabled determination of dependence of sensitivity trends on thermophysical properties.

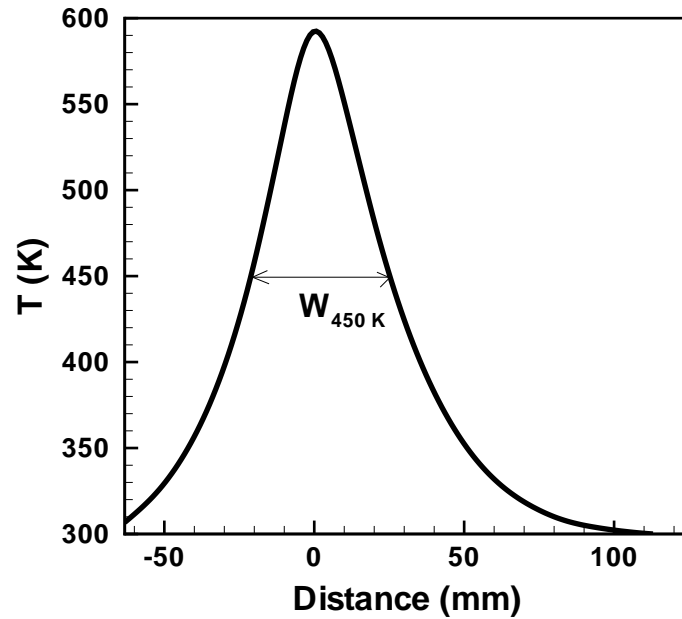


Figure 4.1. Definition of width of thermal cycle.

4.1.2.1 Ti-6Al-4V alloy

The sensitivities of the computed values of torque on the tool, peak temperature and cooling time on the five uncertain parameters (μ_0 , δ_0 , h_{b0} , η , β) were examined. The thermophysical properties of workpiece and tool materials used in calculations are indicated in Table 3.7 and the process parameters are given in 3.8. Torque is included in the calculations because it affects material flow. To determine the sensitivity, one variable was varied while the others were kept constant. The constant values were: $\mu_0 = 0.41$, $\delta_0 = 1.3$, $h_{b0} = 167W/m^2K^{5/4}$, $\eta = 0.7$, $\beta = 0.03$. These values are approximately the mean in the range of values considered for each variable. The range of μ_0 , δ_0 and h_{b0} was determined based on reported values of μ , δ and h_b available in literature (Table 3.1,3.2,3.3). An estimate of the range for values of η is also available (Table 3.4). The value of the scaling factor was based on trial and error done so that the plastic deformation heating away from the tool workpiece interface is not more than 20% of the total heat generation. The basis for this comes from previous research which indicates that plastic deformation heat is a small fraction of the total heat generation [44].

The thermal cycle was computed for a location at the top surface at a distance of 12 mm from the weld centerline in the advancing side. The peak temperature and the width of the thermal cycle at 773 K were determined for the monitoring location. Figure 4.2(a) shows that the peak temperature, T^* , and the width of the thermal cycle at 773 K, W^* , increase with increase in friction parameter, μ_0 , due to more intense frictional heating. As the friction between the tool and the workpiece increases, the torque, M^* decreases due to the softening of material with increase in temperature. Fig. 4.2(b) shows that when δ_0 increases and sticking between the tool and the workpiece decreases, torque decreases. With increase in δ_0 the heating rate decreases mainly because of the decrease in the first term on the right hand side in Equation 2.3 which is the dominant heat generation term. Peak temperature is lowered with increase in δ_0 , while cooling rate increases because of less heat input. Fig. 4.2(c) shows that as the heat transfer coefficient increases, more heat is lost from the workpiece and therefore, the peak temperature and the width of the thermal cycle at 773 K decreases. When the heat transfer coefficient is high, lower temperatures result in increase in yield strength and higher torque. Fig. 4.2(d) and (e) show increase in temperature and cooling time with higher values of η and β which represent increase in plastic deformational heat generation at the tool-workpiece interface and inside the workpiece, respectively. More intense heating results in higher temperatures and softer material, resulting in lower torque.

The results in Fig. 4.2(a) to (e) show that all three output variables, peak temperature, width of the thermal cycle and the torque are sensitive to variations in all the five uncertain input variables. Therefore, all these uncertain input parameters need to be optimized to enhance the reliability of the values of the output variables from the model.

4.1.2.2 1018 Mn Steel

A sensitivity analysis was done to ascertain the role of the five uncertain parameters on computed values of torque on the tool, peak temperature and cooling time. The results are shown in Fig. 4.3(a)-(e). To determine the sensitivity, one variable was varied while the others were kept constant. The thermophysical properties of workpiece and tool materials used in calculations are indicated in Table 3.7 and

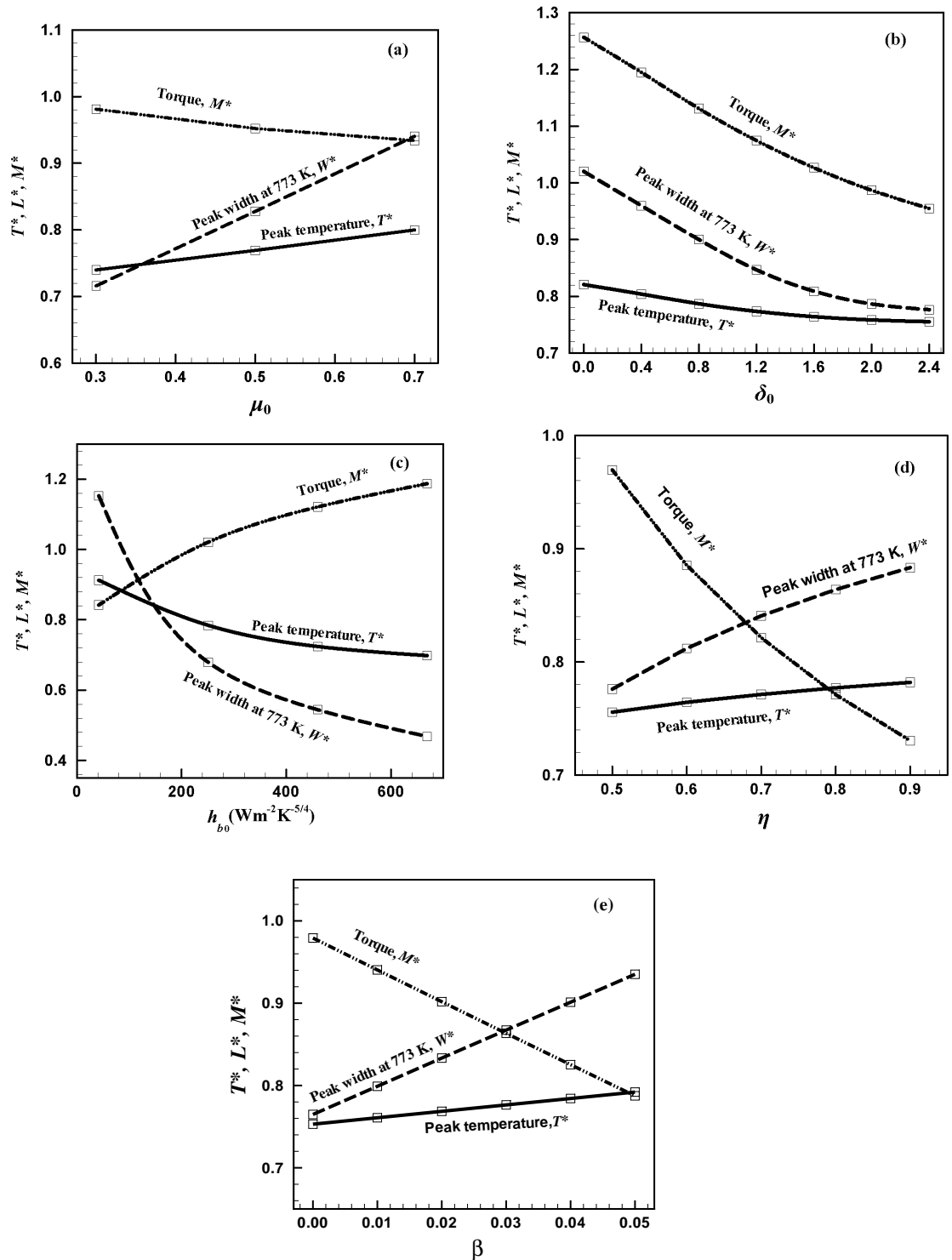


Figure 4.2. Computed dimensionless values of peak temperature, width of the temperature cycle and the torque with change in (a) slip, (b) friction coefficient, (c) heat transfer coefficient at the bottom surface, (d) mechanical efficiency and (e) scaling factor for plastic deformational heat generation rate for the FSW of Ti-6Al-4V alloy. In each case, when one of the parameters is varied, other parameters were kept constant. The welding velocity was 1.6 mm/s and the rotational speed was 275 rpm.

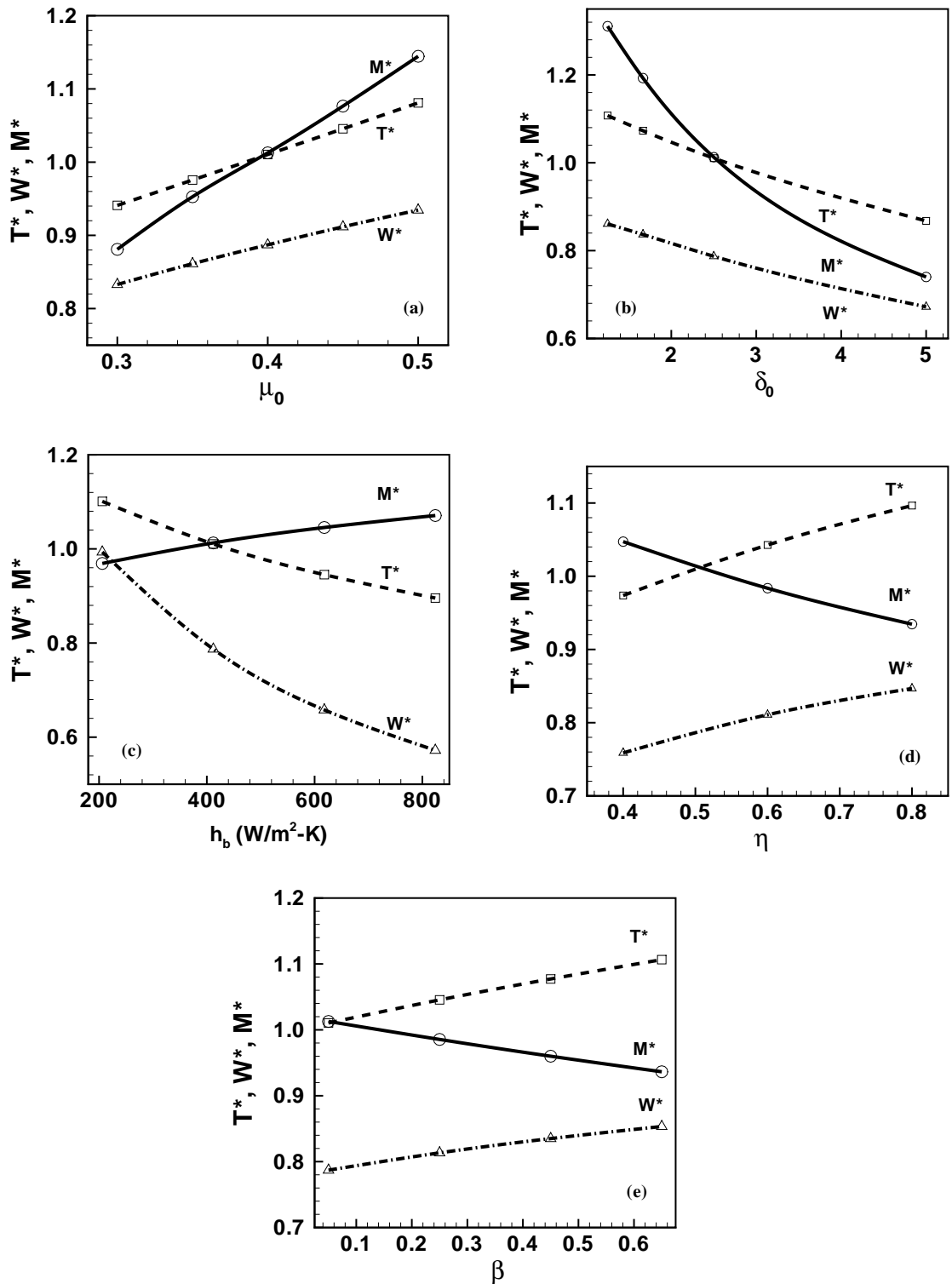


Figure 4.3. Computed dimensionless values of peak temperature, width of the thermal cycle and the torque with change in (a) friction coefficient, (b) slip, (c) heat transfer coefficient at the bottom surface, (d) mechanical efficiency and (e) scaling factor for plastic deformational heat generation rate for the FSW of 1018 Mn steel. In each case, when one of the parameters is varied, other parameters were kept constant. The welding velocity was 0.42 mm/s and the rotational speed was 450 rpm.

the process parameters are given in 3.8. The constant values were: $\mu_0 = 0.4$, $\delta_0 = 2.3$, $h_b = 450W/m^2K$, $\eta = 0.6$, $\beta = 0.3$. These values are approximately the mean in the range of values considered for each variable. The thermal cycle was computed for a location at the top surface at a distance of 12.7 mm from the weld centerline in the advancing side. The peak temperature and the width of the thermal cycle at 420 K were determined for the monitoring location. The peak temperature and the width of thermal cycle were measured at the top surface at a distance of 12.7 mm from the weld centerline in the advancing side. Fig. 4.3(a) shows that the peak temperature and the width of the thermal cycle at 420 K increase with increase in friction parameter, μ_0 , due to more intense frictional heating. As the friction between the tool and the workpiece increases, the torque also increases. This trend is opposite to that for Ti-6Al-4V, as shown in Fig. 4.2(a). This can be explained on the basis of the expression for torque given below:

$$M = \int r_A \times \tau_t dA \quad \text{where} \quad |\tau_t| = (1 - \delta) \tau + \delta \mu_f p \quad (4.7)$$

As μ increases, τ decreases. However, increase in μ offsets the decrease anticipated due to softening of material with increase in temperature and so M increases with increase in μ . Fig. 4.3(b) shows that when δ_0 increases and sticking between the tool and the workpiece decreases, torque decreases. With increase in δ_0 the heating rate decreases mainly because of the decrease in the first term on the right hand side in Equation 2.3 which is the dominant heat generation term. Peak temperature is lowered with increase in δ_0 , while cooling rate increases because of less heat input. Fig. 4.3(c) shows that as the heat transfer coefficient increases, more heat is lost from the workpiece and therefore, the peak temperature and the width of the thermal cycle at 420 K decreases. When the heat transfer coefficient is high, lower temperatures result in harder material and higher torque. Fig. 4.3(d) and (e) show increase in temperature and cooling time with higher values of η and β which represent increase in plastic deformational heat generation at the tool-workpiece interface and inside the workpiece, respectively. More intense heating results in higher temperatures and softer material, resulting in lower torque. The results in Fig. 4.3(a) to (e) show that all three output variables, peak temperature, width of thermal cycle and the torque are sensitive to variations in all the five

uncertain input variables. Therefore, all these uncertain input parameters need to be optimized to enhance the reliability of the values of the output variables from the model.

4.1.2.3 AA 6061-T6 to AA 1200

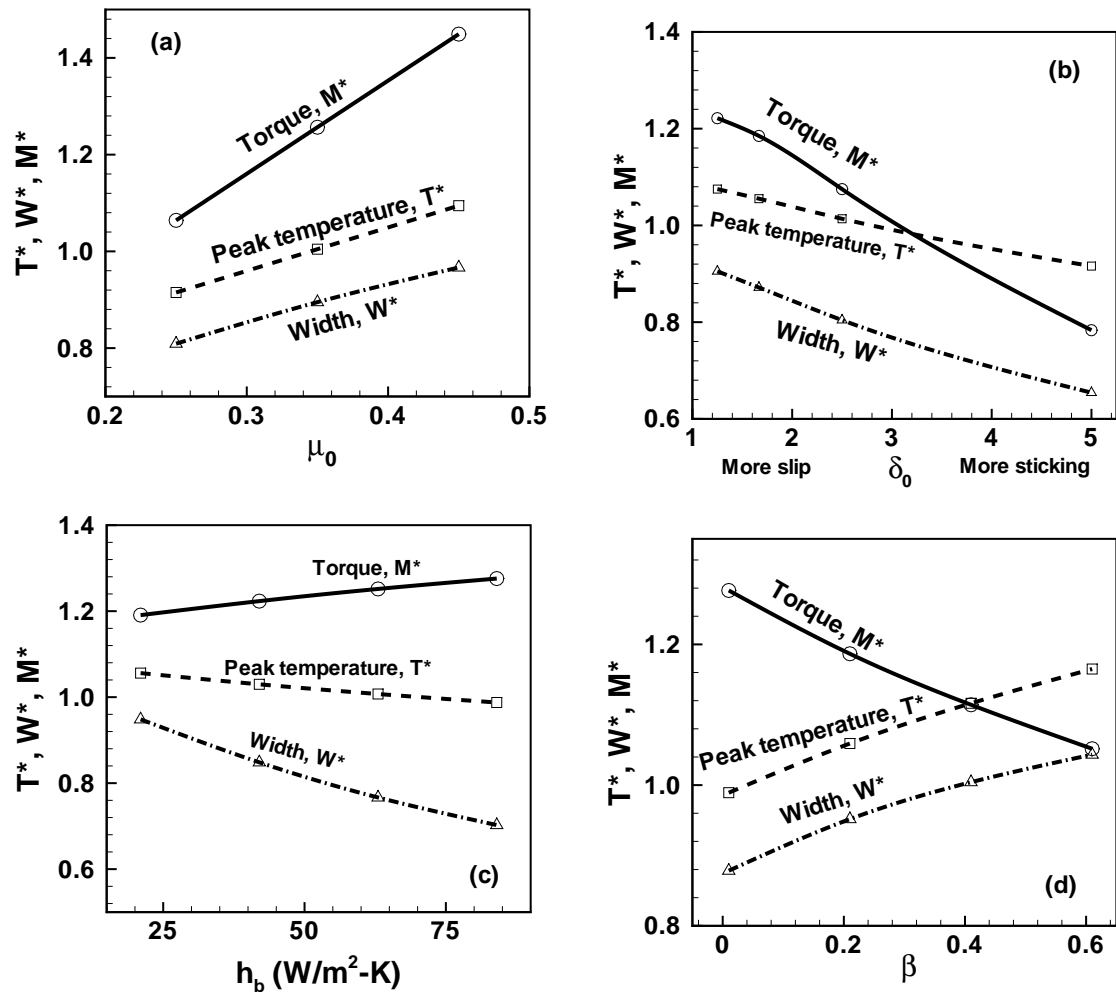


Figure 4.4. Computed dimensionless values of peak temperature, width of the thermal cycle and the torque with change in (c) friction coefficient, (b) slip, (c) heat transfer coefficient at the bottom and (d) scaling factor for plastic deformational heat generation rate for the FSW of dissimilar aluminum alloys. In each case, when one of the parameters is varied, other parameters were kept constant. The welding velocity was 0.42 mm/s and the rotational speed was 450 rpm.

Fig. 4.4(a) shows that as the heat transfer coefficient increases, more heat is

lost from the workpiece and therefore, the peak temperature for the thermal cycle computed at a distance of 13 mm away from the weld centerline in the advancing side, T^* , and the width of the thermal cycle at 523 K, W^* , decrease. When the heat transfer coefficient is high, lower temperatures result in harder material and higher torque. Fig 4.4(b) shows that when δ_0 decreases and more sticking takes place, torque increases as the tool now moves a larger volume of material during its rotation. Temperatures are higher and the thermal cycles are stronger because of more intense deformational heating consistent with the reduction in frictional heating. Higher temperature leads to longer cooling time. Fig. 4.4(c) shows that the peak temperature and the width of the thermal cycle increase with increase in friction coefficient due to more intense frictional heating. As the friction between the tool and the workpiece increases, the torque also increases. It offsets the decrease in torque that has been anticipated due to the softening of material with increase in temperature. Temperature and cooling time increase with increase in viscous heat generation rate, which is proportional to β . More intense heating results in higher temperatures and softer material, resulting in lower torque (Fig 4.4).

4.1.3 Differential Evolution

The goal is to determine unknown parameters in the transport phenomena model. This is done by using inverse modeling based on available experimental data. The problem of inverse modeling is a highly nonlinear, with as many constraints as the number of unknown parameters. For such a non-differentiable problem, the classical calculus-based methods do not perform very well. Evolutionary algorithms provide the advantage of global search capability, robust and effective constraints handling capacity, and are faster because of the inherent parallel search technique.

Differential evolution (DE) is one of the most prominent new generation evolutionary algorithms, proposed by Storn and Price [150]. DE is a fast and robust stochastic search algorithm capable of handling non-differentiable, nonlinear and multimodal objective functions. In a population of potential solutions within an N -dimensional search space, a fixed number of vectors are randomly initialized, then evolved over time to explore the search space and to locate the minima of

the objective function. The advantages of DE, like simple and compact structure, few control parameters, high convergence characteristics, have made it a popular stochastic optimizer. It has been used for many real world applications like determining the ground state of Si-H crystals [151], determination of earthquake hypocenter [152] and optimization of design of digital filters [153].

DE starts to explore the search space by randomly choosing the initial candidate solutions within the constraints. The algorithm tries to locate the global optimum solution for the problem by iterated refining of the population through reproduction and selection. During every generation, a target vector is chosen. Then two other vectors are chosen randomly and their difference is multiplied by a weighting factor. The weighted difference vector obtained is added to a third vector, again chosen randomly from the set of remaining vectors. The generation of new vectors by the combination of vectors randomly chosen from the current population is called mutation. A crossover or recombination operation is performed between the vector obtained and the target vector to obtain the trial vector. This trial vector is then compared with the target vector. Vector with the lower objective value survives into the next generation. Other vectors are also chosen as target vectors and the same process is repeated, till all the vectors are exhausted. Then we move to the next generation and the same sequence of operations is followed. We stop after a fixed number of iterations or when the desired level of optimization is achieved. The scheme is shown schematically in Fig. 4.5.

4.1.3.1 Initialization

Each individual of the DE population consists of a N -dimensional vector, where N is the number of variables in the problem. The initialization of the population can be done on the basis of upper and lower bounds for each parameter. Once bounds are specified, a random number generator can be used to assign each parameter of every vector a value from within the prescribed range. For example, the initial value of the j^{th} parameter of a vector \vec{V} is given by:

$$V_j = rand(0, 1) (U - L) + L \quad (4.8)$$

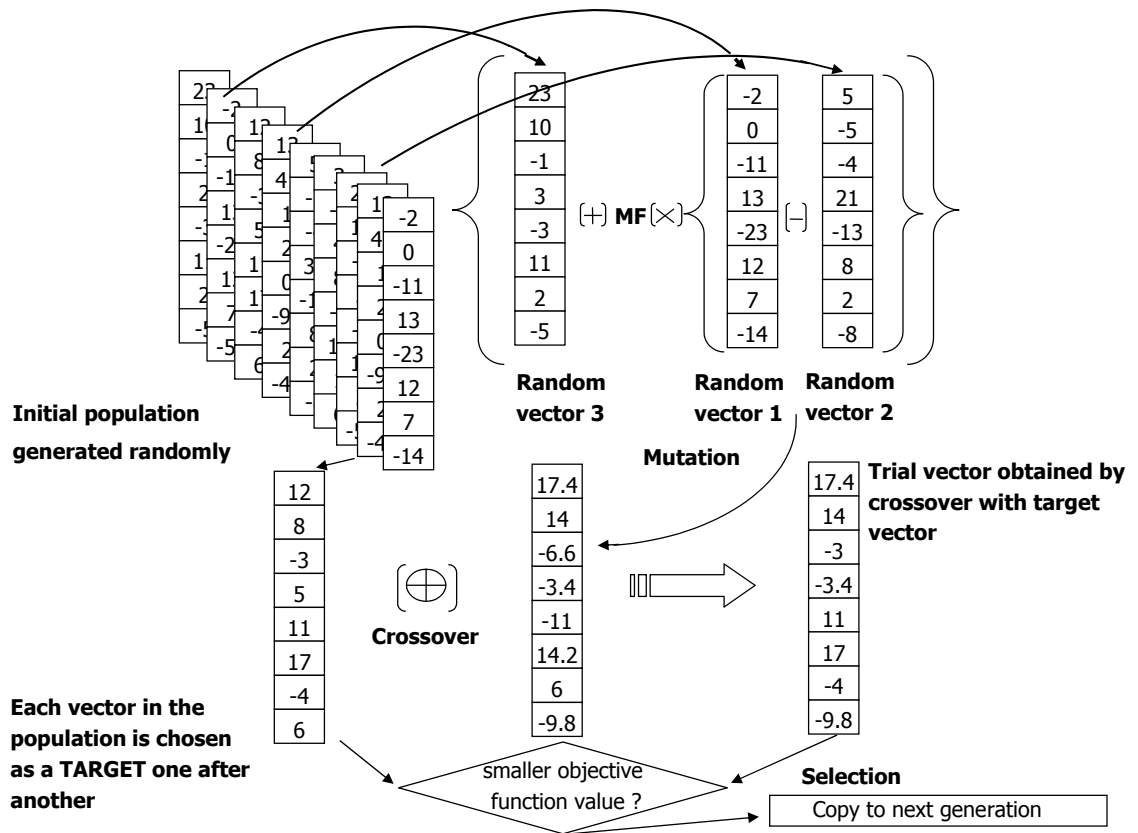


Figure 4.5. Differential Evolution algorithm. MF denotes the mutation factor.

where $rand(0,1)$ is a random number between 0 and 1 and U and L are upper and lower bounds for j^{th} parameter. If a uniform random number generator is used, a uniform population distribution is obtained [154]. This is essential for DE to successfully traverse the search space. Otherwise, if all the initial vectors are same, uniform crossover and mutation will result in the same vector. Therefore uniform initial distribution is necessary for any effective and meaningful search of the solution domain [154].

4.1.3.2 Mutation

Once initialized, DE mutates and recombines the population to produce new vectors. Mutation adds a scaled randomly sampled vector difference to a third vector

to generate a mutant vector \vec{V}_m as shown below:

$$\vec{V}_m = \vec{V}_0 + MF \cdot (\vec{V}_1 - \vec{V}_2) \quad (4.9)$$

where vectors \vec{V}_0, \vec{V}_1 and \vec{V}_2 are distinct. The scaling factor, also called the mutation factor, MF , controls the rate at which the population evolution takes place. The vector \vec{V}_m undergoes crossover with the target vector to generate the trial vector, which is then compared with the target vector, with the one with smaller objective function value surviving into the next generation. The concept of mutating with vector differentials automatically makes mutation self-adjusting, because vector differentials are initially very large for the initial random population and progressively decaying as population converges [151].

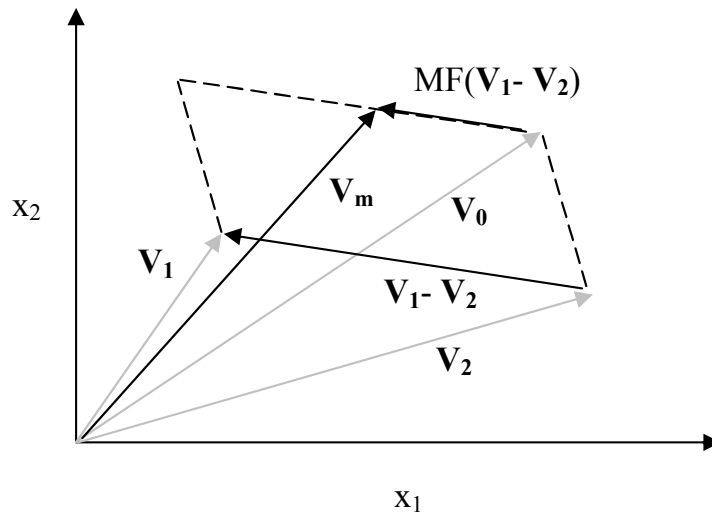


Figure 4.6. Schematic of mutation in 2D space showing how mutant vector \vec{V}_m is produced by adding a weighted differential vector, $MF \cdot (\vec{V}_1 - \vec{V}_2)$ to the base vector \vec{V}_0 .

Boundary constraints are common in real-world problems because parameters often denote physical quantities which have natural bounds. For example, friction coefficient cannot be negative. Though population members already satisfy all constraints, mutant vectors may not as they are obtained by adding a vector differential to a third vector. To overcome this problem, bounce-back method was applied to replace the vector exceeding bounds by one that satisfies bounds.

Figure 4.7 illustrates the bounce-back process in 2-D space

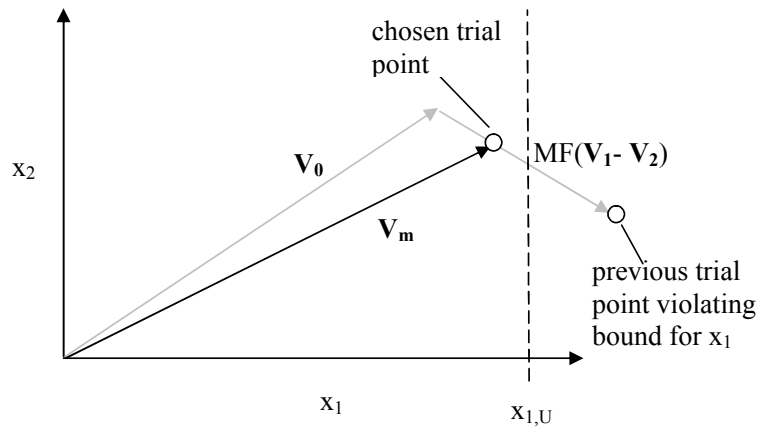


Figure 4.7. Schematic of bounce-back in 2D space showing how new mutant vector \vec{V}_m is obtained if the original mutant vector falls outside the upper boundary constraint of variable x_1 . The first sub-script denotes direction while second sub-script denotes vector. For *e.g.* $x_{1,2}$ denotes component of vector 2 in direction 1.

4.1.3.3 Crossover

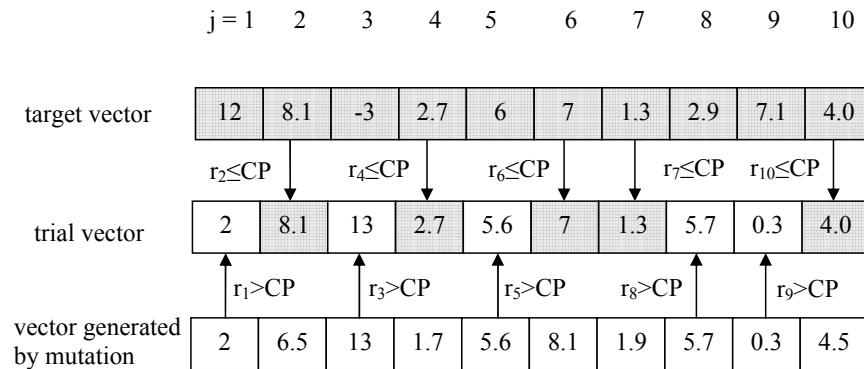


Figure 4.8. Uniform crossover in DE.

To aid the search strategy, crossover is employed along with mutation. During crossover or recombination, parameters from two vectors are merged to create a trial vector. There are several ways to perform crossover: 1) one-point crossover, 2)

multi-point crossover, 3) exponential crossover and 4) uniform crossover. During uniform crossover, each parameter has same probability of inheriting its value from trial vector or vector obtained after mutation. For this reason, uniform crossover does not represent any representational bias [154] and has been used in this study. Figure 4.8 shows that random numbers are generated for each parameter and if the random number is greater than the crossover probability, the value is chosen from the mutant, else, the value of the target vector is copied to the trial vector.

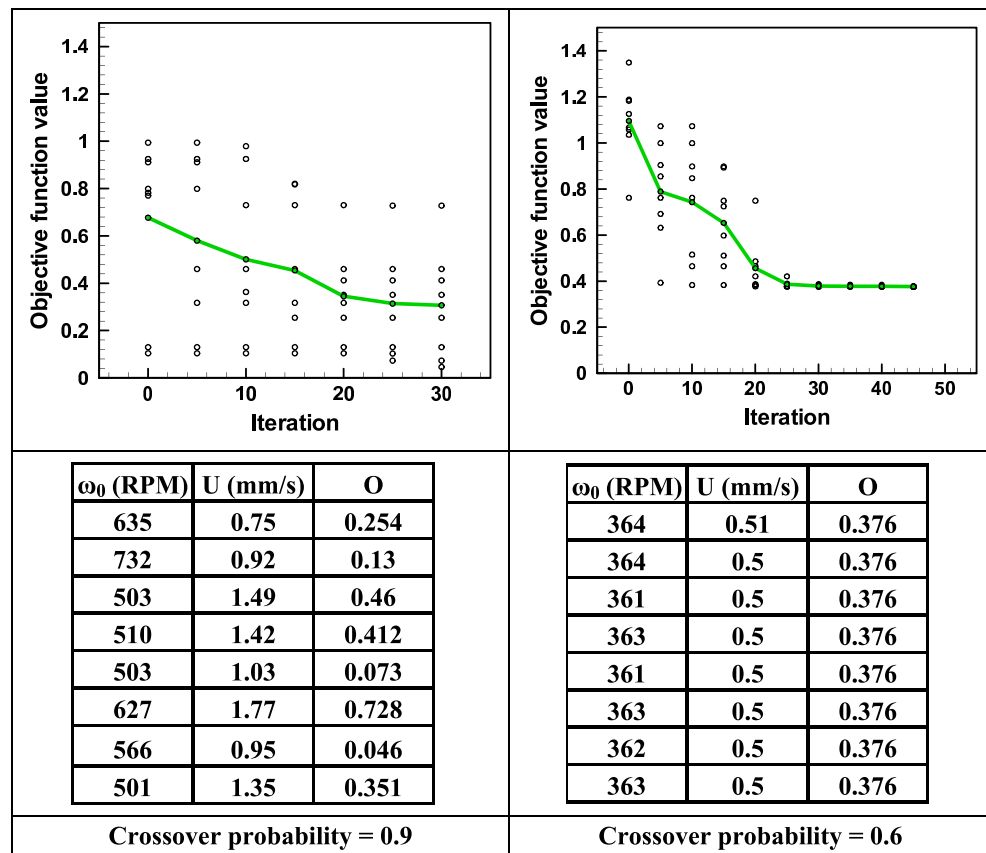


Figure 4.9. Effect of crossover probability on population evolution. The problem and its objective function are defined in section 4.2

Crossover probability, CP , can be any value from 0 to 1. Lower values of CP minimizes disruption by incrementally changing a few parameters of target vector to obtain the trial vector. Higher values of CP increase exploratory tendency of DE by drawing most of the parameters from the mutant vector. Figure 4.9 shows a comparison of population evolution as shown by the the changing distribution

of objective functions for two different crossover probabilities, keeping everything else same. A higher value, close to 1, preserves the diversity of the population which is helpful in obtaining better solution.

4.1.3.4 Selection

The selection of a trial vector is based on its objective function. If the function value of trial vector is smaller than the target vector, trial vector is picked else target vector stays in the solution set. In this sense, the selection process is elitist. Once the new population is obtained, the process of mutation, recombination and selection is repeated until the optimum is located or until preset maximum number of generations is reached.

4.1.4 Results

4.1.4.1 FSW of Ti-6Al-4V

Torque was measured and thermal cycles at three different locations, given in Table 4.2, were used for optimization of uncertain parameters for experiment done at 275 RPM and welding velocity of 1.6 mm/s ($i = 1, j = 3$ in Eqn. 4.5). The thermophysical properties of workpiece and tool materials used in calculations are indicated in Table 3.7 and the process parameters are given in 3.8.

An initial population of 20 individual sets of five variables ($\mu_0, \delta_0, h_{b0}, \eta, \beta$) was generated. Even though Price and Storn [155] recommend a population size of 5 to 20 times the dimensionality of the problem, this could be using an excessive amount. Research with other real coded evolutionary algorithms has produced best results with factors in the range of 1.5 and 2 [156]. Keeping this in consideration, a factor of 4 was used here. After 200 iterations, using a mutation factor of 0.8 and a crossover ratio of 0.9, 20 sets of optimized parameter values were obtained. They are given in table 4.1.

The large value of δ_0 , equivalent to very small δ value indicates considerable sticking between the tool and the workpiece even at the shoulder periphery, where tool velocity is highest. The optimized value of heat transfer coefficient of $418 \text{ W/m}^2\text{K}$ is high enough to take into account considerable heat loss into the backing plate below the workpiece. This value is comparable with the value reported in the

Table 4.1. Optimized sets of uncertain parameters after 200 iterations and the corresponding objective functions, with best set indicated in bold.

μ_0	δ_0	h_{b0} $W/m^2K^{5/4}$	η	β	O
0.7	2.842	418	0.7	0.1	0.469
0.7	2.343	376.2	0.732	0.072	0.496
0.7	2.859	418	0.713	0.1	0.469
0.7	2.44	418	0.7	0.08	0.483
0.698	2.688	418	0.704	0.093	0.476
0.7	2.833	418	0.751	0.098	0.47
0.7	2.362	418	0.739	0.077	0.488
0.7	2.799	418	0.701	0.098	0.471
0.7	1.286	250.8	0.984	0.029	0.652
0.7	2.463	418	0.716	0.082	0.485
0.699	2.711	418	0.743	0.095	0.478
0.699	2.875	376.2	0.7	0.099	0.501
0.7	2.55	418	0.7	0.085	0.479
0.7	2.827	418	0.7	0.099	0.47
0.7	0.695	209	0.718	0.019	0.722
0.7	2.318	418	0.96	0.075	0.491
0.697	2.686	418	0.711	0.096	0.498
0.7	2.227	418	0.7	0.072	0.497
0.7	1.946	334.4	0.958	0.053	0.537
0.7	1.856	418	0.7	0.065	0.521

literature (3.1). The variable, β , which is used to scale down this heat generation term to fit into the context of high viscosity plasticized materials and to confirm to the low value of the plastic deformational heat generation rate experimentally observed in FSW. The numerically calculated torque value of 75 N-m was within 90% of the experimentally measured value of 80 N-m. Thus, the optimized values of all five uncertain parameters were well within the acceptable range of values for each parameter (Tables 3.1, 3.2, 3.3, 3.4).

Figure 4.10 shows the computed thermal cycle for the optimized set of parametric values obtained through DE. A close match between the computed temperature-

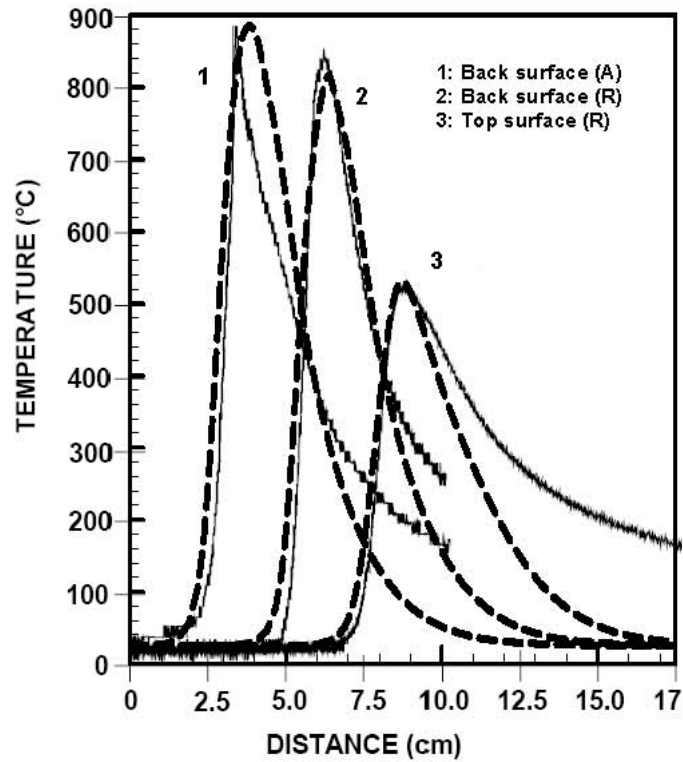


Figure 4.10. Comparison between experimental and calculated temperature profile (indicated as dashed lines) obtained using optimized parameters: $\mu_0 = 0.7$, $\delta_0 = 2.8$, $h_{b0} = 418W/m^2 - K^{5/4}$, $\eta = 0.7$, $\beta = 0.1$. Locations 1, 2 and 3 are indicated in Table 4.2. The distance is measured from the interface between the two plates.

Table 4.2. Position of thermocouple, measured peak value and widths of thermal cycles (Lienert *et. al.* [141]).

Position (R: retreating, A: advancing)	Distance from centerline mm	Measured T_{peak} K	Calculated T_{peak} K	Calculated W_{773K} mm	Measured W_{773K} mm
1- Back(A)	3.175	1160	1162	21.21	23
2- Back(R)	3.175	1129	1110	19.45	20
3- Top(R)	12.192	813	810	9.72	9.5

time variation and the corresponding measured values obtained from the thermocouple can be seen in this figure. The computed average cooling rate in the temperature range of 1173 to 573 K is about 25 K/s, which is well within the range of

cooling rates reported for FSW. For the alloy used in the experiments, the oxygen concentration was 0.18 wt%, and the corresponding β -transus temperature was estimated to be 1254 K (981°C) from the following equation [157]:

$$T_{\beta\text{-transus}} = 1210 + 242.7 \times [\text{wt}\% O] \quad (4.10)$$

The computed peak temperature in workpiece was around 1500 K which is well above the β -transus temperature consistent with the observation of prior β grains in the stir zone.

4.1.4.2 FSW of 1018 Mn steel

Torque on tool and thermal cycle at 12.7 mm away from weld centerline in the advancing side at the top surface were used for optimization of uncertain parameters for experiment done at 450 RPM and welding velocity of 0.42 mm/s ($i = 1, j = 1$ in Eqn. 4.5). The thermophysical properties of workpiece and tool materials used in calculations are indicated in Table 3.7 and the process parameters are given in 3.8.

Table 4.3. Optimized sets of uncertain parameters after 50 iterations and the corresponding objective functions, with best set indicated in bold.

μ_0	δ_0	h_b W/m^2K	η	β	O
0.233	1.1	250.8	0.583	0.186	0.158
0.221	1.35	250.8	0.636	0.08	0.169
0.285	2.08	209	0.682	0.137	0.159
0.221	1.39	209	0.612	0.134	0.155
0.251	1.77	209	0.593	0.083	0.152
0.336	2.15	209	0.679	0.161	0.16
0.294	1.92	250.8	0.652	0.088	0.159
0.477	2.59	209	0.481	0.21	0.163
0.497	3.12	209	0.588	0.204	0.163
0.323	2.13	209	0.605	0.195	0.154

For DE, a population of 12 individual sets of five variables ($\mu_0, \delta_0, h_b, \eta, \beta$)

was generated. Even though a population size of 20 was used for Ti-6Al-4V alloy, where also there were five variables, here the population size is only 2.4 times the dimensionality of the problem. The small value was found to be more efficient as it speeded up the calculation, by carrying only a sufficient number of population members. After 50 iterations, using a mutation factor of 0.8 and a crossover ratio of 0.5, 12 sets of optimized parameter values were obtained. They are given in Table 4.3. The optimized value of the heat transfer coefficient does not vary with the individual solutions and is almost constant at $209 \text{ W/m}^2\text{K}$. For other variables, we get a range of values depending on the individual solution selected.

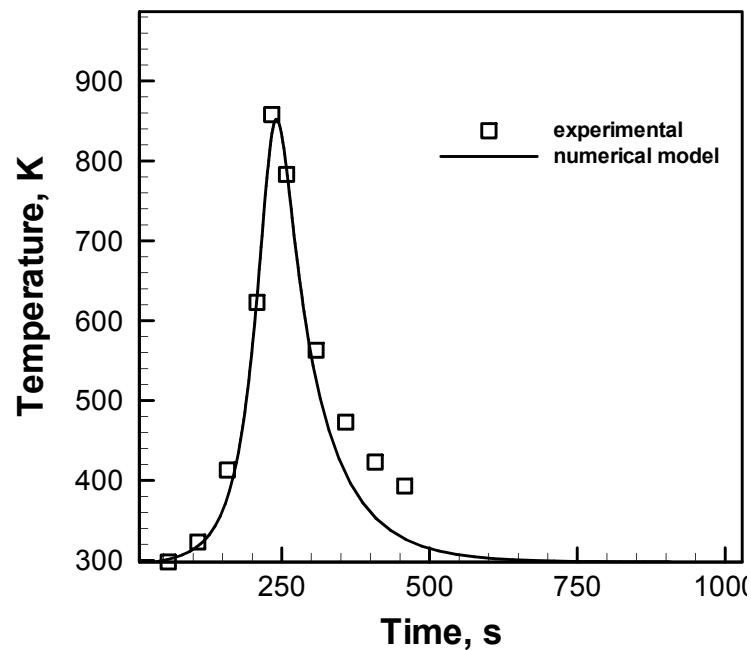


Figure 4.11. Comparison between experimental and calculated time-temperature profile at the top surface, 12.7 mm away from the centerline on the advancing side. The welding velocity was 0.42 mm/s and the rotational speed was 450 rpm.

Fig. 4.11 gives the computed thermal cycle at the top surface at a distance of 12.7 mm away from the weld centerline in the advancing side, obtained when the parametric values determined through DE are used in the heat and plastic flow model. The set of values are indicated in bold in Table 4.3. This set was chosen because it gave the lowest value of objective function, indicating a good match between experimental and measured values. Indeed a close match between

computed and thermocouple measurements can be seen. The torque value for these sets of parameters was 52.9 N-m which is slightly lower than the experimentally measured value of 55 N-m for the same welding conditions. Hence, we see that we can improve the reliability of heat and plastic models in FSW using evolutionary optimization algorithms.

Optimized value of δ_0 is large indicating small δ value which implies considerable sticking between the tool and the workpiece. Heat transfer coefficient of $209 \text{ W/m}^2\text{K}$ is high enough for considerable heat loss into the backing plate below the workpiece and is comparable with the value reported in the literature (3.1). The variable, β , is small suggesting plastic deformational heat generation rate term is small as also observed experimentally [44]. Thus, the optimized values of all five uncertain parameters were well within the acceptable range of values for each parameter as given in Tables 3.1, 3.2, 3.3, 3.4.

4.1.4.3 FSW of AA 6061-T6 to AA 1200

Thermal cycles 13 mm away from weld centerline at the top surface, in the advancing and retreating sides were used for optimization of uncertain parameters for experiments done at 710 RPM, 1000 RPM and 1400 RPM and welding velocity of 1.05 mm/s. Torque data was unavailable for these experiments. Therefore, Eqn. 4.5 reduces to:

$$O = \sqrt{\sum_i \sum_j \left[(1 - T_{ij}^*)^2 + (1 - W_{ij}^*)^2 \right]} \quad (4.11)$$

where $i = 3$ and $j = 2$ for the current problem. The dimensions of the plate and the tool used and the thermo-physical properties of the workpiece and the tool material are given in Table 4.4. Same thermo-physical properties were used for both the aluminum alloys.

Since $i = 3$ in Eqn. 4.11, one calculation of objective function value requires running the heat transfer and plastic flow code three times with three different rotational speed. To reduce the computation time by reducing the dimensionality of the problem, the uncertain parameter of mechanical efficiency (η) was assumed to be equal to 0.8. This can be justified based on inverse modeling calculations

Table 4.4. Input data used for calculations. Thermophysical properties are obtained by curve-fitting of temperature dependent data available in *ASM Handbook* [60] and *Smithells Metals Reference book* [62].

Property/Weld parameter	Value
Workpiece length (x-direction)	450 mm
Workpiece half-width (y-direction)	70 mm
Workpiece thickness	10.0 mm
Shoulder radius	10.0 mm
Pin radius	5.0 mm
Pin length	9.0 mm
Pitch of the thread	1.0 mm
Weld speed	1.05 mm/s
Rotational speed	700–1400 rpm
Axial pressure	18.0 MPa
Tilt angle	0°
Workpiece material	AA6061, AA 1200
Density	2700 kg/m ³
Specific heat capacity, C_p [60] (298-830 K) $929.3 - 0.627T + 1.48 \times 10^{-3}T^2 - 4.33 \times 10^{-8}T^3$	J/kg-K
Thermal conductivity, k [60] (298-830 K) $25.2 + 0.398T + 7.36 \times 10^{-6}T^2 - 2.52 \times 10^{-7}T^3$	W/m-K
Tool	Steel
Density	7860 kg/m ³
Specific heat capacity, C_p [62] (298-1373 K) $468.3 - 8.5T + 3.0 \times 10^{-4}T^2 + 1.8 \times 10^{-7}T^3$	J/kg-K
Thermal conductivity, k [62] (298-1373 K) $3.8 + 9.2 \times 10^{-2}T - 1.8 \times 10^{-4}T^2 + 7.8 \times 10^{-8}T^3$	W/m-K

done by Chao *et. al.* [64], who prescribed values in the range 0.77-0.82. The values of the other four uncertain input parameters were optimized using DE. A population of 10 individual sets of four variables (μ_0 , δ_0 , h_{b0} , β) was generated (2.5 times the dimensionality of problem).

Figure 4.12 indicates that the average objective function value decreased with successive iterations. The decrease in the objective function was most pronounced

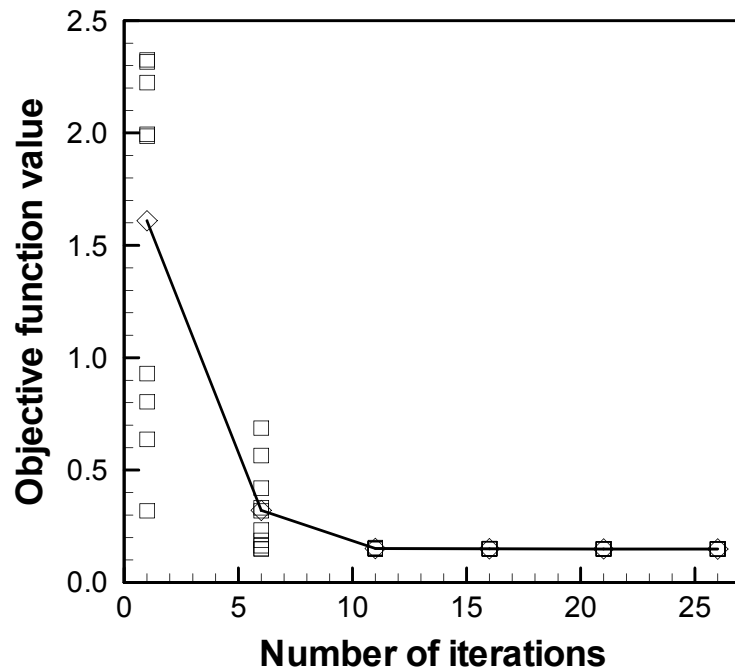


Figure 4.12. Performance of DE with iterations.

during the initial iterations. After 25 iterations, using a mutation factor of 0.8 and a crossover ratio of 0.5, 10 sets of optimized parameter values were obtained. They are given in Table 4.5. The optimized value of the heat transfer coefficient does not vary with the individual solutions and is in the range of $400\text{-}500\text{ W/m}^2\text{-K}$. Since DE is elitist, *i.e.*, the better solution is always picked during selection, we see that diversity of the population steadily decreases.

The set of optimized values of the four uncertain parameters that are used in the heat transfer and plastic flow model are indicated in bold in Table 4.5. Thermal cycle in the weld was calculated using these parameters. A close match between the computed temperature-time variation and the corresponding measured values obtained from the thermocouple can be seen in Fig. 4.13. It shows the computed and experimental thermal cycle at a distance of 13 mm away from the weld center-line in the advancing and retreating sides for dissimilar welds of AA 6061 (advancing) and AA 1200 (retreating).

Table 4.5. Optimized sets of uncertain parameters after 25 iterations and the corresponding objective functions, with best set indicated in bold.

μ_0	δ_0	h_b W/m^2K	β	O
0.488	1.022	418	0.036	0.149
0.487	1.014	418	0.03	0.148
0.484	1.014	418	0.028	0.148
0.482	1.017	460	0.034	0.149
0.479	1.016	460	0.033	0.148
0.489	1.012	418	0.029	0.15
0.49	1.015	418	0.032	0.148
0.492	1.012	502	0.033	0.15
0.499	1.010	502	0.031	0.149
0.499	1.017	418	0.031	0.149

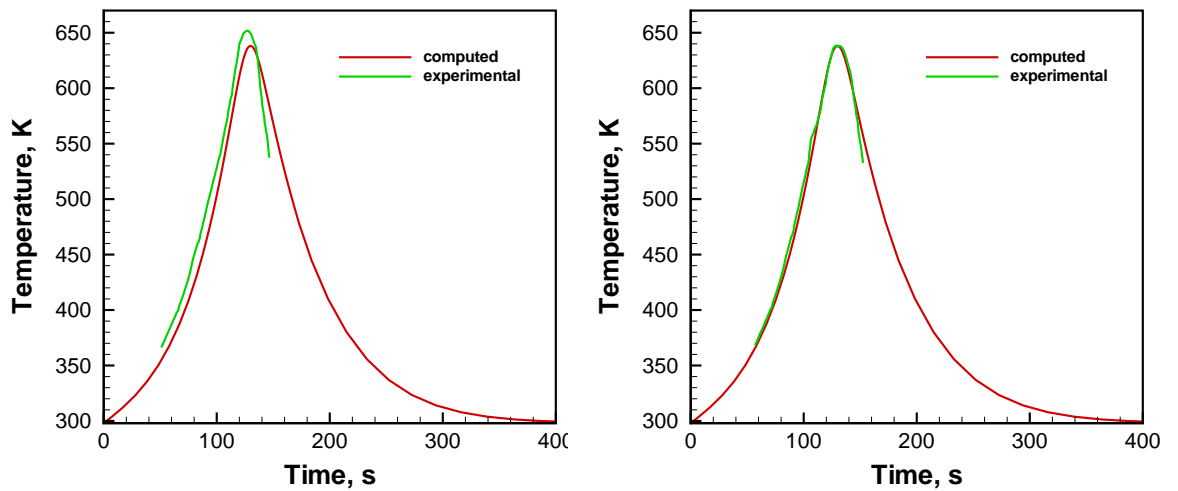


Figure 4.13. Thermal cycle in (a) advancing and (b) retreating sides of dissimilar welds of AA 6061 (advancing) and AA 1200 (retreating) at rotational speed of 710 RPM, translational speed of 0.67 mm/s and axial pressure of 18.47 MPa.

4.2 Tailoring weld attributes

FSW attributes like thermal cycle and torque are strong functions of the welding process parameters like rotational speed, welding velocity and axial pressure of the

tool on the workpiece. A specific thermal cycle and torque can be produced by using multiple sets of these welding process parameters. The available numerical models are unidirectional in nature, *i.e.*, they are designed to calculate velocity and temperature fields for a given set of process parameters. In other words, they cannot predict process parameters to achieve a target weld attribute. However, this is of great practical importance since it will enable welders to easily choose a set of welding parameters and avoid expensive trial and error to get a desired weld attribute

Differential evolution can also be used to determine different set of weld parameters like tool translational and rotational speed to obtain a specific weld attribute. It only differs from the previous approach for improving reliability in that the input variables are welding parameters which can be varied and the previously unknown model parameters have been determined during the reliability study. The desired attributes may be encoded into the objective function as indicated previously.

Among the process parameters in the FSW model, the welding velocity and rotational speed were varied. In order to optimize the values of the process parameters from a experimentally measured thermal cycles, the following objective function is minimized:

$$O = \sqrt{((1 - T^*)^2 + (1 - W^*)^2)} \quad (4.12)$$

where T^* and W^* are non-dimensionalized peak temperature and width of thermal cycle at a specified temperature, respectively, as defined previously:

$$T^* = \frac{T_{cal}}{T_{exp}} \quad \text{and} \quad W^* = \frac{W_{cal}}{W_{exp}} \quad (4.13)$$

These two variables were chosen because they encompass both the peak temperature as well as the heating and cooling rates. The experiments were performed at IIT Bombay by Prof. Amitabha De.

4.3 Results

Dissimilar welds of AA 6351 (advancing)–AA 1200 (retreating) were made at different welding speeds and rotational velocities. The FSW tool was made of tool steel. The thermophysical properties of AA 6061, given in Table 3.7, were used for both AA 6351 and AA 1200 in the heat transfer and plastic flow calculations. The thermophysical properties of tool steel are also given in Table 3.7. The process parameters, tool and workpiece dimensions are given in Table 4.6.

Table 4.6. Data used in calculations.

Process parameter	
Workpiece length (mm)	254
Workpiece half-width (mm)	102
Workpiece thickness (mm)	5.0
Shoulder radius (mm)	10.0
Pin radius (mm)	3.0
Pin length (mm)	4.2
Weld speed (mm/s)	0.67-2.08
Rotational speed (RPM)	355-710

First, the uncertain model parameters (μ_0 , δ_0 , h_{b0} and β) were determined using DE. The uncertain parameter of mechanical efficiency (η) was assumed to be equal to 0.8 [64]. Thermal cycles were measured for dissimilar welds of AA 6351–AA 1200 at different welding speeds and rotational velocities. The measured data used for optimizing the uncertain parameters in the model are given in Table 4.7.

The following optimization function is used ($i=3$, corresponding to the three different sets of welding variables in Table 4.7):

$$O = \sqrt{\sum_i \left[(1 - T_i^*)^2 + (1 - W_{250^\circ C, i}^*)^2 (1 - W_{300^\circ C, i}^*)^2 \right]} \quad (4.14)$$

where subscript 300°C denotes width measured at that temperature for thermal cycle in the advancing side and T^* and L^* are the normalized temperature and

width values as given below:

$$L^* = \frac{T_{cal}}{T_{exp}}, \quad W^* = \frac{W_{cal}}{W_{exp}}$$

The value of the set of optimized parameters is given in Table 4.8. The values obtained are in the same range as that for dissimilar AA 6061-T6–AA 1200 welds.

Figure 4.14 shows the computed thermal cycle at a distance of 12.7 mm, on either side of the weld centerline, for the optimized set of parametric values obtained through DE (indicated in bold in Table 4.8). It can be seen that advancing side temperature is slightly higher than the retreating side. This is so because more heat is generated in the advancing side because of higher relative velocity between the tool and the workpiece on the advancing side.

Once we have the optimized values of the uncertain parameters, we specify a target thermal cycle. To test the model, thermal cycle from an actual welding experiment was specified as the target. It was obtained for welding speed of 1.05 mm/s and rotational speed of 710 RPM, and the resulting thermal cycle had the following attribute: advancing side (12.7 mm from weld centerline) peak temperature was 610 K, retreating side (12.7 mm from weld centerline) peak temperature was 605 K, width of thermal cycle in advancing side at 250°C was 2.9 mm and at 300°C was 1.6 mm.

Values of welding speed, U , and rotational speed, ω , were randomly chosen in the range of 0.5–3.0 mm/s and 300–800 RPM, respectively. A large range was chosen to explore a large domain to include all possible solutions and also to maintain

Table 4.7. Measured thermal cycle attributes used for determining the uncertain parameters.

rotationl speed (RPM)	welding speed (mm/s)	Peak temperature (advancing) (K)	Peak temperature (retreating) (K)	Width at 250°C (advancing) (mm)	Width at 300°C (advancing) (mm)
355	0.67	599	586	40.2	18.9
500	1.05	601	584	23.2	10.8
710	2.08	560	548	21.2	10.4

Table 4.8. Optimized sets of uncertain parameters after 50 iterations and the corresponding objective functions, with best set indicated in bold.

μ_0	δ_0	h_{b0} $W/m^2 K^{5/4}$	β	O
0.790	1.500	418	0.131	1.061
0.627	1.397	418	0.132	1.198
0.779	1.490	418	0.186	1.177
0.798	1.394	418	0.126	0.989
0.790	1.457	418	0.216	0.984
0.635	1.386	125.4	0.196	2.162
0.647	1.489	418	0.192	1.400
0.785	1.407	418	0.116	1.083
0.786	1.379	418	0.180	1.122
0.706	1.024	167.2	0.138	2.098
0.778	1.367	209.0	0.233	1.937
0.673	1.500	418	0.178	0.935
0.743	1.427	418	0.135	1.122
0.731	1.487	418	0.240	1.039
0.772	1.448	125.5	0.174	1.180
0.753	1.483	418	0.151	0.997

the diversity in solutions. The progress of the iterations can be seen in Fig. 4.15, where objective function, as defined in Equation 4.12, decreases progressively indicating that combination of welding variables have been achieved which give thermal cycles having close attribute as specified by the target.

In order to verify the computed solutions, the first test is to check if the population of solutions produced by the model includes a set of welding variables that is close to that used to get the target weld thermal cycle. Note that the welding velocity and rotational speed in the first set in Table 4.9 is very close to the welding speed of 1.05 mm/s and rotational speed of 710 RPM used to obtain the target thermal cycle. Each set of welding variables in Table 4.9 was used to obtain thermal cycles using the forward heat and plastic flow calculation and then compared with those produced by experiment. A good agreement can be seen in calculated

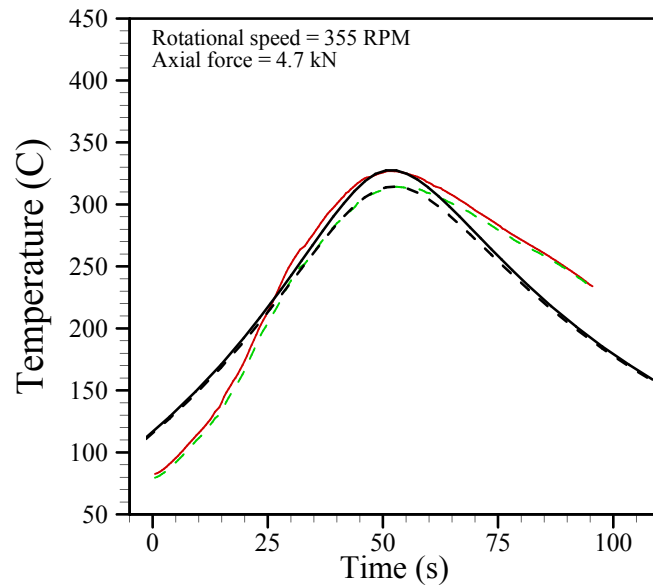


Figure 4.14. Thermal cycle in advancing and retreating sides of AA 6351-AA 1200 dissimilar weld performed at 355 RPM and 0.67 mm/s with axial force of 4.7kN. Solid lines indicate advancing side while broken lines indicate retreating side. Experimentally measured values are indicated in color (gray in BW) while computed thermal cycles are indicated in black. (For interpretation of the references to color in this figure legend, the reader is referred to the electronic version of the thesis.)

thermal cycles in Fig. 4.16.

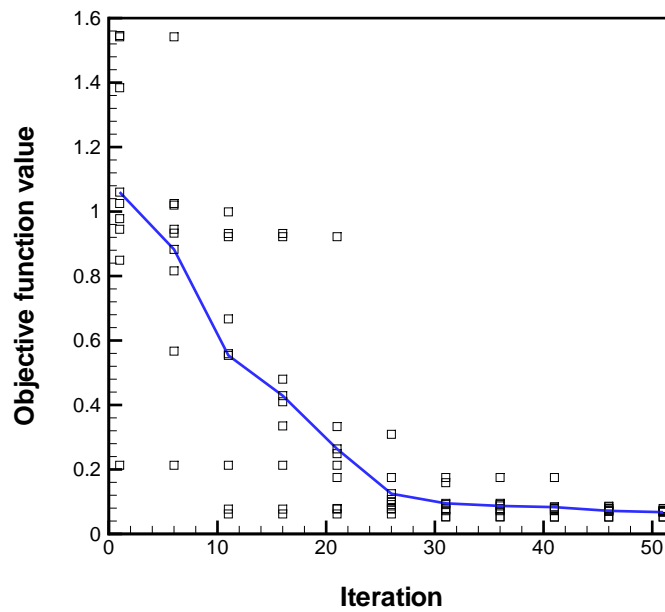
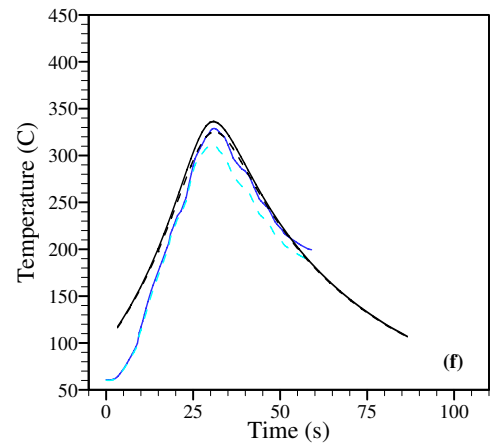
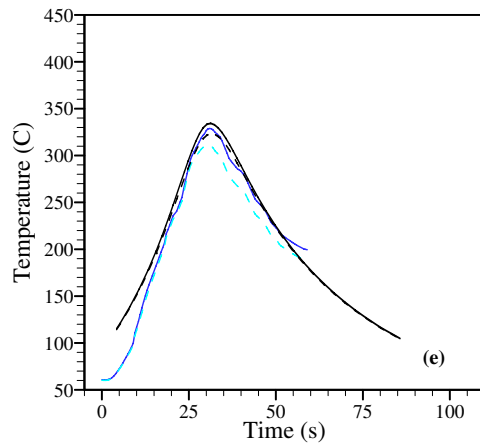
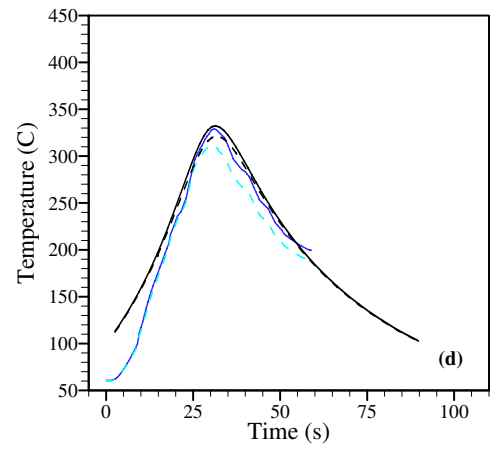
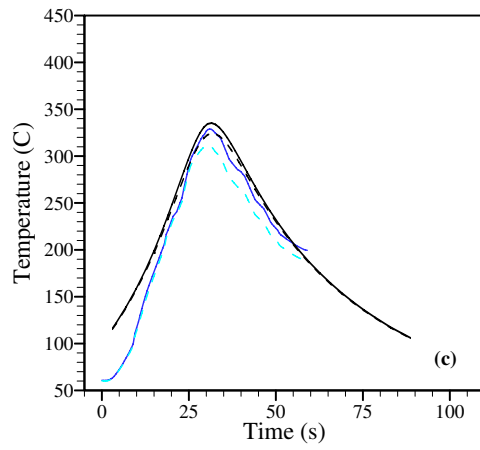
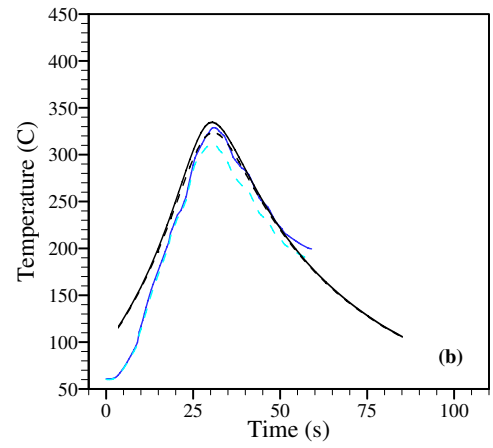
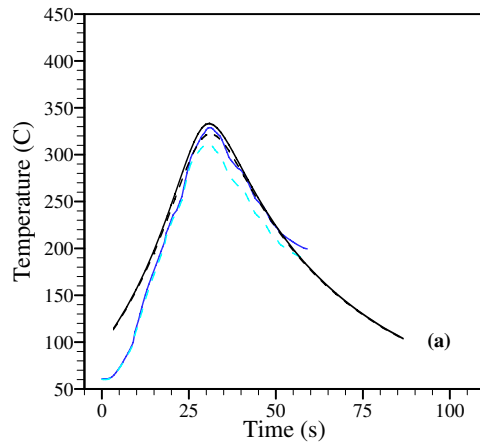


Figure 4.15. Performance of DE with iterations.

Table 4.9. Various combinations of welding variables, *i.e.*, welding velocity and tool rotational speed, obtained using Differential Evolution to achieve the following target thermal cycle: advancing side (12.7 mm from weld centerline) peak temperature = 610 K, retreating side (12.7 mm from weld centerline) peak temperature = 605 K, width of thermal cycle in advancing side at 250°C = 29 mm and width of thermal cycle in advancing side at 300°C = 16 mm.

rotationl speed (RPM)	welding speed (mm/s)	Peak temperature (advancing) (K)	Peak temperature (retreating) (K)	Width at 250°C (advancing) (mm)	Width at 300°C (advancing) (mm)	O
705.9	1.03	612.5	605.1	28	15	0.084
854.9	0.57	616.1	608.7	27	15	0.129
876.0	0.56	617.9	610.3	28	16	0.231
639.7	0.84	615.8	608.8	28	16	0.062
560.3	1.01	612.7	605.5	29	15	0.073
536.3	1.09	617.6	610	28	16	0.136
859.1	0.57	616.5	609.1	29	16	0.147
801.5	0.7	616.6	609.1	28	16	0.164



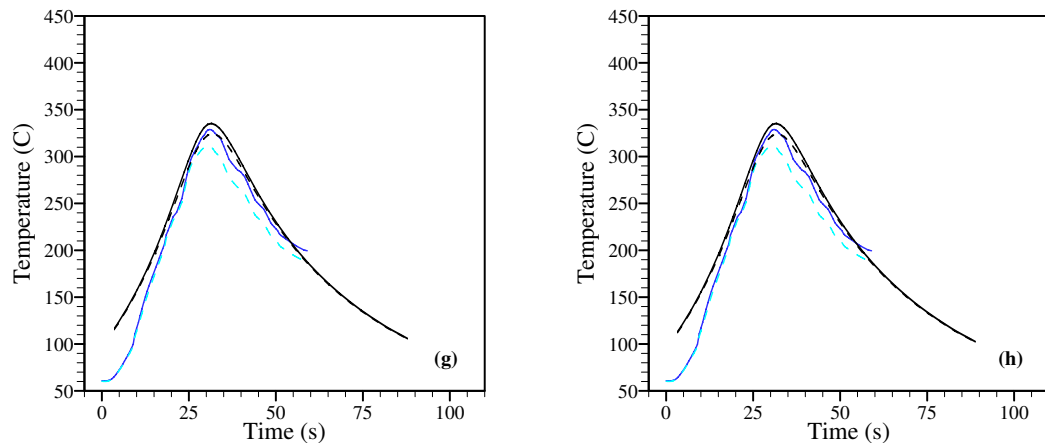


Figure 4.16. Comparison of target thermal cycle with that obtained using differential evolution. Solid lines indicate advancing side while broken lines indicate retreating side. Experimentally measured values are indicated in color (gray in BW) while computed thermal cycles are indicated in black. The calculated thermal cycles correspond to the set of welding parameters in Table 4.9. (For interpretation of the references to color in this figure legend, the reader is referred to the electronic version of the thesis.)

4.4 Summary and conclusions

A numerical model embodying the equations of conservation of mass, momentum and energy was used to examine the sensitivity of important parameters which are friction coefficient, the extent of slip between the tool and the workpiece, the heat transfer coefficient at the bottom of the workpiece, and the fraction of plastic deformation work which is converted to heat, on the computed temperature fields and torque on the tool. These parameters, which cannot be prescribed either from the welding conditions or from fundamental principles, were found to significantly affect both the temperature fields and the torque on the tool for all three materials (Ti-6Al-4V, 1018 Mn steel, AA 6061-T6 to AA 1200). The sensitivity trends are similar for different alloys with different thermophysical properties, in all but one case. Model prediction of torque decreases with increasing friction coefficient in Ti-6Al-4V, while it increases in 1018 Mn steel and aluminum alloy. Temperatures are lowered with decrease in slip and cooling rate increases because of less heat input. As the heat transfer coefficient increases the temperature and the width of the thermal cycle and torque on tool decreases. Higher values of mechanical efficiency

and scaling factor for plastic deformation heating result in intense heating results in higher temperatures and softer material, resulting in lower torque.

The values of the unknown parameters can be obtained from a experimentally measured weld attributes like thermal cycles, TMAZ and torque on tool measured under different welding conditions using Differential Evolution based search algorithm. When the value of unknown parameters determined using DE are plugged into the model, the computed peak temperature, thermal cycle and the torque on the tool agreed very well with the corresponding experimental data. In all case, the extent of slip between the tool and the workpiece is obtained by optimization procedure is small indicating close to sticking condition, even at the outer periphery of the tool shoulder. Previous research [31] suggests that the interfacial condition is close to sticking. The scaling factor for the plastic deformational heat has a small value in all three cases. This agrees with the small value of plastic deformational heat generation rate reported in literature [44]. The mechanical efficiency, bottom heat transfer coefficient and friction coefficient value obtained are in a physically viable range available in literature.

A bi-directional model can be obtained by combining the forward transport phenomena model with DE to give it inverse modeling capabilities. This was used to predict welding process variables like welding velocity and tool rotational speed, necessary to obtain the desired weld attribute in AA 6351-AA 1200 dissimilar welds. The sets of welding velocities and rotational speeds obtained were in a wide range. Welding velocity ranged from 0.56 to 1.09 mm/s while the the rotational speed was in the range of 536.3 to 859.1 RPM. Though, here the experimental data was limited to thermal cycle measurements, torques on tool, shape of TMAZ, etc. can also be set as desired weld attributes. The set of welding variables obtained varied over a large range offering flexibility to choose the welding variables based on experimental constraints. It is shown that agreement between the model predictions and experimentally measured thermal cycles can be obtained, indicating the usefulness of this approach for practical purposes.

Species transport in dissimilar metal joining

FSW is now being used for welding dissimilar alloys with applications in many industries such as aeronautics and automobile. Experimental work has been done to understand dissimilar FS-welds in terms of material combinations, welding variables and weld properties. Jin *et al.* [158] welded pure iron and pure nickel using polycrystalline cubic boron nitride tool and determined the intermixing of metals using TEM and Auger analysis. The analysis revealed a very narrow inter diffusion zone; about $1.5\ \mu\text{m}$ wide in single pass and $1.8\ \mu\text{m}$ wide in double pass joints. Miles *et al.* [159] joined dissimilar-aluminum alloys 5182-0, 5754-0, and 6022-T4 to test the formability of the individual welds compared to the base metals for application in the automotive industry. Cavaliere *et al.* [160] studied the mechanical and microstructural properties of dissimilar 2024 and 7075 aluminum alloys. They observed a net increase in strength in longitudinal direction with respect to transverse direction and improvement in fatigue life compared to 2024 welds but degradation when compared to 7075 welds. Ouyang *et al.* [161] performed a dissimilar FSW of 6061 aluminum to 2024 aluminum to characterize the flow behavior of dissimilar metals. Degree of mixing of dissimilar alloys increases with rotational speeds, but even at high speeds, the mixing is far from complete and a banded structure is observed. Shigematsu *et al.* [162] joined AA 5083 with AA 6061 and performed EPMA to map the distribution of Mg and Cu. They observed non-overlapping Cu-rich and Mg-rich regions indicating very little diffusion and chemical reaction

between Cu-rich AA 6061 (0.85 wt% Mg, 0.4 wt% Cu) and Mg-rich AA 5083 (4 wt% Mg, trace Cu). These represent significant advancement in dissimilar joining. However, numerical modeling has not been used for dissimilar FSW.

No modeling effort has been reported for the FSW of dissimilar alloys to predict the mixing in TMAZ. Here a model is developed for solute redistribution in dissimilar welds due to diffusion and mixing caused by rotational and translational motion of the tool. AA 6061 contains about 0.85 wt% Mg while AA 1200 contains trace amounts of alloying elements. If these two alloys are welded together, the problem of solute redistribution can be simplified to that of redistribution of Mg when pure aluminum is welded to binary aluminum alloy containing 0.85 wt% magnesium. It is assumed that no diffusion takes place into the tool and that no inter-metallic compounds are formed. After solving the equations of conservation of mass, momentum and energy, the equation of species conservation in dilute alloys is solved which gives the three-dimensional distribution of the alloying element after welding. This concentration distribution can be verified experimentally. In addition, the concentration distribution provides an idea about the material flow and mixing in the stir zone. The study of FSW of AA 6061 to AA 1200 provides an excellent way to determine the nature of solute transport which in turn is related to the plastic flow. Comparison of calculated and experimentally determined concentration profiles of Mg across the weld provides important insight about the nature of plastic flow and mixing of magnesium between the two alloys.

5.1 Experiments

An existing vertical milling machine was modified to perform FSW experiments at IIT Bombay. Friction stir welds were made in butt joint configuration for AA6061 to AA1200. Two plates of 90 mm×100 mm×10 mm were clamped rigidly in butt joint configuration on the machine bed using jigs and fixtures. A cylindrical tool with a shoulder of 20 mm diameter and with a pin of length 9.8 mm and 10 mm diameter was used. The pin had skew threads conforming to Whorl profile. The pin was inserted with a slight inclination (2°) into a predrilled hole along the weld

interface. The inclination of the pin with the vertical provided improved consolidation of deforming material on the trailing side of the tool. Six 3.0 mm diameter holes (three on each plate) were drilled in the plates and K-type chromel-alumel thermocouples were brazed to the base plate using Al-Si filler material and a brazing flux (mixture of alkali and alkaline earth chlorides). The plates were clamped at all the sides and placed directly on the bed of the milling machine without any backing plate. An appropriate axial force on the tool shoulder is important for successful FSW process. However, a preset amount of axial force cannot be applied by the vertical milling machine used for the present work. Therefore, the tool shoulder was pressed against the work piece to the maximum possible extent and a maximum axial force of 4.70 kN was measured using Kistler dynamometer.

The nominal composition of the alloys (in wt%) [60] is given here. AA 6061 has 0.4-0.8 Si, max 0.7 Fe, 0.15-0.4 Cu, max 0.15 Mn, 0.8-1.2 Mg, 0.04-0.35 Cr, max 0.25 Zn, max 0.15 Ti, max 0.15 other elements(total), rest Al; 1200 is commercial purity aluminum and has 99.99 wt% Al.

The concentrations of Mg was measured in a transverse cross-section across the weld-center line at depths of 1, 3 and 5 mm from the top surface (schematic shown in inset of Fig. 5.3). The measurement was done at Penn State using electron probe micro-analysis (EPMA) of polished transverse-cut friction-stir welded samples. EPMA can be used for elemental analysis in areas down to 1 μm and also for 2-dimensional elemental mapping using larger beam diameter. It is particularly useful for quantitative chemical analysis of individual phases in multiphase systems and for chemical diffusion studies at materials interfaces. Here the largest possible beam diameter of 50 μm was used to perform the analysis. Selection of a larger diameter allows scanning a large area to obtain an average quantitative value of concentration.

5.2 Mathematical model

The dimensions of the plate and the tool used and the thermo-physical properties of the workpiece and the tool material are given in Table 5.1. Same thermo-physical properties were used for both the aluminum alloys.

The same constitutive equation for viscosity, which has been described in more

Table 5.1. Input data used for calculations. Thermophysical properties are obtained by curve-fitting of temperature dependent data available in *ASM Handbook* [60] and *Smithells Metals Reference book* [62].

Property/Weld parameter	Value
Workpiece length (x-direction)	450 mm
Workpiece half-width (y-direction)	70 mm
Workpiece thickness	10.0 mm
Shoulder radius	10.0 mm
Pin radius	5.0 mm
Pin length	9.0 mm
Pitch of the thread	1.0 mm
Weld speed	1.05 mm/s
Rotational speed	700–1400 rpm
Axial pressure	18.0 MPa
Tilt angle	0°
Workpiece material	AA6061, AA 1200
Density	2700 kg/m ³
Specific heat capacity, C_p [60] (298-830 K) $929.3 - 0.627T + 1.48 \times 10^{-3}T^2 - 4.33 \times 10^{-8}T^3$	J/kg-K
Thermal conductivity, k [60] (298-830 K) $25.2 + 0.398T + 7.36 \times 10^{-6}T^2 - 2.52 \times 10^{-7}T^3$	W/m-K
Tool	Steel
Density	7860 kg/m ³
Specific heat capacity, C_p [62] (298-1373 K) $468.3 - 8.5T + 3.0 \times 10^{-4}T^2 + 1.8 \times 10^{-7}T^3$	J/kg-K
Thermal conductivity, k [62] (298-1373 K) $3.8 + 9.2 \times 10^{-2}T - 1.8 \times 10^{-4}T^2 + 7.8 \times 10^{-8}T^3$	W/m-K

detail in Chapter 2, is used for both the alloys and is given below [49]:

$$\sigma_e = \frac{1}{3\dot{\epsilon}\alpha} \sinh^{-1} \left[\left(\frac{Z}{A} \right)^{\frac{1}{n}} \right] \quad \text{where} \quad Z = \dot{\epsilon} \exp(Q/RT) \quad (5.1)$$

However, the value of the constants were different and are given in Table 5.2.

Table 5.2. Constants used in constitutive equation for viscosity [54].

Alloy	A, s^{-1}	$\alpha, (MPa)^{-1}$	n
6061	2.409×10^8	0.045	3.55
1200	3.902×10^9	0.037	3.84

Since the alloys being welded contain different concentrations of Mg, the changes in the concentration of Mg in the two plates due to welding are examined. Apart from 0.85 wt%, Mg AA 6061 also contains other alloying elements. However, for simplicity, it is treated as a binary alloy for modeling purposes. Similarly, AA 1200 is considered to be pure aluminum. We assume no diffusion takes place into the tool. The equation of conservation of mass of any alloying element present at low concentration is given by:

$$\frac{\partial(u_j C_i)}{\partial x_j} = -U \frac{\partial C_i}{\partial x_1} + \frac{\partial}{\partial x_j} \left(D \frac{\partial C_i}{\partial x_j} \right) \quad (5.2)$$

Here, D denotes temperature dependent chemical-diffusivity given by:

$$D = D_0 \exp \left(-\frac{Q_a}{RT} \right) \quad (5.3)$$

The pre-exponent, D_0 , was $49 \text{ mm}^2/\text{s}$ and activation energy, Q_a , was 124 kJ/mol . These values were obtained from Table 13.4 from *Smithells Metals Reference book* [62] for binary alloy containing 99 at% Al and 1 at% Mg. The values of pre-exponent and activation energy vary with composition. For *e.g.*, $D_0 = 45 \text{ mm}^2/\text{s}$ and $Q_a = 122 \text{ kJ/mol}$ for an alloy containing 96 at% Al and 4 at% Mg [62]. The values are valid in the temperature range of 690-818 K. In the absence of any available data beyond this temperature range, these values of D_0 and Q_a were used for all temperatures encountered during the FSW.

5.3 Results and Discussion

Figure 5.1 shows the computed and experimental thermal cycles at a distance of 13 mm away from the weld center-line in the advancing side. A close match between

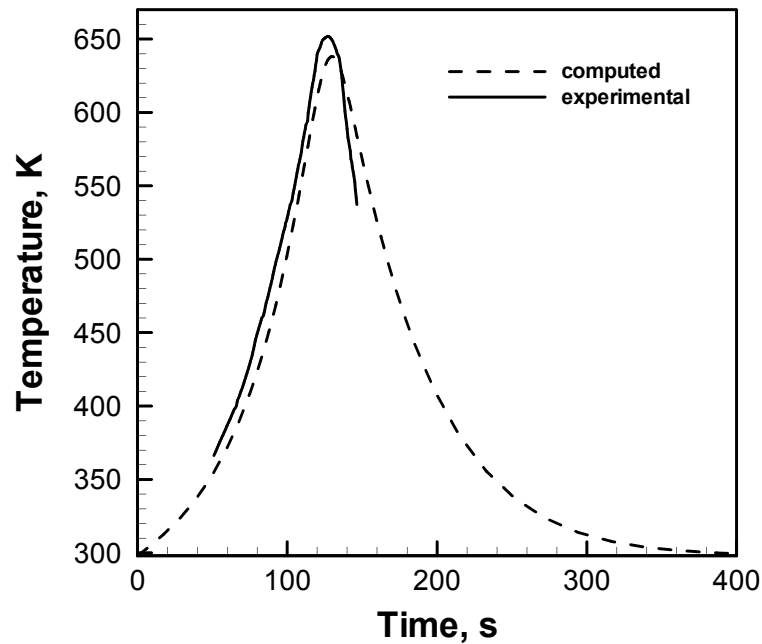


Figure 5.1. Comparison between experimental and calculated time-temperature profile at a point 13 mm away from the centerline on the advancing side. The welding velocity was 1.05 mm/s and the rotational speed was 710 rpm.

the computed temperature-time variation and the corresponding measured values obtained from the thermocouple can be seen in Fig. 5.1. The computed streamlines for the plastic flow are shown in Fig. 5.2. Two important features of flow, material going around the pin in the retreating side and the formation of a stagnant zone in the advancing side, can be observed. The temperature and flow fields are similar in nature to those for similar alloy joining. This is expected because the two alloys have similar thermophysical properties. The difference in alloying elements leads to differences in mechanical properties which do not affect the computed temperature and velocity fields in this case.

The measured and calculated values of Mg concentration across the weld joint are shown in Figures 5.3(a) and (b). Figures 5.3 represents a case with AA 6061 on the advancing side and AA 1200 on the retreating side. The measured concentration distribution across the weld joint depends on the inter-mixing of alloys and also on the movement of the interface between the two alloys. From Fig. 5.3(a), it is clear that there is a lower degree of inter-mixing and greater movement of interface

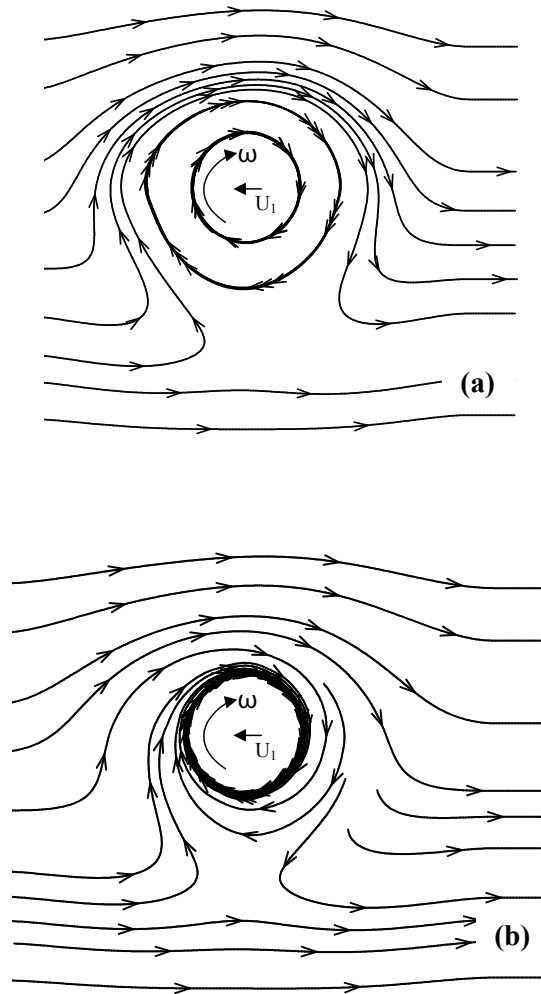


Figure 5.2. Stream-lines in a horizontal plane (a) 3.66mm and (b) 7mm below the top surface, showing plastic flow during FSW. Material flows along the retreating side around the pin, and a stagnant zone forms in the advancing side. The welding velocity was 1.05 mm/s and the rotational speed was 710 rpm.

between AA 6061 and AA 1200. The movement of the interface into the retreating side is lower near the top surface and increases progressively with depth. Numerical results indicate greater inter-mixing. However, both experimental results and numerical calculations show the same trend for movement of the interface. The increased movement of Mg from AA 6061 in the advancing side toward AA 1200 in the retreating side with the increase in depth of the work piece is depicted in both the EPMA measurements and the numerical calculations. In contrast, when

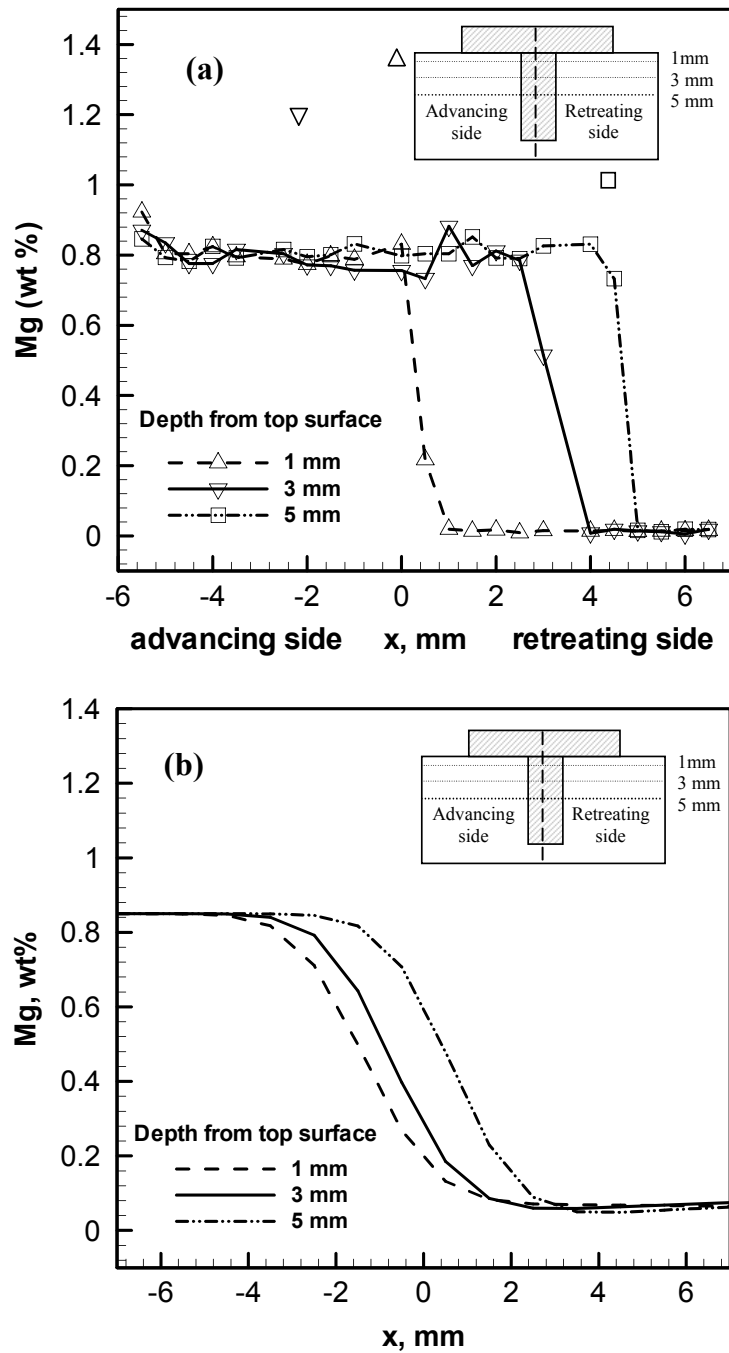


Figure 5.3. (a) Measured and (b) computed concentration profile of Mg at depths of 1, 3 and 5 mm from the top surface, across the weld center-line for AA 6061 (advancing) and AA 1200 (retreating side) weld at 710 RPM and a weld velocity of 1.05 mm/s.

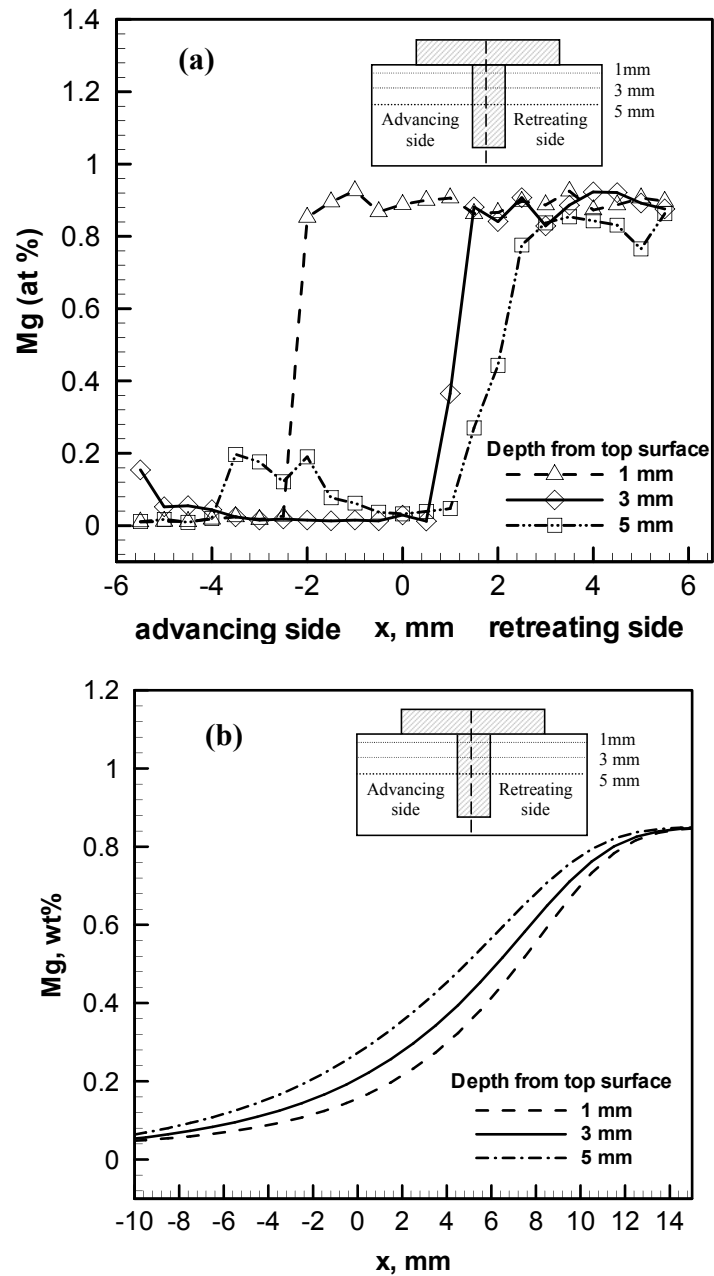


Figure 5.4. (a) Measured and (b) computed concentration profile of Mg at depths of 1, 3 and 5 mm from the top surface, across the weld center-line for AA 1200 (advancing) and AA 6061 (retreating side) weld at 710 RPM and a weld velocity of 1.05 mm/s.

AA 6061 was placed on the retreating side, the interface corresponding to depth of 3 and 5 mm from the top surface moves to the retreating side while the interface at a depth of 1 mm moves towards the advancing side, as indicated in Fig. 5.4(a). The calculated trends in Mg concentrations across weld joint (Fig. 5.4(b)) are slightly different from the corresponding measured results (Fig. 5.4(a)) when Mg containing alloy (AA 6061) is on the advancing side. Although the reason for this mismatch is not clearly known, it is suggested that the difference could be because the calculations assume complete mixing in the plasticized material whereas flow is layered in nature in FSW [138]. The comparison of experimental and computed concentration profiles (Fig. 5.5) showed that continuum hypothesis cannot describe the imperfect mixing of the plasticized alloys during FSW completely.

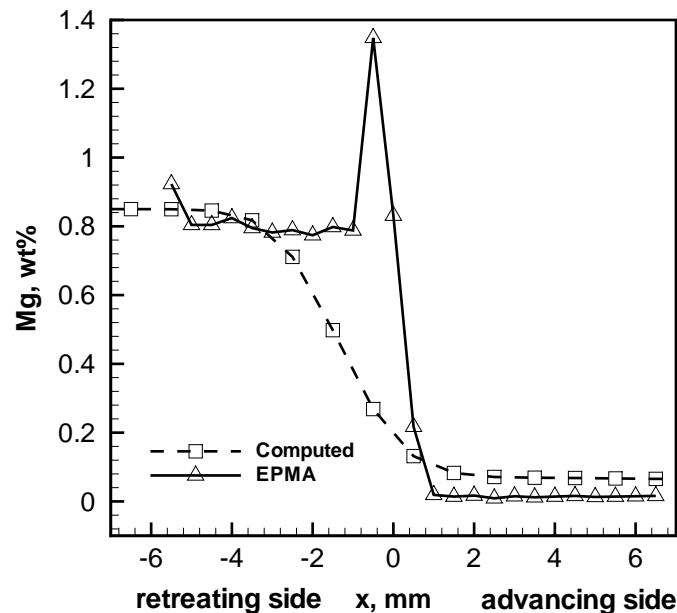


Figure 5.5. Comparison between computed and measured concentration profiles in a transverse weld cross-section of AA 6061 (advancing side) and AA 1200 (retreating) along line 1 mm below the top surface. The rotational speed was 710 RPM and a welding velocity of 1.05 mm/s.

Computed contours of the concentration of Mg near the tool are shown in Figures 5.6 and 5.7 at different depths from the top surface. It is observed from these figures that Mg is drawn towards the direction of rotation of the tool at the

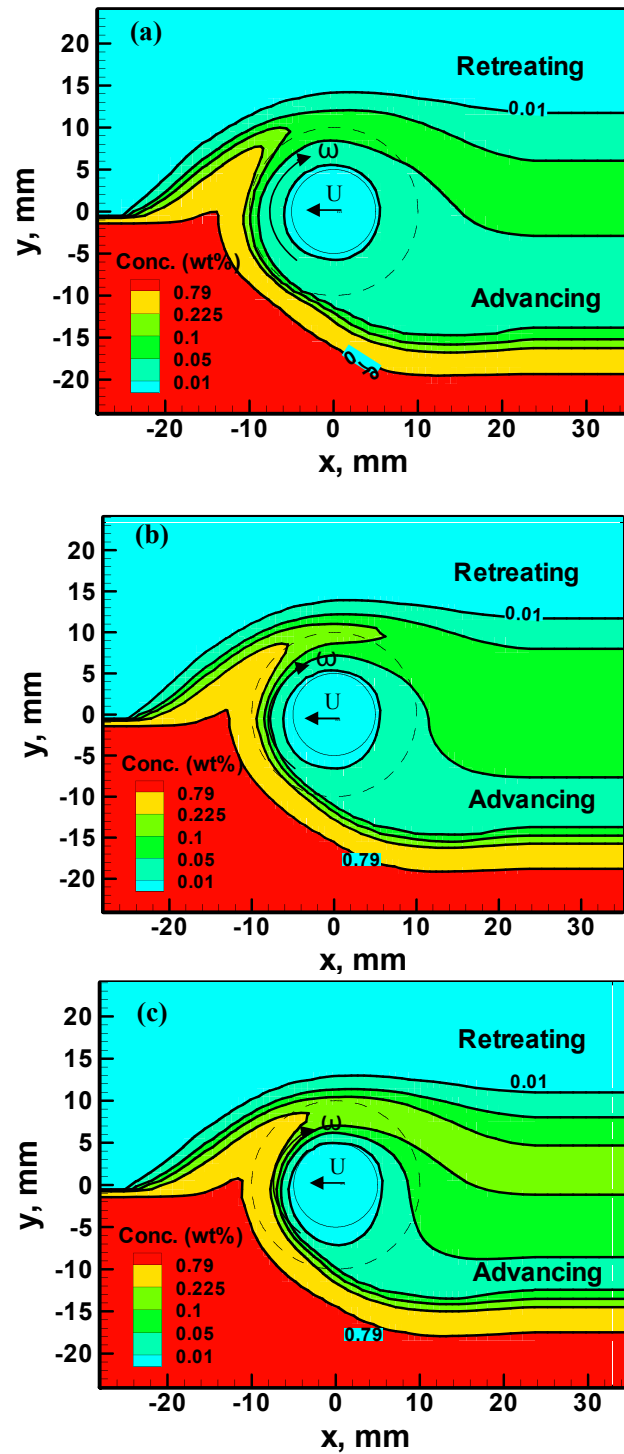


Figure 5.6. Computed concentration profile for magnesium (wt%) near the tool for AA 1200 (retreating) and AA 6061 (advancing side) weld in horizontal planes corresponding to depths of (a) 1, (b) 3 and (c) 5 mm from the top surface. The rotational speed was 710 RPM and a welding velocity of 1.05 mm/s.

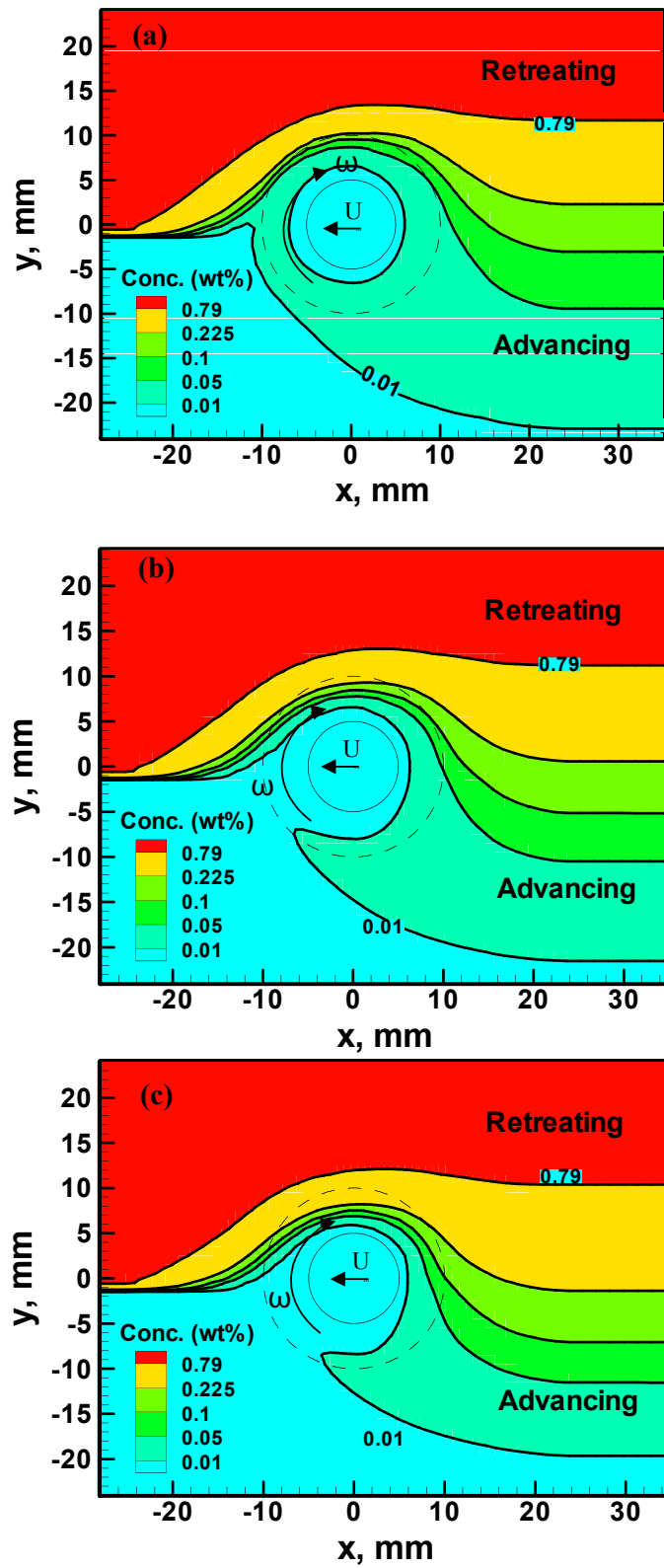


Figure 5.7. (Computed concentration profile for magnesium (wt%) near the tool for AA 1200 (advancing) and AA 6061 (retreating side) weld in horizontal planes corresponding to depths of (a)1, (b) 3 and (c) 5 mm from the top surface. The rotational speed was 710 RPM and the weld velocity was 1.05 mm/s.

leading edge of the tool. Just below the tool shoulder, the plug of material flowing around the tool is larger than that at greater depth. Material is transported from the rear of the tool to the front in the advancing side. Hence the region where plastic flow has occurred becomes depleted in Mg and therefore the front of the tool is rich in Mg. At the middle horizontal plane, the circular plug of material around the tool is small and hence the high concentration region is closer to the tool pin.

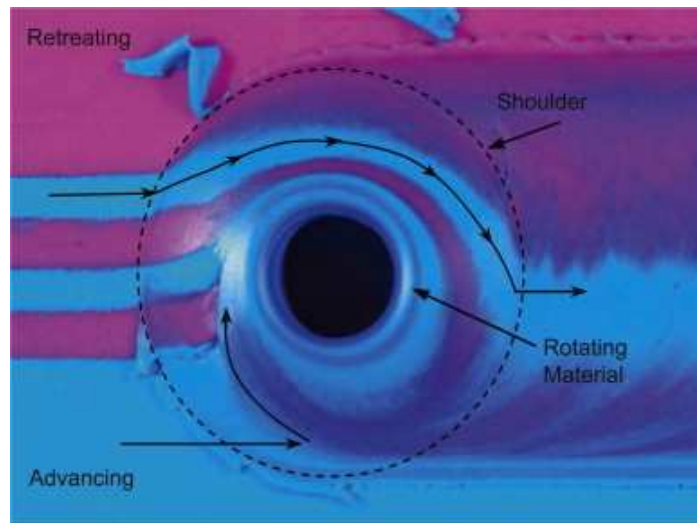


Figure 5.8. Top surface of plasticine welds showing material flow [138].

Liechty *et al.* [138] performed friction stir welding on a workpiece consisting of alternating 2 mm thick vertical layers of light and dark colored plasticine. Figure 5.8 shows the top surface of a stop-action plasticine weld [138]. Far away from the tool pin, there is no deformation. It shows that mixing of material takes place near the pin as it rotates with the tool, indicated by the dark circular region around the pin. Material at the retreating side of the shoulder does not rotate with the tool but simply extrudes past it. The general material flow characteristic matches with that in Fig. 5.7. In the advancing side, material rotates along with the tool pin. This trend is qualitatively similar to the concentration redistribution around the pin shown in Fig. 5.6.

Zettler *et al.* [163] studied Ti-marker flow in FS-welded AA 2024 by using high resolution ($20\mu\text{m}$) computer microtomography. It is a powerful technique

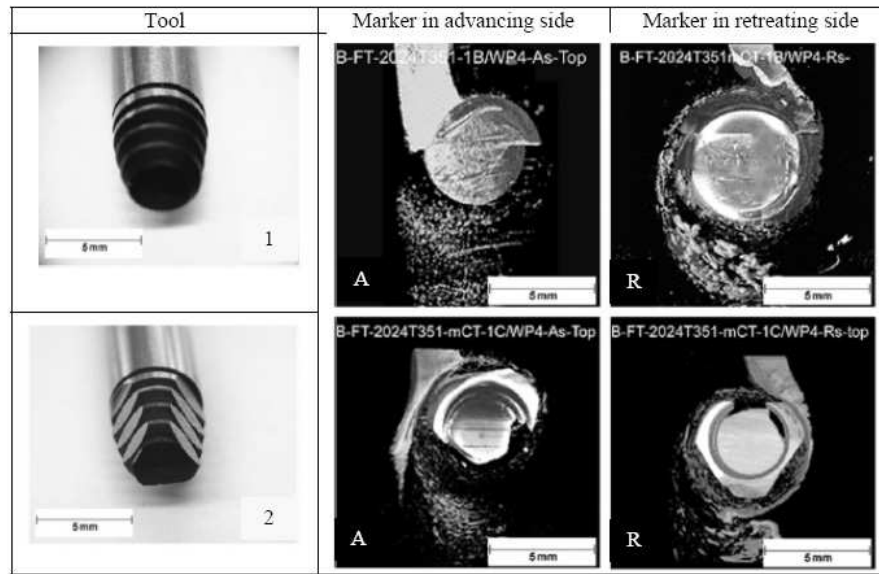


Figure 5.9. Tomographic volume data depicting Ti-marker flow in AA 2024 T351 alloy, with two different tool pins: 1) conical and threaded and 2) conical, threaded with flats. The markers were placed in both A) advancing and R) retreating sides [163].

for the non-destructive 3D investigation of materials using synchrotron radiation. Diffracted X-ray from the material falls on a X-ray camera which converts the X-ray into visible photons. 3D images of the object are reconstructed from a large number of 2D images taken at different angles by reconstruction. The experimental results of Ti-marker flow with two different tool pins: 1) conical and threaded and 2) conical, threaded with flats and for each tool design are given in Fig. 5.9. Two cases with markers placed in (A) advancing and (R) retreating side were studied. The concentration profiles, with Mg on the advancing side (Fig. 5.6), are qualitatively similar to experimental results for Ti-marker shown in Fig. 5.9(A). Both show that the material at the leading edge is sheared in the rotation direction. Figure 5.9(A) and (R) clearly show that the embedded marker material is drawn towards the direction of tool rotation and is deposited behind the pin in the advancing side in both cases (marker on advancing side and marker on retreating side). Zettler *et al.* also observed that the marker placed in the advancing side redistributed as fine particulates, while the marker placed on the retreating side appeared as much larger clumps (compare Fig. 5.9(A) and (R)). The reason for this is not understood.

However, it may also explain why the concentration calculations, with Mg on the retreating side, do not fully agree with the corresponding experimental results as shown in Fig. 5.4.

5.4 Summary and conclusions

Experimental investigation using EPMA and numerical modeling in three dimensional specimens were performed on FS-welded Mg-rich AA 6061 into commercially pure aluminum (AA 1200). Both the experimental and calculated trends show that material at the leading edge is sheared in the rotation direction. Experimental evidence suggests [138] that apart from the circular plug of material, material at the retreating side of the shoulder does not rotate with the tool but simply extrudes past it. This general material flow characteristics can be seen in the streamline plots and correlates well with the concentration fields obtained in the retreating side. In the advancing side, material rotates along with the tool pin [163]. This trend is qualitatively similar to the obtained concentration redistribution around the pin, forming a flow arm around the leading edge of the tool. However, the measured concentration profiles along a line across a transverse cross-section shows a step profile between the two plates indicating incomplete mixing of the dissimilar alloys. Experimentally it is observed that there is an increased amount of movement of the Mg-rich interface from AA 6061 in the advancing side towards AA 1200 in the retreating side with the increase in depth. In contrast, when AA 6061 is on the retreating side, Mg-interface does not move across the weld joint, except very near to the top surface of the specimen. The computed magnesium concentration profile based on its transport by convection and diffusion show the same trend. However, the measured concentration profiles across the weld centerline are more diffused, gradually decreasing from 0.85 wt% Mg in AA 6061 to 0% in AA 1200. The comparison of experimental and computed concentration profiles (Fig. 5.5) showed that continuum hypothesis cannot describe the imperfect mixing of the plasticized alloys during FSW completely.

Concluding Remarks

6.1 Summary and conclusions

Friction stir welding has already been applied in diverse industries, in spite of its short history. At first it was used only to join aluminum alloys. Now, hard materials such as steel and other important engineering alloys can now be welded efficiently using this process. Significant progress has also been made in the fundamental understanding of both the welding process and the structure and properties of the welded joints. The understanding has been useful in expanding the applicability of FSW to new engineering alloys. With better quantitative understanding of the underlying principles of heat transfer, material flow, tool-workpiece contact conditions and effects of various process parameters, efficient tools can be devised and defect free, reliable welds can be obtained based on scientific principles. At the current pace of development, FSW is likely to find widespread use in the future.

Here the aim was to develop a reliable, bi-directional model for heat transfer and plastic flow in similar and dissimilar FSW process. Through synthesis of concepts from diverse disciplines, physics of friction stir welding, real number-based evolutionary algorithm and transport phenomena, a new direction is presented. The special features of the work and the main findings of this investigation are the following:

- Three dimensional temperature and plastic flow fields during friction stir welding are calculated by solving the equations of conservation of mass, mo-

mentum and energy. The spatially variable non-Newtonian viscosity was determined from the computed values of strain rate, temperature and material properties. Temperature dependent thermal conductivity, specific heat and yield strength were considered. The model was tested for four different alloys: 1) AA 6061-T6, 2) 1018 Mn steel, 3) 304L stainless steel and 4) Ti-6Al-4V. The computed results show that significant plastic flow occurs near the tool, where convective heat transfer is the main mechanism of heat transfer. The computed stream trace in the horizontal planes around the tool pin showed the presence of nearly circular closed streamlines indicating the presence of a plug of material. The region of this recirculating flow expands with elevation because of proximity to the relatively larger rotating shoulder. The stream traces also showed that the material flow occurred mainly on the retreating side. The cut-off viscosity above which no significant material flow occurs could be used to determine the shape of thermo-mechanically affected zone for AA 6061 alloys.

- Strain rates depend on the tool geometry, rotational speed and boundary condition for stick-slip at the tool workpiece interface. Maximum strain rate up to 250 s^{-1} were observed in AA 6061 aluminum alloys. This is consistent with reported values of 350 s^{-1} in literature [148] for aluminum alloy welded at different rotational speeds (400-600 rpm) and translational speeds (0.847-2.540 mm/s). Lower values were observed in other alloys which were welded using tool having 2.5 times smaller shoulder diameter.
- Asymmetry in heat transfer and material flow across the weld centerline can be predicted as observed experimentally. The advancing side temperatures are higher, particularly in alloys which have lower thermal conductivity (higher Peclet number), because of greater convective transfer resulting from higher relative velocities in the advancing side compared to the retreating side. The temperature profiles are more or less symmetric about the weld-centerline in aluminum alloys but pronounced asymmetry is observed for other alloys.
- Cooling rates were lower for FSW in comparison to fusion welding. For example, for AA 6061 cooling rate of 5 K/s was obtained in the temperature

range of 700 to 500 K. The relatively low cooling rate is consistent with fairly high energy input per unit length.

- The numerical model embodying the equations of conservation of mass, momentum and energy was used to examine the sensitivity of five important parameters which are friction coefficient, the extent of slip between the tool and the workpiece, the heat transfer coefficient at the bottom of the workpiece, the mechanical efficiency and the scaling factor for viscous dissipation on the computed temperature fields and torque on the tool. These parameters, which cannot be prescribed either from the welding conditions or from fundamental principles, were found to significantly affect both the temperature fields and the torque on the tool. Decrease in slip lowers the temperatures and increases cooling rate because heat input is lowered. As the heat transfer coefficient increases the temperature, the width of the thermal cycle and torque on tool decreases in all cases. Higher values of mechanical efficiency and scaling factor for plastic deformation heating result in intense heating which in turn leads to higher temperatures and softer material, resulting in lower torque for all systems. Torque on the tool may decrease or increase with friction coefficient depending on the material system and range of welding variables.
- When the values of the uncertain parameters were optimized using a small volume of experimental data, the computed peak temperature, thermal cycle and the torque on the tool agreed very well with the corresponding experimental data. This approach was tested for titanium and aluminum alloys and a C-Mn steel.
- In all cases, the extent of slip between the tool and the workpiece obtained by optimization procedure is small indicating close to sticking condition, even at the outer periphery of the tool shoulder. Previous research [31] suggests that the interfacial condition is close to sticking in AA 2024. The mechanical efficiency, bottom heat transfer coefficient and friction coefficient values obtained are in a physically viable range available in literature.
- The optimized extent of scaling factor for plastic deformation heat generation

away from the tool workpiece interface is small in all four alloys consistent with the fact that plastic deformational heat generation rate reported in literature is a small fraction of the total heat generation rate (less than 5%) [44].

- The torque values and the interfacial heat generation rates were computed from shear stress for all the alloys. Therefore, the close agreement between the experimentally measured and the calculated thermal cycles and torque values indicates that the computed shear stress at the tool-workpiece interface is accurate and the optimization of uncertain parameters provide reliable computed results.
- An important difficulty in tailoring weld attributes based on fundamental scientific principles is that the existing process models are unidirectional in the sense that they require, as input, welding parameters, thermophysical properties, tool and work-piece geometry and provide, as output, the temperature and velocity fields and the cooling rates at various locations. A bi-directional model was obtained by combining the transport phenomena model with Differential Evolution. This was used to predict welding process variables like welding speed and tool rotational speed, necessary to obtain the desired weld attribute. The set of welding variables obtained varied over a large range offering flexibility to choose the welding variables based on experimental constraints. It is shown that agreement between the model predictions and experimentally measured thermal cycles can be obtained, indicating the usefulness of this approach for practical purposes.
- The transport and mixing of magnesium from Mg-rich AA 6061 alloy into very low Mg containing AA 1200 were examined both experimentally by EPMA and numerically in the entire volume of the three dimensional specimens. The EPMA measurements showed that transport of magnesium from Mg-rich side to AA 1200 is through bulk movement of alloy and diffusive transport is limited. The spatial variation of concentration distribution showed a step profile between the two plates. The computed magnesium concentration profile based on its transport by convection and diffusion showed a gradual decrease from 0.85% Mg in AA 6061 to 0% Mg in AA 1200. The

comparison of the experimental and computed concentration profiles showed imperfect mixing of the plasticized alloys during FSW where the materials seem to move in layers without significant diffusion.

To summarize, a practically useful model for heat transfer and plastic flow in FSW was developed with an aim to expand the quantitative knowledge base for the relatively new welding process.

6.2 Future Work

Several important key problems and issues remain to be addressed. First, there is a need to combine fundamental knowledge of the FSW process and the knowledge of the evolution of the structure and properties to build intelligent process control models with a goal to achieve, defect free, structurally sound and reliable welds. Ability to predict defects numerically based on welding parameters will be an important tool in the hands of welders.

Tailoring weld structure and properties based on scientific principles still remains an important milestone in FSW. Attainment of this important goal would require new, more reliable and efficient process sub-models and reliable sub-models to describe the evolution of structure and properties of the welded joints. Here it was shown that welding variables like welding velocity and tool rotational speed could be determined to obtain a desired thermal cycle. Similarly, if there is a model for calculation of hardness based on welding variables, inverse modeling could be done to obtain the welding parameters required for a specific hardness profile.

To model hardness in age hardenable aluminum alloys after friction stir welding has been performed, precipitate dissolution and reappearance must be calculated based on thermal cycles. The age hardenable Al-Mg-Si alloys have high tensile strength in the artificially aged condition (T6) due to the presence of β'' precipitates along the $\langle 100 \rangle$ directions in the aluminum matrix. However, they suffer from severe softening in the HAZ due to the dissolution of the β'' phase. This reduces the load-bearing ability of the joint. The accurate calculation of thermal cycles is very important for microstructural modeling as thermal cycle governs the dissolution of the beta phase.

The volume fraction of β'' particles decreases as they dissolve during the weld thermal cycle. On aging, the fraction of β'' hardening precipitates which form depends on the remnant solute present after the weld thermal cycle. Also, the precipitation kinetics of the non-hardening β' particles must be taken into account to determine the volume fraction of β'' particles [164].

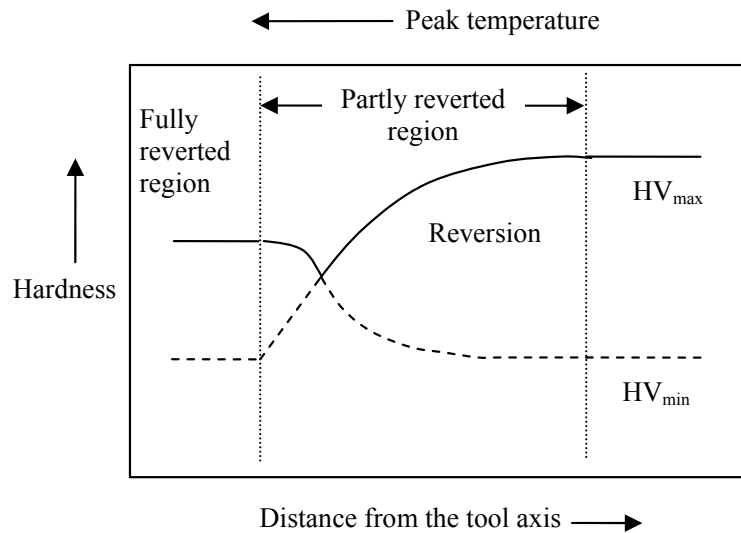


Figure 6.1. A schematic diagram showing dissolution and re-precipitation in age-hardenable aluminum alloys. HV denotes the Vickers hardness number [164].

Strengthening mechanisms operative in an age-hardening aluminum alloy are hardening due to shearing of particles by dislocations (σ_p) and solid solution hardening (σ_{ss}). The strength in the HAZ after welding and subsequent aging can be calculated based on the volume fraction of the precipitates while The strength in the partly reverted region depends on the interplay between two competing processes of dissolution and re-precipitation as shown in Fig. 6.1.

The model can be validated by measuring the volume fraction of the β'' particles using SEM and optical microscopy. Svensson *et al.* [165] reported the use of these techniques for AA 5083 and AA 6082 alloys. Also, Vicker's hardness test can be performed on the cross-sections of the weld zone in both parallel and perpendicular directions to weld direction.

Another interesting problem would be modeling of sub-grain size in the thermo-mechanically affected zone. The sub-grain size can be related to temperature and

strain-rate, or the temperature compensated strain-rate, Zener–Hollomon parameter during steady state deformation [166]:

$$\delta_s^{-m} = A' + B' \ln Z$$

where δ_s is the subgrain-size and A', B' and m are constants. Comparison between experimentally measured and computed grain-sizes will provide closure for the calculation of strain-rate and temperature values in the TMAZ.

Numerical solution of governing equations for heat transfer and plastic flow

Before discretizing the governing equations, the three equations of conservation of momentum and the energy conservation equation are rewritten in the following general form [139]:

$$\frac{\partial \rho u_i \phi_j}{\partial x_i} = \frac{\partial}{\partial x_i} \left(\Gamma \frac{\partial \phi_j}{\partial x_i} \right) + S_j \quad (\text{A.1})$$

where, ϕ is the general dependent variable, Γ is the diffusion coefficient which is equal to viscosity in momentum conservation equation and is equal to thermal conductivity in energy conservation equation, and S is the source term. The indices i or $j = 1, 2$, and 3 represent the x, y and z directions respectively. Thus the governing momentum equations may be modified into the general form:

$$\frac{\partial \rho u_i u_j}{\partial x_i} = \frac{\partial}{\partial x_i} \left(\mu \frac{\partial u_j}{\partial x_i} \right) + S_{u_j} \quad (\text{A.2})$$

where the source term for the momentum equations can be given as:

$$S_{u_j} = -\frac{\partial P}{\partial x_i} + \frac{\partial}{\partial x_i} \left(\mu \frac{\partial u_i}{\partial x_j} \right) - \rho U \frac{\partial u_j}{\partial x_1} \quad (\text{A.3})$$

where P is the pressure, u_i is the velocity in i -direction, μ is the viscosity and U is the welding velocity. Similarly, the energy equation may be rewritten as:

$$\rho C_p \frac{\partial(u_i T)}{\partial x_i} = \frac{\partial}{\partial x_i} \left(k \frac{\partial T}{\partial x_i} \right) + S_T \quad (\text{A.4})$$

where T is the temperature, k is the thermal conductivity and S_T is the source term which includes contribution from any body heat source (S_b) and source term due to welding velocity occurring because we solve in Eulerian frame of reference attached to the workpiece.

$$S_T = S_b - \rho C_p U \frac{\partial T}{\partial x_1} \quad (\text{A.5})$$

The governing equations are discretized using a control volume method, where the workpiece is divided into small rectangular control volumes. Each control volume surrounds a grid point where the scalar variables are stored. Vectors such as the velocities are stored at grid points which are staggered with respect to those of scalar variables like pressure and temperature to ensure the stability of numerical calculation. Thus, the control volumes for scalars are different from those for the vectors. The discretized equations are formulated by integrating the corresponding governing equation over the control volumes using fully implicit hybrid power law scheme. The final discretized form of the Equation A.1 takes the following form [139]:

$$a_P \phi_P = \sum_{nb} a_{nb} \phi_{nb} + S_U \Delta V \quad (\text{A.6})$$

where, ϕ represents a general variable such as velocity or temperature, a represents the coefficient of the variables calculated based on the power law scheme, subscript nb represents the neighbors of a the grid point P, ΔV is the volume of the control volume. The coefficient of ϕ at the point P is defined in terms of neighboring grid points as follows [139]:

$$a_P = \sum_{nb} a_{nb} + S_P \Delta V \quad (\text{A.7})$$

The source term for both temperature and velocity can be a function of the de-

pendent variable itself. A linear dependence is assumed [139]:

$$S = S_U + S_P \phi_P \quad (\text{A.8})$$

where S_U stands for constant part and S_P is the coefficient of ϕ_P .

For the implementation of fixed velocity boundary conditions at the tool pin surface, equation A.6 is modified by assigning a large negative value to S_P , and S_P times u_f (*i.e.* fixed velocity at the interface) to S_U such that the first term on the right hand side become negligible yielding $\phi_P = u_f$. The implementation of heat flux at the top shoulder-workpiece interface also needs some discussion. The boundary condition is given by:

$$k \frac{\partial T}{\partial z} \Big|_{z=z_{max}} = q(x, y) \quad (\text{A.9})$$

where $q(x, y)$ is the portion of the heat generated at the tool shoulder which enters the workpiece. Integrating this equation over the top most boundary control volume, the temperatures at the top most z-grids, nk , may be related to the temperature at the grid points at $nk - 1$ as:

$$T_{i,j,nk} = T_{i,j,nk-1} + \frac{q(x, y)}{k_{i,j,nk}} \Delta z \quad (\text{A.10})$$

where $k_{i,j,nk}$ represent the spatially variable thermal conductivity values at the top most z-grids. Finally the equations at $(nk - 1)$ grid points can be obtained by combining equations A.8 and A.10 as follows:

$$S_U = S_U + a_T \left[\frac{q(x, y)}{k_{i,j,nk}} \Delta z \right] / \Delta V \quad (\text{A.11})$$

The temperature boundary condition at the bottom surface is given by:

$$k \frac{\partial T}{\partial z} \Big|_{z=0} = h_b(T - T_a) \quad (\text{A.12})$$

where h_b is the bottom heat transfer and T_a is the ambient temperature. Integrating the equation over bottom control volume ($k = 1$), the enthalpy may be

expressed in terms of the grid point values at $k = 2$

$$T_{i,j,1} = \frac{\frac{k_1}{\Delta z} T_{i,j,2} + h_b T_a}{\frac{k_1}{\Delta z} + h_b} = C_1 T_{i,j,2} + C_2 \quad (\text{A.13})$$

where,

$$C_1 = \frac{\frac{k_1}{\Delta z}}{\frac{k_1}{\Delta z} + h_b} \quad \text{and} \quad C_2 = \frac{h_b T_a}{\frac{k_1}{\Delta z} + h_b} \quad (\text{A.14})$$

Finally, the equations at grid points for $k = 2$, may be obtained by combining Equations A.8 and A.13 we obtain:

$$S_U = S_U + C_2/\Delta V \quad \text{and} \quad S_P = S_P + C_1 a_B/\Delta V \quad (\text{A.15})$$

Two criteria were used to test for convergence; magnitude of residuals of enthalpy and three velocities, and the overall heat balance. The residual for any variable ϕ is defined as:

$$R = \frac{\sum_{domain} \left| \frac{\sum_{nb} a_{nb} \phi_{nb} + S_U \Delta V}{a_P} - \phi_P \right|}{\sum_{domain} |\phi_P|} \quad (\text{A.16})$$

Values of R less than 5.0×10^{-5} were accepted as converged solution. Heat balance ratio is given by:

$$\theta = \frac{\text{net heat input}}{\text{total heat out} + \text{accumulation}} \quad (\text{A.17})$$

The heat balance ratio $0.95 \leq \theta \leq 1.05$ was accepted as converged solution.

Calculation of heat generated at the pin's vertical surface

Since the tool is circular but the grids are rectangular, and heat generated being proportional to the area, it is important to calculate the arc length, *i. e.*, arc intercepted by the control volume, to accurately determine the heat generated within a control volume. If we calculate arc length in one quadrant, we need not calculate it for other three quadrants. Hence we consider the first quadrant only. To calculate the arc length, we note that either sine or cosine of the arc angle has the form $\frac{k \Delta x}{R}$ or $\frac{m \Delta y}{R}$ respectively, where k and m are integers. The value of the k and m can be uniquely determined for a given intercept point. We calculate $\sin^{-1}\left(\frac{k \Delta x}{R}\right)$ and $\cos^{-1}\left(\frac{m \Delta y}{R}\right)$ for the k and m values corresponding to the intercept point, and the smaller of the two gives the arc angle. From the arc angle, the arc length can be easily calculated.

For example, for the above figure, we calculate the angles as a follows. For point 1, corresponding to angle θ_1 , $kkk = 1$, $jj = 2$

$$\begin{aligned}\sin \theta_1 &= \frac{\Delta x}{R} \Rightarrow \theta_{1s} = \sin^{-1}\left(\frac{\Delta x}{R}\right) \\ \cos \theta_1 &= \frac{\Delta y}{R} \Rightarrow \theta_{1c} = \cos^{-1}\left(\frac{\Delta y}{R}\right) \\ \theta_{1s} &< \theta_{1c} \Rightarrow \theta_{1s} = \theta_{1s}\end{aligned}$$

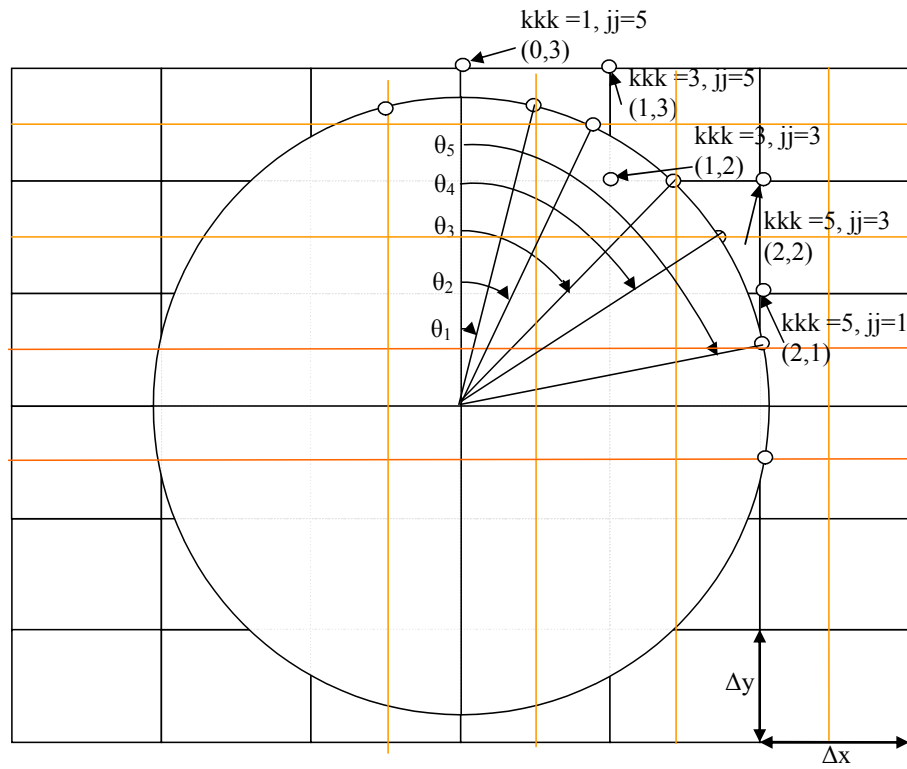


Figure B.1. Calculation of intercepted arc length for rectangular grids.

$$\text{arc length} = R \theta_1 = R \sin^{-1} \left(\frac{\Delta x}{R} \right)$$

Similarly, we calculate other arc angles

$$\cos \theta_2 = \frac{2\Delta y}{R} \Rightarrow \text{arc length} = R(\theta_2 - \theta_1)$$

$$\cos \theta_3 = \frac{\Delta y}{R} \Rightarrow \text{arc length} = R(\theta_3 - \theta_2)$$

$$\sin \theta_4 = \frac{2\Delta x}{R} \Rightarrow \text{arc length} = R(\theta_4 - \theta_3)$$

$$\cos \theta_5 = \frac{0\Delta y}{R} \Rightarrow \text{arc length} = R(\theta_5 - \theta_4)$$

Table B.1. Arc angles calculated for Fig. B.1 ($R = 2.0$, $\Delta x = 0.97$, $\Delta y = 0.726666$).

\sin^{-1} (radian)	\cos^{-1} (radian)	θ (radian)	$\Delta\theta$ (degree)
0.5063632	0.7573389	0.5063632	29.01247
1.325231	0.7573389	0.7573389	14.37985
1.325231	1.198953	1.198953	25.30262
1.325231	1.570796	1.325231	7.235192
1.570796	1.570796	1.570796	14.06986

Bibliography

- [1] THOMAS, W. M. and R. E. DOLBY (2003) “Friction Stir Welding Developments,” in *6th Int. Trends in Welding Research* (S. A. David, T. DebRoy, J. C. Lippold, H. B. Smartt, and J. M. Vitek, eds.), ASM International, Materials Park, Ohio, USA, pp. 203–211.
- [2] THOMAS, W. M., E. D. NICHOLAS, J. C. NEEDHAM, M. G. MURCH, P. TEMPLE-SMITH, and C. J. DAWES (1991), “Friction Stir Butt welding,” International Patent Application no. PCT/GB92/02203.
- [3] THOMAS, W. M. and E. D. NICHOLAS (1997) “Friction stir welding for the transportation industries,” *Materials & Design*, **18**, pp. 269–273.
- [4] CHO, J. H., D. E. BOYCE, and P. R. DAWSON (2005) “Modeling strain hardening and texture evolution in friction stir welding of stainless steel,” *Materials Science and Engineering A*, **398**, pp. 146–163.
- [5] LIU, H., H. FULII, M. MAEDA, and K. NOGI (2003) “Tensile properties and fracture locations of friction–stir welded joints of 6061–T6 aluminium alloy,” *Journal of Materials Science Letters*, **22**, pp. 1061–1063.
- [6] LEE, W. B., C. Y. LEE, W. S. CHANG, Y. M. YEON, and S. B. JUNG (2005) “Microstructural investigation of friction stir welded pure titanium,” *Materials Letters*, **59**, pp. 3315–3318.
- [7] JATA, K. V. and S. L. SEMIATIN (2000) “Continuous dynamic recrystallization during friction stir welding,” *Scripta Materialia*, **43**, pp. 743–748.
- [8] MASAKI, K., Y. S. SATO, M. MAEDA, and H. KOKAWA (2008) “Experimental simulation of recrystallized microstructure in friction stir welded Al alloy using a plane-strain compression test,” *Scripta Materialia*, **58**, pp. 355–360.

- [9] ULYSSE, P. (2002) “Three-dimensional modeling of the friction stir-welding process,” *Journal of Machine Tools & Manufacture*, **42**, pp. 1549–1557.
- [10] COLEGROVE, P. A. and H. R. SHERCLIFF (2004) “Development of Trivex friction stir welding tool Part 2 – three-dimensional flow modelling,” *Science and Technology of Welding*, **9**, pp. 352–361.
- [11] MISHRA, S. and T. DEBROY (2005) “A heat transfer and fluid flow based model to obtain a specific weld geometry using various combinations of welding variables,” *Journal of Applied Physics*, **98** (4), p. article number 044902.
- [12] RAI, R. and T. DEBROY (2006) “Tailoring weld geometry during keyhole mode laser welding using a genetic algorithm and a heat transfer model,” *Journal of Physics D – Applied Physics*, **39**, pp. 1257–1266.
- [13] KUMAR, A. and T. DEBROY (2004) “Guaranteed fillet weld geometry from heat transfer model and multivariable optimization,” *International Journal of Heat and Mass Transfer*, **47** (26), pp. 5793–5806.
- [14] BEVER, M. B., D. L. HOLT, and A. TITCHENER (1973) “Stored energy of cold work,” *Progress in Materials Science*, **17**, pp. 5–192.
- [15] ZHU, Q., C. M. SELLARS, and H. K. D. H. BHADOSHIA (2006) “Quantitative Metallography of Deformed Grains,” *Submitted to Materials Science and Technology*.
- [16] BELOUS, M. V. and V. T. CHEREPIN (1962) “Changes in the Steel Carbide Phase under Influence of Cold Plastic Deformation,” *Fiz. Met. Metalloved.*, **14**, pp. 48–54.
- [17] DANOIX, F., D. JULIEN, X. SAUVAGE, and J. COPREAUX (1998) “Direct evidence of cementite dissolution in drawn pearlitic steels observed by tomographic atom probe,” *Materials Science & Engineering A*, **250**, pp. 8–13.
- [18] UMEMOTO, M., Z. G. LIU, X. J. HAO, K. MASUYAMA, and K. TSUCHIYA (2001) “Formation of nanocrystalline ferrite through rolling and ball milling,” *Materials Science Forum*, **360-362**, pp. 167–174.
- [19] IVANISENKO, Y., I. MACLAREN, R. Z. VALIEV, and H. J. FECHT (2005) “First observation of a shear-induced bcc to fcc transformation in nanocrystalline ferrite,” *Advanced Engineering Materials*, **7**, pp. 1011–1014.
- [20] LOJKOWSKI, W., Y. IVANISENKO, and H.-J. FECHT (2005) “Strain induced cementite dissolution in pearlitic steels as a classical example of mechanical alloying,” *Trans. Indian Institute of Metals*, **58**, pp. 939–1227.

- [21] GORKUNOV, E. S., S. V. GRACHEV, S. V. SMIRNOV, V. M. SOMOVA, S. M. ZADVORKIN, and L. E. KAR'KINA (2005) "Relation of Physical-Mechanical Properties to the Structural Condition of Severely Deformed Patented Carbon Steels at Drawing," *Russian Journal of Nondestructive Testing*, **41**, pp. 65–79.
- [22] MCCLURE, J. C., W. TANG, L. E. MURR, X. GUO, Z. FENG, and J. E. GOULD (1998) "A thermal model for friction stir welding," in *Trends in Welding Research* (J. M. Vitek, S. A. David, J. A. Johnson, H. B. Smartt, and T. DebRoy, eds.), ASM International, Ohio, USA, pp. 590–595.
- [23] RUSSELL, M. J. and H. SHERCLIFF (1999) "Analytical modelling of friction stir welding," in *Analytical modelling of friction stir welding Russell, M J; Shercliff, R Inalco '98: Seventh International Conference on Joints in Aluminium*, TWI, TWI, Cambridge, U. K., pp. 197–207.
- [24] FENG, Z., J. E. GOULD, and T. J. LIENERT (1998) "A heat flow model for friction stir welding of steel," in *Hot deformation of aluminium alloys* (T. R. Bieler, ed.), TMS–AIME, Warrendale, Pennsylvania, USA, pp. 149–158.
- [25] SONG, M. and R. KOVACEVIC (2003) "Thermal modeling of friction stir welding in a moving coordinate system and its validation," *International Journal of Machine Tools & Manufacture*, **43**, pp. 605–615.
- [26] SONG, M. and R. KOVACEVIC (2003) "Numerical and experimental study of the heat transfer process in friction stir welding," *Journal of Engineering Manufacture*, **217**, pp. 73–85.
- [27] SONG, M. and R. KOVACEVIC (2004) "Heat transfer modelling for both workpiece and tool in the friction stir welding process: a coupled model," *Proceedings of the Institution of Mechanical Engineers Part B: Journal of Engineering Manufacture*, **218**, pp. 17–33.
- [28] ZHANG, H. W., Z. ZHANG, and J. T. CHEN (2005) "Effect of angular velocity of pin on material flow during friction stir welding," *Acta Metallurgica Sinica*, **41**, pp. 853–859.
- [29] ZHANG, H. W., Z. ZHANG, and J. T. CHEN (2005) "Finite element simulation of the friction stir welding process," *Materials Science and Engineering A*, **403**, pp. 340–348.
- [30] CHEN, C. M. and R. KOVACEVIC (2003) "Finite element modeling of friction stir welding - thermal and thermomechanical analysis," *International Journal of Machine Tools & Manufacture*, **43**, pp. 1319–1326.

- [31] SCHMIDT, H., J. HATTEL, and J. WERT (2004) “An analytical model for the heat generation in friction stir welding,” *Modelling and Simulation in Materials Science and Engineering*, **12**, pp. 143–157.
- [32] SCHMIDT, H. and J. HATTEL (2004) “Heat source models in simulation of heat flow in friction stir welding,” *International Journal of Offshore and Polar Engineering*, **14**, pp. 296–304.
- [33] SCHMIDT, H. and J. HATTEL (2005) “Modelling heat flow around tool probe in friction stir welding,” *Science and Technology of Welding and Joining*, **10**, pp. 176–186.
- [34] SCHMIDT, H. and J. HATTEL (2005) “A local model for the thermomechanical conditions in friction stir welding,” *Modelling and Simulation in Materials Science and Engineering*, **13**, pp. 77–93.
- [35] KHANDKAR, M. Z. H. and J. A. KHAN (2001) “Thermal modeling of overlap Friction Stir Welding for Al-alloys,” *Journal of Materials Processing and Manufacturing Science*, **10**, pp. 91–105.
- [36] KHANDKAR, M. Z. H., J. A. KHAN, and A. P. REYNOLDS (2003) “Prediction of temperature distribution and thermal history during friction stir welding: input torque based model,” *Science and Technology of Welding and Joining*, **8**, pp. 165–174.
- [37] NANDAN, R., G. G. ROY, and T. DEBROY (2006) “Numerical simulation of three-dimensional heat transfer and plastic flow during friction stir welding,” *Metallurgical & Materials Transactions A*, **37A**, pp. 1247–1259.
- [38] NANDAN, R., G. G. ROY, T. J. LIENERT, and T. DEBROY (2006) “Numerical modelling of 3D plastic flow and heat transfer during friction stir welding of stainless steel,” *Science and Technology of Welding and Joining*, **11**, pp. 526–537.
- [39] NANDAN, R., G. G. ROY, T. J. LIENERT, and T. DEBROY (2007) “Three-dimensional heat and material flow during friction stir welding of mild steel,” *Acta Materialia*, **55**, pp. 883–895.
- [40] ROSAKIS, P., A. J. ROSAKIS, G. RAVICHANDRAN, and J. HODOWANY (2000) “A thermodynamic internal variable model for the partition of plastic work into heat and stored energy in metals,” *Journal of the Mechanics and Physics of Solids*, **48**, pp. 581–607.
- [41] KONG, H. S. and M. F. ASHBY (1991) “Friction-Heating Maps and Their Applications,” *MRS Bulletin*, **16**, pp. 41–48.

- [42] HODOWANY, J., G. RAVICHANDRAN, A. J. ROSAKIS, and P. ROSAKIS (2000) "Partition of plastic work into heat and stored energy in metals," *Experimental mechanics*, **40**(2), pp. 113-123, 0014-4851.
- [43] SIMAR, A., J. LECOMTE-BECKERS, T. PARDOEN, and B. DE MEESTER (2006) "Effect of boundary conditions and heat source distribution on temperature distribution in friction stir welding," *Science and Technology of Welding and Joining*, **11**, pp. 170-177.
- [44] BASTIER, A., M. H. MAITOURNAM, K. VAN DANG, and F. ROGER (2006) "Steady state thermomechanical modelling of friction stir welding," *Science and Technology of Welding and Joining*, **11**, pp. 278-288.
- [45] LIENERT, T. J., J. W. L. STELLWAG, B. B. GRIMMETT, and R. W. WARKE (2003) "Friction Stir Welding Studies on Mild Steel," *Welding Journal, Research Supplement*, **82**, pp. 1s-9s.
- [46] DENG, Z., M. R. LOVELL, and K. A. TAGAVI (2001) "Influence of material properties and forming velocity on the interfacial slip characteristics of cross wedge rolling," *Manufacturing Science and Engineering*, **123**, pp. 647-653.
- [47] KHAN, J. A., L. XU, and Y. J. CHAO (1999) "Prediction of nugget development during resistance spot welding using coupled thermal-electrical-mechanical model," *Science and Technology of Welding and Joining*, **4**, pp. 201-207.
- [48] XU, S., X. DENG, A. P. REYNOLDS, and T. U. SEIDEL (2001) "Finite element simulation of material flow in friction stir welding," *Science and Technology of Welding and Joining*, **6**, pp. 191-193.
- [49] ZIENKIEWICZ, O. C. and I. C. CORMEAU (1972) "Visco-Plasticity Solution by Finite-Element Process," *Archives of Mechanics*, **24**, pp. 872-889.
- [50] SELLARS, C. M. and W. J. MCTEGART (1966) "On the mechanism of hot deformation," *Acta Metallurgica*, **14**, pp. 1136-1138.
- [51] SHEPPARD, T. and D. S. WRIGHT (1979) "Determination of Flow-Stress .1. Constitutive Equation for Aluminum-Alloys at Elevated-Temperatures," *Metals Technology*, **6**, pp. 215-223.
- [52] WRIGHT, D. S. and T. SHEPPARD (1979) "Determination of Flow-Stress .2. Radial and Axial Temperature Distribution during Torsion Testin," *Metals Technology*, **6**, pp. 224-229.
- [53] ZENER, C. and J. H. HOLLOMON (1944) "Effect of Strain Rate Upon Plastic Flow of Steel," *Journal of Applied Physics*, **15**, pp. 22-32.

- [54] SHEPPARD, T. and A. JACKSON (1997) “Constitutive equations for use in prediction of flow stress during extrusion of aluminium alloys,” *Materials Science and Technology*, **13**, pp. 203–209.
- [55] BRUSCHI, S., S. POGGIO, F. QUADRINI, and M. E. TATA (2004) “Weldability of Ti–6Al–4V alloy at high temperatures and strain rates,” *Materials Letters*, **58**, pp. 3622–3629.
- [56] HART, E. (1976) “Constitutive relations for the nonelastic deformation of metals,” *Journal of Engineering Materials and Technology*, **98**, pp. 193–202.
- [57] FISHER, E. S. (1966) “Temperature Dependence of Elastic Moduli in Alpha Uranium Single Crystals,” *Journal of Nuclear Materials*, **18**, pp. 39–54.
- [58] DONG, P., F. LU, J. K. HONG, and Z. CAO (2001) “Coupled thermomechanical analysis of friction stir welding process using simplified models,” *Science and Technology of Welding and Joining*, **6**, pp. 281–287.
- [59] HEURTIER, P., M. JONES, C. DESRAYAUD, J. H. DRIVER, F. MONTHEILLET, and D. ALLEHAUX (2006) “Mechanical and thermal modelling of Friction Stir Welding,” *Journal of Materials Processing Technology*, **171**, pp. 348–357.
- [60] DAVIS, J. R. (1990) *ASM Handbook: Nonferrous Alloys and Special-Purpose Material*, vol. 2, ASM International, Ohio, USA.
- [61] LONG, X. and S. K. KHANNA (2005) “Modelling of electrically enhanced friction stir welding process using finite element method,” *Science and Technology of Welding and Joining*, **10**, pp. 482–487.
- [62] BRANDES, E. A. and G. B. BROOL (1999) *Smithells Metals Reference Book*, 7th ed., Butterworth–Heinemann.
- [63] BOYER, R., G. WELSCH, and E. W. C. (EDITORS) (1994) *Materials Properties Handbook: Titanium Alloys*, ASM International, Materials Park, Ohio, USA.
- [64] CHAO, Y. J., X. QI, and W. TANG (2003) “Heat transfer in friction stir welding - Experimental and numerical studies,” *Journal of Manufacturing Science and Engineering*, **125**, pp. 138–145.
- [65] “Thermophysical properties of tungsten: <http://aries.ucsd.edu/LIB/PROPS/PANOS/w.html>,” .
- [66] BUFFA, G., J. HUA, R. SHIVPURI, and L. FRATINI (2006) “Design of the friction stir welding tool using the continuum based FEM model,” *Materials Science & Engineering A*, **419**, pp. 381–388.

- [67] ASKARI, A., S. SILLING, B. LONDON, and M. MAHONEY (2004) “Modelling, analysis and validation of friction stir welding and processing,” *Journal of Metals*, **56**, pp. 245–246.
- [68] BELL, R. L. (2005) “An Isotropic Material Remap Scheme for Eulerian Codes,” in *2nd International Conference on Cybernetics and Information Technologies, Systems and Applications (CITSA 2005)*.
- [69] BOYCE, D. E., P. R. DAWSON, B. SIDLE, and T. GNÄUPEL-HEROLD (2006) “A multiscale methodology for deformation modeling applied to friction stir welded steel,” *Computational Materials Science*, **38**, pp. 158–175.
- [70] COLEGROVE, P. A. and H. R. SHERCLIFF (2005) “3-Dimensional CFD modelling of flow round a threaded friction stir welding tool profile,” *Journal of Materials Processing Technology*, **169**, pp. 320–327.
- [71] SEIDEL, T. U. and A. P. REYNOLDS (2003) “Two-dimensional friction stir welding process model based on fluid mechanics,” *Science and Technology of Welding and Joining*, **8**, pp. 175–183.
- [72] COLEGROVE, P. A. and H. R. SHERCLIFF (2004) “Two-dimensional CFD modelling of flow round profiled FSW tooling,” *Science and Technology of Welding and Joining*, **9**, pp. 483–492.
- [73] FRIGAARD, O., O. GRONG, and O. T. MIDLING (2001) “A process model for friction stir welding of age hardening aluminium alloys,” *Metallurgical & Materials Transactions A*, **32**, pp. 1189–1200.
- [74] SCHMIDT, H., T. L. DICKERSON, and J. HATTEL (2006) “Material flow in butt friction stir welds in AA2024-T3,” *Acta Materialia*, **54**, pp. 1199–1209.
- [75] GUERRA, M., C. SCHMIDT, J. C. MCCLURE, L. E. MURR, and A. C. NUNES (2002) “Flow patterns during friction stir welding,” *Materials Characterisation*, **49**, pp. 95–101.
- [76] SEIDEL, T. U. and A. P. REYNOLDS (2001) “Visualization of the material flow in AA2195 friction-stir welds using a marker insert technique,” *Metallurgical & Materials Transactions A*, **32**(2879–2884).
- [77] COLEGROVE, P. A. and H. R. SHERCLIFF (2004) “Development of Trivex friction stir welding tool Part 1 - two-dimensional flow modelling and experimental validation,” *Science and Technology of Welding and Joining*, **9**, pp. 345–351.
- [78] MAHONEY, M., C. RHODES, J. FLINTOFF, R. SPURLING, and W. BINGEL (1998) “Properties of friction-stir-welded 7075 T651 aluminum,” *Metallurgical and Materials Transactions A*, **29A**(7), pp. 1955 - 1964.

- [79] RHODES, C., M. MAHONEY, W. BINGEL, R. SPURLING, and C. BAMPTON (1997) "Effect of friction stir welding on microstructure of 7075 aluminum," *Scripta Materialia*, **36**(1), pp. 69 - 75.
- [80] LIU, G., L. MURR, C.-S. NIOU, J. MCCLURE, and F. VEGA (1997) "Microstructural aspects of the friction-stir welding of 6061-T6 aluminum," *Scripta Materialia*, **37**(3), pp. 355 - 361.
- [81] COLLIGAN, K. (1999) "Material flow behavior during friction stir welding of aluminum," *Welding Journal, Research Supplement*, **78**, pp. 229s-237s.
- [82] SCHNEIDER, J. A. and A. C. NUNES (2004) "Characterization of plastic flow and resulting microtextures in a friction stir weld," *Metallurgical & Materials Transactions B*, **35**, pp. 777-783.
- [83] BAILLAS, G. and C. D. DONNE (2000) "Characterisazion of friction stir welded joints of the aluminium alloy AA 2024-T3 by laser extensometry," *Materialprufung*, **42**, pp. 236-239.
- [84] KRISHNAN, K. N. (2002) "On the formation of onion rings in friction stir welds," *Materials Science & Engineering A*, **327**, pp. 246-251.
- [85] NORMAN, A. F., T. BROUGH, and P. B. PRAGNELL (2000) "High resolution EBSD analysis of the grain structure in an AA2024 friction sir weld," in *Aluminium alloys 2000: Their physical and mechanical properties, Parts 1-3*, vol. 331-3, pp. 1713-1718.
- [86] BOOTH, D. and I. SINCLAIR (2002) "Fatigue of friction stir welded 2024-T351 aluminium alloy," in *Aluminium alloys 2002: Their physical and mechanical properties, Parts 1-3*, vol. 396-4, pp. 1671-1676.
- [87] LEE, W. B., Y. M. YEON, and S. B. JUNG (2003) "The joint properties of dissimilar formed Al alloys by friction stir welding according to the fixed location of materials," *Scripta Materialia*, **49**, pp. 423-428.
- [88] ATTALLAH, M. M., C. L. DAVIS, and M. STRANGWOOD (2007) "Influence of base metal microstructure on microstructural development in aluminium based alloy friction stir welds," *Science and Technology of Welding and Joining*, **12**, pp. 361-369.
- [89] SATO, Y. S., H. KOKAWA, K. IKEDA, M. ENOMOTO, S. JOGAN, and T. HASHIMOTO (2001) "Microtexture in the friction-stir weld of an aluminum alloy," *Metallurgical & Materials Transactions A*, **32**, pp. 941-948.
- [90] FONDA, R. W., K. E. KNIPLING, and J. F. BINGERT (2008) "Microstructural evolution ahead of the tool in aluminium friction stir welds," *Scripta Materialia*, **58**, pp. 343-348.

- [91] FRATINI, L., G. BUFFA, D. PALMERI, J. HUA, and R. SHIVPURI (2006) “Material flow in FSW of AA7075-T6 butt joints: Numerical simulations and experimental verifications,” *Science and Technology of Welding and Joining*, **11**, pp. 412–421.
- [92] AYER, R., H. JIN, R. MUELLER, S. LING, and S. FORD (2005) “Interface structure in a Fe-Ni friction stir welded joint,” *Scripta Materialia*, **53**, pp. 1383–1387.
- [93] PEEL, M. J., A. STEUWER, P. J. WITHERS, T. DICKERSON, Q. SHI, and H. SHERCLIFF (2006) “Dissimilar friction stir welds in AA5083-AA6082. Part I: Process parameter effects on thermal history and weld properties,” *Metallurgical and Materials Transactions A*, **37A**(7), pp. 2183–2193.
- [94] AVILA, R. E. (2006) “A variational model for shear stress in friction stir welding based on the weld shape in transverse sections,” *Modelling and Simulation in Materials Science and Engineering*, **14**, pp. 689–702.
- [95] SATO, Y., M. URATA, and H. KOKAWA (2002) “Parameters controlling microstructure and hardness during friction-stir welding of precipitation-hardenable aluminum alloy 6063,” *Metallurgical & Materials Transactions A*, **33**(3), pp. 625–635.
- [96] ZHAO, Y. H., S. B. LIN, Z. Q. HE, and L. WU (2006) “Microhardness prediction in friction stir welding of 2014 aluminium alloy,” *Science and Technology of Welding and Joining*, **11**, pp. 178–182.
- [97] CHANG, C. I., C. J. LEE, and J. C. HUANG (2004) “Relationship between grain size and Zener–Holloman parameter during friction stir processing in AZ31 Mg alloys,” *Scripta Materialia*, **51**, pp. 509–514.
- [98] COLEGROVE, P. A. and H. R. SHERCLIFF (2006) “CFD modelling of friction stir welding of thick plate 7449 aluminium alloy,” *Science and Technology of Welding and Joining*, **11**, pp. 429–441.
- [99] BHADESHIA, H. K. D. H. (2008) “Mathematical models in materials science,” *Materials Science and Technology*, **24**, pp. 128–135.
- [100] THOMAS, W. M., K. I. JOHNSON, and C. S. WIESNER (2003) “Friction stir welding—recent developments in tool and process technologies,” *Advanced Engineering Materials*, **5**, pp. 485–490.
- [101] THOMAS, W. M. (2003) “Friction stir welding - Recent developments,” *Materials Science Forum*, **426–4**, pp. 229–236.

- [102] THOMAS, W. M., D. G. STAINES, and K. I. J. P. EVANS (2003) “Com-stir - Compound motion for friction stir welding and machining,” *Advanced Engineering Materials*, **5**, pp. 273–274.
- [103] MISHRA, R. and Z. MA (2005) “Friction stir welding and processing,” *Materials Science & Engineering R: Reports*, **50**(1-2), pp. 1 - 78.
- [104] ZHAO, Y. H., S. B. LIN, F. QU, and L. WU (2006) “Influence of pin geometry on material flow in friction stir welding process,” *Materials Science and Technology*, **22**, pp. 45–50.
- [105] LEE, W. B. and S. B. JUNG (2004) “The joint properties of copper by friction stir welding,” *Materials Letters*, **58**, pp. 1041–1046.
- [106] LEE, S. H., J. Y. KANG, H. N. HAN, K. H. OH, H. C. LEE, D. W. SUH, and S. J. KIM (2005) “Variant Selection in Mechanically-induced Martensitic Transformation of Metastable Austenitic Steel,” *ISIJ International*, **45**, pp. 1271–1219.
- [107] MANDAL, A. and P. ROY (2006) “Modeling the compressive strength of molasses–cement sand system using design of experiments and back propagation neural networks,” *Journal of Materials Processing Technology*, **180**, pp. 167–173.
- [108] CRAWFORD, R., G. E. COOK, A. M. STRAUSS, D. A. HARTMAN, and M. A. STREMLER (2006) “Experimental defect analysis and force prediction simulation of high weld pitch friction stir welding,” *Science and Technology of Welding and Joining*, **11**, pp. 657–665.
- [109] LIU, H. J., H. FUJII, M. MAEDA, and K. NOGI (2004) “Tensile fracture location characterisation of friction stir welded joints of different aluminium alloys,” *Journal of Materials Science and Technology*, **20**, pp. 103–105.
- [110] KIMA, Y. G., H. FUJII, T. TSUMURA, T. KOMAZAKI, and K. NAKATA (2006) “Three defect types in friction stir welding of aluminium die casting alloys,” *Materials Science & Engineering A*, **415**, pp. 250–254.
- [111] LEAL, R. and A. LOUREIRO (2004) “Defect formation in friction stir welding of aluminium alloys,” *Advanced Materials Forum II*, **455–456**, pp. 299–302.
- [112] FUJII, H., R. UEJI, Y. TAKADA, H. KITAHARA, N. TSUJI, K. NAKATA, and K. NOGI (2006) “Friction stir welding of ultrafine grained interstitial free steels,” *Materials Transactions JIM*, **47**, pp. 239–242.
- [113] REYNOLDS, A. P., W. TANG, M. POSADA, and J. DELOACH (2003) “Friction stir welding of DH36 steel,” *Science and Technology of Welding and Joining*, **8**, pp. 455–460.

- [114] ELANGO VAN, K. and V. BALASUBRAMANIAN (2007) “Influences of pin profile and rotational speed of the tool on the formation of friction stir processing zone in AA2219 aluminium alloy,” *Materials Science & Engineering A*, **459**, pp. 7–18.
- [115] KIMAPONG, K. and T. WATANABE (2005) “Effect of welding process parameters on mechanical properties of FSW lap joint between aluminium alloy and steel,” *Materials Transactions*, **46**(2211–2217).
- [116] WITHERS, P. J. and H. K. D. H. BHADSHIA (2001) “Residual Stress Part 1 - Measurement Techniques,” *Materials Science and Technology*, **17**, pp. 355–365.
- [117] WITHERS, P. J. and H. K. D. H. BHADSHIA (2001) “Residual Stress Part 2 - Nature and Origins,” *Materials Science and Technology*, **17**, pp. 366–375.
- [118] FRANCIS, J. A., H. J. STONE, S. KUNDU, R. B. ROGGE, H. K. D. H. BHADSHIA, P. J. WITHERS, and L. KARLSSON (2007) “Transformation Temperatures and Welding Residual Stresses in Ferritic Steels,” in *Proceedings of PVP2007, ASME Pressure Vessels and Piping Division Conference*, American Society of Mechanical Engineers, ASME, San Antonio, Texas, pp. 1–8.
- [119] OHTA, A., N. SUZUKI, Y. MAEDA, K. HIRAOKA, and T. NAKAMURA (1999) “Superior fatigue crack growth properties in newly developed weld metal,” *International Journal of Fatigue*, **21**, pp. S113–S118.
- [120] STEFANESCU, D., C. E. TRUMAN, D. J. SMITH, and P. S. WHITEHEAD (2006) “Improvements in residual stress measurement by the incremental centre hole drilling technique,” *Experimental Mechanics*, **46**, pp. 417–427.
- [121] YA, M., F. L. DAI, and J. LU (2003) “Study of nonuniform in-plane and in-depth residual stress of friction stir welding,” *Journal of Pressure Vessel Technology – Transactions of the ASME*, **125**, pp. 201–208.
- [122] JAMES, M. N., D. G. HATTINGH, D. J. HUGES, L. W. WEI, E. A. PATTERSON, and J. Q. D. FONSECA (2004) “Synchrotron diffraction investigation of the distribution and influence of residual stresses in fatigue,” *Fatigue and Fracture of Engineering Materials and Structures*, **27**, pp. 609–622.
- [123] PEEL, M., A. STEUWER, M. PREUSS, and P. J. WITHERS (2003) “Microstructure, mechanical properties and residual stresses as a function of welding speed in aluminium AA5083 friction stir welds,” *Acta Materialia*, **51**(16), pp. 4791–4801.

- [124] CHEN, C. M. and R. KOVACEVIC (2006) “Parametric finite element analysis of stress evolution during friction stir welding,” *Journal of Engineering Manufacture*, **220**, pp. 1359–1371.
- [125] KHANDKAR, M. Z. H., J. A. KHAN, A. P. REYNOLDS, and M. A. SUTTON (2006) “Predicting residual thermal stresses in friction stir welded metals,” *Journal of Materials Processing Technology*, **174**, pp. 195–203.
- [126] SOUNDARARAJAN, V., S. ZEKOVIC, and R. KOVACEVIC (2005) “Thermo-mechanical model with adaptive boundary conditions for friction stir welding of Al 6061,” *International Journal of Machine Tools & Manufacture*, **45**, pp. 1577–1587.
- [127] STARON, P., M. KOCAK, and S. WILLIAMS (2002) “Residual stresses in friction stir welded Al sheets,” *Applied Physics A – Materials Science and processing*, **74**, pp. S1161–S1162.
- [128] RICHARDS, D. G., P. B. PRAGNELL, P. J. WITHERS, S. W. WILLIAMS, A. WESCOTT, and E. C. OLIVER (2006) “Geometry effects when controlling residual stresses in friction stir welds by mechanical tensioning,” *Residual Stress VII*, **524–525**, pp. 71–76.
- [129] SUTTON, M. A. (2006) “Limited weld residual stress measurements in fatigue crack propagation: Part II. FEM-based fatigue crack propagation with complete residual stress fields,” *Fatigue and Fracture of Engineering Materials and Structures*, **29**, pp. 537–545.
- [130] JOHN, R., K. V. JATA, and K. SADANANDA (2003) “Residual stress effects on near-threshold fatigue crack growth in friction stir welds in aerospace alloys,” *International Journal of Fatigue*, **25**, pp. 939–948.
- [131] DE, A. and T. DEBROY (2005) “Reliable calculations of heat and fluid flow during conduction mode laser welding through optimization of uncertain parameters,” *Welding Journal*, **84**, pp. 101s–112s.
- [132] DE, A. and T. DEBROY (2006) “Probing unknown welding parameters from convective heat transfer calculation and multivariable optimization,” *Journal of Physics D – Applied Physics*, **37 (1)**, pp. 140–150.
- [133] KUMAR, A., W. ZHANG, and T. DEBROY (2005) “Improving reliability of modelling heat and fluid flow in complex gas metal arc fillet welds - part I: an engineering physics model,” *Journal of Physics D – Applied Physics*, **38**, pp. 119–126.

- [134] MASON, J. J., A. J. ROSAKIS, and G. RAVICHANDRAN (1994) “On the strain and strain–rate dependence of the fraction of plastic work converted to heat – an experimental–study using high–speed infrared detectors and the Klosky bar,” *Journal of Materials Processing Technology*, **17**, pp. 135–145.
- [135] BHATTACHARYYA, D., P. J. RICHARDS, and A. A. SOMASHEKAR (1992) “Modelling of metal extrusion using the package,” *Journal of Materials Processing Technology*, **35**(1), pp. 93–111.
- [136] SCHUHMAN, R. (1952) *Metallurgical Engineering*, vol. 1, Addison-Wesley Press.
- [137] COLLIGAN, K. J. and R. S. MISHRA (2008) “A conceptual model for the process variables related to heat generation in friction stir welding of aluminum,” *Scripta Materialia*, **58**(5), pp. 327–331.
- [138] LIECHTY, B. C. and B. W. WEBB (2008) “Modeling the frictional boundary condition in friction stir welding,” *International Journal of Machine Tools and Manufacture*, **48**(12–13), pp. 1474–1485.
- [139] PATANKAR, S. V. (1980) *Numerical Heat Transfer and Fluid Flow*, Hemisphere Publishing Corporation, New York.
- [140] ZHU, X. K. and Y. J. CHAO (2004) “Numerical simulation of transient temperature and residual stresses in friction stir welding of 304L stainless steel,” *Journal of Materials Processing Technology*, **146**, pp. 263–272.
- [141] NANDAN, R., T. J. LIENERT, and T. DEBROY (2008) “Toward reliable calculations of heat and plastic flow during friction stir welding of Ti-6Al-4V alloy,” *International Journal of Materials Research*, **99**, pp. 434–444.
- [142] ROY, G. G., R. NANDAN, and T. DEBROY (2006) “Dimensionless correlation to estimate peak temperature during friction stir welding,” *Science and Technology of Welding and Joining*, **11**, pp. 606–608.
- [143] SUNDEN, B. (1992) “Viscous heating in forced convective heat-transfer across a circular cylinder at low Reynolds number,” *International Journal for Numerical Methods in Engineering*, **35**(4), pp. 729–736.
- [144] HASSAN, K. A. A., P. B. PRAGNELL, A. F. NORMAN, D. A. PRICE, and S. W. WILLIAMS (2003) “effect of welding parameters on nugget zone microstructure and properties in high–strength aluminium alloy friction stir welds,” *Science and Technology of Welding and Joining*, **8**, pp. 257–268.
- [145] SU, P., A. GERLICH, M. YAMAMOTO, and T. H. NORTH (2007) “Formation and retention of local melting films in AZ91 friction stir spot welds,” *Journal of Material Science*, **42**, pp. 9954–9965.

- [146] SCHMIDT, H. B. and J. H. HATTEL (2008) "Thermal modelling of friction stir welding," *Scripta Materialia*, **58**, pp. 332–337.
- [147] ARBEGAST, W. J. (2008) "A flow-partitioned deformation zone model for defect formation during friction stir welding," *Scripta Materialia*, **58**(5), pp. 372-376.
- [148] DARRAS, B. M. and M. K. KHRAISHEH (2008) "Analytical modeling of strain rate distribution during friction stir processing," *JOURNAL OF MATERIALS ENGINEERING AND PERFORMANCE*, **17**(2), pp. 168-177.
- [149] GOLDBERG, D. E. (1989) *Genetic algorithms in search, optimization, and machine learning*, Addison-Wesley Pub. Co., Reading, Mass.
- [150] STORN, R. and K. PRICE (1997) "Differential evolution - A simple and efficient heuristic for global optimization over continuous spaces," *Journal of Global Optimization*, **11**(4), pp. 341-359.
- [151] CHAKRABORTI, N., K. MISRA, P. BHATT, N. BARMAN, and R. PRASAD (2001) "Tight-binding calculations of Si-H clusters using genetic algorithms and related techniques: Studies using differential evolution," *Journal of Phase Equilibria*, **22**(5), pp. 525-530.
- [152] RUZEK, B. and M. KVASNICKA (2001) "Differential evolution algorithm in the earthquake hypocenter location," *Pure and Applied Geophysics*, **158**(4), pp. 667-693.
- [153] STORN, R. (2005) "Designing nonstandard filters with differential evolution," *Ieee Signal Processing Magazine*, **22**(1), pp. 103-106.
- [154] PRICE, K. V., R. M. STORN, and J. A. LAMPINEN (2005) *Differential evolution : a practical approach to global optimization*, Natural computing series, Springer, Berlin; New York.
- [155] PRICE, K. and R. STORN (1997) "Differential evolution," *Dr Dobbs Journal*, **22**(4), pp. 18-24.
- [156] MAYER, D. G., J. A. BELWARD, and K. BURRAGE (2001) "Robust parameter settings of evolutionary algorithms for the optimisation of agricultural systems models," *Agricultural Systems*, **69**(3), pp. 199-213.
- [157] KAHVECI, A. I. and G. E. WELSCH (1986) "Effect of Oxygen on the Hardness and Alpha-Beta-Phase Ratio of Ti-6Al-4V Alloy," *Scripta Metallurgica*, **20**(9), pp. 1287-1290.

- [158] JIN, H. W., R. AYER, R. MUELLER, S. LING, and S. FORD (2006) "Metallography of dissimilar Fe-Ni joint by friction stir welding," *International Journal of Offshore and Polar Engineering*, **16**(3), pp. 228-232.
- [159] MILES, M. P., D. W. MELTON, and T. W. NELSON (2005) "Formability of friction-stir-welded dissimilar-aluminum-alloy sheets," *Metallurgical and Materials Transactions a-Physical Metallurgy and Materials Science*, **36A**(12), pp. 3335-3342.
- [160] CAVALIERE, P., E. CERRI, and A. SQUILLACE (2005) "Mechanical response of 2024-7075 aluminium alloys joined by Friction Stir Welding," *Journal of Materials Science*, **40**(14), pp. 3669-3676.
- [161] OUYANG, J. H. and R. KOVACEVIC (2002) "Material flow and microstructure in the friction stir butt welds of the same and dissimilar aluminum alloys," *Journal of Materials Engineering and Performance*, **11**(1), pp. 51-63.
- [162] SHIGEMATSU, I., Y. J. KWON, K. SUZUKI, T. IMAI, and N. SAITO (2003) "Joining of 5083 and 6061 aluminum alloys by friction stir welding," *Journal of Materials Science Letters*, **22**(5), pp. 353-356.
- [163] ZETTLER, R., T. DONATH, J. F. DOS SANTOS, F. BECKMAN, and D. LOHWASSER (2006) "Validation of marker material flow in 4mm thick friction stir welded Al2024-T351 through computer microtomography and dedicated metallographic techniques," *Advanced Engineering Materials*, **8**(6), pp. 487-490.
- [164] BRATLAND, D. H., O. GRONG, H. SHERCLIFF, O. R. MYHR, and S. TJOTTA (1997) "Modelling of precipitation reactions in industrial processing," *Acta Materialia*, **45**(1), pp. 1-22.
- [165] SVENSSON, L. E., L. KARLSSON, H. LARSSON, B. KARLSSON, M. FAZZINI, and J. KARLSSON (2000) "Microstructure and mechanical properties of friction stir welded aluminium alloys with special reference to AA 5083 and AA 6082," *Science & Technology of Welding & Joining*, **5**(5), pp. 285-296, 1362-1718.
- [166] DUAN, X. and T. SHEPPARD (2003) "Computation of substructural strengthening by the integration of metallurgical models into the finite element code," *Computational Materials Science*, **27**(3), pp. 250-258.

Vita

Rituraj Nandan

Rituraj Nandan was born in Patna (Bihar), India on September 10, 1981. He did his primary schooling in Mt. Carmel School, Giridih and Don Bosco Academy, Patna before joining Delhi Public School, Bokaro for secondary school education. In July 2000, he entered the Indian Institute of Technology, Kharagpur, India where he pursued a four-year program leading to the degree of Bachelor of Technology in Metallurgical and Materials Engineering. He graduated in May 2004. In August 2004, he joined the Department of Materials Science and Engineering at The Pennsylvania State University, University Park, to pursue graduate research under the guidance of Professor Tarasankar DebRoy.

He received American Welding Society Graduate Fellowship Grant for 2007-2009 and was given Academic Excellence award in 2007 by the department of Materials Science and Engineering at Penn State. His publications during Ph.D are listed below:

- Metallurgical and Materials Transactions A, 2006, vol. 37, pp. 1247-1259.
- Science and Technology and Welding and Joining, 2006, vol. 11, pp. 526-537.
- Science and Technology and Welding and Joining, 2006, vol. 11, pp. 606-608.
- Acta Materialia, 2007, vol. 55(3), pp. 883-895.
- Welding Journal, 2007, vol. 86, pp. 231s-240s.
- Mathematical Modeling of Weld Phenomena 8, 2007, vol. 86, pp. 505-530.
- International Journal of Materials Research, 2008, pp. 434-444.
- Welding Handbook, 2007, 9th ed., vol. 3, pp. 211-261, AWS, Miami, FL.
- Progress in Materials Science, 2008, vol. 53(6), pp. 980-1023.
- Scripta Materialia, 2009, vol. 60(1), pp. 13-16.